

A Coupled Local Mode Approach to Laterally
Heterogeneous Anisotropic Media, Volume Scattering,
and T -wave Excitation

Darin J. Soukup

A dissertation submitted in partial fulfillment
of the requirements for the degree of

Doctor of Philosophy

University of Washington

2004

Program Authorized to Offer Degree: Department of Earth and Space Sciences

UMI Number: 3139544

INFORMATION TO USERS

The quality of this reproduction is dependent upon the quality of the copy submitted. Broken or indistinct print, colored or poor quality illustrations and photographs, print bleed-through, substandard margins, and improper alignment can adversely affect reproduction.

In the unlikely event that the author did not send a complete manuscript and there are missing pages, these will be noted. Also, if unauthorized copyright material had to be removed, a note will indicate the deletion.

UMI[®]

UMI Microform 3139544

Copyright 2004 by ProQuest Information and Learning Company.

All rights reserved. This microform edition is protected against unauthorized copying under Title 17, United States Code.

ProQuest Information and Learning Company
300 North Zeeb Road
P.O. Box 1346
Ann Arbor, MI 48106-1346

University of Washington
Graduate School

This is to certify that I have examined this copy of a doctoral dissertation by

Darin J. Soukup

and have found that it is complete and satisfactory in all respects,
and that any and all revisions required by the final
examining committee have been made.

Chair of Supervisory Committee:



Robert I. Odom

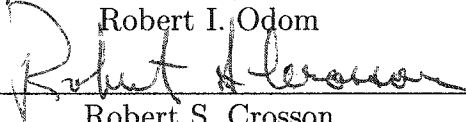
Reading Committee:



John R. Booker



Robert I. Odom



Robert S. Crosson

Date:

July 29, 2004

In presenting this dissertation in partial fulfillment of the requirements for the doctoral degree at the University of Washington, I agree that the Library shall make its copies freely available for inspection. I further agree that extensive copying of this dissertation is allowable only for scholarly purposes, consistent with "fair use" as prescribed in the U.S. Copyright Law. Requests for copying or reproduction of this dissertation may be referred to Proquest Information and Learning, 300 North Zeeb Road, Ann Arbor, MI 48106-1346, to whom the author has granted "the right to reproduce and sell (a) copies of the manuscript in microform and/or (b) printed copies of the manuscript made from microform."

Signature *Dan J. Sahp*

Date *July 29, 2004*

University of Washington

Abstract

A Coupled Local Mode Approach to Laterally
Heterogeneous Anisotropic Media, Volume Scattering,
and T -wave Excitation

by Darin J. Soukup

Chair of Supervisory Committee:

Professor Robert I. Odom
Department of Earth and Space Sciences

This dissertation presents theoretical and numerical results for the coupled local mode formalism applied to the seismo-acoustic wavefield in generally anisotropic range-dependent media. General anisotropy affects the form of the elastic stiffness tensor, which directly affects the polarization of the local modes, the frequency and angular dispersion curves, the coupling and scattering of the local modes in range-dependent media, and also introduces the effects of nearly degenerate modes. The effects of anisotropy and the combination of anisotropy and lateral heterogeneity are examined for 1-D and 2-D models, respectively. Horizontally polarized shear motion is determined to play an important role in seismo-acoustic wave propagation, where modes have significant bottom interaction with anisotropic sediments at low frequencies. The discrete modes for tilted anisotropy are best described as quasi-P-SV, quasi-SH, and generalized P-SV-SH modes with particle motions in all three Cartesian coordinate directions.

Lateral heterogeneity is introduced through interface and volume terms. The

relative significance of deterministic and stochastic effects from the interface and volume scattering terms are considered. New stochastic volume scattering terms are derived by applying perturbation theory to the elastic equations of motion and boundary conditions. Anisotropy enhances modal scattering, which leads to the loss of signal coherence, and apparent energy loss if not properly accounted for.

Coupled-mode scattering theory is applied to the T -wave excitation problem. Modal scattering from lateral heterogeneity along the seafloor is shown to convert energy from the directly excited hybrid crustal-acoustic modes to propagating acoustic modes. Both refraction from a sloping seafloor and seafloor scattering act as T -wave generation mechanisms, with each mechanism entering the modal scattering theory as separate terms. In addition, fault type is strongly correlated with T -wave excitation efficiency, while low shear speed sediment cover enhances T -wave generation. The discrete modes contribute to the majority of the seismic source field for shallow sources, and the continuum spectrum becomes increasingly important with greater source depth.

TABLE OF CONTENTS

List of Figures	iv
List of Tables	vii
Chapter 1: Introduction	1
Chapter 2: Anisotropy Background	8
2.1 Transversely Isotropic Elastic Symmetry	8
2.2 Bond Transformation	11
2.3 Chapter Summary	16
Chapter 3: 1-D Plane Layered Anisotropic Structure	18
3.1 Modal Formalism for Plane Layered Anisotropic Structure	18
3.2 Anisotropic Model and Numerical Code	25
3.3 Slowness Curves	29
3.4 Angular and Frequency Dispersion Curves	33
3.5 Generalized Modes for Anisotropic Media	42
3.6 Chapter Summary	54
Chapter 4: Anisotropy and Geometrical Heterogeneity	57
4.1 Coupled Local Mode Formalism for Range-Dependent Anisotropic Media	57
4.2 Laterally Heterogeneous Anisotropic Media	60
4.3 Deterministic Interface Coupling Matrices	62
4.4 Stochastic Interface Coupling Matrices	69

4.5	Chapter Summary	73
Chapter 5:	Deterministic and Stochastic Volume Scattering	77
5.1	Description of Deterministic Elastic Moduli	78
5.2	Numerical Modeling for Deterministic Volume Scattering	80
5.3	Coupled Local Mode Formalism for Stochastic Volume Heterogeneity	82
5.4	Stochastic Perturbation of Elastic Moduli	87
5.5	Stochastic Volume Coupling Matrices	92
5.6	Chapter Summary	97
Chapter 6:	<i>T</i>-wave Excitation and Coupled Local Modes	98
6.1	Coupled-Mode Scattering Theory and <i>T</i> -wave excitation	101
6.2	Fault Type Events, Continuum Modes, and Sediment Cover Effects on <i>T</i> -wave Generation	107
6.3	Chapter Summary	116
Chapter 7:	Summary and Conclusions	119
	Glossary	124
	References	127
	Appendix A: VTI Anisotropy Parameterization	135
	Appendix B: Elastic Stiffness Tensor and Matrix Notation	138
	Appendix C: Bond Transformation of TI Symmetric Structures	145
	Appendix D: Symmetry Planes and Wave Polarizations	150
	Appendix E: Equations of Motion and First Order Equations	157

Appendix F: Differential Operator A	160
Appendix G: Deterministic and Stochastic Coupling Matrices	165

LIST OF FIGURES

1.1	VTI Compositionally Layered Structure and Tilted TTI Symmetry	3
1.2	Fixed Cartesian Coordinate System	4
2.1	Lines of Constant Elevation and Azimuth	14
2.2	Sensitivity of the C_{11} Element to Angular Rotations	16
3.1	1-D Plane Layered Homogeneous Anisotropic Structure	19
3.2	Velocity and Density Profile of 1-D Plane Layered Anisotropic Structure	27
3.3	VTI Slowness Curves for XY, XZ, YZ-Planes	31
3.4	Slowness Curves for Symmetry Axis Rotations	32
3.5	Frequency Dispersion Curves & "Solotone" Effect	34
3.6	Angular Dispersion Curves	36
3.7	Stacked Angular Dispersion Curves	41
3.8	Pure P-SV and SH Modes	45
3.9	P-SV Mode for X, Y, and Z Axes	46
3.10	Sample quasi-P-SV, quasi-SH, and P-SV-SH Modes	47
3.11	Sample Invariant Acoustic Mode	48
3.12	Frequency Dependence of an Invariant Acoustic Mode	49
3.13	Switching of Modal Characteristics	50
3.14	Source Excitation of P-SV and SH Modes	52
3.15	Source Excitation of quasi-P-SV, quasi-SH, and P-SV-SH Modes	53
4.1	2-D Layered Laterally Heterogeneous Anisotropic Structure	61

4.2	\mathbf{B}_{qr} Deterministic Interface Terms for P-SV and SH Modes	64
4.3	\mathbf{B}_{qr} Deterministic Interface Terms for quasi-P-SV, quasi-SH, and P-SV-SH modes	65
4.4	\mathbf{B}_{qr} Interface Term Coupling Matrix for Near Degeneracy	67
4.5	Moment Tensor Excitation and Coupling Matrices	70
4.6	\mathbf{S}_{qr} Stochastic Interface Terms for P-SV and SH Modes	72
4.7	\mathbf{S}_{qr} Stochastic Interface Terms for quasi-P-SV, quasi-SH, and P-SV-SH Modes	74
5.1	\mathbf{B}_{qr} Deterministic Volume Terms for P-SV and SH modes	81
5.2	\mathbf{B}_{qr} Deterministic Volume Terms for quasi-P-SV, quasi-SH, and P-SV-SH Modes	83
5.3	Stochastic Perturbation of Density and Elastic Moduli	89
5.4	\mathbf{H}_{qr} Stochastic Interface Terms for P-SV and SH Modes	93
5.5	\mathbf{H}_{qr} Stochastic Interface Terms for quasi-P-SV, quasi-SH, and P-SV-SH Modes	94
5.6	\mathbf{H}_{qr} Stochastic Volume Scattering Terms for P-SV and SH modes	95
5.7	\mathbf{H}_{qr} Stochastic Volume Scattering Terms for quasi-P-SV, quasi-SH, and P-SV-SH Modes	96
6.1	1 st Acoustic Mode and Hybrid Crustal-Acoustic Mode	102
6.2	Initial seismo-acoustic wavefield	103
6.3	Scattered seismo-acoustic wavefield	105
6.4	Wavefield Sensitivity to Source Type	106
6.5	Seismic Fault Type Events	107
6.6	Strike Angle Dependence	108
6.7	Downslope Conversion and Scattering Comparison	110

6.8	Fault Type Effect on Initial and Scatter Wavefields	112
6.9	Continuum Modes	113
6.10	Sediment Cover Effects	114
6.11	A Comparison of \mathbf{H}_{qr} and \mathbf{S}_{qr} Stochastic Interface Scattering Terms .	115
D.1	Elastic Stiffness Matrix for TTI	156

LIST OF TABLES

3.1	Velocity/Density Profile	28
3.2	Mode Wavelength Ranges	29
3.3	Phase Velocities of Invariant Acoustic Modes	38
3.4	P-SV and SH Particle Motion Independence	44
4.1	Symmetry Axis Orientation and Coupling	68
A.1	Love Notation	135
A.2	Takeuchi and Saito Notation	136
A.3	Backus Notation	137
B.1	Abbreviated Subscript Notation	139

ACKNOWLEDGMENTS

Professor Robert I. Odom, thank you for your wit, insight, guidance, encouragement, as well as patience over the years. I admire your zeal for science, and I sincerely appreciate all of the knowledge and support you have contributed to my graduate experience. May you continue to push forward the frontiers of science everyday. I would also like to thank the members of my supervisory and reading committees for reading this work, and helping shape its content.

I wish to thank Mark Ortmeyer for the many lunch time conversations which have been welcomed diversions and helped restore my sanity. Many thanks to everyone at the Monroe Vineyard for your belief in me and spurring me on to finish the work set before me. And many, many thanks to all of my family, and to everyone who has become my family. You have been an incredible source of strength during this educational journey.

And my most heartfelt thanks to my wife, Brooke, for your support has been unfailing and your understanding beyond measure. I could never have done this without you. Thank you for for your kind words, refreshing perspective, practical wisdom, and loving heart during these many years. Your encouragement, sacrifice, and longsuffering patience will never be forgotten.

This research was supported by the Office of Naval Research and by the University of Washington Applied Physics Laboratory Graduate Student Support Fund. Additional thanks to Professor Jeffrey Park from the Department of Geology and Geophysics of Yale University for the use of the ANIPROP code.

DEDICATION

To my most beloved wife Brooke

Chapter 1

INTRODUCTION

This dissertation presents both theoretical and numerical results which provide the foundation for modeling seismo-acoustic wave propagation in 1-D homogeneous anisotropic and 2-D range-dependent anisotropic shallow water environments. There is an apparent trade-off between anisotropy and lateral heterogeneity, and it can be difficult to separate the two effects in a propagating signal. However, some analytical expressions concerning the trade-offs between anisotropy and heterogeneity may be obtained, such as done by Mochizuki (1997). The motivation of this work is to begin the process of unraveling these two effects theoretically and numerically and consider them separately within a coupled-mode framework.

The forward seismo-acoustic wave propagation problem is studied in the context of anisotropy, and deterministic and stochastic lateral heterogeneity. Shallow water environments may be highly variable, with both lateral heterogeneity and anisotropy being almost ubiquitous in the seafloor bottom/subbottom regions. Some common causes of lateral heterogeneity in shallow water environments are marine sediment composition, non-planar boundaries, rough surfaces, strong density and/or velocity contrasts, and variations in water column depth and/or sediment cover thickness. Shallow water sediments exhibit considerable lateral heterogeneity over short ranges (Stoll *et. al.*, 1994). In addition to lateral heterogeneity, anisotropy is often an intrinsic property of marine sediments. Marine sediments exhibit anisotropy and high velocity gradients in shear velocity (Ewing *et. al.*, 1992). Anisotropy in material

properties can lead to observed anisotropic effects in fluid flow(permeability), heat or electrical conductivity (resistivity), stress and strains, or elastic properties for example (Friedman and Jones, 2001). When considering acoustic propagation, the elastic properties of anisotropic marine sediments are of primary concern. Possible sources of elastic anisotropy in marine sediments are reported to be the alignment of cracks and/or pores in the sediment structure, preferred orientation of mineral grains, and lamination as a result of compositional layering. (Carlson *et. al.*, 1984).

Marine sediments often have transversely isotropic elastic symmetry (TI) with the fast velocity directions in the plane parallel to the bedding plane and the slow velocity direction along the normal of the bedding plane as shown in Figure 1.1. The slow velocity direction is parallel to an infinite fold symmetry axis \hat{s} , also shown in Figure 1.1. It is likely this type of elastic anisotropy observed in marine sediments is predominantly due to compositional layering (Carlson *et. al.*, 1984).

There exists a wide body of literature on the investigations of wave propagation in TI environments, and much recent work has been done investigating more generalized anisotropy. The majority of investigations have concentrated on TI elastically symmetric media with a vertical symmetry axis(VTI), where $\hat{s} = \hat{z}$ as in Figure 1.1, or with a horizontal symmetry axis(HTI), where $\hat{s} = \cos \varphi \hat{x} + \sin \varphi \hat{y}$. Figure 1.1 and Figure 1.2 show the fixed coordinate frame of reference. An example of a VTI medium is the horizontally layering of fine isotropic sediments, and an HTI medium can be produced by the introduction of vertical parallel cracks in isotropic sediments. Although VTI and HTI are completely adequate for some geophysical applications, there are many instances where a more general orientation of the symmetry axis \hat{s} is needed, and should be considered to complement the existing body of VTI and HTI work. Simply having VTI or HTI layered sediments with non-horizontal bedding planes provides an example of a TI medium with a non-vertical and non-horizontal tilted symmetry axis. Anisotropic variations other than azimuthal may also be considered, where the anisotropic symmetry axis \hat{s} is allowed to tilt in both azimuth φ

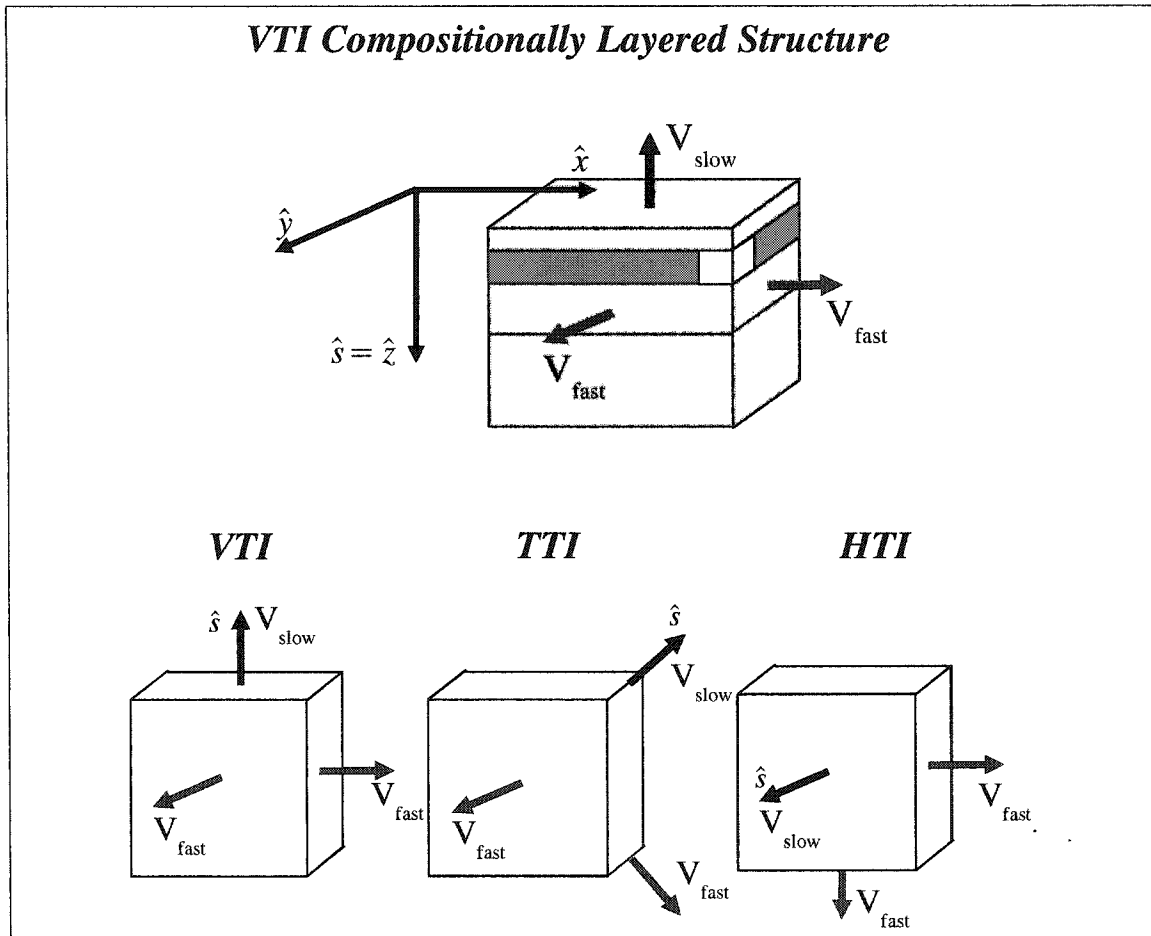


Figure 1.1: A representative elastically symmetric transversely isotropic structure (TI) due to compositional layering. The fast velocity directions \mathbf{V}_{fast} are normal to \hat{s} and parallel to the bedding plane. The slow velocity direction \mathbf{V}_{slow} is parallel to the vertical symmetry axis. A TI structure with a vertical symmetry axis is labeled as VTI or azimuthally isotropic. The geometrical orientation of the anisotropy depends on the orientation of the symmetry axis \hat{s} . The bottom figures are expansions of the the white block of material from the top figure. A structure can be transversely isotropic with a vertical, tilted (neither vertical nor horizontal), or horizontal symmetry axis and be classified as VTI, TTI, or HTI respectively. For a VTI orientation, the fast velocity direction is in the horizontal plane. A TTI orientation results in the fast velocity direction being contained to an oblique plane and the HTI orientation restricts the fast velocity directions to a vertical plane normal to the symmetry axis \hat{s} . Note that the slow velocity direction (\mathbf{V}_{slow}) always corresponds with the symmetry axis direction \hat{s} .

Fixed Cartesian Coordinate System

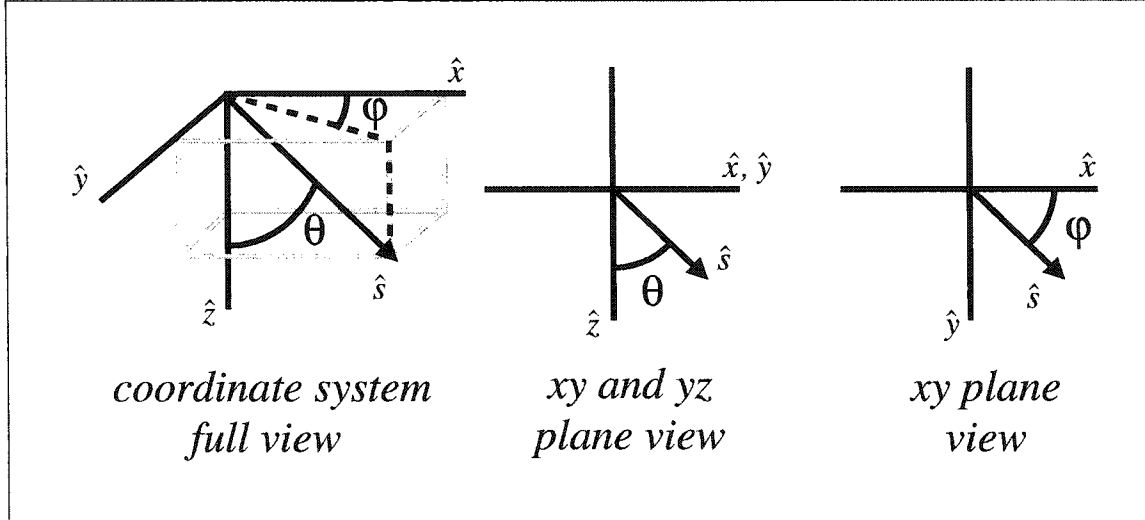


Figure 1.2: The Cartesian coordinate system is defined with the x-direction corresponding with the direction of propagation, the z-direction is positive downwards, and the y-direction is free of any lateral variations. The symmetry axis \hat{s} is defined in reference to the fixed Cartesian coordinate system by the spherical coordinate angles θ and φ . The angle between the z-axis and the symmetry axis \hat{s} is described by θ . The angle between the projection of the symmetry axis \hat{s} onto the horizontal plane and the x-direction is described by φ .

and elevation θ , the angle in the horizontal coordinate plane and the angle with respect to the vertical axis respectively. Martin *et. al.* (1997), Thomson *et. al.* (1997), and Zhu and Dorman (2000) provide complementary results to the work presented in this dissertation. In addition, Martin *et. al.* (1997) provides an excellent summary of work relevant to the topic of anisotropy and coupled modes.

A modal description of an acoustic signal is helpful in determining which regions the signal predominantly propagates in. An acoustic signal may be composed of acoustic modes, hybrid crustal-acoustic modes also known as seismo-acoustic modes, and crustal modes. A pure acoustic mode propagates energy in the water column and has very little interaction with the bottom/subbottom. A pure crustal mode

propagates its energy in the sediment and basement layers. The hybrid crustal-acoustic mode has significant energy in both the water column and the underlying sediment and basement layers.

Neglecting any seafloor bottom/subbottom elastic properties may be a reasonable approach for problems involving high frequencies where the depth of the water column is much greater than the wavelength of the acoustic signal of interest. For these problems the acoustic signal may be entirely contained within the water column and may not interact with the elastic properties of the seafloor. However, for low frequencies and shallow water environments the bottom interaction of the acoustic signal becomes significant, and affects the propagation of the acoustic signal. An seismo-acoustic wavefield will interact with the bottom/subbottom at some portion if not the entire length of the propagation path. Therefore, the characteristics of the acoustic signal are influenced by interactions with the seafloor and seabed. Energy from the acoustic wavefield can be scattered, radiated into the bottom, or absorbed by attenuation, resulting in a signal that is more accurately described as seismo-acoustic. It is these effects of scattering and seafloor interaction that this dissertation addresses. The seismo-acoustic signal then is composed of both acoustic modes and hybrid crustal-acoustic modes. In this work the focus remains predominantly on acoustic and hybrid crustal-acoustic modes (seismo-acoustic modes) with energy within the fluid layer. Park and Odom (1998) investigate the effects of VTI elastic symmetry on local modes and on the coupling of local modes, focusing on sediment modes. Their model has been modified to facilitate the study of acoustic and seismo-acoustic modes in a generally anisotropic medium. The work of Park and Odom (1998,1999) is extended by including a more generalized description of anisotropy found in marine sediments. A modal formalism and coupled local mode formalism are used to examine the seismo-acoustic wave propagation in 1-D and 2-D anisotropic models respectively. The coupled local mode formalism is not necessary for wave propagation in a 1-D homogeneous plane layered anisotropic structure.

However, the coupled local mode formalism is an appropriate method for the 2-D range-dependent anisotropic wave propagation problem. Therefore the method of modes is also applied when the wave propagation problem reduces to a 1-D homogeneous plane layered anisotropic structure. The effect of symmetry axis rotations on the propagating modes are investigated.

The body of the dissertation centers around two distinct models. The first model describes general anisotropy for a 1-D homogeneous plane layered structure. The effects of anisotropy, entirely independent of any range-dependence are considered. The second model focuses on the effects of anisotropy in combination with lateral heterogeneity, expressed in a 2-D range-dependent medium. Anisotropic effects on mode coupling and scattering, induced by lateral heterogeneity are considered.

Chapter 2 provides some background on anisotropy, and the treatment of the elastic moduli in this dissertation. An introduction to TI elastic symmetry and nomenclature is found in section 2.1 and section 2.2 demonstrates the usefulness of the Bond transformation in obtaining a generalized elastic stiffness tensor. The chapter concludes with a brief chapter summary in section 2.3. Chapter 3 discusses anisotropy and wave propagation for a 1-D homogeneous anisotropic plane-layered structure. A brief description of the modal formalism of Maupin(1988) as applied to the 1-D anisotropic structure is contained in section 3.1. The anisotropic model/profile is described in section 3.2 and slowness curves are considered in section 3.3. Section 3.4 covers angular and frequency dispersion curves while section 3.5 provides the resulting generalized eigenfunctions. The chapter summary is found in section 3.6. The combined effects of anisotropy and geometrical lateral heterogeneity are presented in chapter 4, beginning in section 4.1 with a brief discussion on the coupled local mode formalism of Maupin (1988) for a 2-D range-dependent anisotropic structure. The description of the 2-D range-dependent anisotropic structure and its velocity/density profile is found in section 4.2 and a discussion on coupled local modes, including deterministic coupling matrices, eigenfunctions, and dispersion curves is presented

in section 4.3. A similar treatment of the stochastic boundary coupling terms is described in section 4.4. The discussion of results are contained in the chapter summary of section 4.5. Deterministic and stochastic volume terms are considered in chapter 5 of this dissertation. The deterministic lateral dependence of the elastic moduli are considered in section 5.1, and numerical calculations of deterministic volume coupling terms are presented in section 5.2. Sections 5.3 and 5.4 deal with incorporating stochastic variations into the coupled-mode formalism and the elastic moduli respectively. Stochastic volume scattering matrices are discussed in section 5.5. Another summary concludes this chapter in section 5.6. Chapter 6 applies the modal scattering theories from the previous chapters to the T -wave excitation problem. The first section 6.1 of the T -wave chapter 6 has been previously published (Park *et. al.*, 2001) with minor changes to reflect the dissertation content. Section 6.2 presents additional T -wave excitation considerations. The summary of the Park *et. al.* (2001) paper has also been included in the section 6.3, the T -wave chapter summary. The dissertation is concluded with a final overall summary in chapter 7.

The notation used along with definitions of variables or parameters can be found in the Glossary. A variety of useful relations, such as theory, and concepts concerning anisotropy have been collected and presented in the appendices. Appendix A defines some possible forms of anisotropy parameterization, while Appendix B expands on the elastic stiffness tensor and matrix notation. Appendix C elaborates on the specifics of the Bond transform for a TI medium and symmetry planes and wave polarizations are considered in Appendix D for TI elastic symmetry. A generalized form of the first order equations are contained in Appendix E. Appendix F provides further insight on the differential operator \mathbf{A} from the equations of motion and Appendix G defines the coupling matrix \mathbf{B}_{qr}

Chapter 2

ANISOTROPY BACKGROUND

Background on anisotropy and the form of the elastic stiffness matrix is presented as a foundation for the following chapters. A description of transversely isotropic elastic symmetry is given. The Bond transformation is used to obtain an arbitrary symmetry axis \hat{s} , and therefore an arbitrary orientation of the transverse medium. In addition, the sensitivity of elements of the elastic stiffness matrix to angular rotations is considered. Both analytical and numerical results of the rotational sensitivity are presented.

2.1 Transversely Isotropic Elastic Symmetry

Nomenclature for anisotropy has not been standardized in the literature. This poses a problem that Crampin (1989) and Winterstein(1990) recognized over a decade ago. Because transverse isotropy is used with multiple meanings in the current literature, any possible confusion is attempted to be eliminated by explicitly stating the nomenclature used in this work.

For the purposes of this dissertation, a general anisotropic medium is defined by an elastic stiffness tensor belonging to the transversely isotropic elastic symmetry system. The nomenclature of Winterstein (1990) is used, where TI refers to a medium with transversely isotropic elastic symmetry having an infinite-fold symmetry axis. A medium retains its TI elastic symmetry regardless of the orientation of the symmetry axis or any physical rotation of the media. A TI medium with a vertical, horizontal, or arbitrarily tilted symmetry axis is labeled VTI, HTI, and TTI respectively.

The term "transverse" in transverse isotropy refers to any direction which is perpendicular to the symmetry axis of the medium and not to a fixed coordinate direction. Occasionally a TI medium may be referred to as azimuthally isotropic if the symmetry axis is vertical. As noted by Winterstein (1990), TI has occasionally been used to refer to a VTI medium. In addition, hexagonal symmetry has often been used interchangeably with the TI symmetry in the wave propagation communities. Both TI and hexagonally symmetric media have the same strain-energy functions, and the elastic equation of motion will be exactly the same for both media.

Elastically, a hexagonally symmetric and TI symmetric medium look exactly the same, but compositionally or structurally they are quite different. It is likely that a real earth structure would belong to the transverse isotropy symmetry class, and according to Winterstein (1990), sediments are unlikely to be structurally hexagonally symmetric. Elastically, TI and hexagonal symmetries have the exact same degree of symmetry, since both require five elastic constants. However, structurally TI has a higher degree of symmetry and is closer in symmetry to isotropy than the hexagonal symmetry. This is a result of TI having an infinite-fold symmetry axis (cylindrical symmetry), while the hexagonal symmetry only has a six-fold symmetry.

A TI elastic symmetry system is distinguished by a unique form of the elastic stiffness tensor. The elastic stiffness tensor has five independent moduli that define the individual elements. Each element of the tensor is a linear combination of the five independent moduli, which can be parameterized into several forms. They may be expressed as velocities, elastic moduli, or even a combination of ratios of velocities and elastic moduli (see Appendix A). In comparison, a fluid is described by one elastic moduli and an isotropic material is described by only two elastic moduli. Although the elastic symmetry has been limited to transverse isotropy for this work, the theory and some portions of the code can incorporate more general anisotropy (up to 21 independent elastic moduli). The elastic stiffness matrix ${}^a\mathbf{C}$ for a VTI medium is described in equation (2.1). The A, C, F, L, N and $H = A - 2N$ represent the VTI

elastic moduli in Love (1944) notation. The 6×6 abbreviated subscript matrix ${}^a\mathbf{C}$ contains all of the information of the elastic stiffness tensor, C_{ijkl} (see Appendix B).

$${}^a\mathbf{C} = \begin{bmatrix} A & H & F & 0 & 0 & 0 \\ H & A & F & 0 & 0 & 0 \\ F & F & C & 0 & 0 & 0 \\ 0 & 0 & 0 & L & 0 & 0 \\ 0 & 0 & 0 & 0 & L & 0 \\ 0 & 0 & 0 & 0 & 0 & N \end{bmatrix} \quad \text{where } H = A - 2N \quad (2.1)$$

The form or appearance of the elastic stiffness matrix is similar to an orthorhombic symmetric medium. They share the same non-zero elements and the same zero elements. The TI medium has a higher degree of symmetry than the orthorhombic medium, which has nine independent constants. The VTI medium in equation 2.1 may be thought of having the appearance of a quasi-orthorhombic medium. Such similarities with other symmetry systems are helpful when the elastic stiffness matrix ${}^aC_{IJ}$ is rotated to more general orientations.

The elastic moduli A, C, F, L, N from the above VTI medium in equation (2.1) can be related to velocities for compressional and shear plane-waves in the medium. The following describe the wave velocities for horizontally transmitted plane waves within the xy-plane.

$$\alpha_H \equiv \sqrt{\frac{A}{\rho}} \quad \text{compressional waves} \quad (2.2)$$

$$\beta_H \equiv \sqrt{\frac{N}{\rho}} \quad \text{horizontally polarized shear waves} \quad (2.3)$$

$$\beta_V \equiv \sqrt{\frac{L}{\rho}} \quad \text{vertically polarized shear waves} \quad (2.4)$$

A vertically transmitted plane wave parallel to the z-axis have the velocities

$$\alpha_V \equiv \sqrt{\frac{C}{\rho}} \quad \text{compressional waves} \quad (2.5)$$

$$\beta_V \equiv \sqrt{\frac{L}{\rho}} \quad \text{shear waves} \quad (2.6)$$

The elastic constant F is not typically defined in terms of a plane wave velocity. Muyzert and Snieder (2000) relate the elastic parameter F to a velocity of a wave propagating in a vertical plane between a source and receiver, and assign a velocity γ to the elastic parameter. Muyzert and Snieder (2000) indicate that Anderson (1961) relates this velocity γ to a wave with an incidence angle of 45° with the vertical axis.

$$\gamma \equiv \sqrt{\frac{F}{\rho}} \quad \text{velocity within the vertical } xz\text{-plane} \quad (2.7)$$

where $\gamma^2 = \alpha^2 - 2\beta^2$ in an isotropic medium.

The α and β represent the compressional and shear velocities, respectively, and the subscripts H and V denote the horizontal and vertical displacement directions. When $A = C = \lambda + 2\mu$, $L = N = \mu$, and $F = \lambda$, the medium is isotropic and rotationally independent.

2.2 Bond Transformation

Using the Bond transform for tilting a structure's symmetry axis has been suggested by Crampin (1981) and Winterstein (1990) and actually implemented for acoustic body waves by Auld (1990) and recently by Zhu and Dorman (2000) and Okaya and McEvilly (2003). The Bond transformation is applied in the study of global modes and coupled local modes to obtain a general rotation of the elastic stiffness matrix with TI symmetry.

A formalism similar to Crampin (1981) is used where the propagation direction is assumed to always coincide along a fixed coordinate direction, the x-axis. The elastic stiffness tensor is rotated in order to consider anisotropy with various symmetry axis orientations. This is equivalent to keeping the elastic stiffness tensor fixed and varying the direction of propagation. The first method is preferred because the theory does not need to be modified for each directional change, only the elements of the elastic stiffness tensor need to be changed. A physical reasonableness to the modeling should be retained. Randomly perturbing various elements of C_{IJ} can lead

to a non-physical elastic stiffness matrix. By starting with a real physical model, the reasonableness of the model is maintained regardless of any rotation of the medium. Odom *et. al.* (1996) provides a good summary of the conditions which constrain the elastic moduli of a TI elastically symmetric medium. Another advantage of the Bond Transformation is working with a 6×6 matrix with only 36 individual elements rather than a fourth order tensor with 81 individual elements, of which at most 21 can be independent. Complex tensor transformations are replaced with simple matrix multiplication to transform the elastic stiffness matrix to any arbitrary orientation.

The elastic stiffness matrix is a function of the spherical coordinate angles θ and φ when ${}^a C_{IJ} = {}^a C_{IJ}(\theta, \varphi)$. Rotating the elastic stiffness matrix ${}^a C_{IJ}$ essentially changes the form of the elastic stiffness tensor, and how the matrix or tensor is populated. This directly affects the solution of the equation of motion as the elements of ${}^a C_{IJ}$ change.

For an isotropic medium, the direction of propagation does not matter. All planes are symmetry planes and all directions are symmetry axis directions. The elements of the elastic stiffness tensor do not change with any rotation of the medium. For an anisotropic medium, the velocity of plane waves vary with propagation direction through the medium. The elements of the elastic stiffness tensor change with any rotation of the medium. For a TI elastically symmetric medium, five independent elastic moduli along with two polar coordinates relating the symmetry axis and the propagation direction are needed to adequately describe the velocity of plane wave through the medium. The elements of ${}^a C_{IJ}$ are linear combinations of the five independent constants, being functions of the polar angles θ and ϕ .

While the elastic stiffness matrix may be rotated, the physical boundaries, discontinuities and the boundary conditions of the 1-D structure remain fixed. The procedure for implementing the Bond transformation is to rotate the elastic stiffness matrix with respect to a fixed set of coordinate axes. In general three angles ψ, θ, φ are needed to transform the elastic stiffness matrix ${}^a C_{ij}$ to any arbitrary orientation.

The rotations are taken first about the z-axis, next about the y-axis, and finally about the z-axis again. ψ is an angle in the xy-plane and corresponds to the first rotation about the z-axis. The angle θ is defined in the xz-plane and corresponds to the second rotation about the y-axis. The final angle φ is also defined in the xy-plane which corresponds to the third rotation about the vertical axis. When the starting medium is VTI, only rotations through the angles θ and φ need to be considered. In figure 1.1 the Bond transformation is visually demonstrated. The elastic stiffness matrix representing the elastic constants within the layer can be rotated to any arbitrary orientation, as shown by the white blocks at the bottom of the figure.

The spherical coordinates of the symmetry axis directions, $\hat{s} = \hat{s}(\theta, \varphi)$ can be projected onto a unit sphere. When tilting the symmetry axis, the symmetry axis traces lines of constant elevation on the unit sphere as φ is varied and remains θ fixed. Similarly, keeping φ fixed at some value and varying the value of θ traces lines of constant azimuth. The lines of constant elevation represent changes in azimuthal anisotropy and the lines of constant azimuth representation changes in elevational anisotropy. These are shown as red arcs in figure 2.1.

Applying the Bond Transformation to the unrotated elastic moduli elements within ${}^a\mathbf{C}''$:

$${}^a\mathbf{C}' = [\mathbf{M}^y][{}^a\mathbf{C}''][\mathbf{M}^y]^T \quad \text{Bond transformation about y-axis} \quad (2.8)$$

$${}^a\mathbf{C} = [\mathbf{M}^z][{}^a\mathbf{C}'][\mathbf{M}^z]^T \quad \text{Bond transformation about z-axis} \quad (2.9)$$

\mathbf{M}^y and \mathbf{M}^z are transformation matrices (e.g. Auld, 1990) about the y-axis and z-axis respectively, and are defined for an elastic stiffness tensor with TI symmetry in the Appendix C.

Substituting equation (2.8) into equation (2.9) and using the matrix multiplication property $[\mathbf{M}^z\mathbf{M}^y]^T = [\mathbf{M}^y]^T[\mathbf{M}^z]^T$ to obtain:

$${}^a\mathbf{C} = [\mathbf{R}][{}^a\mathbf{C}''][\mathbf{R}]^T \quad \text{where } \mathbf{R} = \mathbf{M}^z\mathbf{M}^y. \quad (2.10)$$

Lines of Constant Elevation and Azimuth

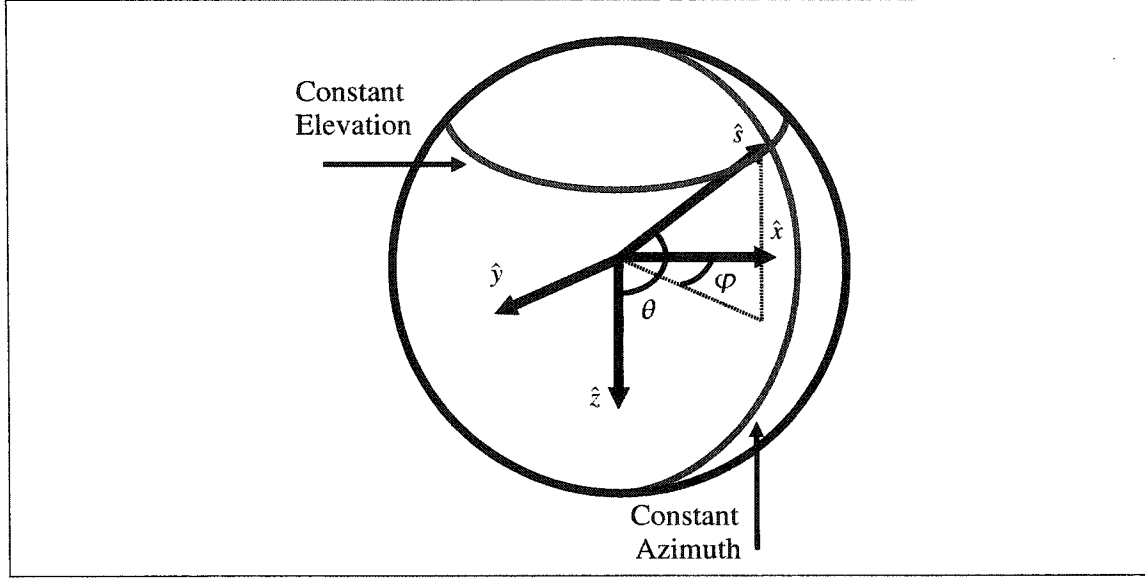


Figure 2.1: Any tilt of the symmetry axis with respect to the fixed coordinate system results in an azimuthal, elevational, or a combination of azimuthal and elevational change in anisotropy. The red line in the horizontal plane represents changes of azimuth φ of the symmetry axis and the red line in the vertical plane represents changes in elevation θ of the symmetry axis.

The individual elements of the elastic-stiffness tensor can be found by the following relation for a medium with TI elastic symmetry.

$$\begin{aligned}
 {}^a C_{IJ} &= A(R_{i1}R_{j1} + R_{i2}R_{j2}) + H(R_{i1}R_{j2} + R_{i2}R_{j1}) \\
 &+ F(R_{i1}R_{j3} + R_{i2}R_{j3} + R_{i3}R_{j1} + R_{i3}R_{j2}) + CR_{i3}R_{j3} \\
 &+ L(R_{i4}R_{j4} + R_{i5}R_{j5}) + NR_{i6}R_{j6}
 \end{aligned} \tag{2.11}$$

The elements of ${}^a C_{IJ}$ are dependent upon the orientation of the symmetry axis through the elements of \mathbf{R} . A rotation of the symmetry axis changes the value of any given element in C_{IJ} , where the specific elements of C_{IJ} remain linear combinations of A, C, F, L, N as demonstrated by equation(2.11). The tractable, analytic form for the rotated elastic stiffness matrix found in equation (2.11) is due to the large number

of elements with zero-values for a VTI medium, as shown in equation (2.1).

The sensitivity of the ${}^a C_{IJ}$ elements rotation can be determined by taking the derivative of equation (2.11) with respect to θ and φ . The derivative with respect to a generic angle Δ is:

$$\frac{\partial({}^a \mathbf{C})}{\partial \Delta} = \frac{\partial({}^a C_{IJ})}{\partial \Delta} \quad \text{where } \Delta = \theta \text{ or } \varphi \quad (2.12)$$

The angular sensitivity of a TI symmetric medium with an arbitrarily tilted symmetry axis may be express as:

$$\begin{aligned} \frac{\partial({}^a C_{IJ})}{\partial \Delta} = & A \left(\frac{\partial R_{i1}}{\partial \Delta} R_{j1} + R_{i1} \frac{\partial R_{j1}}{\partial \Delta} + \frac{\partial R_{i2}}{\partial \Delta} R_{j2} + R_{i2} \frac{\partial R_{j2}}{\partial \Delta} \right) \\ & + H \left(\frac{\partial R_{i1}}{\partial \Delta} R_{j2} + R_{i1} \frac{\partial R_{j2}}{\partial \Delta} + \frac{\partial R_{i2}}{\partial \Delta} R_{j1} + R_{i2} \frac{\partial R_{j1}}{\partial \Delta} \right) \\ & + F \left(\frac{\partial R_{i1}}{\partial \Delta} R_{j3} + R_{i1} \frac{\partial R_{j3}}{\partial \Delta} + \frac{\partial R_{i2}}{\partial \Delta} R_{j3} + R_{i2} \frac{\partial R_{j3}}{\partial \Delta} \right. \\ & \quad \left. \frac{\partial R_{i3}}{\partial \Delta} R_{j1} + R_{i3} \frac{\partial R_{j1}}{\partial \Delta} + \frac{\partial R_{i3}}{\partial \Delta} R_{j2} + R_{i3} \frac{\partial R_{j2}}{\partial \Delta} \right) \\ & + C \left(\frac{\partial R_{i3}}{\partial \Delta} R_{j3} + R_{i3} \frac{\partial R_{j3}}{\partial \Delta} \right) \\ & + L \left(\frac{\partial R_{i4}}{\partial \Delta} R_{j4} + R_{i4} \frac{\partial R_{j4}}{\partial \Delta} + \frac{\partial R_{i5}}{\partial \Delta} R_{j5} \right) + R_{i5} \frac{\partial R_{j5}}{\partial \Delta} \\ & + N \left(\frac{\partial R_{i6}}{\partial \Delta} R_{j6} + R_{i6} \frac{\partial R_{j6}}{\partial \Delta} \right) \end{aligned} \quad (2.13)$$

Each element of the ${}^a C_{IJ}$ matrix may be evaluated through equation (2.11) and equation (2.13). Figure 2.2 plots the ${}^a C_{11}$ element and its angular sensitivity as functions of θ and φ .

Auld (1990) provides a good treatment of the Bond transformation and additional details are also included in Appendix C. Appendix D contains a useful and instructional tutorial on symmetry planes and wave polarizations for a TI medium. Similar to Okaya and McEvelly (2003), quasi symmetries have been determined for TI symmetry when the symmetry axis \hat{s} is rotated to specific orientations. Whereas they determined that rotations about the y-axis result in a monoclinic form of the

Sensitivity of the C_{11} Element to Angular Rotations

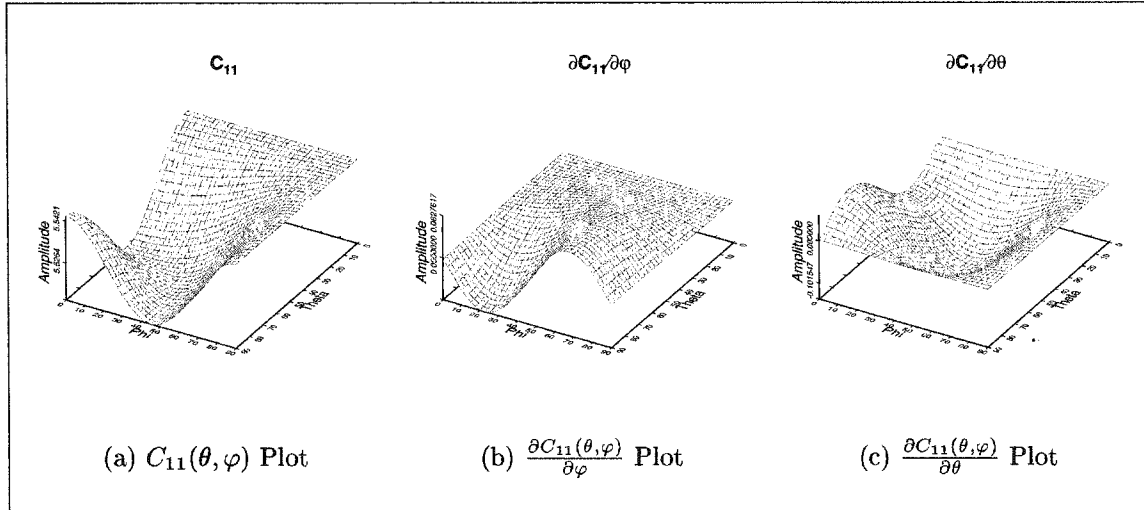


Figure 2.2: The C_{11} element of the elastic stiffness matrix ${}^a C_{IJ}$ is shown in Figure 2.2(a) for various angles of θ and φ . This is a numerical plot of equation 2.11. Figures 2.2(b) and 2.2(c) plot the sensitivity of the C_{11} element to the angles φ and θ respectively.

elastic stiffness matrix, the rotations in Appendix D show that rotations where the symmetry axis remains in any of the coordinate planes results in a quasi-monoclinic form of the elastic stiffness matrix.

2.3 Chapter Summary

Horizontal shear motion is often ignored or neglected in the modeling of acoustic signals, where the majority of attention has been placed on the P-SV motion. However, marine sediments support shear motion, and therefore must be treated elastically. In addition, marine sediments are almost ubiquitously anisotropic. Since it usually cannot be prearranged to record a seismo-acoustic signal in a symmetry plane, tilted anisotropy cannot be completely ignored. The form of anisotropy expressed in the elastic stiffness matrix ${}^a C_{IJ}$ directly shapes the formulation of the equations of

motion. Therefore, the form of the elastic stiffness matrix, and its symmetry in relation to the propagation direction affects the wave propagation in the seismo-acoustic waveguide. Understanding the properties of the anisotropy leads to a better understanding of the equations of motion used to describe the propagation of a signal in a seismo-acoustic waveguide. The Bond transformation has been used to simplify the rotation of the 4th order elastic stiffness tensor C_{ijkl} to an equivalent matrix rotation . Analytical forms for the rotated elastic stiffness matrix, and its sensitivity to angular rotations have been derived for elastically symmetric transverse isotropy.

Chapter 3

1-D PLANE LAYERED ANISOTROPIC STRUCTURE

A study of a 1-D homogeneous plane-layered structure, with the absence of any range-dependence is presented. By assuming anisotropic sediments, the elastic properties of the sediment layers are allowed to vary with propagation direction. Specifically, energy propagating along different directions within the sediment layers will result in the wave propagating at different velocities. These anisotropic sediments are assumed to have TI elastic symmetry with an arbitrarily oriented symmetry axis (\hat{s}). The effect of anisotropy on propagating modes, including changes in phase and group velocities, and eigenfunction polarizations are investigated.

3.1 Modal Formalism for Plane Layered Anisotropic Structure

A modal representation of the Green's function for the 1-D seismo-acoustic wave propagation problem is employed, with the expression of the wavefield as a superposition of global modes. The global modes are defined as the eigenfunctions (displacement and tractions) of a 1-D homogeneous anisotropic structure. The homogeneous plane-layered medium is infinite in the xy-plane, and the global modes are the eigenfunctions appropriate for the entire domain and path of propagation. The initial mode excitation may be determined by an appropriate source term.

The modal representation of the wavefield is a convenient method of solving the non-separable first order coupled equations of motion. The modes also provide a natural way of observing how sources and material parameters affect the wavefield. However, some limitations exist. The computation time for calculating the modes

and therefore the wavefield becomes larger as the number of layers of the model and/or frequency increases. This can be inconvenient for very detailed analyses.

1-D Plane Layered Homogeneous Anisotropic Structure

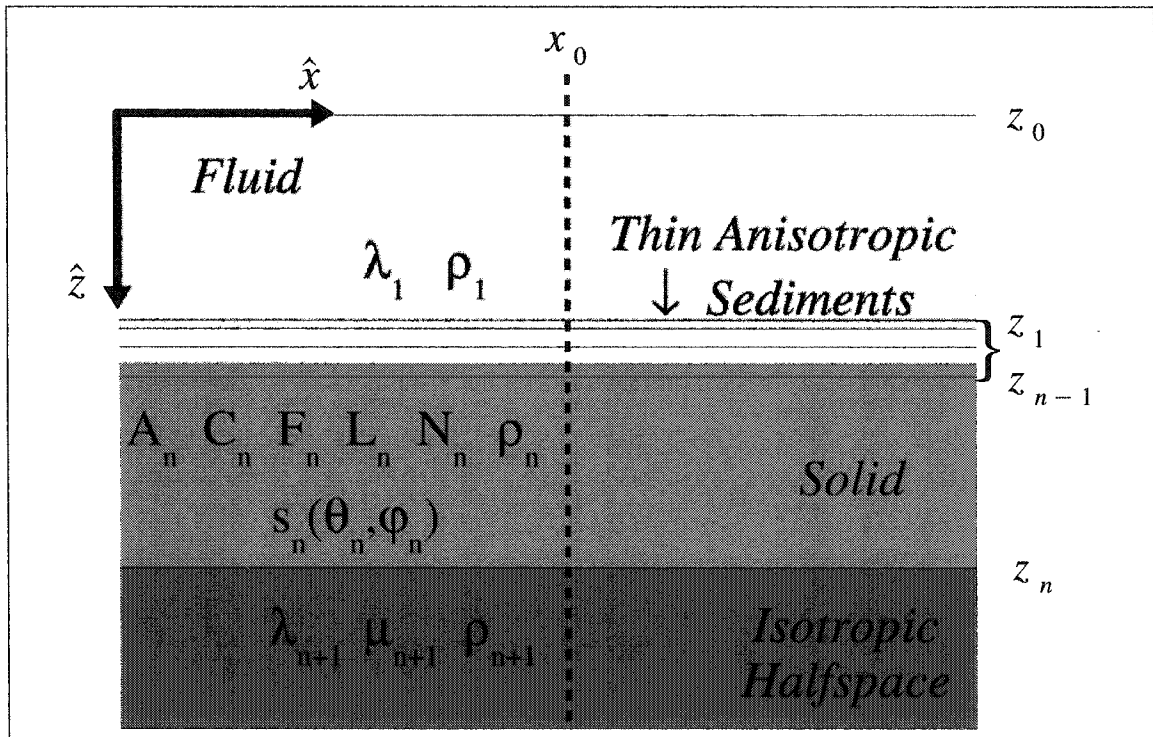


Figure 3.1: A 1-D plane layered homogeneous anisotropic structure representation of shallow water environments. The model contains fluid layers over thin anisotropic and/or isotropic sediments, additional sediment and/or basement layers, and is terminated by an isotropic halfspace. There are no lateral variations in the structure, and the elastic parameters only vary with depth. The anisotropy is restricted to elastically symmetric transverse isotropy, but the symmetry axis \hat{s} may have any arbitrary orientation.

The modal formalism based on Maupin's (1988) theory is presented for a 1-D plane layered seismo-acoustic environment with general anisotropy as shown in figure 3.1. This modal approach to the equations of motion has the advantage of allowing the physics of propagation to be examined on a mode by mode basis and is formally

exact. The modal theory arises out of the equations of motion and is a convenient first order theory. Additional and complimentary work with coupled-modes are given by Odom (1986), Maupin (1988), Odom *et. al.*(1996),and Park and Odom (1998, 1999). The theory for the 1-D plane layered wave propagation problem contains two critical steps: i) expressing the equation of motion as a first order differential equation and ii) solving the wave-equation with a superposition of global modes. For this chapter the application of the modes is limited to deterministic anisotropic structures. In addition, only the discrete modes are considered, while the continuum modes and their contribution are neglected. Attenuation is also ignored, although the theory remains valid for the inclusion of attenuation, since complex quantities have been accounted for throughout the theory. Weak attenuation could easily be included as a perturbation.

As previously shown in figure 1.1 and 1.2, a Cartesian coordinate system is assumed with wave propagation progressing in the horizontal direction parallel to the x-axis. The y-axis, the transverse direction, is the geometric symmetry axis for the 1-D medium along which material properties remain constant. This direction corresponds to the motion of a pure horizontally polarized shear wave. The z-axis is the vertical direction, positive downwards, and corresponds to the direction of motion of a pure vertically polarized shear wave.

The Einstein summation convention is assumed unless otherwise noted. The theory development uses both Woodhouse(1974) and abbreviated subscript notation (e.g. Auld, 1990), also known as Voigt notation (e.g. Nye, 1957), for representing the fourth order elastic stiffness tensor, C_{ijkl} . The Woodhouse notation is used primarily to represent a general anisotropic medium in the modal theory and the coupled local mode theory (chapter 4), and the abbreviated subscript notation is convenient for rotating the elastic stiffness matrix through the Bond transformation. In order to avoid some confusion, a superscript notation has been introduced. The superscripts w and a imply Woodhouse and abbreviated subscript notations respectively (i.e. ${}^w\mathbf{C}$

or ${}^a\mathbf{C}$). The indices of the fourth order elastic stiffness tensor are $iklj$ rather than the conventional $ijkl$ in order to facilitate the mapping between tensor notation and the matrix notation of Woodhouse (1974). In addition, lower case indices vary over ranges of $i, k, l, j = 1, 2, 3$ while upper case indices vary over ranges of $I, J = 1, 2, 3, 4, 5, 6$. A more detailed account of elastic stiffness tensor and matrix representations are located in Appendix B.

$$\begin{aligned} \mathbf{C} &= C_{iklj} && \text{fourth order elastic stiffness tensor} \\ {}^a\mathbf{C} &= {}^aC_{IJ} && 6 \times 6 \text{ abbreviated subscript elastic stiffness matrix} \\ {}^w\mathbf{C} &= ({}^wC_{ij})_{kl} && 9 \times 9 \text{ Woodhouse elastic stiffness matrix} \end{aligned}$$

The 3-component displacement field vector $\mathbf{w} = (w_1, w_2, w_3)$ is assumed to be in harmonic form and involves a double Fourier transform over y and t of the displacement field $\mathbf{w}(x, y, z, t)$:

$$\mathbf{w}(x, z, k_y, \omega) = \int_{-\infty}^{+\infty} \int_{-\infty}^{+\infty} \mathbf{w}(x, y, z, t) \exp(-ik_y y + i\omega t) dy dt \quad (3.1)$$

Note that the physics convention of the Fourier Transform has been used, the same as Aki and Richards (1980). The double Fourier transform has a mixed sign convention consistent for wave propagation problems. In contrast, Maupin(1988) used the engineering convention of the Fourier Transform. The right going wavefields in this work have a phase factor in the form:

$$\exp(ik_x x - i\omega t) \quad (3.2)$$

Throughout this work, all references to the displacement, traction, and stress-displacement vectors incorporate the double Fourier transform. The 3-component tractions can be expressed as:

$$\mathbf{t}_i = {}^wC_{ij} \frac{\partial \mathbf{w}}{\partial x_j} \quad (3.3)$$

where the elastic stiffness matrix, ${}^w C_{ij}$, is in Woodhouse (1974) notation. Each traction vector relates to stress elements in the form $\mathbf{t}_i = (\tau_{i1}, \tau_{i2}, \tau_{i3})$ for $i = 1, 2, 3$.

The equations of motion have the same general form for both fluid and solid media. The equations of motion are found in equation (E.1) of Appendix E. For solid media a 6-component displacement-stress vector $\mathbf{u} = (\mathbf{w}, \mathbf{t})^T$ can be introduced, where $\mathbf{t} = \mathbf{t}_1$. For fluid media, a 2-component displacement-stress vector may be defined as $\mathbf{u} = (\mathbf{w}, \mathbf{t})^T$ where $\mathbf{w} = w_1$ and $\mathbf{t} = \tau_{ii}$ (no summation). The first order equation of motion for the 1-D plane-layered structure shown in figure 3.1 can now be expressed as:

$$\frac{\partial \mathbf{u}}{\partial x} = \mathbf{A} \mathbf{u} - \mathbf{F} \quad (3.4)$$

A more generalized form of the first order equation is found in Appendix E. The boundary conditions are expressed as:

$$\begin{aligned} [\tau_{ii}]_m &= [\mathbf{w}_3]_m = 0 \\ [\mathbf{t}_3]_n &= [\mathbf{w}]_n = 0 \end{aligned} \quad (3.5)$$

where the m^{th} subscript is for fluid-fluid and fluid-solid interfaces and the n^{th} subscript is for solid-solid interfaces. A free-slip boundary condition is imposed on the horizontal displacements at the fluid-solid interfaces. The solid-solid interfaces are assumed to be welded contacts where the displacement vector \mathbf{w} and the traction vector \mathbf{t}_3 are continuous across the interfaces. For fluid-fluid interfaces and fluid-solid interfaces the displacements, w_3 , and the vertical stress, τ_{33} , are assumed to be continuous across the interfaces. Following the notation of Maupin(1988), the square brackets with a subscript (e.g. $[quantity]_{n,m}$) in equation (3.5) and the following equations represent the evaluation of a quantity across the interface m or n . The quantity may be continuous or discontinuous and the evaluation is taken from the bottom of the interface to the top of the interface. For example, a discontinuity in the elastic stiffness matrix across the n th interface would be expressed as:

$$[{}^a C_{ij}]_n = {}^a C_{ij} \Big|_{n^+} - {}^a C_{ij} \Big|_{n^-} \quad (3.6)$$

The differential operator \mathbf{A} , described in Maupin (1988), from equation (3.4) and the boundary conditions from equation (3.5) contain the physics of the 1-D problem for the plane layered homogeneous anisotropic structure. Implicit in the \mathbf{A} operator is the elastic stiffness matrix ${}^w\mathbf{C}$ which represents a TI elastically symmetric medium with an arbitrary symmetry axis. The orientation of the symmetry axis is defined by the two angles θ and φ as in figure 1.2 and figure 2.1. To obtain a general rotation of the elastic stiffness matrix with TI symmetry, the Bond transformation is utilized. The elements of the \mathbf{A} operator may be real or complex. Attenuation may be included as complex values when the medium becomes visco-elastic. Although attenuation effects are currently neglected, the complex form of the elements of the \mathbf{A} operator are retained. The generalized form of the operator \mathbf{A} in equation (E.18) of Appendix E is not complex for perfectly elastic (non-attenuating) media, but the form used by Maupin (1988) remains complex due to the explicit derivative with respect to the y -coordinate. The form of \mathbf{A} can be found in Appendix F for a fluid medium, a general solid anisotropic medium, as well as for specific tilted TI orientations where meaningful analytical results can be obtained. \mathbf{F} from equation (3.4) is the sum of an external source \mathbf{F}^S .

$$\mathbf{F} = \mathbf{F}^S = \begin{pmatrix} \mathbf{0} \\ \mathbf{f}^S \end{pmatrix} \quad (3.7)$$

A modal description of the wavefield is employed, and the reader is reminded that the modal representation of the wavefield is formally exact. The modes are independent solutions for the equations of motion and are functions only of depth. The initial wavefield, \mathbf{u} is expressed as a superposition of global modes $\mathbf{u}^r = (\mathbf{w}^r, \mathbf{r}^t)^T$ weighted by source excitation amplitude coefficients c_r^0 . The horizontal wave number is $k^r(\xi)$ and x_s denotes the source position.

$$\mathbf{u} = (\mathbf{w}, \mathbf{t})^T = \sum_r c_r^0 \exp\left(i \int_{x_s}^x k^r(\xi) d\xi\right) \mathbf{u}^r(z) \quad (3.8)$$

The modal description of the wavefield in equation (3.8) is for the discrete modes only,

and the continuum modes have been neglected. The seismo-acoustic signal propagating within the 1-D plane-layered waveguide will experience geometrical spreading as the signal propagates along the x-direction. The modes of the homogeneous plane-layered medium are also energy normalized.

$$\left(\frac{2}{\pi k^r (x - x_s)} \right)^{\frac{1}{2}} \quad \text{geometrical spreading term} \quad (3.9)$$

$$\left(\frac{1}{8v_c^r U^r I^r} \right)^{\frac{1}{2}} \quad \text{energy normalization term} \quad (3.10)$$

where v_c^r , U^r , and I^r are the phase velocity, group velocity, and energy integral of the mode r respectively as defined by Aki and Richards (1980).

Note that no assumptions have yet been made about the nature of the symmetry of the elastic layers in the modal theory. The theory describes propagation where the elastic regions have general triclinic anisotropy - a medium described by 21 independent elastic moduli. One consequence of restricting wave propagation to the x-direction is the reduction in the number of elastic elements from the elastic stiffness tensor C_{ijkl} needed to describe the medium. For the 3-D propagation problem, all 21 elements of the elastic stiffness tensor would be needed and included in the differential operator \mathbf{A} . For the 2-D propagation problem with propagation along the x-direction in a medium with triclinic symmetry, the total number of elastic elements needed from C_{ijkl} is 15. These fifteen elements of the elastic stiffness matrix remain linear combinations of the original 21 independent elastic moduli when ${}^a C_{IJ}$ has been rotated.

$${}^a \mathbf{C} = \begin{bmatrix} C_{11} & & C_{13} & C_{14} & C_{15} & C_{16} \\ & & & & & \\ C_{31} & & C_{33} & C_{34} & C_{35} & C_{36} \\ C_{41} & & C_{43} & C_{44} & C_{45} & C_{46} \\ C_{51} & & C_{53} & C_{54} & C_{55} & C_{56} \\ C_{61} & & C_{63} & C_{64} & C_{65} & C_{66} \end{bmatrix} \quad (3.11)$$

The second row and the second column of the elastic stiffness matrix in abbreviated subscript notation are not used in the 2-D wave propagation theory within the xz-plane. Using the symmetry relationships for the elastic stiffness tensor, the 15 elements of the abbreviated elastic stiffness matrix needed are:

$$\begin{aligned}
 & {}^a C_{11}, {}^a C_{13}, {}^a C_{14}, {}^a C_{15}, {}^a C_{16} \\
 & {}^a C_{33}, {}^a C_{34}, {}^a C_{35}, {}^a C_{36}, {}^a C_{44} \\
 & {}^a C_{45}, {}^a C_{46}, {}^a C_{55}, {}^a C_{56}, {}^a C_{66}
 \end{aligned} \tag{3.12}$$

The propagating seismo-acoustic signal will only be sensitive to these 15 elements of the elastic stiffness matrix, regardless of whether the elastic stiffness matrix is rotated or not. Essentially, the 2-D description excludes any sensitivity to the elements in the 2nd row and 2nd column of the elastic stiffness matrix. Zhu and Dorman (2000) also report a dependence of 15 elements for the elastic stiffness tensor for a general TI medium.

Every term in the differential operator \mathbf{A} which contains elastic moduli also contains the elements of the 3×3 submatrix ${}^w C_{11}$. It is reasonable to expect that the equations of motion and therefore the modes are sensitive to the changes in these elastic elements.

$${}^a C_{11}, {}^a C_{15}, {}^a C_{16}, {}^a C_{55}, {}^a C_{56}, {}^a C_{66} \tag{3.13}$$

3.2 Anisotropic Model and Numerical Code

Nine parameters are necessary to describe each elastic layer. The necessary parameters include the thickness of the layer, the density, the five elastic moduli, and the two polar angles for the symmetry axis. The elastic moduli A, C, F, L, N describe the intrinsic elastic symmetry of the layer, the polar angles describe the orientation of the symmetry, and the thickness describes the boundaries of the layer.

It is assumed that all anisotropic layers have the same symmetry axis orientation. The elastic properties are constant within each layer, where each layer may have its own degree of anisotropy, except the last layer which is defined as a uniform isotropic halfspace.

A sediment model that is representative of a typical marine sediment profile has been chosen. A typical sediment structure with TI anisotropy has its symmetry axis normal to the bedding planes. The density for typical sediments range from $1.90 - 2.49\text{g/cm}^3$, while compressional speeds vary from $1.87 - 4.87\text{km/s}$ and the degree of velocity variation due to anisotropy varies from 1-13% (Carlson *et al.*, 1984) The degree of anisotropy typically increases with depth, where sediments with bedding exhibit a higher degree of anisotropy than unbedded sediments. The global modes are determined for a 1-D plane layered medium with the velocity/density profile shown in figure 3.2.

The model is a variation of the Berge *et. al.* (1991) profile, and similar to the model used by Odom *et. al.* (1996) and Park and Odom (1998). The velocity and density profile is based upon a data set acquired *in situ* near the New Jersey coast from Berge *et. al.* (1991), with the addition of a deeper water column and an oceanic crustal component. The model consists of an isovelocity fluid layer, five thin anisotropic sediment layers and seven thin isotropic layers, a higher velocity subbottom layer, and a uniform isotropic halfspace as a basement layer. The model has a water column depth of 100m. The low shear speed sediments have a total thickness of 27.5m and overlay higher speed sediments 372.5m thick. The degree of anisotropy varies from 11% to 15% for the shear velocities. The compressional speeds of all the layers are isotropic. Figure 3.2 shows the velocity/density profile, while table 3.1 provides the parameter values for the model structure.

Table 3.1 indicates that the elastic symmetry is actually a reduced version of the TI elastic symmetry. In all of the layers $A = C$, leaving only four independent elastic moduli. This effectively places all of the anisotropy in the difference between

Velocity and Density Profile of 1-D Plane Layered Anisotropic Structure

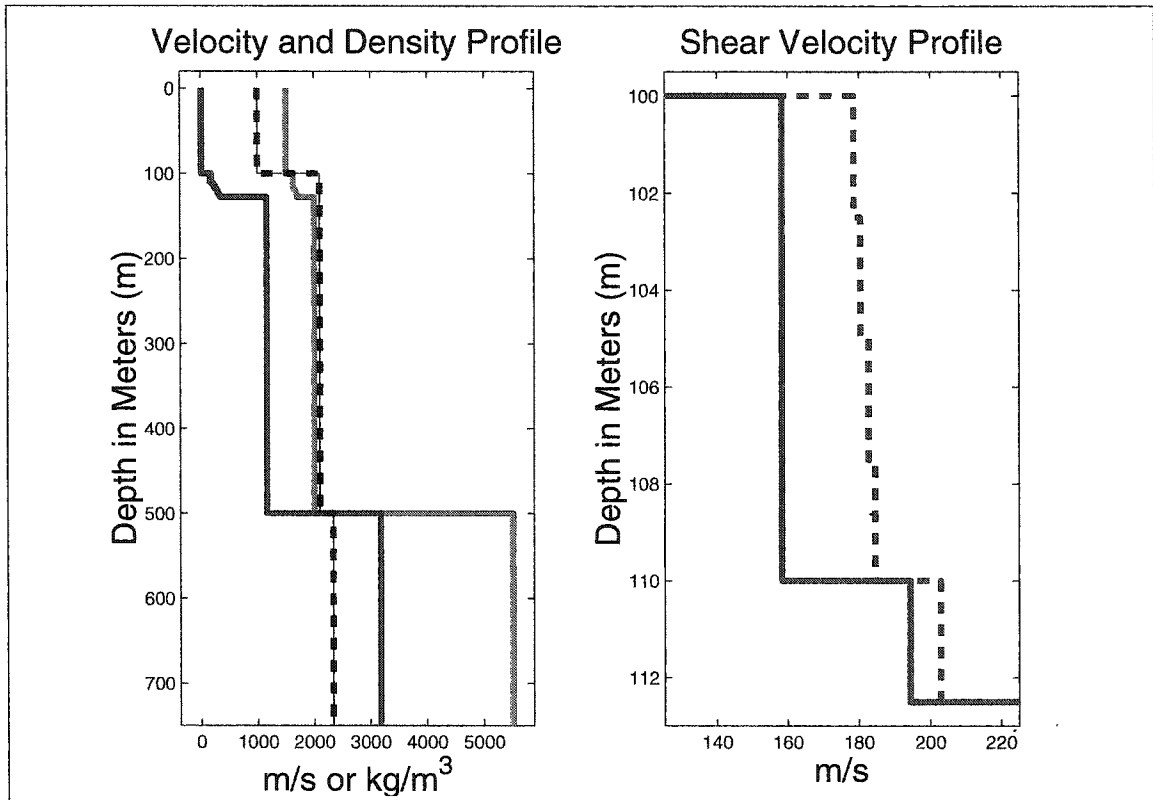


Figure 3.2: The velocity and density profile of the starting VTI medium. The red, blue, and dotted black lines represent the shear velocity, compressional velocity, and density respectively with depth. The profile on the right is an enlargement of the thin sediment region to show the shear wave velocity splitting within the anisotropic layers. The solid red line represents the vertical shear speed β_V and the dotted red line represents the horizontal shear speed β_H . Note that the velocity profile lacks any compressional anisotropy

the shear moduli N and L . The anisotropy is purely shear in nature, where the compressional velocity is isotropic and the shear velocity is transversely isotropic. Berge *et. al.*'s (1991) experiment was insensitive to compressional wave anisotropy.

The Berge *et. al.* (1991) data set is altered further by allowing the symmetry axis of the TI layers to vary. With the modified Berge *et. al.* model as a starting

Table 3.1: Velocity/Density Profile

DEPTH	$A = {}^aC_{11}$	$C = {}^aC_{33}$	$F = {}^aC_{13}$	$L = {}^aC_{44}$	$N = {}^aC_{66}$	ρ
100.00	2.250	2.2	2.2	0.0000	0.0000	1000
2.50	5.544	5.544	5.376	0.0526	0.0669	2100
2.50	5.544	5.544	5.376	0.0526	0.0683	2100
2.50	5.544	5.544	5.376	0.0526	0.0700	2100
2.50	5.544	5.544	5.376	0.0526	0.0714	2100
2.50	5.586	5.586	5.376	0.0792	0.0864	2100
2.50	5.586	5.586	5.366	0.1100	0.1100	2100
2.50	5.649	5.649	5.383	0.1330	0.1330	2100
2.50	5.754	5.754	5.438	0.1580	0.1580	2100
2.50	5.859	5.859	5.495	0.1820	0.1820	2100
2.50	5.964	5.964	5.550	0.2070	0.2070	2100
2.50	6.069	6.069	5.607	0.2310	0.2310	2100
372.50	8.400	8.400	2.798	2.8010	2.8010	2100
1000.00	70.634	70.634	23.528	23.5530	23.5530	2335

VTI medium, the symmetry axis is rotated for all the anisotropic layers by using the Bond transformation as discussed previously.

A phase velocity ordering is used for all of the modes when considering the eigenfunctions, dispersion curves, and coupling matrices. The modes are ordered from smallest phase velocity to the largest phase velocity, where the lowest order mode has the lowest phase velocity and the highest ordered mode has the highest phase velocity. Note that the phase velocity ordering scheme is independent of polarizations of the particular modes, therefore the phase velocity ordering is still used when the P-SV and SH modes propagate independently. This is slightly different than

Odom *et. al.* (1996), and Park and Odom (1998) where only the P-SV modes were included in the phase velocity ordering of the modes, and the SH modes were not included. The mode finding code developed by Park (1996) calculates the eigenvalues and eigenfunctions, which is an extension of the Chen (1993) algorithm. The ANIPROP code (Park, 1996) has been modified to include fluid layers and used to generate eigenvalues and eigenfunctions for each given model. The fluid/solid reflection and transmission coefficients were determined using the method of Mallick and Frazer (1991), when adding the fluid layers to ANIPROP.

The model, described in this chapter is characterized by propagating acoustic modes which have phase velocities within the range of $1500m/s$ and $2000m/s$ for frequencies between $10.0Hz$ and $100.0Hz$. The corresponding wavelengths at $50.0Hz$ would be $\lambda = 30m$ and $\lambda = 40m$ respectively. The computations were carried out on a desktop PC with dual 400MHz processors.

Table 3.2: Mode Wavelength Ranges

Phase Velocity	10.0Hz	20.0Hz	30.0Hz	40.0Hz	50.0Hz	75.0Hz
1500.0m/s	150.00m	75.00m	50.00m	37.50m	30.0m	40.00m
2000.0m/s	200.00m	100.00m	66.67m	50.00m	40.00m	26.67m

3.3 Slowness Curves

Slowness curves reveal the nature of anisotropy in the direction of propagation. The slowness curves show the inverse of the velocities of three mutually orthogonal plane-waves propagating in an anisotropic medium: quasi-P, quasi-SV, and quasi-SH. Velocities and therefore slownesses of the medium are determined numerically solving

the Christoffel equation 3.14 (e.g. Auld 1990).

$$\begin{aligned} (k^2\gamma_{ij} - \rho\omega^2\delta_{ij})v_j &= 0 \\ |k^2\gamma_{ij} - \rho\omega^2\delta_{ij}| &= 0 \end{aligned} \quad (3.14)$$

Solving the characteristic equation could be attempted analytically, which involves a cubic polynomial. Although there exists an analytical solution to the general cubic equation (first published by the Italian mathematician Girolamo Cardano in 1545, English translation published by M.I.T. Press, 1968), it is not very insightful for the general elastic stiffness tensor. The characteristic equation to be solved is:

$$\begin{aligned} & - \left(\frac{\rho\omega^2}{k^2} \right)^3 + (\gamma_{11} + \gamma_{22} + \gamma_{33}) \left(\frac{\rho\omega^2}{k^2} \right)^2 + (\gamma_{23}\gamma_{32} + \gamma_{12}\gamma_{21} \\ & + \gamma_{13}\gamma_{31} - \gamma_{11}\gamma_{22} - \gamma_{11}\gamma_{33} - \gamma_{22}\gamma_{33}) \left(\frac{\rho\omega^2}{k^2} \right) \\ & + \gamma_{11}\gamma_{22}\gamma_{33} - \gamma_{11}\gamma_{23}\gamma_{32} - \gamma_{12}\gamma_{21}\gamma_{33} + \gamma_{13}\gamma_{21}\gamma_{32} \\ & + \gamma_{12}\gamma_{23}\gamma_{31} - \gamma_{13}\gamma_{22}\gamma_{31} = 0 \end{aligned} \quad (3.15)$$

Slowness curves may be considered where the symmetry axis remains along a fixed direction and the propagation direction is allowed to vary. The slowness curves for the first anisotropic sediment layer, as described by line 2 of table 3.1 are shown in Figure 3.3. The slowness curves show plane-wave propagation in the xy, xz, and yz-planes.

Figure 3.3 shows the slowness curves for the xy, xz, and yz propagating planes for symmetry axes aligned with the \hat{z} , \hat{x} , and \hat{y} axes respectively. The quasi-P plane waves are entirely isotropic in nature, being rotationally invariant and all anisotropy is only in the shear velocities. For a modal description of a seismo-acoustic wavefield in a waveguide, the P and SV polarizations are always coupled together as P-SV modes. Therefore, any variation in the SV plane-wave velocity will affect the P-SV propagating modes, even without any variation in the P plane-wave velocities.

Figure 3.4 shows the slowness curves for the xz propagation plane for 36 symmetry axes orientations within the first quadrant. The intervals of θ and φ are 0° , 20° , 40° ,

VTI Slowness Curves for XY, XZ, YZ-Planes

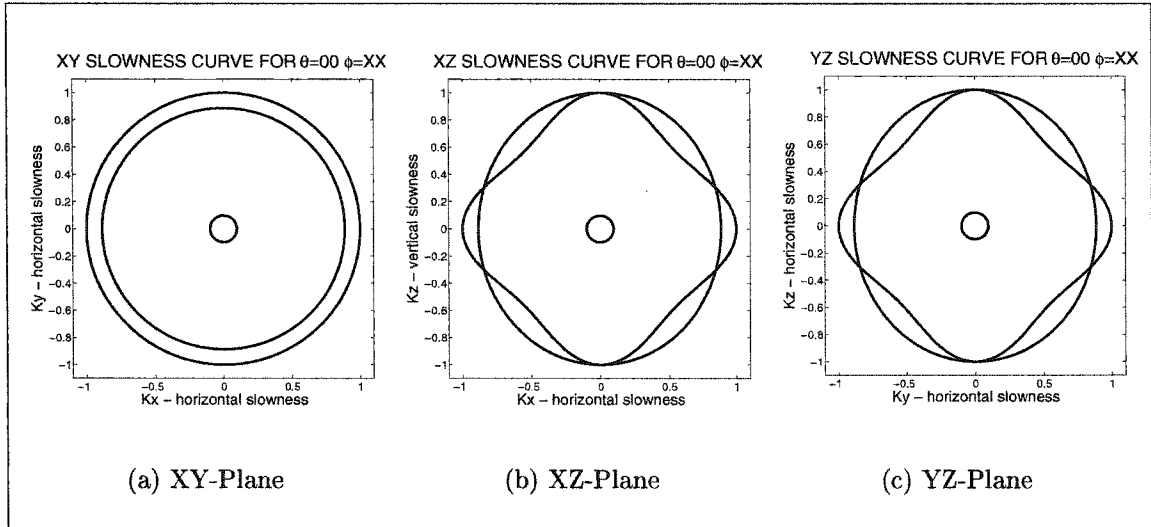


Figure 3.3: The slowness curves for the xy , xz , and yz -planes for a VTI anisotropic sediment layer, where $\hat{s} = \hat{z}$. The inner circle is the compressional slowness, indicating the absence of any anisotropy in the compressional velocity. The outer paths represent the vertical and horizontal shear slownesses. In Figure (a) there is complete shear velocity splitting. Both Figures (b) and (c) reveal shear velocity singularities at $\theta = 0^\circ, 180^\circ$ and $\theta \approx 70^\circ, 110^\circ$.

$50^\circ, 70^\circ$, and 90° . The horizontal axis of the figure is the φ axis, where rows represent changes in the azimuthal angle φ . The vertical axis of the figure is the θ axis, where columns represent changes in the elevational angle θ . Note that all of the slowness curves in the fifth row are degenerate along the z -axis. These are slowness curves for propagation in the xz -plane at $\theta = 70^\circ$ and $\varphi = 0^\circ, 20^\circ, 40^\circ, 50^\circ, 70^\circ, 90^\circ$. The two shear velocities remain degenerate for propagation along the z -axis for all variations of φ . When the shear velocities are degenerate along the z -axis, then the modes separate into two subfamilies of P-SV and SH modes that propagate independently. This is the same mechanism for a VTI medium, where the degenerate shear velocities along the vertical direction allow the SH and P-SV modes propagate independently.

The line singularities for a TI medium are dependent upon the the specific values

Slowness Curves for Symmetry Axis Rotations

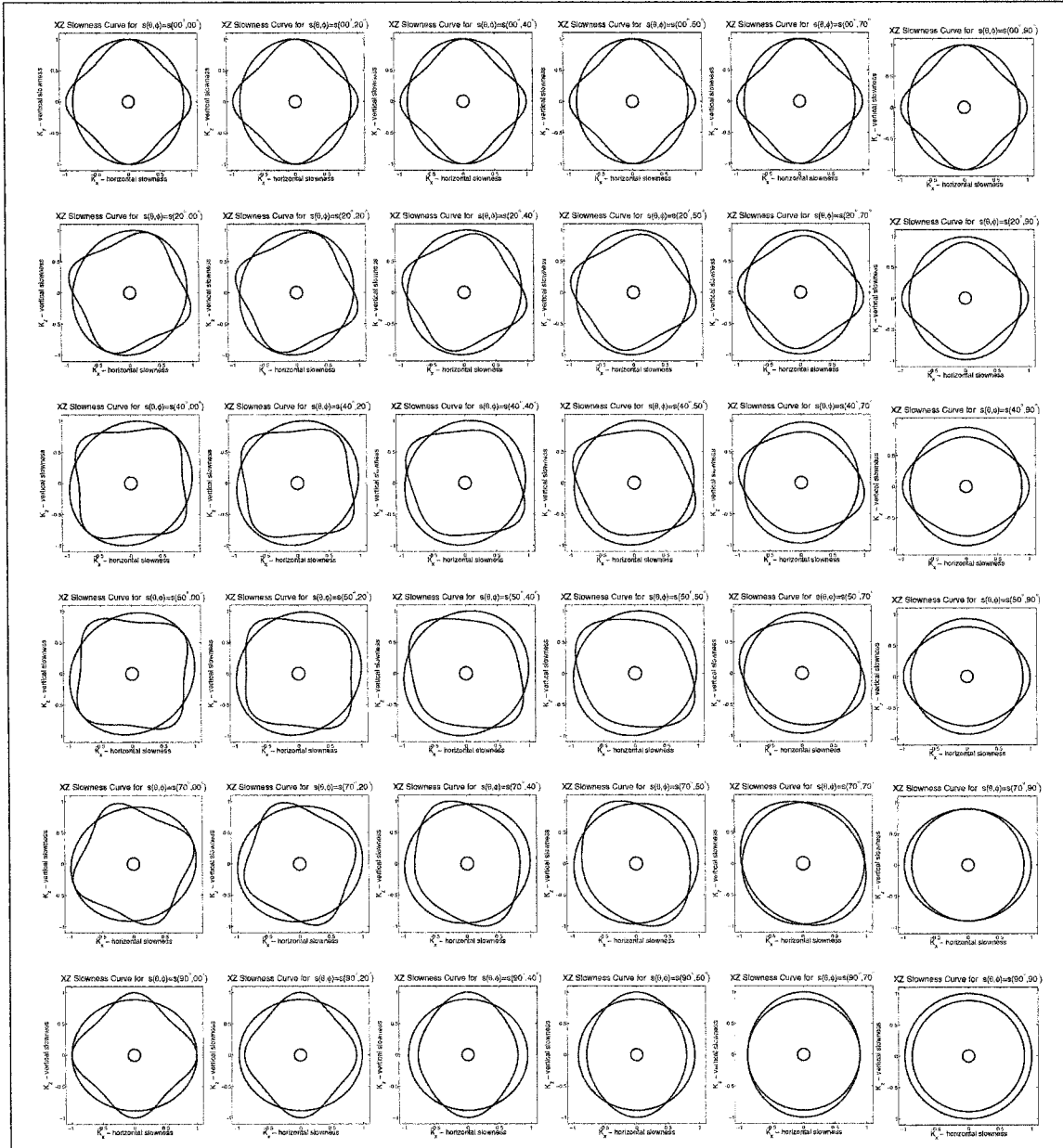


Figure 3.4: The figure shows the slowness curves for orientations of the symmetry axis \hat{s} within the first quadrant. Each slowness figure indicates a change in azimuth or elevation of symmetry axis. The horizontal rows represents variations of θ and the vertical columns represents variations of ϕ . The slowness curves are shown for the xz-plane for an anisotropic marine sediment layer.

of the elastic moduli A, C, F, L, N . Every different TI model may have a line singularity at a different value of elevation θ . The TI medium used in this dissertation has a line singularity at approximately 70° elevation. When $\theta = 70^\circ$, the line singularity nearly intersects the z-axis. The shear plane-wave velocities may become degenerate, but the polarization of the two shear waves still remain orthogonal.

The slowness surfaces for VTI media have singularities. These are instances where the plane waves (body waves) become degenerate. This only occurs for the shear waves in the model considered in this dissertation. The P-wave slowness sheet doesn't have any singularities, and is a perfect sphere. The two shear wave slowness sheets have two kiss singularities and two line singularities (Crampin; 1981,1984,1989,1991). For the VTI medium, line singularities occur at θ approximately 70° and 110° , and kiss singularities occur at $\theta = 0^\circ$ and $\theta = 180^\circ$. A kiss singularity occurs where two phase-velocity sheets touch tangentially at isolated points. The kiss singularity occurs where the slowness sheet intersects the symmetry axis \hat{s} . A kiss singularity always occurs in a medium with transverse isotropic elastic symmetry. A line singularity occurs where two slowness sheets intersect. The slowness sheets intersect in the plane perpendicular to the symmetry axis \hat{s} . Crampin (1989,1991) contain 3-D schematics that graphically distinguish between the different types of singularities.

3.4 Angular and Frequency Dispersion Curves

A dispersion curve shows how the velocities of a set of modes change with the variation of a particular independent variable. The phase or group velocities of the modes trace out branches as the independent parameter is varied. The dispersion curves are functions of ω , θ , and φ which are defined as the frequency, angle of symmetry axis \hat{s} tilt in the vertical plane θ , and angle of symmetry axis \hat{s} tilt in the horizontal plane φ .

Fixing the symmetry axis orientation by keeping θ and φ constant while varying

Frequency Dispersion Curves & "Solotone" Effect

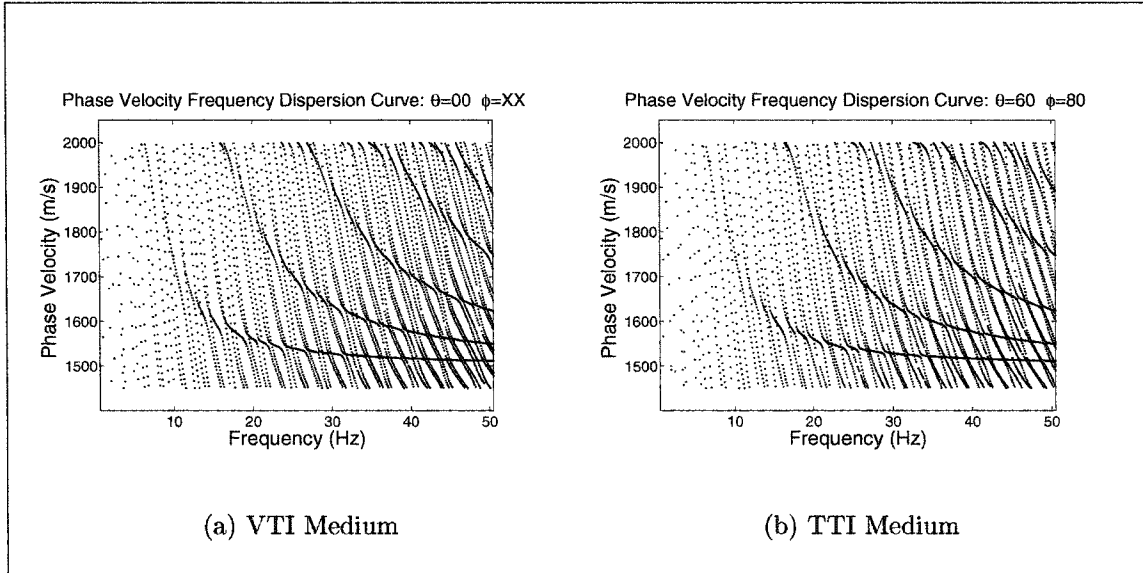


Figure 3.5: Frequency dispersion curves for modal phase velocities between 1500m/s and 2000m/s , for the VTI ($\hat{s}(\theta, \varphi) = \hat{s}(0^\circ, 0^\circ)$) and a TTI ($\hat{s}(\theta, \varphi) = \hat{s}(60^\circ, 80^\circ)$). The dispersion curves for the VTI symmetry in (a) and TTI symmetry (b) are very similar. Both figures clearly show the "solotone" effect, the dark bands in both figures (a) and (b). The modal phase velocities trace out vertical paths that are nearly parallel in figure (a). The even parallel nature is disrupted when the phase velocities approach the value of an "invariant" mode. The modal phase velocities in figure (b) also trace out vertical paths, but a braiding effect can be seen to occur between adjacent phase velocity traces. The dark bands that represent the phase velocities of the "invariant" modes are frequency dependent, but they vary more slowly than for the non-invariant modes.

ω results in a standard frequency dispersion curve. For a 1-D model, the frequency dispersion curves in figure 3.5 show how the number of acoustic modes and the phase velocity of the model vary with frequency. The frequency dispersion curves produce vertical branches in phase or group velocity. The frequency dispersion curve for the general TTI medium looks very much like the frequency dispersion curves for isotropic or VTI media. In both frequency dispersion curves of figure 3.5, note the "solotone" effect, where the spacing of the eigenvalues cluster to form apparent

"solotone" branches, the dark bands in the figures. The modes that contribute to the "solotone" branches are the modes sensitive only to the isotropic portion of the model, and are therefore labeled as "invariant acoustic modes". The "solotone" effect is due to discontinuities in the density and elastic moduli of the model. The solotone effect is a direct result of the inclusion of an elastic bottom structure for the sediments and basement layers. This effect has been documented by Lapwood(1975), Kennett *et. al.*(1983), and Alenitsyn(1998). The "solotone" branches are not a result of any anisotropy in the model, however the invariant modes that contribute to the "solotone" branches play an important role in angular dispersion curves. This solotone effect is frequency dependent. The number of modes in the 1500m/s-2000m/s range increases with frequency, and the number of acoustic/invariant modes become more numerous as the frequency increases. Another feature worth noting in the frequency dispersion curves occurs for the eigenvalues at higher frequencies. Figure 3.5(b) reveals modes that are closely spaced together and experience a braiding effect, where the two eigenvalues appear to become intertwined, even though they do not cross. This effect is not seen for the VTI case in figure 3.5(a) where the quasi-P-SV and quasi-SH modes propagate independently.

Fixing the value of ω and θ while varying φ creates an azimuthal angular dispersion curve. Keeping ω and φ constant while varying θ creates an elevational angular dispersion curve. The phase and group velocities of the modes are first computed for a beginning symmetry axis orientation $\hat{s}(\theta, \varphi)$. The symmetry axis \hat{s} in the angular dispersion curves is then allowed follow lines of constant elevation or constant azimuth on a unit sphere as described in figure 2.1.

The VTI and TTI models appear similar, when observing the frequency dispersion curves in figure 3.5. The differences between the models become much more evident in the angular dispersion curves. An angular dispersion curve with variations in θ or φ produce horizontal branches of phase or group velocities. Figure 3.6 displays azimuthal angular dispersion curves on the top (figures 3.6(a) and 3.6(b)) and

Angular Dispersion Curves

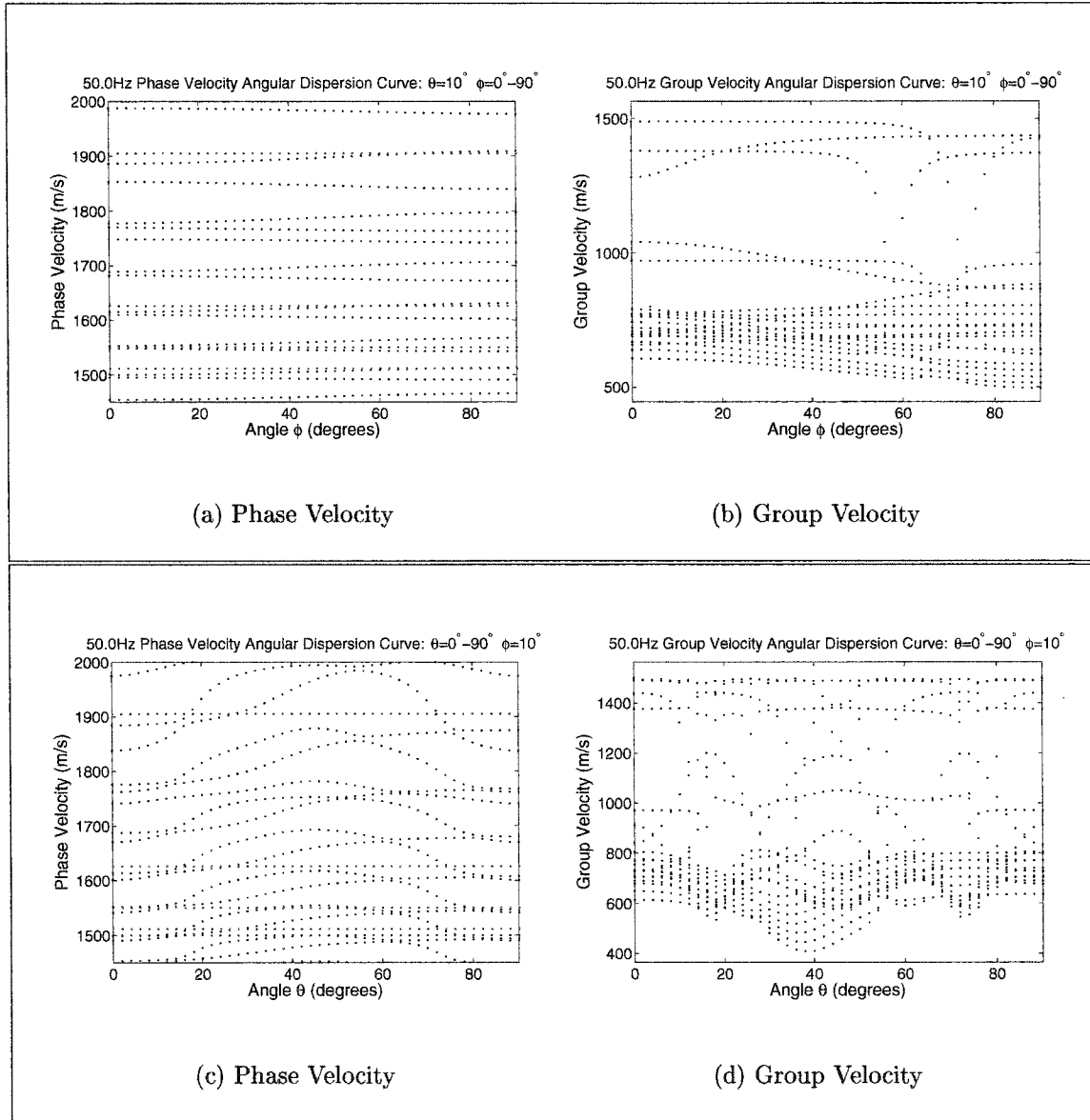


Figure 3.6: Angular dispersion curves for both phase and group velocities at 50.0Hz. Figure (a) and (b) show the angular dispersion curves for the phase and group velocities respectively for $\hat{s}(\theta, \varphi) = \hat{s}(10^\circ, 0^\circ - 90^\circ)$. Figure (c) and (d) represent the angular dispersion curves for the phase and group velocities respectively for $\hat{s}(\theta, \varphi) = \hat{s}(0^\circ - 90^\circ, 10^\circ)$. In general, changes in elevation (θ) have a larger effect on the phase and group velocities than changes in azimuth (φ).

elevational angular dispersion curves on the bottom (figures 3.6(c) and 3.6(d)). The left most figures (figures 3.6(a) and 3.6(c)) are the phase velocity angular dispersion curves and the figures on the right (figures 3.6(b) and 3.6(d)) are the group velocity angular dispersion curves. Note that a rectangular grid is used rather than a polar grid for the angular dispersion curves. The velocities are displayed on the vertical axis, and the angle variations are on the horizontal axis. A visual inspection of the angular dispersion curves reveals that a complexity exists when considering anisotropy. The dispersion branches show many instances where the branches approach one another. The phase velocities appear to attract and repel one another as the tilt angle varies for the 1-D model. It is evident that the the greatest changes in phase and group velocities occur for the elevational angular dispersion curves (changes in θ).

The eigenvalues do not remain evenly spaced. Near 0° the variations are small and the curvature of the dispersion branches are nearly flat. For azimuthal variations in φ there are less converging and diverging of the dispersion branches and the spacing of the eigenvalues remain more even. Take note of the horizontal branches that occur at approximately 1511m/s, 1550m/s, 1625m/s, and 1904m/s at 50.0Hz, which have been highlighted in red in Figures 3.6(a) and 3.6(c). These are the dispersion branches for the invariant acoustic modes at 50.0Hz. The phase velocities for the invariant acoustic modes for other frequencies are found in table 3.3.

The phase velocity of these modes scarcely change for any variations of the symmetry axis direction, in either the azimuthal or elevational dispersion curves. These modes are the same invariant acoustic modes that participate in the "solotone" effect in the frequency dispersion curves. The frequency "solotone" effect precisely predicts the invariant modes that sample the isotropic part of the model which are not sensitive to any tilt of the symmetry axis. Because of the constancy of these modes, they allow for an "angular solotone" effect to occur when another mode branch sensitive to tilt angle approaches. These modes that are affected by the tilt of the symmetry axis are labeled "sensitive modes". The phase branches do not actually intersect, but as

the sensitive mode approaches the invariant mode, their characteristics switch. The invariant mode branch takes on the character of the sensitive mode branch and the sensitive mode branch takes the character of the invariant mode branch. When the P-SV and SH modes coalesce into a single family of quasi-P-SV and quasi-SH modes or P-SV-SH modes, then any neighboring phase velocity branch may approach the invariant acoustic mode branches and switch characteristics.

Table 3.3: Phase Velocities of Invariant Acoustic Modes

Frequency	Mode 1	Mode 2	Mode 3	Mode 4	Mode 5	Mode 6
10.0Hz						
20.0Hz	1560m/s					
30.0Hz	1528m/s	1637m/s				
40.0Hz	1517m/s	1577m/s	1920m/s			
50.0Hz	1511m/s	1550m/s	1626m/s	1905m/s		
75.0Hz	1506m/s	1524m/s	1556m/s	1606m/s	1679m/s	1757m/s

An example of this can be seen in figure 3.13 of the eigenfunction section 3.5, which will be discussed in further detail later. Two sensitive mode branches can also approach one another. The branches do not actually cross, but they effectively take on the characteristics of the other mode. It appears that when two mode branches that are sensitive to the tilt of the symmetry axis, that they are modes of different wave types. A quasi-P-SV mode approaches a quasi-SH mode or vice versa. When the P-SV and SH modes propagate independently, then only the P-SV modes will approach the invariant acoustic modes and switch characteristics.

The angular dispersion curves are sampled discretely, so the near crossing of the branches may lack some strong curvature in the narrow angular ranges. A degeneracy in the mode eigenvalues (phase velocities) occurs when $c_r = c_q$ or $k_r = k_q$. The two

modes combine into a single composite mode which is mutually orthogonal to all of the other modes in the basis set. The result is still a set of mutually orthogonal modes, but the number of modes is reduced as the two modes combine into a single mode. As two modes become nearly degenerate, the phase and group velocities and mode shapes move toward a single phase and group velocity and mode shape. When the eigenvalues become nearly degenerate, then the branches either pinch close together, or indicate an apparent crossing. An actual crossing of the dispersion branches does not need to occur in order for the mode order sequence to change. The phase velocity branches appear to cross, but they never actually cross because of the numerical method imposed by the ANIPROP code. Park(1996) applies an approximate plane wave solution when the reflectivity matrix is nearly defective. The reflection matrix is formally defective when two eigenvalues are repeated, and only one eigenfunction is shared for the duplicated eigenvalues. The treatment of the defective matrix is necessary for numerical stability in ANIPROP, as two eigenvalues become degenerate or nearly degenerate. In the real earth, the modes likely never cross because heterogeneity and roughness would destroy the degeneracy. Polarization of the modes, whether predominantly P-SV or SH, cannot be inferred directly by a visual inspection of the curves, apart from the invariant acoustic modes.

Findings similar to Martin *et. al.* (1997) and Thomson (1997) have been observed, where the group velocity branches cross, but they do not necessarily correspond to crossings of plane-waves in the slowness diagrams. Their phase and group velocity dispersion curves show many of the same features as the angular dispersion curves. Martin *et. al.* (1997) report the crossing of the phase velocities in azimuthal angular dispersion curves. Several observations include the pinching together of the phase velocity branches, apparent crossings of the phase velocity branches, as well as changes in the mode order sequence. Mode ordering can change for variations in θ or φ . The change in the sequence of the modes occurs for both types of angular dispersion curves, azimuthal and elevation. The branches approach very closely without

actually touching.

The angular dispersion branches of the modes are symmetrical over a 180° range, with the mirror symmetry plane occurring at 90° . This is true for changes in θ or φ . For propagation in the xz -plane, the P-SV angular dispersion branches are symmetrical over a 90° range and the mirror symmetry occurring at 45° . The SH angular dispersion branches are not symmetrical over the range of $0^\circ - 90^\circ$ in the xz -plane.

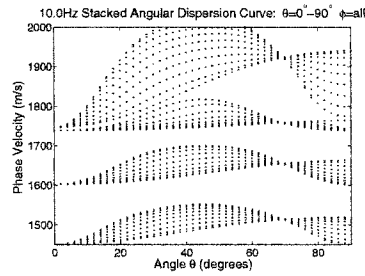
The group velocity angular dispersion curves are helpful in revealing how quickly the velocity of the energy of a mode changes with the rotation of the symmetry axis. The invariant acoustic modes have particularly stable group velocities for changes in θ or φ . The group velocity of the invariant acoustic modes only tend to change when near degeneracies occur and the mode characteristics are being switched with another mode. Other modes reveal group velocity changes as the symmetry axis sweeps across constant lines of azimuth or elevation. The group velocities are particularly sensitive to changes in the characteristics of the modes due to apparent branch crossings in the phase velocities. The group velocities change rapidly when another mode approaches. These changes occur over an angular range that correspond to the near crossings of the phase velocity branches.

The higher group velocities belong to the invariant acoustic modes. These are similar to the "banded" modes discussed in Thomson(1997). When the sensitive modes transition into an invariant mode, the group velocities of both modes converge, and then cross. The sensitive mode's group velocity then resumes the invariant's place, and the invariant mode becomes a sensitive mode with a lower group velocity.

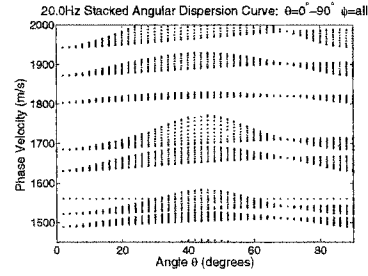
It is usually easier to interpret the azimuthal angular dispersion curves than the elevation angular dispersion curves as in figure 3.6. However, additional insight into the mode branch sensitivity to the tilt of the symmetry axis \hat{s} may be gained when the velocity data for an entire set of elevation angular dispersion curves is stacked.

Figure 3.7 shows the stacked elevation angular dispersion curves for several fre-

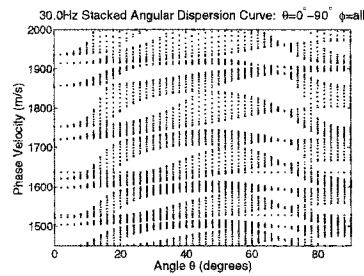
Stacked Angular Dispersion Curves



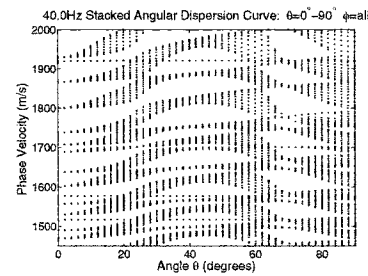
(a) Frequency = 10.0Hz



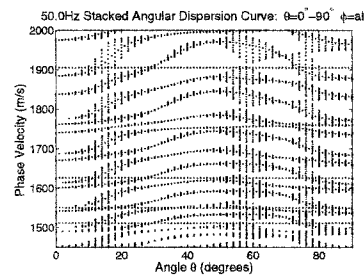
(b) Frequency = 20.0Hz



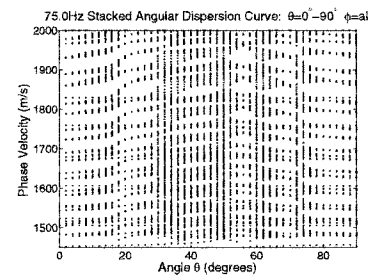
(c) Frequency = 30.0Hz



(d) Frequency = 40.0Hz



(e) Frequency = 50.0Hz



(f) Frequency = 75.0Hz

Figure 3.7: The stacked angular dispersion curves show the dependence and sensitivity of the dispersion branches on variations of the angles θ and φ for a range of frequencies. The thickness of an envelope indicates the sensitivity of a particular mode to changes in azimuth (φ). Note the convergence of the phase velocities at 0° and approximately 70° . This is where the shear velocities become nearly degenerate.

quencies. The number of modes and character of the curves is frequency dependent. The width of the envelopes reveals the sensitivity of the modes to changes in azimuth at a particular angle θ . At 50.0Hz when θ is near 0° the envelope is narrow and the phase branches are only slightly dispersed. This is true of the branches near 70° as well. The envelope has the largest width in the θ range from $5^\circ - 30^\circ$, $45^\circ - 65^\circ$, and $75^\circ - 90^\circ$ for Figure 3.7(e) at 50.0Hz.

3.5 Generalized Modes for Anisotropic Media

The focus for this section is on the effect anisotropy has on the modes - eigenfunctions. The concept of generalized modes of Crampin (1981) is used to describe modes with particle motion in all three coordinate directions. Any lateral heterogeneity is neglected for now, but will be included in chapter 4. In addition the crustal modes are ignored, and only the modes which contribute primarily to an acoustic or seismo-acoustic signal are considered. These are the discrete modes within the phase velocity range of 1500m/s - 2000m/s. From the angular dispersion curves it has been demonstrated that changes in the orientation of the symmetry axis can have a dramatic impact on the eigenvalues of the propagating modes. How these variations in the modal eigenvalues affect the characteristics of the eigenfunctions are now considered.

The most distinctive feature of acoustic wave propagation in anisotropic media is 3-D polarization of the particle motion. The polarization of the modes depends on the angle between the propagation direction and the symmetry axis direction of the anisotropic media. The properties of the elastic stiffness matrix determine the degree with which the modes share particle motion polarizations. Crampin (1981) notes that the two independent wave types, P-SV and SH, of isotropy coalesce into a single family of generalized modes with three dimensional elliptical motion for general anisotropy. The once pure P-SV modes acquire SH motion and the once pure SH

modes acquire P-SV motion. This results in quasi-P-SV and quasi-SH modes or generalized P-SV-SH modes, which possess polarizations into all three coordinate directions.

The eigenfunctions are generally complex in value. Anytime the single generalized family of modes for anisotropic media separate into two independent family of modes, the components of the eigenfunctions become purely real or purely imaginary. When a medium exhibits more generalized anisotropy, the eigenfunctions may have both real and imaginary components in the three coordinate directions. The imaginary components represent a phase delay in the time domain.

As discussed in Appendix D, the form of the elastic stiffness tensor affects the eigenvalues of the modal basis in the seismo-acoustic waveguide. Special symmetry axis orientations exist where P-SV and SH motions propagate independently in TI symmetric media. In an isotropic medium, the pure P-SV and pure SH modes do not share the same particle motion polarizations. The medium is completely rotationally symmetric. For a TI elastically symmetric medium, the P-SV particle motions and the SH particle motions propagate independently when the symmetry axis \hat{s} lies within the sagittal plane or along one of the three coordinate axes, as summarized by Table 3.4. The sagittal plane is defined as the vertical plane containing the propagation direction. Since the propagation direction is assumed to be parallel to the x-axis, the sagittal plane is parallel to the xz-plane.

A visual interpretation of the eigenfunctions at 50.0Hz in figure 3.8 reveals the P-SV modes have polarizations only in the xz-plane, and the SH modes have polarization in the y-direction. The pure SH modes are all rather similar to one another, with no particle motion in the fluid, and the largest amplitudes in the thin anisotropic sediments. The shape of P-SV and SH eigenfunctions are similar to the propagating modes for an equivalent isotropic medium. Schoenberge and Costa (1991) found that SH waves in a stratified monoclinic medium can be modeled using an equivalent stratified isotropic medium for propagation in the plane of symmetry. In instances

Table 3.4: P-SV and SH Particle Motion Independence

Coordinate Axes:
$\hat{s}(\theta, \varphi) = \hat{s}(90^\circ, 0^\circ) = \hat{x}$
$\hat{s}(\theta, \varphi) = \hat{s}(90^\circ, 90^\circ) = \hat{y}$
$\hat{s}(\theta, \varphi) = \hat{s}(0^\circ, 0^\circ) = \hat{z}$
Sagittal Plane:
$\hat{s}(\theta, \varphi) = \hat{s}(all, 0^\circ)$
Line Singularity:
$\hat{s}(\theta, \varphi) = \hat{s}(70^\circ, all)$
$\hat{s}(\theta, \varphi) = \hat{s}(110^\circ, all)$

where the P-SV and SH modes propagate independently, it may not be entirely necessary to implement anisotropic modeling. When the P-SV and SH particle motions propagate independently in a plane layered homogeneous medium (i.e. the absence of scattering), only the P-SV modes are necessary to represent the seismo-acoustic wavefield. The SH modes (e.g. 3.8(b)) are purely sediment and crustal modes when they propagate independently.

As shown in figure 3.9 the mode shape of mode 9 does not vary dramatically when the symmetry axis \hat{s} is aligned with any of the three coordinate axes. This is typical of any of the modes when the symmetry axis \hat{s} is aligned parallel to one of the coordinate axes. The P-SV and SH motions are also separable when $\theta = 70^\circ$. These symmetry axis orientations correspond to one of the line singularities in the TI elastically symmetric medium. The eigenfunctions are complex, but otherwise very similar to those in figure 3.8.

As seen in figures 3.8 and 3.10, there is no SH motion in the fluid layers. Even in the generalized eigenfunctions, motion is suppressed in the y-direction because

Pure P-SV and SH Modes

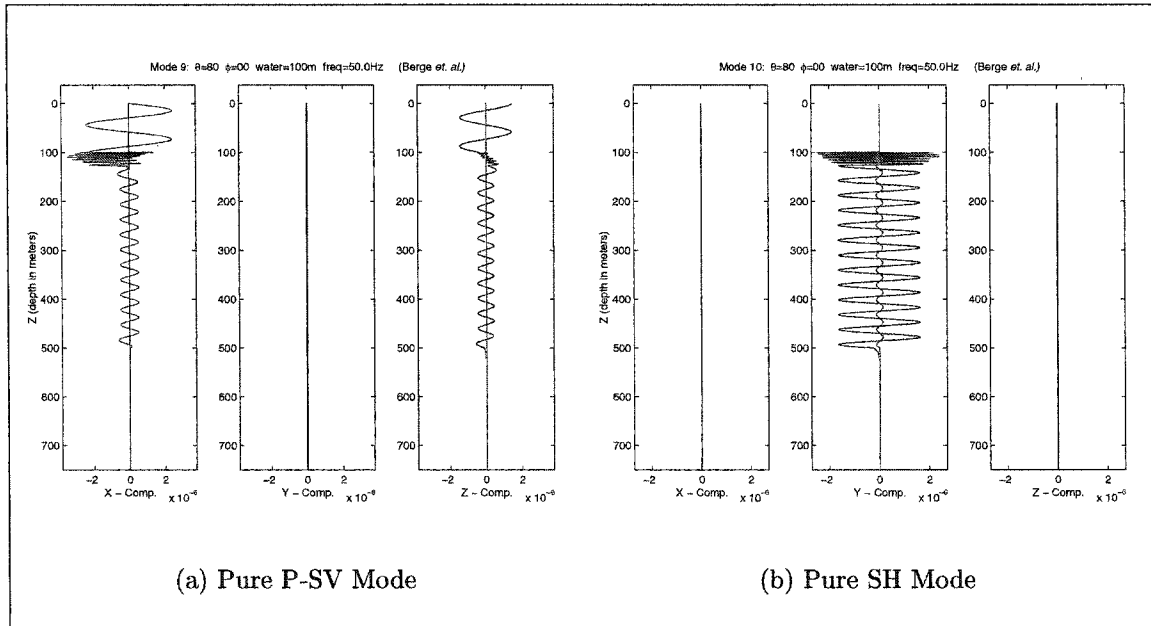


Figure 3.8: These are example pure P-SV and SH modes for $\hat{s}(\theta, \varphi) = \hat{s}(80^\circ, 0^\circ)$. This is an instance where the elastic stiffness matrix is quasi-monoclinic and the pure P-SV and SH modes have completely separate polarizations. The P-SV mode has particle motion in the sagittal plane and the SH mode has particle motion in the y-coordinate-direction of the horizontal plane.

the fluid layer can not support any shear stress. However, y-displacements in the generalized eigenfunctions do become evident in the bottom/subbottom layers for a tilted symmetry axis.

For more general tilt of the symmetry axis away from the sagittal plane or coordinate axes, ${}^a C_{IJ}$ has the form of a quasi-triclinic elastic stiffness matrix. For these general geometries, the modes of the waveguide belong to the generalized eigenfunctions. They have polarization in all three coordinate directions, as shown in figure 3.10. The modes can be classified as predominantly quasi-P-SV or predominantly quasi-SH for most symmetry axis orientations. Energy begins to appear in the SH component of the quasi-P-SV modes as shown in figure 3.10(a). A similar effect for

P-SV Mode for X, Y, and Z Axes

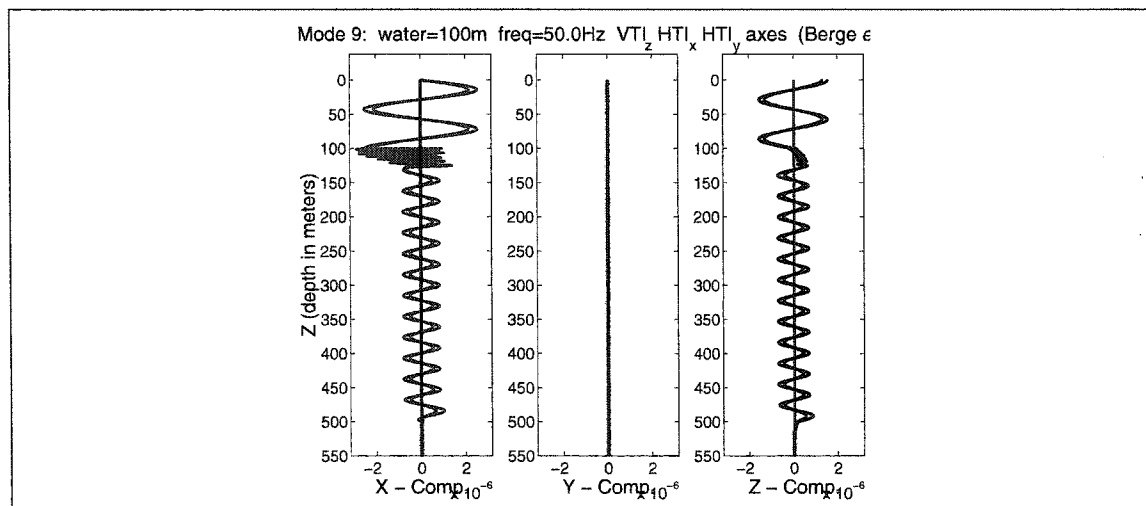


Figure 3.9: The P-SV mode remains polarized in the sagittal plane when the symmetry axis $\hat{s} = \hat{x}, \hat{y}, \hat{z}$. The mode shapes are similar when the symmetry axis is aligned parallel to any of the three coordinate axis directions.

the quasi-SH eigenfunctions is shown in figure 3.10(b). As the symmetry axis is tilted away from the vertical the quasi-SH eigenfunctions gain particle motion in the x and z-directions. However, some symmetry axis orientations exist where it is impossible to label a mode as predominantly quasi-P-SV or quasi-SH. These modes can be more accurately described as composite P-SV-SH modes. As shown in figure 3.10(c), the amplitudes in the x, y, and z-directions all have similar magnitudes for the P-SV-SH modes. The quasi-P-SV, quasi-SH, and P-SV-SH modes possess both P-SV and SH particle motion characteristics. This is a direct result of treating the sediments and bottom/subbottom as elastic.

Additional quasi-P-SV, quasi-SH, and P-SV-SH modes are shown in Figure 3.15 when the symmetry axis $\hat{s}(\theta, \varphi) = \hat{s}(80^\circ, 20^\circ)$. The x, y, and z components of displacement are in figures 3.15(a), 3.15(b), and 3.15(c) respectively. Notice that the amplitudes of the modes are about the same magnitude in the three coordinate direc-

Sample quasi-P-SV, quasi-SH, and P-SV-SH Modes

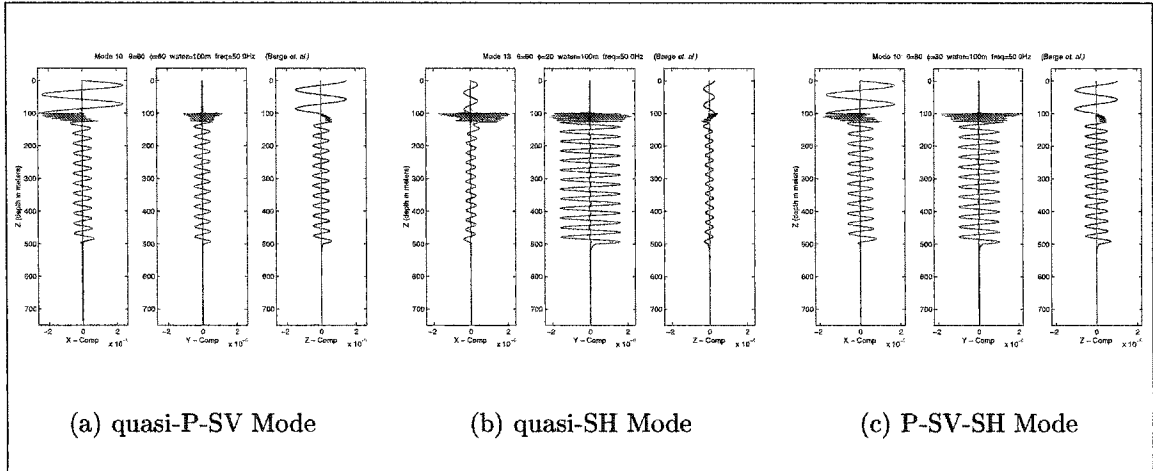


Figure 3.10: The quasi-P-SV mode in figure (a) has gained some particle motion in the y-direction, but still has particle motion predominantly in the sagittal plane. The quasi-SH mode in figure (b) has gained particle motion in the sagittal plane, but the mode remains predominantly polarized along the y-direction. The P-SV-SH mode in figure (c) has polarizations in all three coordinate directions and attributes of both P-SV and SH modes.

tions. The x- and z-components resemble hybrid acoustic-sediment particle motions, and the y-components resemble the displacements of sediment modes. The modes that are sensitive to the low shear speed sediment layers tend to have large displacement oscillations at the depths where the low shear speed sediments occur. Because all of the anisotropy for the models presented in this dissertation is contained in the low shear speed sediments, the degree of displacement oscillation in the sediment layers directly indicates any mode's sensitivity to anisotropy.

Some of the modes have the majority of their energy in the water column and the isotropic portions of the model. They have relatively little particle motion in the anisotropic sediment regions of the model. These invariant modes are predominantly quasi-P-SV acoustic modes with very little particle motion in the y-direction. Because these eigenfunctions are dominated by the isotropic features of the model, they

Sample Invariant Acoustic Mode

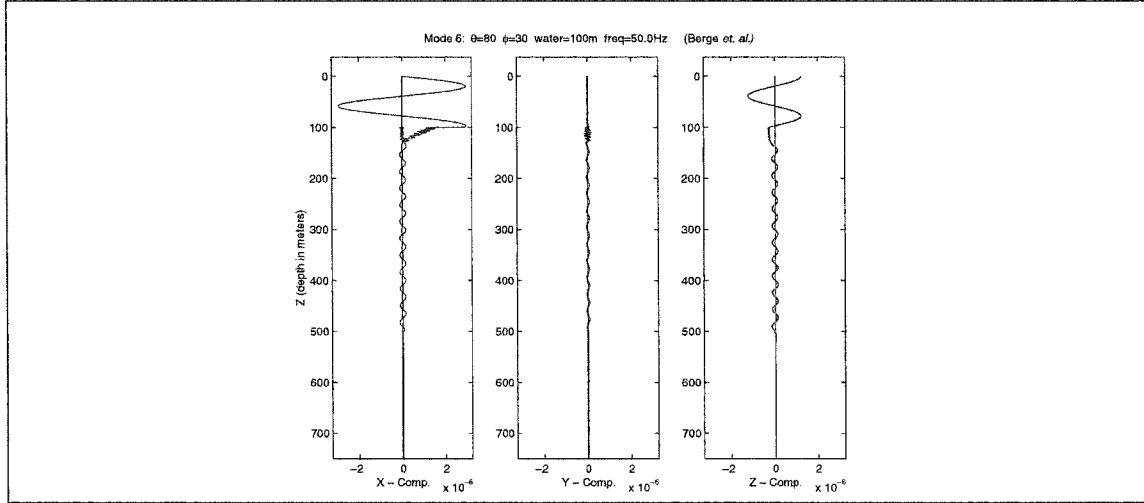


Figure 3.11: An example of an invariant acoustic mode at 50.0Hz for $\hat{s}(\theta, \varphi) = \hat{s}(80^\circ, 30^\circ)$. The mode only gains a very small portion of particle motion in the y-direction. In addition, only small oscillations are observed in the anisotropic sediment layers, compared to the modes in Figures 3.8 - 3.10.

are only slightly affected by any tilt of the symmetry axis within the anisotropic sediments. They closely resemble the P-SV acoustic modes for isotropy and symmetry axis orientations where P-SV and SH mode propagate independently. An example of an invariant acoustic mode is shown in figure 3.11. These invariant acoustic modes are the same modes that participate in the frequency and angular solotone effects observed in the dispersion curves. The acoustic modes are more sensitive to the anisotropy at lower frequencies. As the frequency increases, the acoustic modes' phase and group velocities become more invariant, indicating they become less sensitive to the anisotropy. These acoustic modes then become the invariant acoustic modes seen in the dispersion curves that participate in the "solotone" effect. An example of the frequency dependence of an acoustic mode is shown in figure 3.12. The figure shows the 1st acoustic mode for $\hat{s} = \hat{z}$. The x-component and z-component particle motions are shown in Figures 3.12(a) and 3.12(b) respectively.

Frequency Dependence of an Invariant Acoustic Mode

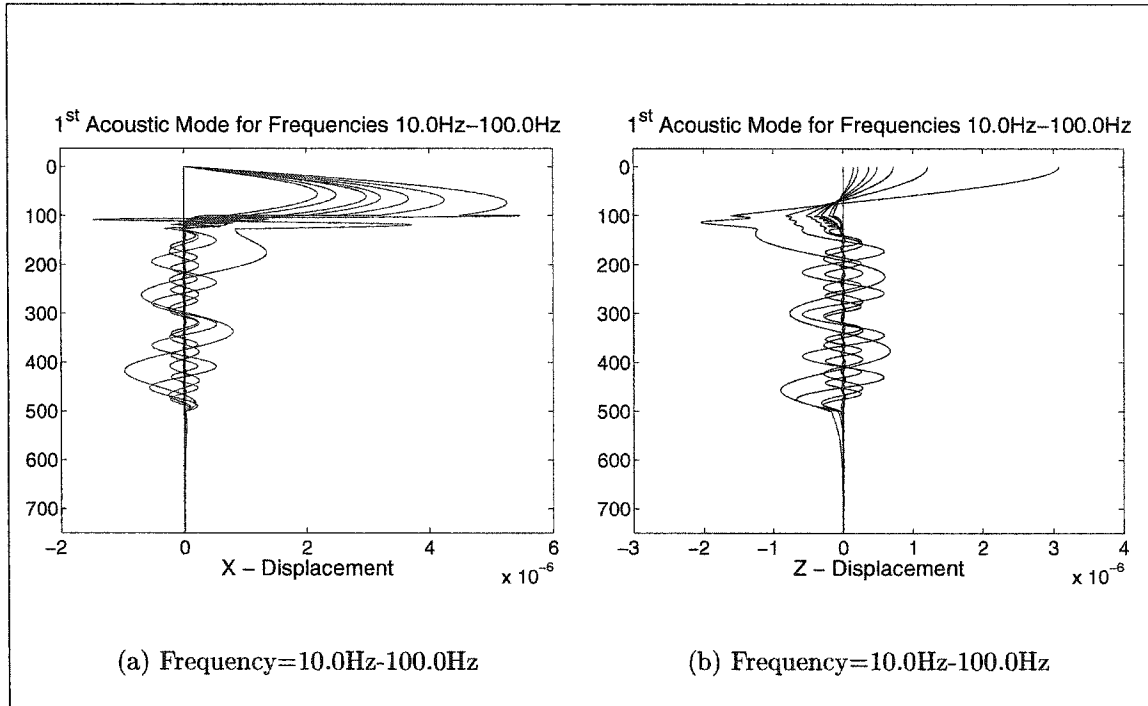


Figure 3.12: The characteristics of the 1st acoustic mode are shown for several frequencies. Figure (a) shows the x-component of displacement and figure (b) shows the z-component of displacement, for a frequency range of 10.0Hz-100.0Hz. The acoustic mode shown has a single zero crossing in the z-component particle displacement within the fluid layer at higher frequencies. The modal amplitude tends to decrease with increasing frequency.

In order to satisfy the boundary conditions between a fluid and anisotropic solid for the equations of motion, the particle motion in the y-direction must be included. The modes in figure 3.10 clearly show that as the symmetry axis \hat{s} tilts away from the vertical, the P-SV particle motion is no longer independent of the SH motion. Quasi-SH, quasi-P-SV and P-SV-SH modes are needed for an accurate representation of the seismo-acoustic wavefield.

For the dispersion curves in Figure 3.6, near degeneracies occurred for P-SV modes, even when the SH modes propagate independently. These near degenera-

Switching of Modal Characteristics

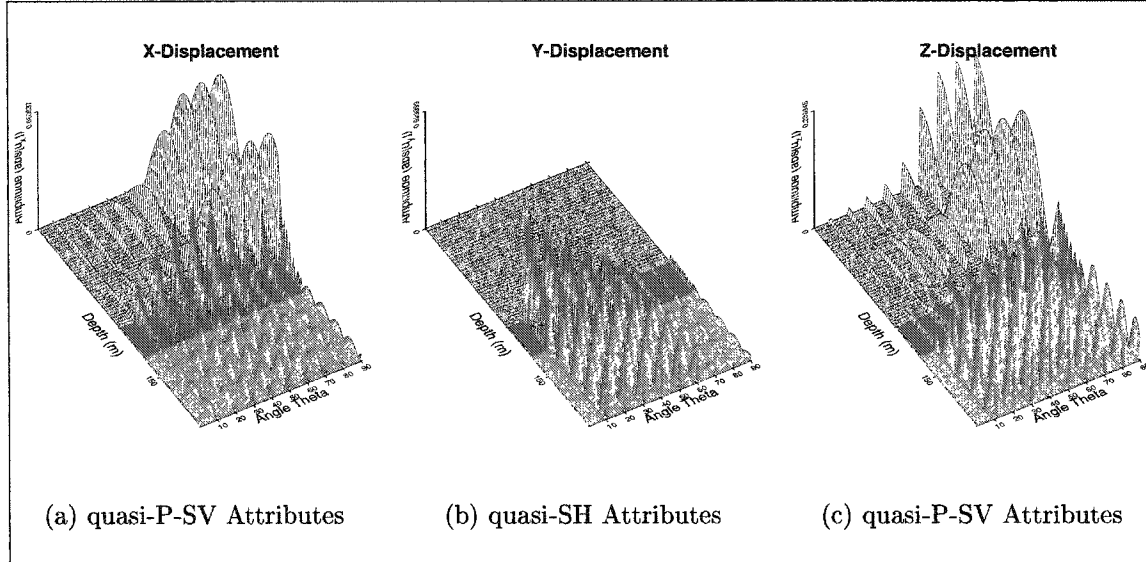


Figure 3.13: The x,y, and z particle displacements of a mode switches characteristics with another mode due to a near degeneracy. The near degeneracy occurs as the symmetry axis \hat{s} is varied in θ . In this case the quasi-SH mode becomes a quasi-P-SV mode as $\theta = 0^\circ - 90^\circ$.

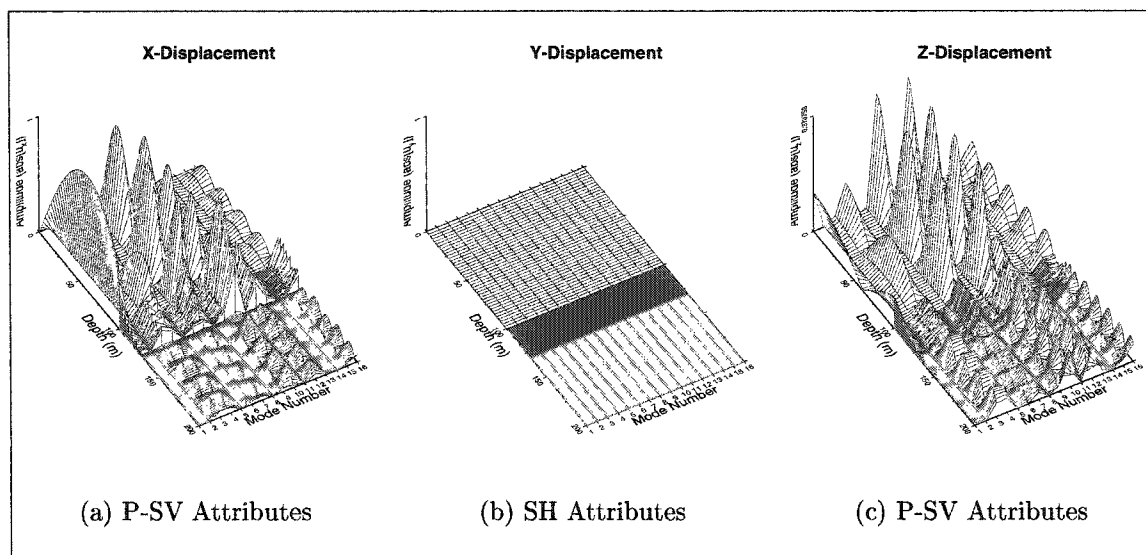
cies are due entirely to the solotone effect, where the phase and group velocities of the invariant acoustic modes are almost stationary. The near degeneracies seen in Figure 3.6 affect the characteristics of the modes. Even though the dispersion curves do not cross, the characteristics of the modes switch. This is seen in the dispersion branches when a sensitive mode becomes an invariant mode. Figure 3.13 shows how the characteristics of the modes changes as the angle θ varies. Figures 3.13(a), 3.13(b), and 3.13(c) show the displacements for the x, y, and z-directions respectively. The mode begins as a predominantly quasi-SH mode and transforms into a predominantly quasi-P-SV as the angle θ varies. The characteristics of the quasi-SH mode are taken on by the quasi-P-SV mode and the characteristics of quasi-P-SV mode are taken on by the quasi-SH mode. The identity of the mode in figure 3.13 is exchanged as it closely approaches the quasi-P-SV mode. As the modes approach near

degeneracy, the eigenfunctions of both modes transition towards composite modes with characteristics of both modes. There can exist two P-SV-SH modes that closely resemble each other as the modes become nearly degenerate.

The mode order sequence does not remain fixed for increases in frequency or changes in symmetry axis orientations. The sense of mode ordering is somewhat lost when the two sets of independent mode types coalesce into a single set of generalized P-SV-SH modes. The sequence of the mode ordering is not completely clear as the symmetry axis is tilted. The switching of modes is a complex function of the phase and group velocity relationships with the phase velocities approaching one another and where the group velocities actually cross. For TI elastic symmetry, the mode ordering of the eigenfunctions does not necessarily stay fixed as the symmetry angle is tilted. The mode ordering may change when two modes approach one another, and the mode order sequence tends to remain the same for the eigenfunctions at lower frequencies. At lower frequencies, the eigenvalues tend to be spaced further apart and near degeneracies are not as likely to occur. As the frequency increases, the eigenvalues become more closely spaced, as is evident in the the dispersion figures 3.5 and 3.6. Near degeneracies have a higher occurrence as the frequency increases, and the modes switch characteristics more often. Although it may be insightful to keep track of individual modes and their characteristics as they transition from quasi-P-SV to quasi-SH or vice versa, it really is not necessary. The modal formalism of section 3.1 does not require all of the modes to be individually identified as P-SV, SH quasi P-SV, quasi SH or P-SV-SH. All that is needed is to be sure and include all of the modes important to the seismo-acoustics waves composition.

The modes of the shallow water waveguide may be directly excited by any number of source types. When the P-SV and SH modes propagate independently, then the polarization of the acoustic modes are more source dependent as shown by figure 3.14. An explosive source will excite only P-SV motion (x and z-displacements). The displacements for the x, y, and z-directions excited by an explosive source are

P-SV and SH Explosive Source Modes



P-SV and SH Double Couple Source Modes

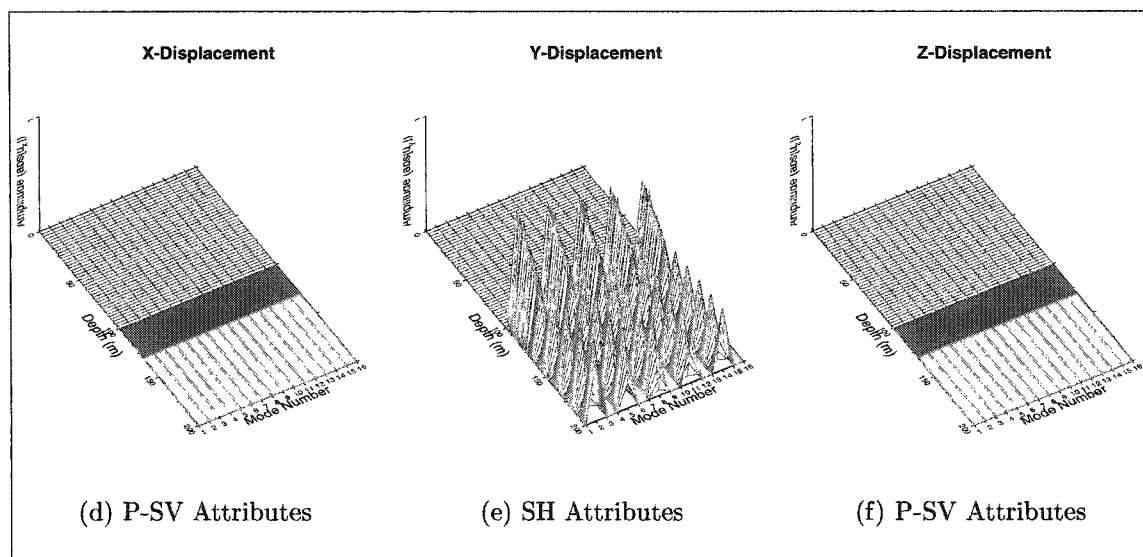
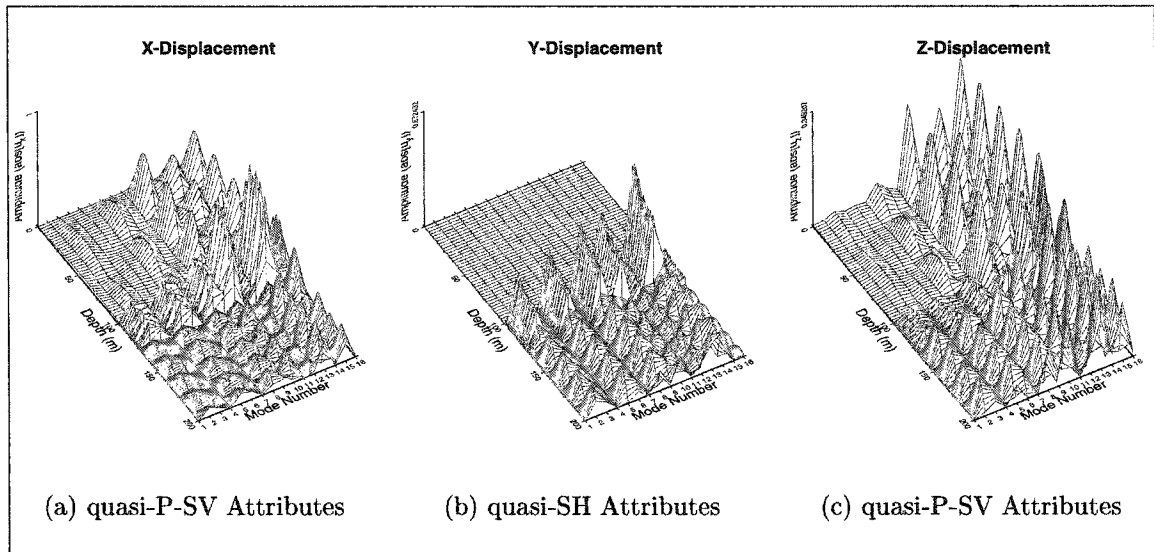


Figure 3.14: Figures (a), (b), and (c) show the x, y, and z displacements for an explosive source respectively. Figures (d), (e), and (f) show the x, y, and z displacements for a double couple source respectively. The modes of a quasi-monoclinic medium are similar to the modes of an isotropic or VTI medium, where the P-SV and SH particle motions propagate independently. An explosive source only excites modes with particle motion in the sagittal plane. A double couple source in the horizontal plane only excites modes with particle motion in the horizontal plane.

quasi-P-SV, quasi-SH, and P-SV-SH Explosive Source Modes



quasi-P-SV, quasi-SH, and P-SV-SH Double Couple Source Modes

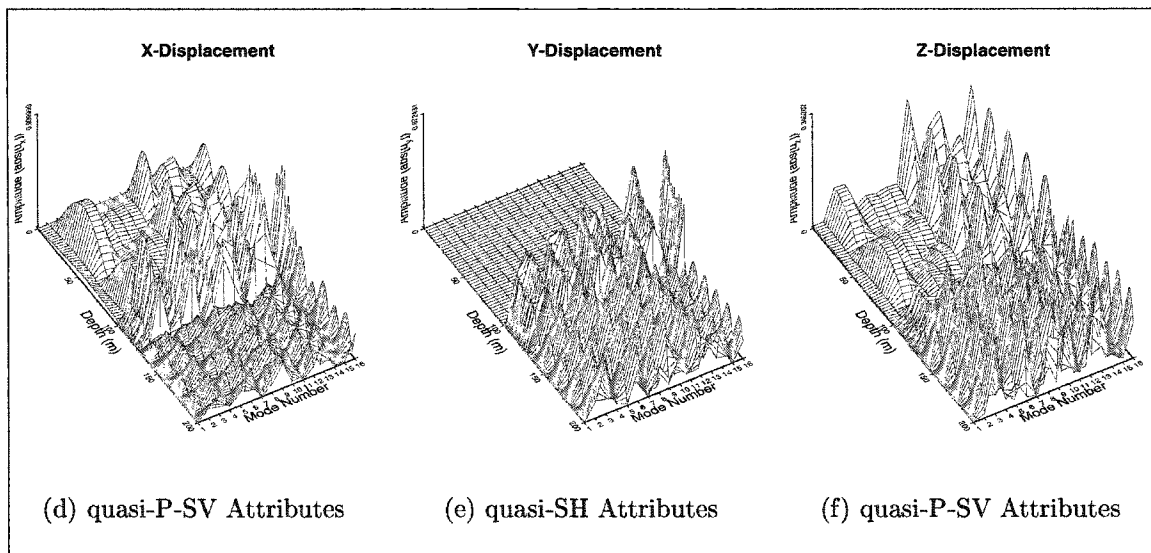


Figure 3.15: Both explosive and double couple sources are effective at exciting modes with 3-D particle motion, a result of the introduction of anisotropy into the sediments. Note that the double couple source is more effective at exciting the lower order modes, than the explosive source. The figures show the displacement of modes with phase velocities between the of 1500m/s and 2000m/s, for a TTI medium at 50.0Hz. The x, y and z-components of displacement are shown in figures (a) & (d), (b) & (e), and (c) & (f) respectively.

shown in figures 3.14(a), 3.14(b), and 3.14(c) respectively. Moment tensor sources can also be of interest for some acoustic wave propagation problems, such as T -wave excitation (Park *et. al.*, 2001). A pure double couple in the xy -plane will only excite SH motion as displayed in figures 3.14(d), 3.14(e), and 3.14(f). The excitation of the P-SV and SH modes can be compared to the excitation of quasi-P-SV, quasi-SH, and P-SV-SH modes. Using an explosive source, energy becomes evident in the x , y , and z -displacement directions in figures 3.15(a), 3.15(a), and 3.15(a) respectively. The significance is that the wavefield will contain y -displacements in the absence of any heterogeneity or scattering. Using a double-couple source contained in the horizontal plane, excitation of x , y , and z -displacements again becomes evident as shown in figures 3.15(d), 3.15(e), and 3.15(f) modes. Here, a shear source is able to excite modes which contribute to a seismo-acoustic wavefield. Because of the 3-D polarization of the modes, they may be excited by a wide range of sources.

The generalized mode structure is significant for shallow water media. With the bottom interacting modes, acoustic energy can leave the water column. It can then be attenuated by the low shear velocity sediments, and redistributed to other predominantly sediment modes. In addition, energy from other sources or signals, such as noise, from the sediment and bottom layers can enter the water column through these bottom interacting modes. With the anisotropic bottom interacting modes, there exists a greater opportunity for the energy to become redistributed and leave or enter the water column. This is due to the three component nature of the eigenfunctions. Therefore, in the presence of anisotropy, attenuation of bottom interacting modes could be underestimated if isotropy is assumed.

3.6 Chapter Summary

A seismo-acoustic signal may be represented by a superposition of acoustic, hybrid crustal-acoustic, and crustal modes. It is important to note that, the modal formalism

does not require all of the modes to be individually identified as P-SV, SH quasi P-SV, quasi SH or P-SV-SH. All that is required is for all of the modes which contribute to the seismo-acoustics signal to be included into the modal representation. However, it is instructive to consider the individual modes, since they help bring understanding into the physics of propagation.

The form of the elastic stiffness tensor determines whether the local modes propagate independently as P-SV and SH modes or coalesce into a set of quasi-P-SV, quasi-SH, and generalized P-SV-SH modes. This distinction greatly affects the polarization of the propagating signal. Since it usually cannot be prearranged to record a seismo-acoustic signal in a symmetry plane, the effects of tilted anisotropy cannot be completely ignored. Conversion of acoustic energy into horizontally polarized shear motion can be expected at fluid/solid boundaries where lateral heterogeneity or anisotropy exists in the solid layer. As a result, one consequence of the presence of anisotropy is that the seismo-acoustic signals can have a significant portion of their energy in horizontally polarized shear motion (SH and quasi-SH) even in the absence of any range-dependence. This is in contrast to an isotropic or VTI elastic medium, where all acoustic energy propagates independently of any horizontally polarized shear motion. In the absence of any scattering, all particle motion for an acoustic signal would be restricted to the sagittal plane for isotropic and VTI media. For general anisotropy the compressional motion (quasi-P), vertically polarized shear motion (quasi-SV) and horizontally polarized shear motion (quasi-SH) no longer propagate independently.

Horizontally polarized shear motion experiences higher attenuation than compressional motion, with intrinsic SH attenuation approximately 2-3 times larger than compressional wave attenuation, or even larger in low shear speed sediments. Because shear motions experience higher attenuation than compressional motion, this could be an important loss mechanism for acoustic signals with significant seafloor interaction. The SH motion could have a profound effect on the propagation of the

acoustic signal. The signal may experience more energy loss than an equivalent signal propagating in an isotropic model or only fluid layers. Therefore, in the presence of anisotropy, attenuation of bottom interacting modes would be underestimated if isotropy is assumed. Hughes *et. al.* (1990) observed that high propagation loss in thin sediment layers is due to absorption of shear waves in the sediment. Acoustic energy with quasi-SH modes or quasi-SH displacement components would contribute to the loss reported by Hughes *et. al.* (1990).

The frequency and angular dispersion curves give insight into the characteristics of specific modes. They indicate which modes are sensitive to anisotropy, and which modes remain invariant to the anisotropy and its symmetry axis orientation. The mode set being divided into both sensitive and invariant modes may account for why anisotropy is often successfully introduced and modeled as a perturbation. Since not all of the modes are sensitive to the anisotropic layers, the impact of the anisotropy is limited by contribution of the sensitive modes, while the invariant modes still contribute an isotropic aspect to the seismo-acoustic signal.

Horizontal shear motion has historically been ignored or neglected in the modeling of acoustic signals, with the majority of attention placed on acoustic P-SV motion. However, any description of seismo-acoustic signal propagation which ignores SH motion in these type of environments would be incomplete. Particle motion in the three coordinate directions must be included into the seismo-acoustic wavefield. It has been demonstrated that an elastic treatment of the bottom and subbottom of the shallow water environment at low frequencies is necessary for understanding the propagation of the seismo-acoustic energy for tilted anisotropy.

Chapter 4

ANISOTROPY AND GEOMETRICAL HETEROGENEITY

It is helpful to separate the effects of anisotropy and the effects of heterogeneity in a complicated medium. In chapters 2 and 3 the effect of anisotropy in the absence of heterogeneity was investigated. Now consider the effect of lateral heterogeneity on the coupling of local modes for VTI and TTI media. The local modes are defined as the eigenfunctions of a 1-D model that is the local equivalent of the range-dependent model at a fixed position x_o . The local modes are weighted by range-dependent amplitude coefficients, which can be determined by solving an evolution equation. This evolution equation depends on the coupling matrix \mathbf{B}_{qr} which contains all of the physics for the redistribution of energy between coupled local modes. \mathbf{B}_{qr} contains the elastic moduli of the model, lateral derivatives of the elastic moduli, the local eigenfunctions, and the vertical derivatives of the local eigenfunctions. The local modes are orthogonal, but any lateral heterogeneity breaks the orthogonality of the modes, and allows them to couple, where energy is redistributed between the modes. Building upon the previous discussions concerning homogeneous plane-layered anisotropic media, now consider the wave propagation effects for a 2-D range-dependent model.

4.1 Coupled Local Mode Formalism for Range-Dependent Anisotropic Media

The theory presented for the 1-D homogeneous anisotropic plane-layered halfspace of section 3.1 can be extended. The method of coupled local modes is applied to the 2-D range-dependent seismo-acoustic wave propagation problem. Any introduc-

tion of lateral heterogeneity leads to two additional steps in solving the equations of motion. As for the previous homogeneous anisotropic plane-layered medium, the equations of motion can be expressed as a first order differential equation and the solution of the coupled first order equations are expressed in terms of the basis of local modes. In addition, the interface boundary conditions must be transformed into equivalent localized volume forces, and an evolution equation for the amplitude coefficients which describes the coupling between modes in a range-dependent medium must be obtained. The specific deterministic anisotropic structure of the medium is assumed to be known for the model.

The modal theory in Section 3.1 is extended by following the the coupled local mode formalism of Maupin (1988). The boundary conditions for geometrical heterogeneity along interfaces may be expressed as:

$$[\mathbf{t}(\hat{n})_3]_n = [\mathbf{w}(\hat{n})]_n = 0, \quad \text{for the } n^{\text{th}} \text{ interface} \quad (4.1)$$

The coupled local mode formalism also assumes that all tractions vanish at the free surface, imposes a free-slip boundary at any fluid-solid interfaces, and enforces a radiation condition at infinity. In addition, the displacement and tractions are considered continuous across interface normals.

Consider an effective volume force term \mathbf{F}^T arising from traction discontinuities along the interfaces.

$$\mathbf{F} = \mathbf{F}^S + \mathbf{F}^T = \begin{pmatrix} \mathbf{0} \\ \mathbf{f}^S \end{pmatrix} + \begin{pmatrix} \mathbf{0} \\ [\mathbf{t}]_n \delta(z - h_n(x)) \end{pmatrix}$$

This additional effective volume force will be found in the coupling terms of the local modes. The interfaces between fluid layers are considered planar, and do not contribute an equivalent volume force.

As before, a modal description of the wavefield is assumed, where the local modes are independent solutions for the non-separable equation of motion. The wavefield, \mathbf{u}

is expressed as a superposition of local modes $\mathbf{u}^r(z; x)$ weighted by range-dependent amplitude coefficients $c_r(x)$.

$$\mathbf{u} = (\mathbf{w}, \mathbf{t})^T = \sum_r c_r(x) \exp\left(i \int_{x_s}^x k^r(\xi) d\xi\right) \mathbf{u}^r(z; x) \quad (4.2)$$

where $k^r(\xi)$ is the local horizontal wave number, and x_s denotes the source position.

Substituting the Ansatz (4.2) into the equation of motion (3.4), taking the scalar product with respect to local mode \mathbf{u}^q , and then evaluating the scalar product integrals results in an evolution equation for the amplitude coefficients $c_r(x)$.

$$\frac{\partial c_q}{\partial x} = \mathbf{B}_{qr} c_r \quad (4.3)$$

where the coupling matrix \mathbf{B}_{qr} is defined as:

$$\mathbf{B}_{qr} = \left(- \left\langle \mathbf{u}^q, \frac{\partial \mathbf{u}^r}{\partial x} \right\rangle + i \sum_n \dot{h}_n \mathbf{w}^{q*} [\mathbf{t}^r]_n \right) \exp\left(i \int_0^x (k^q - k^r) d\xi\right) \quad (4.4)$$

and the Hermitian scalar product is defined as:

$$\langle \mathbf{u}^q, \mathbf{u}^r \rangle = i \int_0^\infty (\mathbf{w}^{*q} \mathbf{t}^r - \mathbf{t}^{*q} \mathbf{w}^r) dz \quad (4.5)$$

The range-dependent amplitude coefficients are determined from the solution of equation (4.3). The combined effects of heterogeneity and anisotropy on the eigenfunctions are studied through the coupling matrix \mathbf{B}_{qr} . For a deterministic medium, \mathbf{B}_{qr} is a mode coupling matrix which essentially determines how much of the modal energy from local mode r is redistributed into local mode q . The coupling matrix contains an inner product which introduces volume terms and interface terms. It contains the local eigenfunctions, their vertical derivatives, and the material properties as well as any lateral heterogeneities. The range-dependent amplitude coefficients are determined from the solution of equation (4.3). \mathbf{B}_{qr} would be a diagonal matrix, describing self-modal coupling, for a homogeneous plane-layered medium. The local modes are all mutually orthogonal, preventing any redistribution of energy between the modes. Some heterogeneity needs to exist for the coupling matrix \mathbf{B}_{qr} to contain

off diagonal terms that leads to mode coupling. The heterogeneity may be sloping or rough interfaces, volume variations, or both. A full expanded form of the coupling matrix \mathbf{B}_{qr} can be found in Appendix C.

The deterministic coupling matrix of Maupin (1988) contains both boundary interface terms and volume terms. When the material properties are assumed to be constant within each layer of the model, then the derivatives of elastic moduli are zero. All volume terms in the coupling matrix \mathbf{B}_{qr} become zero, and only the interface terms of the \mathbf{B}_{qr} matrix remain. Therefore in the absence of material property variations:

$$\begin{aligned}
\mathbf{B}_{qr} = & \frac{1}{k^q - k^r} \left(\sum_n \dot{h}_n \left[-\mathbf{w}^{q*} \rho \omega^2 \mathbf{w}^r - \frac{\partial \mathbf{w}^{q*}}{\partial z} Q_{33} \frac{\partial \mathbf{w}^r}{\partial z} + \mathbf{w}^{q*} Q_{22} \mathbf{w}^r p^2 \right. \right. \\
& \left. \left. - \frac{\partial \mathbf{w}^{q*}}{\partial z} (C_{31} C_{11}^{-1}) \mathbf{t}^r - \mathbf{t}^{q*} (C_{11}^{-1} C_{13}) \frac{\partial \mathbf{w}^r}{\partial z} + \mathbf{t}^{q*} C_{11}^{-1} \mathbf{t}^r \right]_n \right) \\
& - \dot{h} \left(-\frac{\partial t_{33}^{q*}}{\partial z} \frac{1}{\rho \omega^2} \frac{\partial t_{33}^r}{\partial z} - t_{33}^{q*} \left(\frac{1}{\lambda} - \frac{p^2}{\rho \omega^2} \right) t_{33}^r + w_1^{q*} \rho \omega^2 w_1^r \right) \Big|_{h_f(x)^-} \\
& - i \dot{h} \left((k^q - k^r) (w_1^{q*} t_{33}^r + t_{33}^{q*} w_1^r) \right) \Big|_{h_f(x)^+} \exp \left(i \int_0^x (k^q - k^r) d\xi \right) \quad (4.6)
\end{aligned}$$

where $h_f(x)$ describes the range dependence of the fluid/solid interface boundary. The ${}^w Q_{ij}$ matrix is defined as:

$${}^w Q_{ij} = {}^w C_{ij} - ({}^w C_{i1}) ({}^w C_{11}^{-1}) ({}^w C_{1j}) \quad (4.7)$$

4.2 Laterally Heterogeneous Anisotropic Media

The coupling matrices are compared to reveal how modal energy redistributes when anisotropy and range-dependence are present. The VTI model will be compared to a general anisotropic TTI medium.

The shallow 2-D water environment has a bottom/subbottom with complex elastic properties that vary in both direction and location. Figure 4.1 shows a representation

of a 2-D range-dependent model. The thin anisotropic sediments are modeled as in chapters 2 and 3.

2-D Layered Laterally Heterogeneous Anisotropic Structure

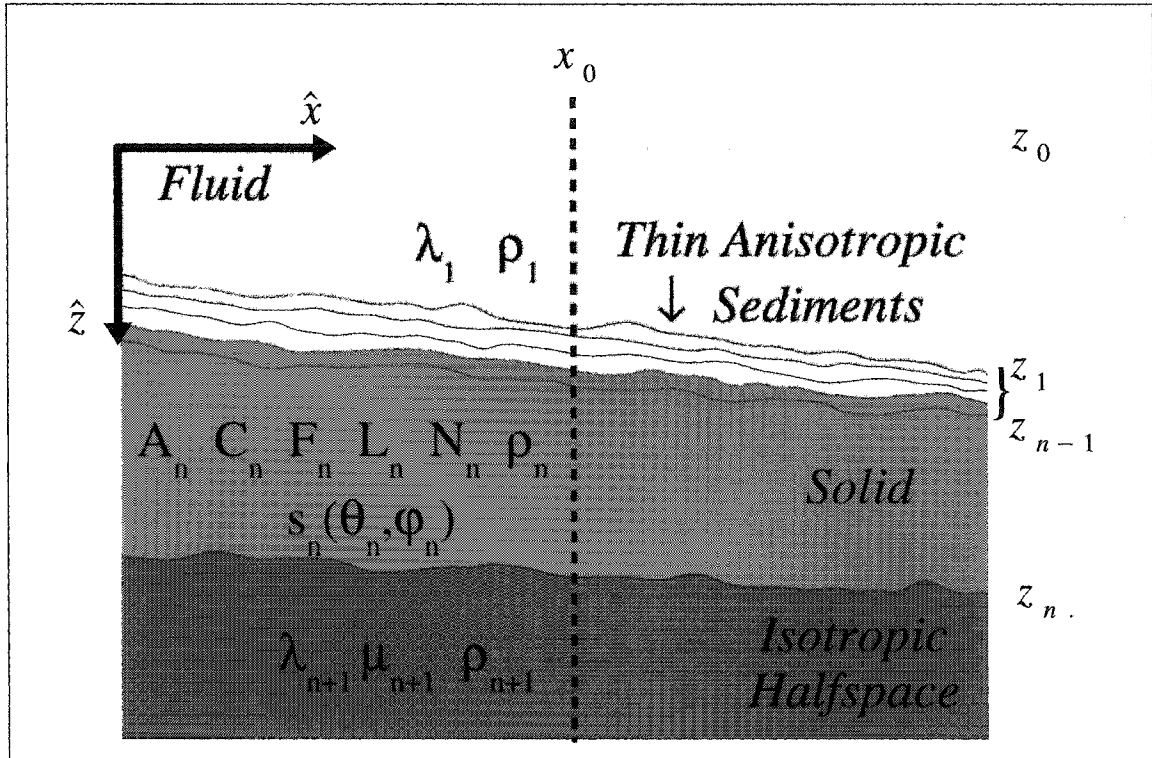


Figure 4.1: A 2-D laterally heterogeneous anisotropic structure. The structure contains fluid layers over thin range-dependent anisotropic and/or isotropic sediments, additional range-dependent sediments and/or basement layers, and is terminated by an isotropic halfspace. The elastic moduli may vary in both range and depth. The local equivalent of this 2-D model at x_0 is the plane-layered homogeneous anisotropic model in figure 3.1.

When investigating the effects of anisotropy in a 2-D range-dependent seismic environment, 1-D profiles are generated that are the local equivalent of the range-dependent model shown in figure 4.1. At a particular point x_0 of the 2-D range-dependent model, a 1-D profile is created with the same elastic properties and depth dependence as the 2-D model. For example, the density and elastic moduli of

the 2-D model are described in the 1-D profile as:

$$\rho(x_o; z) = \rho(z)$$

$$A(x_o; z) = A(z)$$

$$C(x_o; z) = C(z)$$

$$F(x_o; z) = F(z)$$

$$L(x_o; z) = L(z)$$

$$N(x_o; z) = N(z)$$

The model is range-dependent with elastic sediments and bottom layers. The anisotropy belongs to the transversely isotropic elastic symmetry class, and is only in the thin sediment layers. All other layers remain isotropic. The elastic parameters are known and assumed to be deterministic in nature, while ignoring any small scale variations that would be evident in a real earth structure.

For the 1-D profile, the same model as shown in figure 3.1 and table 3.1 is used. The 1-D vertical profiles are the plane layered homogeneous anisotropic structure considered previously in Sections 2 and 3.

4.3 Deterministic Interface Coupling Matrices

The form of the lateral heterogeneity in the deterministic interface coupling matrices is restricted to non-horizontal bedding planes (interface boundaries). The coupling matrix \mathbf{B}_{qr} essentially determines how much of local mode r is redistributed into mode q . For isotropy, when the symmetry axis \hat{s} is within the sagittal plane, or \hat{s} is aligned to one of the coordinate axes, the pure SH and P-SV particle motions propagate independently. Any mode coupling is dominated by nearest neighbor interactions between modes of the same wave type. If the modes involved in the \mathbf{B}_{qr} matrix are strictly different wavetypes with completely separate polarizations, then the coupling between the different wavetypes will be zero. Only SH/SH and P-SV/P-SV coupling

is observed between the modes. Figure 4.2 shows the \mathbf{B}_{qr} coupling matrices for pure P-SV and SH modes at 20.0Hz, 30.0Hz, 40.0Hz, and 50.0Hz.

The white elements in the coupling matrices represent zero values. Note that the diagonal elements, which represents the self-coupling of a mode or the phase of the mode, have also been set to zero. It appears that the coupling between modes may not be dominated by nearest-neighbor interactions, but in fact the modes are only coupling with their respective wave types and the coupling is strongest for the nearest mode of the same wave type. Absolutely no coupling occurs between the SH and P-SV local modes. If the P-SV and SH modes are separated and then grouped first by modal wavetype, and second by phase velocity, then the nearest-neighbor coupling of Odom *et. al.* (1996) is observed.

As the symmetry axis is tilted, coupling can occur between any generalized mode regardless of mode wavetypes, as shown in figure 4.3. The quasi-P-SV, quasi-SH, and generalized P-SV-SH modes may have energy in all three coordinate directions, allowing the modes to be available for a wide redistribution of energy whenever lateral heterogeneity is present. The mode coupling may be dominated by nearest-neighbor interactions or by non-nearest-neighbor interactions. The strength of the coupling depends on the closeness of the phase velocities of the modes and the degree of similarity between the eigenfunctions. However, the 3-D particle motion of the local modes allow coupling between all of the modes, whether of similar or dissimilar polarization.

Figure 4.3 shows the \mathbf{B}_{qr} coupling matrices for a symmetry axis orientation where $\hat{s}(\theta, \varphi) = \hat{s}(10^\circ, 20^\circ)$. Note that all of the modes couple to some degree. The invariant acoustic modes have polarizations predominantly in the sagittal plane. The invariant modes appear at higher frequencies in isotropic, VTI, and TTI media. They are essentially insensitive to most tilt of the symmetry axis \hat{s} within thin anisotropic sediment layers. These modes couple weakly with any predominantly quasi-SH modes when lateral heterogeneity is present. In contrast, the invariant acoustic modes may

B_{qr} Interface Term Coupling Matrix for VTI Media

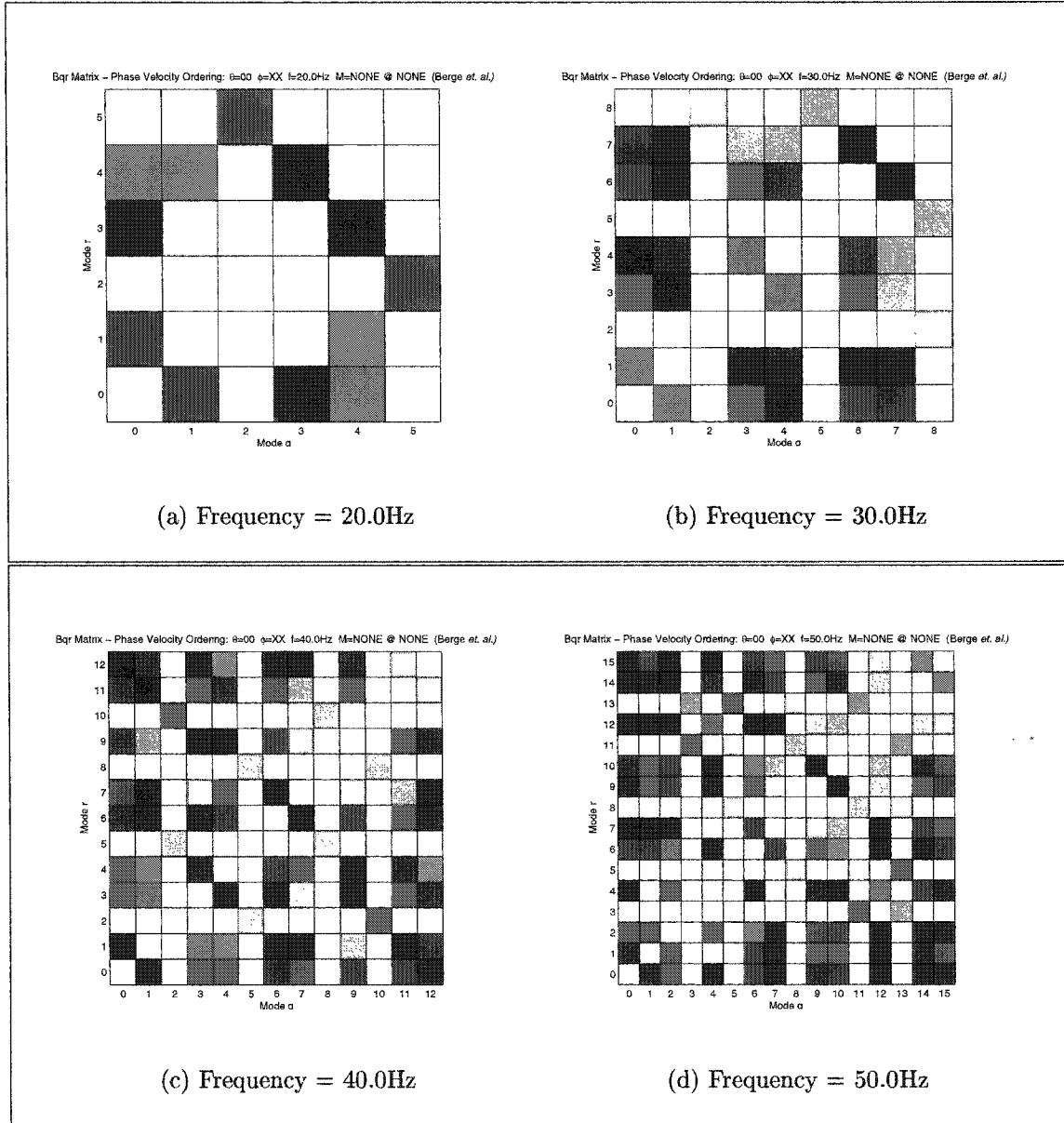


Figure 4.2: B_{qr} coupling matrices for P-SV and SH modes at 20.0Hz-50.0Hz when $\hat{s}(\theta, \varphi) = \hat{s}(0^\circ, 0^\circ)$. The coupling is restricted to P-SV/P-SV and SH/SH coupling. The white spaces indicate that there is no P-SV/SH exists.

B_{qr} Interface Term Coupling Matrix for TTI Media

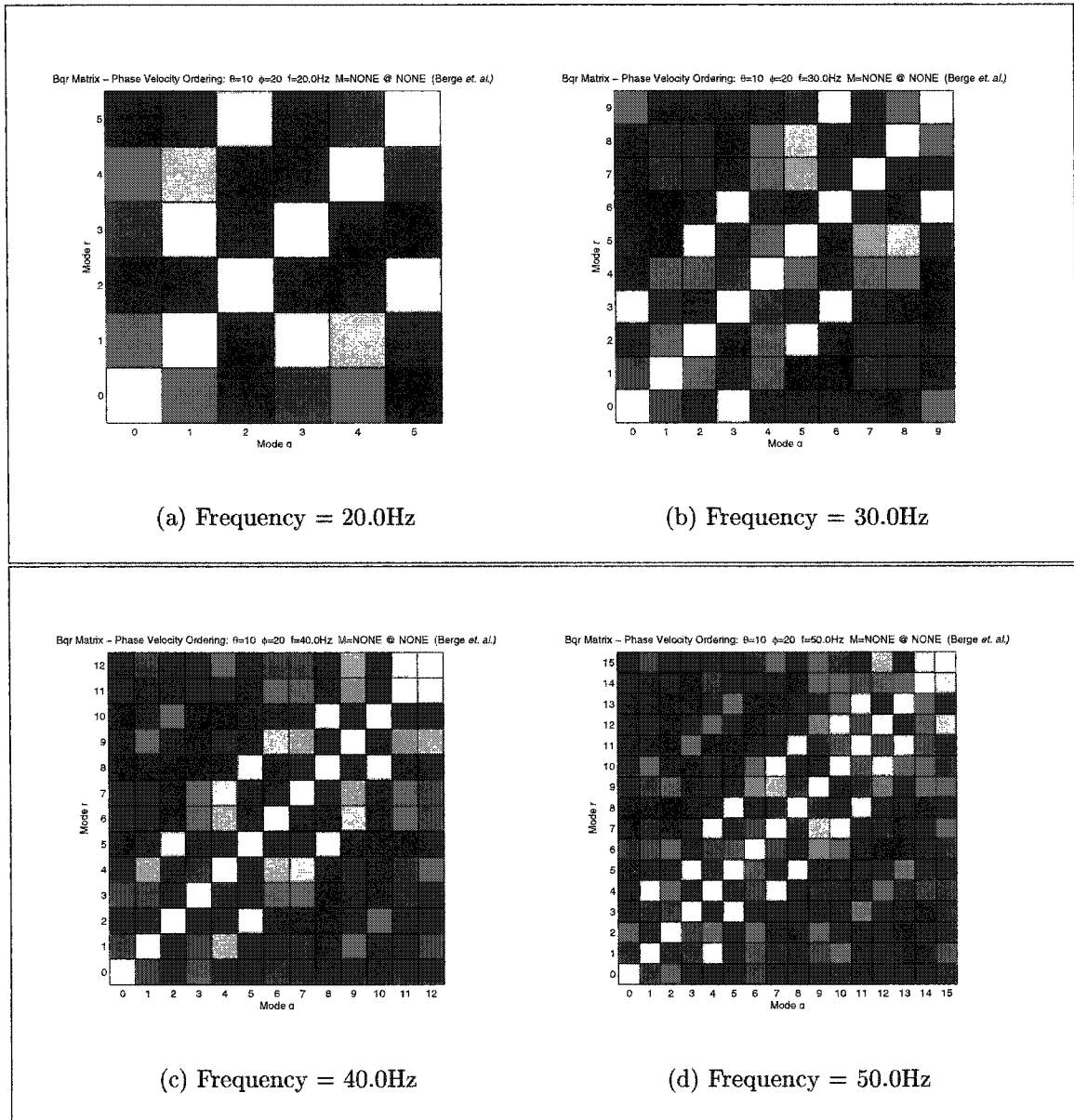


Figure 4.3: B_{qr} coupling matrices for quasi-P-SV, quasi-SH, and P-SV-SH modes at 20.0Hz-50.0Hz. Any mode may coupling into any other mode without the restrictions to the quasi-monoclinic symmetries shown in Figure 4.2.

couple strongly with any quasi-P-SV, generalized P-SV-SH, or quasi-SH modes with significant particle motion polarizations in the sagittal plane.

Near degeneracies play an important role in the coupling of local modes. Since the \mathbf{B}_{qr} coupling matrix is directly dependent upon the spacing of the eigenvalues as well as the polarization of the modes, it is important to consider what happens as the eigenvalues become degenerate. Many near degeneracies in the modal phase velocities can be seen in Figure 3.6(c) between $10^\circ - 20^\circ$ and $70^\circ - 80^\circ$. For the near degenerate case $c_r \approx c_q$ and $k_r \approx k_q$, and when two modes are degenerate, then $c_r = c_q$ and $k_r = k_q$. The wavenumber dependence of the coupling matrix \mathbf{B}_{qr} can be factored out as a Δk term.

$$\mathbf{B}_{qr} = \frac{1}{\Delta k} \mathbf{B}_{qr}' \quad (4.8)$$

As the difference between the mode phase velocities becomes smaller, the contribution to the coupling matrix \mathbf{B}_{qr} may become larger.

$$\frac{1}{\Delta k} = \frac{1}{k^q - k^r} = \frac{c^q c^r}{\omega(c^r - c^q)} \quad (4.9)$$

The coupling of the two modes is expected to become very large as they approach a near degenerate state. Higher order modes must have closer spaced eigenvalues than lower order modes to obtain the same Δk value. The \mathbf{B}_{qr} coupling matrix may be dominated by such interaction of closely spaced modes. The coupling at near degeneracies is not infinite, but the closely spaced phase velocities, and therefore the closely spaced wavenumbers of the two discrete modes, can dominate the coupling term between the modes, as shown in figure 4.4(a). When the nearest-neighbor contributions are removed as in figure 4.4(b), then the \mathbf{B}_{qr} coupling matrix is similar to the one in figure 4.3(d). As the modal phase velocities converge, the polarizations of the modes become more alike.

In contrast, when the spacing of two eigenvalues is large, then the coupling between two modes may become weak. In addition, if two eigenfunctions have rather

B_{qr} Interface Term Coupling Matrix for Near Degeneracy

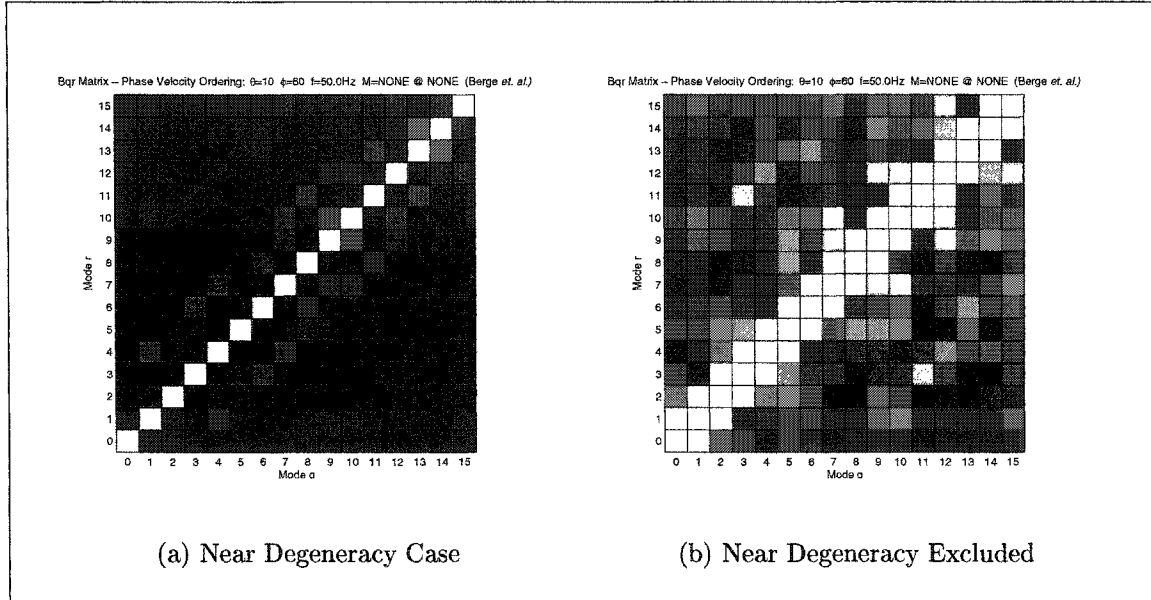


Figure 4.4: Coupling matrices showing the effects of near degeneracy for $\hat{s}(\theta, \varphi) = \hat{s}(10^\circ, 60^\circ)$ at 50.0Hz. Nearly degenerate in phase velocity, two modes may strongly couple and dominate the appearance of the coupling matrix. When the nearest-neighbor coupling terms are removed, the coupling matrix resembles those of 4.3

dissimilar polarizations then the coupling may also be weak, if the wave numbers of the two modes are not in close proximity to one another. An example of when the polarizations are completely dissimilar is when pure P-SV and SH local modes propagate independently, as observed in figure 4.2. In general, eigenfunctions with different polarizations will tend to couple more weakly than eigenfunctions that have similar polarizations. The strongest coupling occurs between modes of similar polarizations. For an isotropic case only P-SV modes may have similar polarizations with other P-SV modes, and only SH modes may have similar polarizations with other SH modes. For the more general anisotropic case, two modes with particle motions in all three polarization directions and closely space eigenvalues will exhibit strong coupling.

Table 4.1: Symmetry Axis Orientation and Coupling

\hat{s} quasi-Monoclinic Medium:
SH/SH
P-SV/P-SV
quasi-Triclinic Medium:
quasi-P-SV/quasi-SH
quasi-P-SV/quasi-P-SV
quasi-P-SV/P-SV-SH
quasi-SH/quasi-SH
quasi-SH/P-SV-SH
P-SV-SH/P-SV-SH

Table 4.1 summarizes the combinations of wave types that will couple for a TTI medium.

When the symmetry axis \hat{s} allows for a quasi-triclinic *form* of the elastic stiffness tensor all the modes are excited regardless of the source type, and all the modes are involved in the coupling, although some modes' contribution is much smaller than others. The coupling matrix \mathbf{B}_{gr} results suggest that the combination of a tilted symmetry axis and lateral heterogeneity is rather efficient at scattering a seismic-acoustic signal.

Figure 4.5 shows the \mathbf{B}_{gr} coupling matrices for four moment tensor sources, which are of interest for T -wave excitation. The figure clearly shows which modes are excited when the source modes are pure P-SV and SH modes with separate polarizations. The explosive source in figure 4.5(a) clearly shows that the SH modes are excluded entirely, as they are not excited at all. A double couple source in the xz -plane produces a similar coupling matrix to the explosive source, where again the SH modes are not

directly excited, as shown in figure 4.5(c). The double couple sources in the xy-plane and the yz-plane only excite the SH modes, as shown in figures 4.5(b) and 4.5(d) respectively.

4.4 Stochastic Interface Coupling Matrices

Stochastic rough boundaries are added to the non-horizontal interface boundaries of section 4.3. Park and Odom (1999) have successfully included both deterministic bathymetry terms and rough boundary interface terms for isotropic and transverse isotropy media into the coupled mode equations. The formulation for the scattering coupling matrix \mathbf{S}_{qr} presented by Park and Odom (1999) is valid for more general anisotropy symmetries, such as those already discussed previously. The terms of the coupling matrix can be cast in a form that only includes the displacement \mathbf{w} , the traction vector \mathbf{t} , and their respective derivatives. This gives uniformity, where all of the coupling matrices may be expressed in terms of the stress-displacement vector $\mathbf{u} = (\mathbf{w}, \mathbf{t})^T$ and its derivatives.

The evolution equation for coupling due to stochastic rough interfaces come from the dissertation of Minkyu Park (1997):

$$\begin{aligned}
\frac{\partial d_q}{\partial x} &= \sum_r \left(\left(\langle \mathbf{u}^q, \frac{\partial \mathbf{u}^r}{\partial x} \rangle + i \sum_n \dot{h}_n^0 [\mathbf{w}^{q*} \cdot \mathbf{t}^r]_n \right) \exp \left(i \int_0^x (k^r - k^q) d\xi \right) \right) d_r \\
&\quad + \sum_r \mathbf{D}_{qr} c_r + \sum_r \mathbf{E}_{qr} \frac{\partial c_r}{\partial x} \\
&= \sum_r \mathbf{B}_{qr} d_r + \sum_r \mathbf{D}_{qr} c_r + \sum_r \sum_s \mathbf{E}_{qs} \mathbf{B}_{sr} c_r \\
&= \sum_r \mathbf{B}_{qr} d_r + \sum_r \mathbf{S}_{qr} c_r
\end{aligned} \tag{4.10}$$

The \mathbf{B}_{qr} matrix is defined the same as in section 4.1 and Appendix G. The matrices $\mathbf{D}_{\alpha\beta}$ and $\mathbf{E}_{\alpha\beta}$ are defined as:

$$\mathbf{D}_{qr} = i \sum_n \gamma_n \frac{1}{\sqrt{1 + (\dot{h}_n^0)^2}} \left(\left[\mathbf{w}^{q*} \cdot \frac{\partial \mathbf{t}^r(\hat{\mathbf{n}}_o)}{\partial z} \right]_n - i k^r \dot{h}_n^0 [\mathbf{w}^{q*} \cdot \mathbf{t}^r(\hat{\mathbf{n}}_o)]_n \right)$$

B_{qr} Interface Term Coupling Matrix for Explosive and Seismic Sources

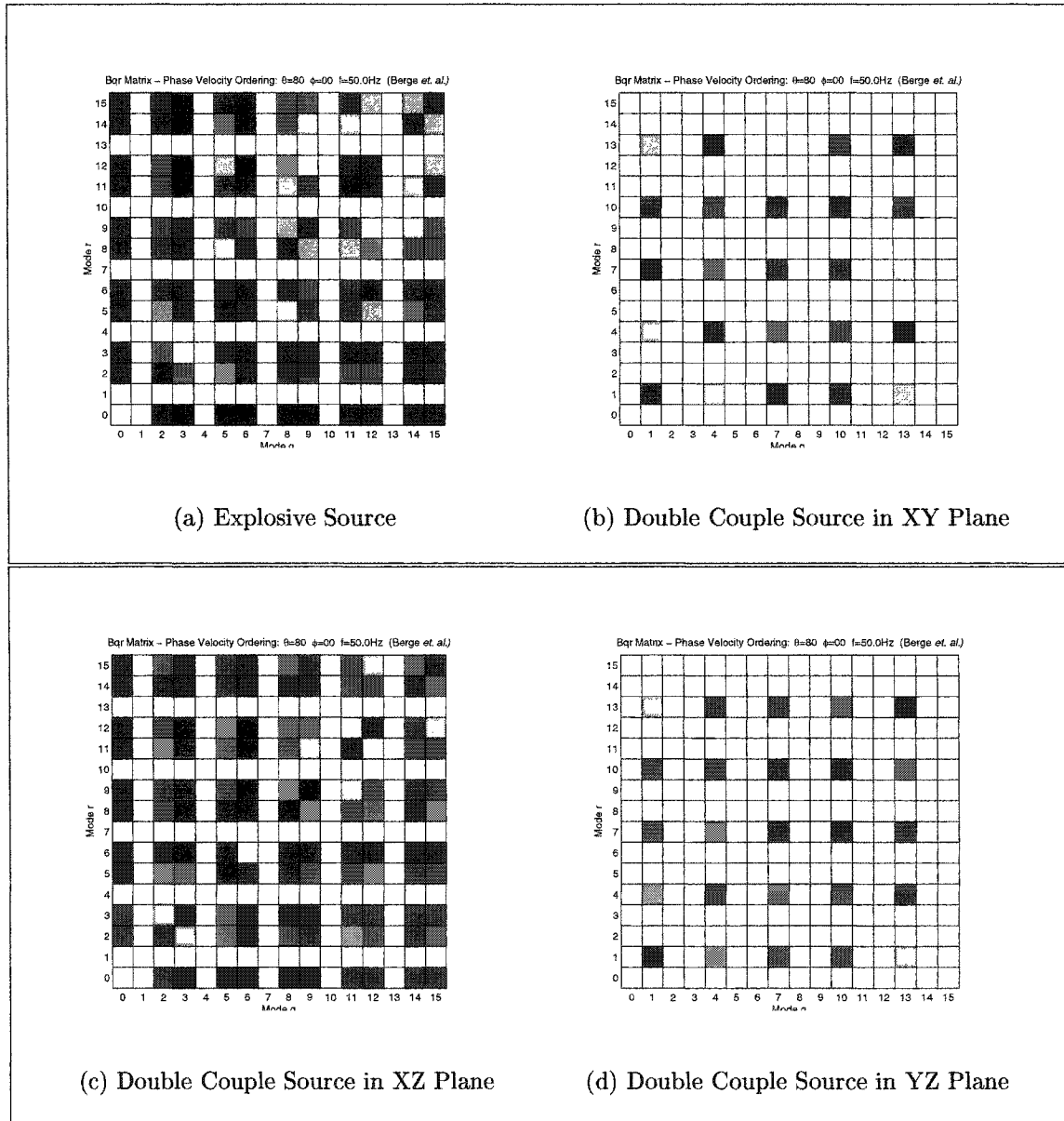


Figure 4.5: The excitation of P-SV and SH modes by explosive and double couple sources for $\hat{s}(\theta, \varphi) = \hat{s}(80^\circ, 0^\circ)$.

$$\begin{aligned}
& + (\dot{h}_n^0)^2 \left[\mathbf{w}^{q*} \cdot \frac{\partial \mathbf{t}^r(\hat{\mathbf{n}}_o)}{\partial z} \right]_n + \frac{\dot{h}_n^0 \ddot{h}_n^0}{1 + (\dot{h}_n^0)^2} [\mathbf{w}^{q*} \cdot \mathbf{t}^r(\hat{\mathbf{n}}_o)]_n \\
& + \frac{\dot{h}_n^0 \ddot{h}_n^0}{\sqrt{1 + (\dot{h}_n^0)^2}} [\mathbf{w}^{q*} \cdot \mathbf{t}^r(\hat{\mathbf{x}})]_n \exp \left(i \int_0^x (k^r - k^q) d\xi \right), \quad (4.11)
\end{aligned}$$

$$\mathbf{E}_{qr} = -i \sum_n \gamma_n \frac{\dot{h}_n^0}{\sqrt{1 + (\dot{h}_n^0)^2}} [\mathbf{w}^{q*} \cdot \mathbf{t}^r(\hat{\mathbf{n}}_o)]_n \exp \left(i \int_0^x (k^r - k^q) d\xi \right), \quad (4.12)$$

Note the sign correction for the fourth term of the \mathbf{D}_{qr} matrix from Park and Odom (1999) equation (36). The function γ_n is defined as a zero-mean stochastic process, that adds roughness to a deterministic reference boundary. Additional restraints on γ_n are reported by Park (1997). After some algebra, the matrices can be expressed as:

$$\begin{aligned}
\mathbf{D}_{qr} & = i \sum_n \gamma_n \left(\left[\mathbf{w}^{q*} \cdot \frac{\partial \mathbf{t}_3^r}{\partial z} \right]_n - \dot{h}_n^0 \left[\mathbf{w}^{q*} \cdot \frac{\partial \mathbf{t}_1^r}{\partial z} \right]_n \right. \\
& \quad \left. + ik^r \frac{(\dot{h}_n^0)^2}{1 + (\dot{h}_n^0)^2} [\mathbf{w}^{q*} \cdot \mathbf{t}_1^r]_n + \frac{\dot{h}_n^0 \ddot{h}_n^0}{(1 + (\dot{h}_n^0)^2)^2} [\mathbf{w}^{q*} \cdot \mathbf{t}_1^r]_n \right) \\
& \quad \times \exp \left(i \int_0^x (k^r - k^q) d\xi \right), \quad (4.13)
\end{aligned}$$

$$\mathbf{E}_{qr} = i \sum_n \gamma_n \frac{(\dot{h}_n^0)^2}{1 + (\dot{h}_n^0)^2} [\mathbf{w}^{q*} \cdot \mathbf{t}_1^r]_n \exp \left(i \int_0^x (k^r - k^q) d\xi \right), \quad (4.14)$$

The derivative of the traction vector \mathbf{t}_3 can be determined from the original equations of motion. The vertical derivative of the tractions \mathbf{t}_3 can be expressed as:

$$\frac{\partial \mathbf{t}_3}{\partial z} = -\rho\omega^2 \mathbf{w} - \frac{\partial \mathbf{t}_1}{\partial x} \quad (4.15)$$

where it has been assumed that all propagation is restricted to the xz-plane, and all derivatives in the y-coordinate direction are zero.

Figures 4.6 and 4.7 present the scattering coupling matrix \mathbf{S}_{qr} for a VTI medium and TTI where $\hat{s}(\theta, \varphi) = (10^\circ, 20^\circ)$ respectively.

The rows and columns of \mathbf{S}_{qr} represent the primary and scattered modes respectively. Figure 4.6 is similar to those presented by Park and Odom (1999), except

S_{qr} Interface Term Scattering Matrix for VTI Media

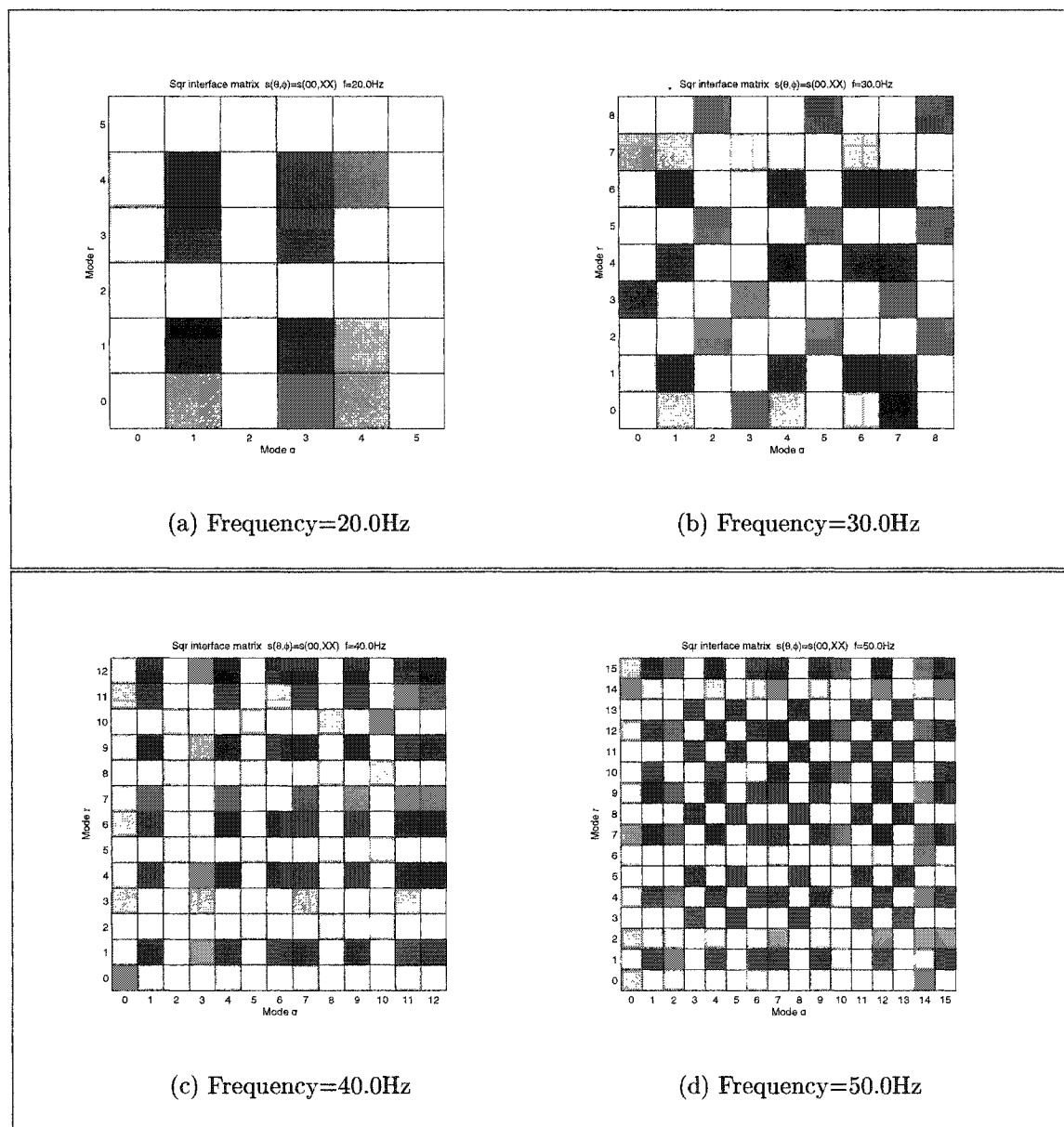


Figure 4.6: S_{qr} coupling matrices for P-SV and SH modes at 20.0Hz-50.0Hz. The rows represent modes from the primary wavefield, and the columns represent the modes from the scattered wavefield.

that SH modes have been included into the mode sets. Figure 4.7 represents the extension of the work presented by Odom and Park (1999) to a more general case of anisotropy, where the symmetry axis of the TI elastically symmetric medium may have any arbitrary orientation. The symmetry axis, $\hat{s}(\theta, \varphi) = (10^\circ, 20^\circ)$, is not too far from vertical. Some of the scattered modes are preferentially excited, while others are less excited. Scattered modes 2, 4, and 5 from Figure 4.7(c), represented by columns 2, 4, and 5 respectively, are excited to a much smaller degree than scattered modes 0, 3, 4, 7, 9, and 11. At the frequency of 40.0Hz (Figure 4.7(c)), it can be seen that the primary modes 1, 4, 6, 7, 9, and 12, represented by rows 1, 4, 6, 7, 9, and 12 contribute the most to resulting scattered wavefield. What is interesting is the characteristics of these modes. The primary modes 0, 3, and 11 are invariant acoustic modes, with the majority of their energy in the isotropic portion of the model. They do not contribute to the scattered wavefield as strongly as the more sensitive modes. This implies that the energy will remain coherent longer in these modes than the sensitive modes. However, these same invariant modes from the scattered wavefield receive more energy than the sensitive type modes. This implies that rough interface boundaries tend to preferentially redistribute energy from sensitive modes to invariant modes. This may indicate that energy from seismic sources below that water column would be preferentially scattered into invariant acoustic modes, which would remain coherent longer. Such mechanism could help explain T -wave generation.

4.5 Chapter Summary

A generalized set of P-SV-SH modes is required to correctly model seismo-acoustic signals where tilted anisotropy is present. Since there no longer exists a clear distinction between pure P-SV and SH modes, all modes can carry energy for the seismo-acoustic signal. The implication is that all of the modes are intricately coupled for even weak anisotropy, and therefore more modes are available in anisotropic media

S_{qr} Interface Term Scattering Matrix for TTI Media

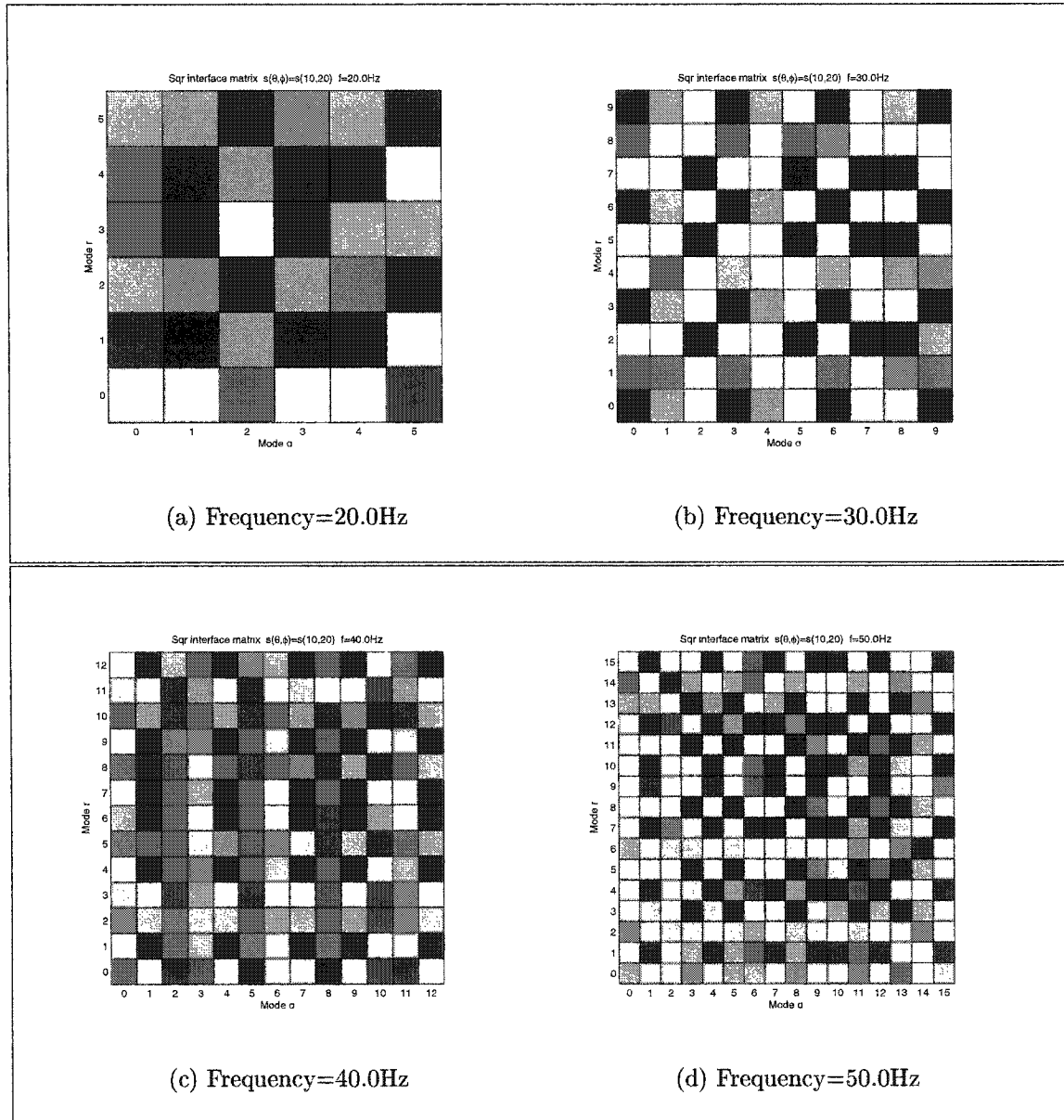


Figure 4.7: S_{qr} coupling matrices for quasi-P-SV, quasi-SH, and P-SV-SH modes at 20.0Hz-50.0Hz. The rows represent modes from the primary wavefield, and the columns represent the modes from the scattered wavefield.

for the redistribution of energy. The magnitude of anisotropy as well as the direction of the symmetry axis have been observed to be of equal importance. Any rotation of the symmetry axis away from vertical (e.g. non-horizontal bedding planes) will cause energy to be transferred between the modes, even if lateral variation is weak. The elements of the \mathbf{B}_{qr} and \mathbf{S}_{qr} coupling matrices give insight into the degree of energy distribution between modes due to heterogeneity in the presence of anisotropy. Heterogeneity is very efficient at redistributing energy among modes in anisotropic media. The combination of lateral heterogeneity and anisotropy can be effective at scattering a signal, and energy may become broadly redistributed among all of the propagating modes. Any lateral heterogeneity can cause the modes to couple, and the coupling tends to become stronger as the phase velocities associated with the local modes converge to similar values. In contrast, the isotropic and transversely isotropic modes transfer energy only to a few nearest-neighbor modes of the same wavetype (e.g. modes having the same polarizations). In nearest neighbor energy transfer, lower order modes couple to the nearest lower order modes and higher order modes transfer energy to the nearest higher order mode. With the introduction of even modest amounts of anisotropy, it becomes possible for higher order modes to directly transfer energy into lower order modes without cascading down through multiple nearest neighbor interactions.

Acoustic energy can leave the water column through bottom interacting modes. The energy can then be attenuated by the low shear velocity sediments, and redistributed to other predominantly sediment modes. In addition, energy from other sources or signals, such as noise, from the sediment and bottom layers can enter the water column through these bottom interacting modes. With the anisotropic bottom interacting modes, there exists a greater opportunity for the energy to become redistributed and leave or enter the water column. This is due to the 3-D nature of the eigenfunctions, which are a direct result of the elastic treatment of the bottom sediments and subbottom structure. Therefore, in the presence of anisotropy, attenuation

of bottom interacting modes would be underestimated if isotropy is assumed.

Chapter 5

DETERMINISTIC AND STOCHASTIC VOLUME SCATTERING

The investigations of the previous chapters are complemented by including volume scattering terms for anisotropic media into the coupled local mode formalism. A considerable amount of work has been done in the area of volume scattering by many others. The volume scattering theory and numerical analysis presented is preceded by the work Aki and Richards (1980), Beran (1994) and Tracy and Schmidt (1997) to name a few. Aki and Richards (1980) provide a perturbation approach to volume scattering. Beran (1994) applied a statistical modal analysis to scattering by random density fluctuations in a plate, where cross-modal terms are retained. Tracy and Schmidt (1997) investigate the effects of surface roughness and volume fluctuations on the seismo-acoustic field.

Park and Odom (1999) have successfully included boundary terms (both deterministic and stochastic) for isotropic and transverse isotropy media into the coupled mode equations. Their work has been extended to more general anisotropy in chapter 4. A natural step towards a more complete description of the forward problem is the inclusion of volume heterogeneity, in the presence of isotropic, transverse isotropic and more general anisotropic media. This chapter begins with considering deterministic volume scattering, and then stochastic perturbations to the the material parameters is considered.

5.1 Description of Deterministic Elastic Moduli

The deterministic coupling matrix \mathbf{B}_{qr} of Maupin (1988) contains both boundary interface terms and volume terms. The expanded form of the deterministic coupling matrix \mathbf{B}_{qr} is found in Appendix G. In the absence of any lateral heterogeneity along the interface boundaries, all layer interfaces are horizontal planar boundaries ($\dot{h}_n = 0$), and only the deterministic volume terms of \mathbf{B}_{qr} remain. Several assumptions are made about the nature of the density and elastic moduli in considering heterogeneity of the material parameters. First, let the x and z -dependence of the density and elastic moduli be separable, as in equation (5.1). It is also assumed that there is no heterogeneity in the water column. When the elastic moduli and density have range dependence, where $\dot{\rho} \neq 0$ and ${}^w\dot{C}_{ij} \neq 0$ (with the dot representing a derivative with respect to the range coordinate), then it is assumed that the all of the elastic moduli of the elastic stiffness matrix and density have the same range dependence. The rotated elastic stiffness matrix contains elements which are the linear combinations the the five elastic moduli A, C, F, L, N as described by equation (2.11). Therefore the assumption of a single range-dependent function greatly simplifies the problem by avoiding a unique range-dependent function for each element of the elastic stiffness matrix. The elastic moduli and density are modified by a range-dependent function $g(x)$, where $g(x) \neq 0$ (to prevent dividing by zero) and $\dot{g}(x)$ may have a zero value.

$$\begin{aligned}
 \rho(x, z) &= g_o(x)\rho_o(z) \\
 {}^wC_{ij}(x, z) &= g_o(x)({}^wC_{ij}(z))_o \\
 {}^wC_{ij}^{-1}(x, z) &= \frac{1}{g_o(x)}({}^wC_{ij}^{-1}(z))_o
 \end{aligned} \tag{5.1}$$

The o subscript in the above equation and the following equations indicates that $g_o(x)$ is deterministic in nature, with the absence of any stochastic properties. Using the results from equation (5.1), the range-dependence of the elastic matrices in the

\mathbf{B}_{qr} coupling matrix may be determined.

$$\begin{aligned} {}^w Q_{ij} &= g_o(x)({}^w C_{ij})_o - g_o(x)({}^w C_{i1})_o \frac{1}{g_o(x)} ({}^w C_{11}^{-1})_o g_o(x) ({}^w C_{ij})_o \\ &= g_o(x) ({}^w C_{ij} - {}^w C_{i1} {}^w C_{11}^{-1} {}^w C_{ij})_o \\ &= g_o(x) ({}^w Q_{ij})_o \end{aligned} \quad (5.2)$$

$${}^w C_{11}^{-1} = \frac{1}{g_o(x)} ({}^w C_{11}^{-1})_o \quad (5.3)$$

$${}^w C_{11}^{-1} {}^w C_{1j} = \frac{1}{g_o(x)} ({}^w C_{11}^{-1})_o g_o(x) ({}^w C_{1j})_o = ({}^w C_{11}^{-1} {}^w C_{1j})_o \quad (5.4)$$

$${}^w C_{i1} {}^w C_{11}^{-1} = g_o(x) ({}^w C_{i1})_o \frac{1}{g_o(x)} ({}^w C_{11}^{-1})_o = ({}^w C_{i1} {}^w C_{11}^{-1})_o \quad (5.5)$$

The horizontal derivative of the density and elastic moduli may be taken, where the x-derivative of $g_o(x)$ describes the rate of change of the material properties.

$$\begin{aligned} \dot{\rho} &= \dot{g}_o(x) \rho_o(z) \\ {}^w \dot{Q}_{ij} &= \dot{g}_o(x) ({}^w Q_{ij})_o \\ {}^w \dot{C}_{11}^{-1} &= -\dot{g}_o(x) \frac{1}{g_o^2(x)} ({}^w C_{11}^{-1})_o \\ ({}^w C_{11}^{-1} \dot{{}^w C}_{1j}) &= 0 \\ ({}^w C_{i1} \dot{{}^w C}_{11}^{-1}) &= 0 \end{aligned} \quad (5.6)$$

where the dot indicates the horizontal derivative of the elements of the elastic stiffness matrix or the horizontal derivative of the product of the elements of the elastic stiffness matrix.

The x dependent terms can be factored out of the volume integral of the \mathbf{B}_{qr} matrix.

$$\begin{aligned} B_{qr} &= \frac{1}{k^q - k^r} (\dot{g}_o(x) \int_{h_f(x)}^{\infty} \left(\mathbf{w}^{q*} \rho_o(z) \omega^2 \mathbf{w}^r - \frac{\partial \mathbf{w}^{q*}}{\partial z} (Q_{33}(z)_o) \frac{\partial \mathbf{w}^r}{\partial z} \right. \\ &\quad - \mathbf{w}^{q*} ip(Q_{23}(z)_o) \frac{\partial \mathbf{w}^r}{\partial z} + \frac{\partial \mathbf{w}^{q*}}{\partial z} (Q_{32}(z)_o) ip \mathbf{w}^r \\ &\quad \left. - \mathbf{w}^{q*} (Q_{22}(z)_o) \mathbf{w}^r p^2 - \frac{1}{g_o^2(x)} \mathbf{t}^{q*} (C_{11}^{-1}(z)_o) \mathbf{t}^r \right) dz \end{aligned} \quad (5.7)$$

The function $\dot{g}_o(x)$ serves a similar role as the deterministic slope $\dot{h}_o(x)$ does for the interface terms of the \mathbf{B}_{qr} matrix. The deterministic volume terms of \mathbf{B}_{qr} are proportional to the rate of change of the material properties.

The deterministic aspects of the material properties could be further generalized by allowing each elastic modulus have its own range-dependence. If it is still assumed that the x and z-dependence are separable, then the deterministic x-dependence could be factored out for each term in the \mathbf{B}_{qr} matrix, and the volume integral evaluated separately for each term. However, all of the elastic moduli should be correlated, so the assumption of a single range-dependence should be fairly good.

These results are valid for any generally anisotropic deterministic structure, with the assumption that the x-dependence is separable from the z-dependence of the elastic moduli. The deterministic coupling matrix \mathbf{B}_{qr} remains a symmetric matrix regardless of whether it contains volume terms, interface terms, or both.

5.2 Numerical Modeling for Deterministic Volume Scattering

The deterministic volume terms from the \mathbf{B}_{qr} matrix are calculated for the same model which was used in chapter 4 to calculate the deterministic and stochastic interface terms. An evaluation point x_o has been chosen where $\dot{h}_o(x_o) = 0$, and the value of the functions $g(x_o)$ and $\dot{g}(x_o)$ evaluated at the point x_o are both equal to 1. This assumption ensures that only the contributions to the \mathbf{B}_{qr} matrix are the deterministic volume terms.

The volume terms for the \mathbf{B}_{qr} matrix in Figure 5.1 indicated that the weakest coupling exists between the SH modes and other SH modes. The strongest coupling is between the P-SV modes and other P-SV modes. There is no SH/P-SV coupling for the VTI medium

The volume integral terms which contribute to the \mathbf{B}_{qr} in coupling matrix Figure 5.1 and Figure 5.2 seem very similar to the interface terms presented in Figures 4.2 and 4.3 of chapter 4. One advantage of evaluating the coupling matrix with a symmetry axis near the vertical, is that the modes can be clearly defined as quasi P-SV, quasi-SH, and invariant. In Figure 5.2(c), modes 0, 3, and 11 are invariant

B_{qr} Deterministic Volume Term Coupling Matrix for P-SV and SH Modes

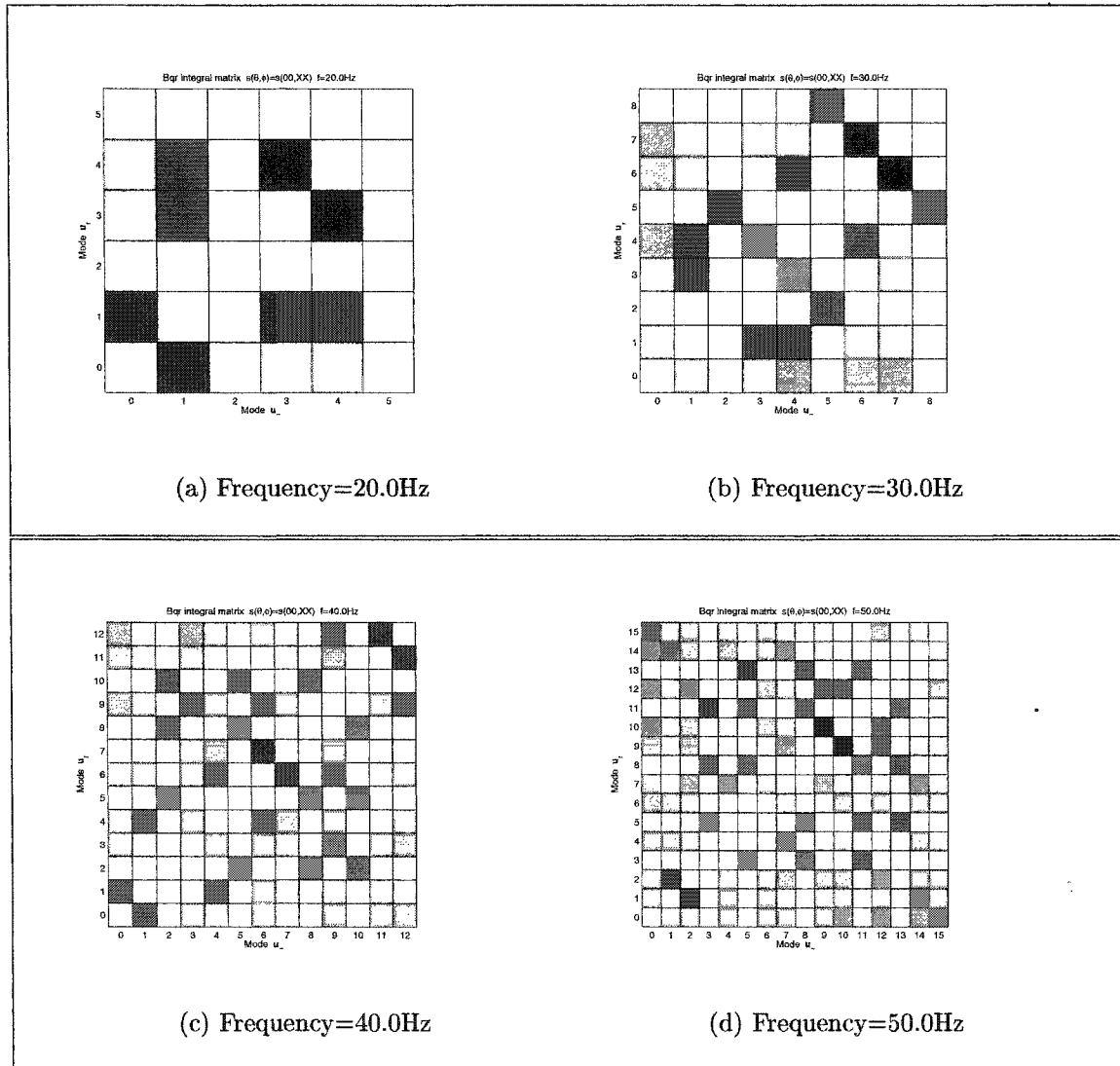


Figure 5.1: B_{qr} coupling matrices for P-SV and SH modes at 20.0Hz-50.0Hz. The weakest coupling is SH/SH coupling and the P-SV/P-SV coupling is the strongest in the figures.

acoustic modes, modes 2, 5, 8, and 10 are quasi SH modes, and modes 1, 4, 6, 7, 9, and 12 are quasi P-SV modes. The strongest coupling for the volume terms occurs between the quasi P-SV and other quasi P-SV modes. In contrast, quasi SH modes couple very weakly with other quasi SH modes. The intermediate coupling involves combinations of invariant, quasi P-SV, and quasi-SH modes.

5.3 Coupled Local Mode Formalism for Stochastic Volume Heterogeneity

The combined effects of anisotropy and stochastic volume heterogeneity on wave propagation are now considered. The method of coupled local modes is again used to represent the displacement-stress wavefield, as presented in chapter 4, and extended by including stochastic volume scattering terms. Volume scattering terms are included in the coupled mode equations for general anisotropic heterogeneous media using perturbation theory. Since the exact parameterization of any structure cannot be precisely known, one way to represent the structure is to use an average deterministic model and then incorporate additional random variations. The elastic moduli and density of each layer are assumed to have a mean deterministic part, which may include large variations, and a smaller scale stochastic fluctuation. After the application of perturbation theory to the coupled mode equations and the boundary conditions, the displacement-stress field may be expressed as a sum of a primary 0th order wavefield and a 1st order scattered field. This approach introduces random volume scattering to the problem. The inclusion of random variations cause the signal to scatter and energy to transfer between the individual modes of the model. In general, density variations promote backscattering and variations in the elastic moduli generate predominantly forward scattering.

The 0th order solution corresponds to the deterministic range-dependent medium, and the 1st order solution provides a correction due to the scattering from the small-

\mathbf{B}_{qr} Deterministic Volume Term Coupling Matrix for quasi-P-SV,
quasi-SH modes, and P-SV-SH

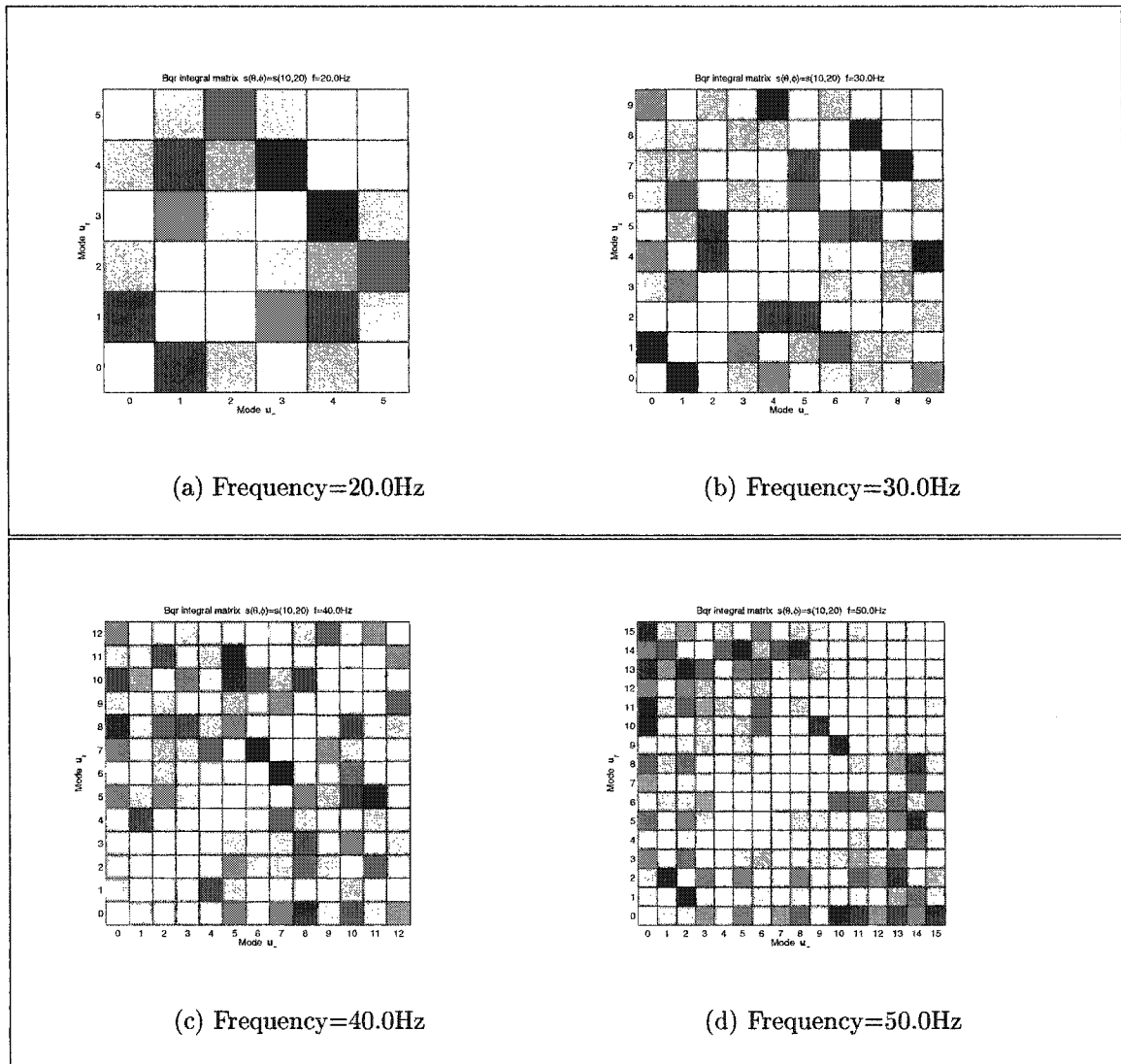


Figure 5.2: \mathbf{B}_{qr} coupling matrices for quasi-P-SV, quasi-SH, and P-SV-SH modes at 20.0Hz-50.0Hz. The coupling between quasi P-SV modes is the strongest, while coupling between quasi SH modes remains weak. The intermediate values of coupling arise from cross of modes of different wavetypes between combinations of invariant, quasi P-SV, and quasi SH modes.

scale random fluctuations. The primary and scattered wavefields are each dependent upon a unique set of mode coupling coefficients, c_r and s_r respectively. The primary wavefield mode coupling coefficients give insight into the distribution of modal energy due to the deterministic structure. Similarly, the scattered field mode coupling coefficients reveal how modal energy is redistributed due to random fluctuations of the density and elastic moduli.

The coupling between coherent modes and scattered modes is described. Consider the case where a coherent mode \mathbf{u}_r couples to coherent mode \mathbf{u}_q , where coherent mode \mathbf{u}_r couples to scattered mode \mathbf{u}_q , and where scattered mode \mathbf{u}_r couples to scattered mode \mathbf{u}_q . The goal is to determine the coupling matrices \mathbf{B}_{qr} and \mathbf{H}_{qr} which describe these coupling interactions. New volume scattering correction terms are derived by applying perturbation theory to the equations of motion and boundary conditions. Perturbation theory is applied to the first order coupled equation (3.4), and the density and elastic moduli perturbations are incorporated into the \mathbf{A} operator. Consider the following perturbation expansions of the stress-displacement vector, the differential operator \mathbf{A} , and the traction vector:

$$\begin{aligned}\mathbf{u}(x, z) &= \mathbf{u}_o(x, z) + \varepsilon \mathbf{u}_1(x, z) + \varepsilon^2 \mathbf{u}_2(x, z) + \varepsilon^3 \mathbf{u}_3(x, z) + \dots \\ \mathbf{A}(x, z) &= \mathbf{A}_o(x, z) + \varepsilon \mathbf{A}_1(x, z) + \varepsilon^2 \mathbf{A}_2(x, z) + \varepsilon^3 \mathbf{A}_3(x, z) + \dots \\ [\mathbf{t}]_n &= [\mathbf{t}_o]_n + \varepsilon [\mathbf{t}_1]_n + \varepsilon^2 [\mathbf{t}_2]_n + \varepsilon^3 [\mathbf{t}_3]_n + \dots\end{aligned}\quad (5.8)$$

The expanded expressions are then substituted into the equation (3.4).

$$\begin{aligned}\frac{\partial}{\partial x}(\mathbf{u}_o + \varepsilon \mathbf{u}_1 + \varepsilon^2 \mathbf{u}_2 + \varepsilon^3 \mathbf{u}_3 + \dots) &= \\ (\mathbf{A}_o + \varepsilon \mathbf{A}_1 + \varepsilon^2 \mathbf{A}_2 + \varepsilon^3 \mathbf{A}_3 + \dots)(\mathbf{u}_o + \varepsilon \mathbf{u}_1 + \varepsilon^2 \mathbf{u}_2 + \varepsilon^3 \mathbf{u}_3 + \dots) &+ \\ + \sum_n \dot{h}_n \begin{pmatrix} 0 \\ [\mathbf{t}_o]_n + \varepsilon [\mathbf{t}_1]_n + \varepsilon^2 [\mathbf{t}_2]_n + \varepsilon^3 [\mathbf{t}_3]_n + \dots \end{pmatrix} \delta(z - h_n(x)) &\end{aligned}\quad (5.9)$$

Collecting orders of ε results in:

$$\frac{\partial \mathbf{u}_o}{\partial x} = \mathbf{A}_o \mathbf{u}_o + \sum_n \dot{h}_n \begin{pmatrix} 0 \\ [\mathbf{t}_o]_n \end{pmatrix}\quad (5.10)$$

$$\frac{\partial \mathbf{u}_1}{\partial x} = \mathbf{A}_o \mathbf{u}_1 + \mathbf{A}_1 \mathbf{u}_o + \sum_n \dot{h}_n \begin{pmatrix} 0 \\ [\mathbf{t}_1]_n \end{pmatrix} \quad (5.11)$$

$$\frac{\partial \mathbf{u}_2}{\partial x} = \mathbf{A}_o \mathbf{u}_2 + \mathbf{A}_1 \mathbf{u}_1 + \mathbf{A}_2 \mathbf{u}_o + \sum_n \dot{h}_n \begin{pmatrix} 0 \\ [\mathbf{t}_2]_n \end{pmatrix} \quad (5.12)$$

$$\frac{\partial \mathbf{u}_3}{\partial x} = \mathbf{A}_o \mathbf{u}_3 + \mathbf{A}_1 \mathbf{u}_2 + \mathbf{A}_2 \mathbf{u}_1 + \mathbf{A}_3 \mathbf{u}_o + \sum_n \dot{h}_n \begin{pmatrix} 0 \\ [\mathbf{t}_2]_n \end{pmatrix} \quad (5.13)$$

⋮

Parameters with a o subscript (e.g. \mathbf{u}_o) are unperturbed deterministic values and belong to the homogeneous equation. Equation (5.10) is the same deterministic equation already treated in chapters 3 and 4.

The total wavefield is represented as the combination of a primary field and a scattered field, $\mathbf{u}(x, z) = \mathbf{u}_o(x, z) + \mathbf{u}_1(x, z)$, both superpositions of local modes \mathbf{u}^r . The primary wavefield results from the average deterministic portion of the model and the scattered wavefield results from the small-scale random fluctuations in the model.

$$\begin{aligned} \mathbf{u}_o(x, z) &= \sum_r c_r(x) \exp\left(i \int_0^x k^r(\xi) d\xi\right) \mathbf{u}^r(z; x) \\ \mathbf{u}_1(x, z) &= \sum_r s_r(x) \exp\left(i \int_0^x k^r(\xi) d\xi\right) \mathbf{u}^r(z; x) \end{aligned} \quad (5.14)$$

Note that the scattering amplitude coefficient s_r is not to be confused with the symmetry axis \hat{s} of the anisotropic medium. A single scattering theory is used, and it is assumed that the Born approximation applies to this problem. It is assumed that any single scattering event is weak, and does not require the primary field to be renormalized. Therefore the primary waves are unchanged by their propagation through the heterogeneous medium. The energy conservation law is violated, because scattered waves should in fact remove some fraction of the primary wave energy. The Born approximation also limits the scope of the research, where the results are valid

only for weak stochastic heterogeneity. However, the deterministic heterogeneity can be strong.

Evolution equations for the primary and scattered fields are derived after substituting \mathbf{u}_0 and \mathbf{u}_1 from equation (5.14) into equations (5.10) and (5.11), taking the Hermitian product with mode \mathbf{u}^q , and doing some additional algebra. For the primary field, the coefficients $c_q(x)$ are determined from the same evolution equation as for the unperturbed deterministic model of chapter 4.

$$\frac{\partial c_q}{\partial x} = \sum_r \mathbf{B}_{qr} c_r \quad (5.15)$$

Substituting the primary and scatter wavefields from equation (5.14) into equation (5.11).

$$\begin{aligned} & \frac{\partial}{\partial x} \left(\sum_r s_r(x) \exp \left(i \int_0^x k^r(\xi) d\xi \right) \mathbf{u}^r(z; x) \right) \\ &= \mathbf{A}_0 \sum_r s_r(x) \exp \left(i \int_0^x k^r(\xi) d\xi \right) \mathbf{u}^r(z; x) \\ &+ \mathbf{A}_1 \sum_r c_r(x) \exp \left(i \int_0^x k^r(\xi) d\xi \right) \mathbf{u}^r(z; x) \\ &+ \sum_n \dot{h}_n \left(\begin{array}{c} 0 \\ \left[\sum_r s_r(x) \exp \left(i \int_0^x k^r(\xi) d\xi \right) \mathbf{t}^r(z; x) \right]_n \end{array} \right) \end{aligned} \quad (5.16)$$

It is assumed that each summation series in equation (5.16) uniformly converges to a generally complex function. This allows the the order of summation and differentiation to be interchangeable. Also, let $\exp(i\phi^r(x)) = \exp \left(i \int_0^x k^r(\xi) d\xi \right)$

$$\begin{aligned} & \sum_r \frac{\partial s_r(x)}{\partial x} \exp(i\phi^r(x)) \mathbf{u}^r(z; x) + \sum_r s_r(x) \frac{\partial}{\partial x} \exp(i\phi^r(x)) \mathbf{u}^r(z; x) \\ &+ \sum_r s_r(x) \exp(i\phi^r(x)) \frac{\partial \mathbf{u}^r(z; x)}{\partial x} = \mathbf{A}_0 \sum_r s_r(x) \exp(i\phi^r(x)) \mathbf{u}^r(z; x) \\ &+ \mathbf{A}_1 \sum_r c_r(x) \exp(i\phi^r(x)) \mathbf{u}^r(z; x) \\ &+ \sum_n \dot{h}_n \left(\begin{array}{c} 0 \\ \left[\sum_r s_r(x) \exp(i\phi^r(x)) \mathbf{t}^r(z; x) \right]_n \end{array} \right) \end{aligned} \quad (5.17)$$

The horizontal derivative of the exponential term can be expressed as:

$$\frac{\partial}{\partial x} (\exp(i\phi^r(x))) = \frac{\partial \phi^r(x)}{\partial x} \exp(i\phi^r(x)) = ik^r(x) \exp(i\phi^r(x)) \quad (5.18)$$

where the differentiation of a definite integral has been used:

$$f(x) = \frac{\partial}{\partial x} \left(\exp \left(i \int_a^x f(\xi) d\xi \right) \right) \quad (5.19)$$

In addition, the local mode solution to the homogeneous equation can be applied, where

$$ik^r(x_i) \mathbf{u}^r(x_i, z) = \mathbf{A} \mathbf{u}^r(x_i, z) \quad (5.20)$$

where x_i denotes some lateral x-coordinate point where the local modes \mathbf{u}^r have been determined. The evolution equation for the amplitude coefficients of the scattered field may be obtained by substituting equations (5.18) and (5.20) into equation (5.17), taking the Hermitian product with mode \mathbf{u}^q , and simplifying with additional algebra:

$$\frac{\partial s_q}{\partial x} = \sum_r \mathbf{B}_{qr} s_r + \sum_r \mathbf{H}_{qr} c_r \quad (5.21)$$

The \mathbf{B}_{qr} coupling matrix in the stochastic evolution equation (5.21) has the same form as the unperturbed problem. The \mathbf{B}_{qr} matrix essentially describes how much on scattered mode \mathbf{u}_r goes into mode \mathbf{u}_q . The range dependent scattering coefficients s_q are determined from the solution of equation (5.21). The scattered field mode coupling coefficients from \mathbf{H}_{qr} give insight into the distribution of modal energy due to scattering in the presence of heterogeneity and anisotropy. The expanded form of the stochastic volume scattering matrix \mathbf{H}_{qr} is located in Appendix G.

5.4 Stochastic Perturbation of Elastic Moduli

The form of the \mathbf{H}_{qr} scattering matrix directly depends on the form of \mathbf{A}_1 . Therefore, the description of the heterogeneity of the elastic moduli directly affects the form that the scattering matrix \mathbf{H}_{qr} takes. The \mathbf{H}_{qr} stochastic volume scattering matrix has

been included into the coupled local formalism for a general anisotropic medium. The expanded form of the \mathbf{H}_{gr} matrix from Appendix G contains perturbed values of the density and elastic moduli. The density and elastic constants within each layer may exhibit both deterministic and stochastic volume heterogeneity, where material properties are separated into two parts: an averaged deterministic function and a small-scale stochastic function γ . It is assumed that $1 \gg |\gamma|$. As in chapter 4, the γ function is assumed to be a zero-mean stochastic process.

$$\begin{aligned}
\rho(x, z) &= \rho_o(x, z) + \varepsilon\rho(x, z)_1 \\
&= \rho_o(x, z) \left(1 + \varepsilon \frac{\rho(x, z)_1}{\rho_o(x, z)} \right) \\
&= \rho_o(x, z)(1 + \varepsilon\gamma_3)
\end{aligned} \tag{5.22}$$

$$\begin{aligned}
C_{ijkl}(x, z) &= C_{ijkl}(x, z)_o + \varepsilon C_{ijkl}(x, z)_1 \\
&= C_{ijkl}(x, z)_o \left(1 + \varepsilon \frac{C_{ijkl}(x, z)_1}{C_{ijkl}(x, z)_o} \right) \\
&= C_{ijkl}(x, z)_o(1 + \varepsilon\gamma_4)
\end{aligned} \tag{5.23}$$

$$\begin{aligned}
C_{ijkl}^{-1}(x, z) &= \frac{1}{C_{ijkl}(x, z)_o + \varepsilon C_{ijkl}(x, z)_1} \\
&= \frac{1}{C_{ijkl}(x, z)_o \left(1 + \varepsilon \frac{C_{ijkl}(x, z)_1}{C_{ijkl}(x, z)_o} \right)} \\
&= \frac{1}{C_{ijkl}(x, z)_o(1 + \varepsilon\gamma_4)} \\
&\approx \frac{1}{C_{ijkl}(x, z)_o}(1 - \varepsilon\gamma_4)
\end{aligned} \tag{5.24}$$

where the parameter ε is introduced for bookkeeping purposes to keep track of the orders of perturbation, and C_{ijkl} in this section represents a specific $ijkl^{th}$ element of the fourth order elastic stiffness tensor, rather the actual tensor itself. The terms with the o subscripts are the reference values and the terms with the subscripts of 1 are the perturbation values.

The gammas in equations (5.22) and (5.23) are defined as:

$$\gamma_2(x, z) = \frac{\rho_1(x, z)}{\rho_o(x, z)} \tag{5.25}$$

$$\gamma_4(x, z) = \frac{C_{ijkl}(x, z)_1}{C_{ijkl}(x, z)_o} \quad (5.26)$$

Deterministic and Stochastic Characteristics of the Density and Elastic Moduli

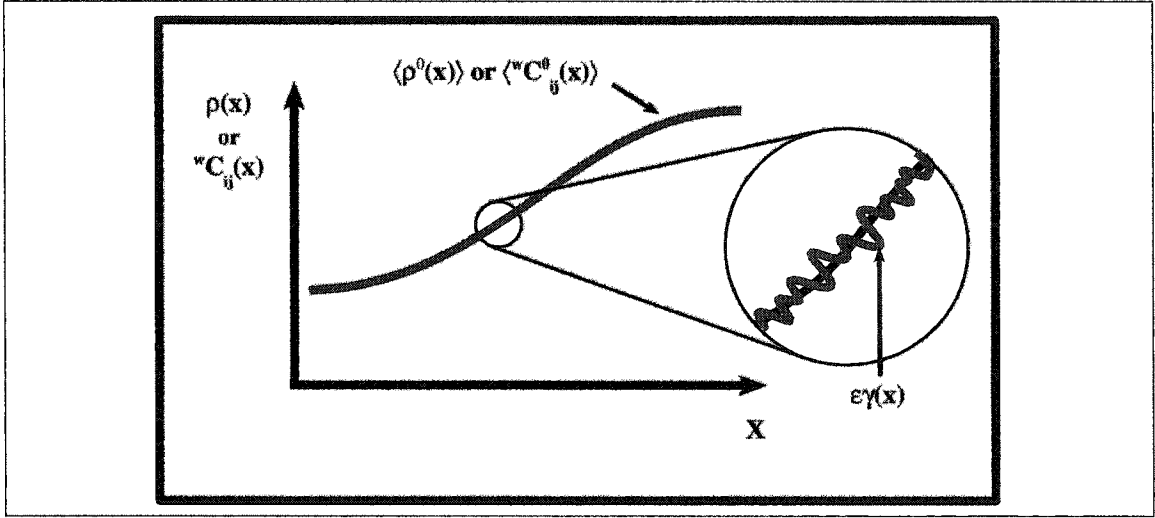


Figure 5.3: A schematic to demonstrate the deterministic and stochastic nature of the density and elastic moduli. The deterministic features are assumed to be smooth and continuous in the x -direction. The stochastic portion is a small-scale perturbation, where $1 \gg |\gamma|$

Another linear perturbation approach can also be applied to the elastic moduli, which are a function of density and velocity.

$$C_{ijkl}(x, z) = \rho(x, z)V^2(x, z) \quad (5.27)$$

The velocity may be perturbed similarly to ρ and C_{ijkl} in equations (5.22) and (5.23).

$$\begin{aligned} V(x, z) &= V_o(x, z) + \varepsilon V_1(x, z) \\ &= V_o(x, z) \left(1 + \varepsilon \frac{V_1(x, z)}{V_o(x, z)} \right) \\ &= V_o(x, z)(1 + \varepsilon \gamma_5(x, z)) \end{aligned} \quad (5.28)$$

where the gamma in equation (5.28) is defined as:

$$\gamma_5(x, z) = \frac{V_1(x, z)}{V_o(x, z)} \quad (5.29)$$

Substituting the definitions of ρ and V into equation (5.27) and only keeping perturbation terms of order 0 and ε

$$C_{ijkl}(x, z) = \rho_o(x, z)(V_o(x, z))^2(1 + \varepsilon(\gamma_2(x, z) + 2\gamma_5(x, z))) \quad (5.30)$$

$$\begin{aligned} &= \rho_o(x, z)(V_o(x, z))^2(1 + \varepsilon\gamma_4(x, z)) \\ &= C_{ijkl}(x, z)_o(1 + \varepsilon\gamma_4(x, z)) \end{aligned} \quad (5.31)$$

where $\gamma_4(x, z) = (\gamma_2(x, z) + 2\gamma_5(x, z))$ and $C_{ijkl}(x, z)_o = \rho_o(x, z)(V_o(x, z))^2$. This results in the same perturbation equation as equation (5.23).

The elastic parameters are therefore perturbed following the general description found in equation (5.31). The anisotropy is assumed to have transversely isotropic elastic symmetry, where the five elastic constants A, C, F, L, N describe the medium. All of the elastic parameters for all of the layers are described as having the same random statistics of $\gamma(x, z)$, where $|\gamma(x, z)| \ll 1$. The five parameters along with the symmetry axis orientation \hat{s} determine the values of the elastic stiffness matrix $C_{ijkl}(x, z)_o$ and the perturbed stochastic elastic stiffness matrix $C_{ijkl}(x, z)_1$. For TI elastic symmetry, the five elastic moduli are then:

$$\begin{aligned} A(x, z) &= A(x, z)_o(1 + \varepsilon\gamma) \\ C(x, z) &= C(x, z)_o(1 + \varepsilon\gamma) \\ F(x, z) &= F(x, z)_o(1 + \varepsilon\gamma) \\ L(x, z) &= L(x, z)_o(1 + \varepsilon\gamma) \\ N(x, z) &= N(x, z)_o(1 + \varepsilon\gamma) \end{aligned} \quad (5.32)$$

For the medium to be physically reasonable, the elastic moduli must obey some restrictions, the elastic parameters A, C, F, L, N cannot just have any arbitrary value.

A structure with transverse isotropic elastic symmetry follows the following restrictions from Odom *et. al.* (1996):

$$\begin{aligned}
C &\geq 0 \\
L &\geq 0 \\
C &\geq F \\
N &\geq L \\
C &\geq \frac{4}{3}L \\
A &\geq N \geq 0 \\
C(A - N) &\geq F^2 \\
(A - L)(C - L) &\geq (F + L)^2
\end{aligned} \tag{5.33}$$

To ensure the physical reasonableness of the five independent elastic parameters, the restrictions of equation (5.33) are enforced. Substituting the perturbed elastic moduli from equation(5.32) into the transverse isotropic elastic symmetry restrictions, and simplifying gives.

$$\begin{aligned}
C_0 &\geq 0 \\
L_0 &\geq 0 \\
C_0 &\geq F_0 \\
N_0 &\geq L_0 \\
C_0 &\geq \frac{4}{3}L_0 \\
A_0 &\geq N_0 \geq 0 \\
C_0(A_0 - N_0) &\geq F_0^2 \\
(A_0 - L_0)(C_0 - L_0) &\geq (F_0 + L_0)^2 \\
1 + \varepsilon\gamma &\geq 0
\end{aligned} \tag{5.34}$$

Because of the linear nature of the elastic moduli perturbations, and the assumption that all the elastic moduli have the same stochastic dependence, the restrictions

are the same form as equation (5.33) with an additional restriction on $\gamma(x, z)$. The last restriction is already ensured by the previous assumption that $1 \gg |\gamma|$. The perturbed elastic moduli can now be determined.

$$\begin{aligned}
{}^w Q_{ij} &\approx ({}^w C_{ij})_o(1 + \varepsilon\gamma) - ({}^w C_{i1})_o(1 + \varepsilon\gamma)({}^w C_{11}^{-1})_o(1 - \varepsilon\gamma) \\
&\quad \times ({}^w C_{ij})_o(1 + \varepsilon\gamma) \\
&\approx ({}^w C_{ij} - {}^w C_{i1} {}^w C_{11}^{-1} {}^w C_{1j})_o(1 - \varepsilon\gamma) \\
&\approx ({}^w Q_{ij})_o(1 + \varepsilon\gamma)
\end{aligned} \tag{5.35}$$

$${}^w C_{11}^{-1} = ({}^w C_{11}^{-1})_o(1 + \varepsilon\gamma) \tag{5.36}$$

$${}^w C_{11}^{-1} {}^w C_{1j} \approx ({}^w C_{11}^{-1})_o(1 - \varepsilon\gamma)({}^w C_{1j})_o(1 + \varepsilon\gamma) \tag{5.37}$$

$$\approx ({}^w C_{11}^{-1} {}^w C_{1j})_o \tag{5.38}$$

$${}^w C_{i1} {}^w C_{11}^{-1} \approx ({}^w C_{i1})_o(1 + \varepsilon\gamma)({}^w C_{11}^{-1})_o(1 - \varepsilon\gamma) \tag{5.39}$$

$$\approx ({}^w C_{i1} {}^w C_{11}^{-1})_o \tag{5.40}$$

5.5 Stochastic Volume Coupling Matrices

The coupled local mode theory with stochastic volume terms is applied to a general 2-D range-dependent and laterally heterogeneous medium, as shown in Figure 4.1. The local modes are determined from a plane-layered medium that is the local equivalent of the range dependent medium. The medium is assumed to have a known deterministic structure, where the variations can be large. A 1-D profile is developed at a defined lateral positions (e.g. x_o), and is the local equivalent of the range-dependent medium. Examples of the modes are presented in chapter 2 of this dissertation.

The \mathbf{H}_{qr} stochastic volume scattering matrix is based on the normalized local modes, without any specific source excitation. The \mathbf{H}_{qr} matrix describes how much of coherent mode \mathbf{u}_r goes into the scattered mode \mathbf{u}_q .

H_{qr} Stochastic Interface Term Scattering Matrix for P-SV and SH Modes

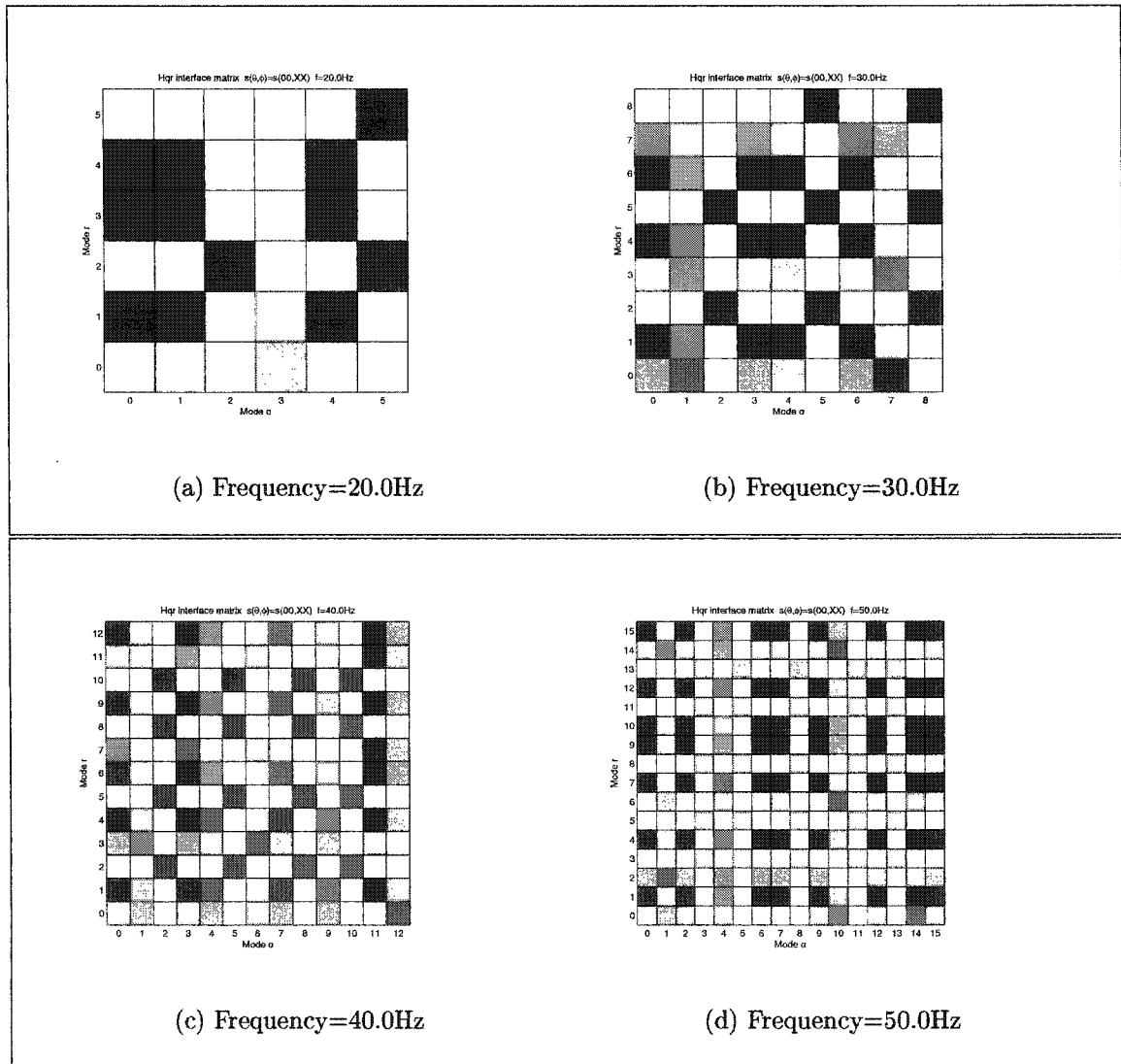


Figure 5.4: H_{qr} stochastic interface terms for P-SV and SH modes at 20.0Hz-50.0Hz. The strongest scattering occurs for coherent modes \mathbf{u}_r coupling into their scattered mode counterpart \mathbf{u}_q where $q = r$. Strong coupling also occurs between the coherent P-SV modes and the scattered P-SV modes. The coherent SH modes experience the weakest scattering

\mathbf{H}_{gr} Stochastic Interface Term Scattering Matrix for quasi-P-SV,
quasi-SH and P-SV-SH modes

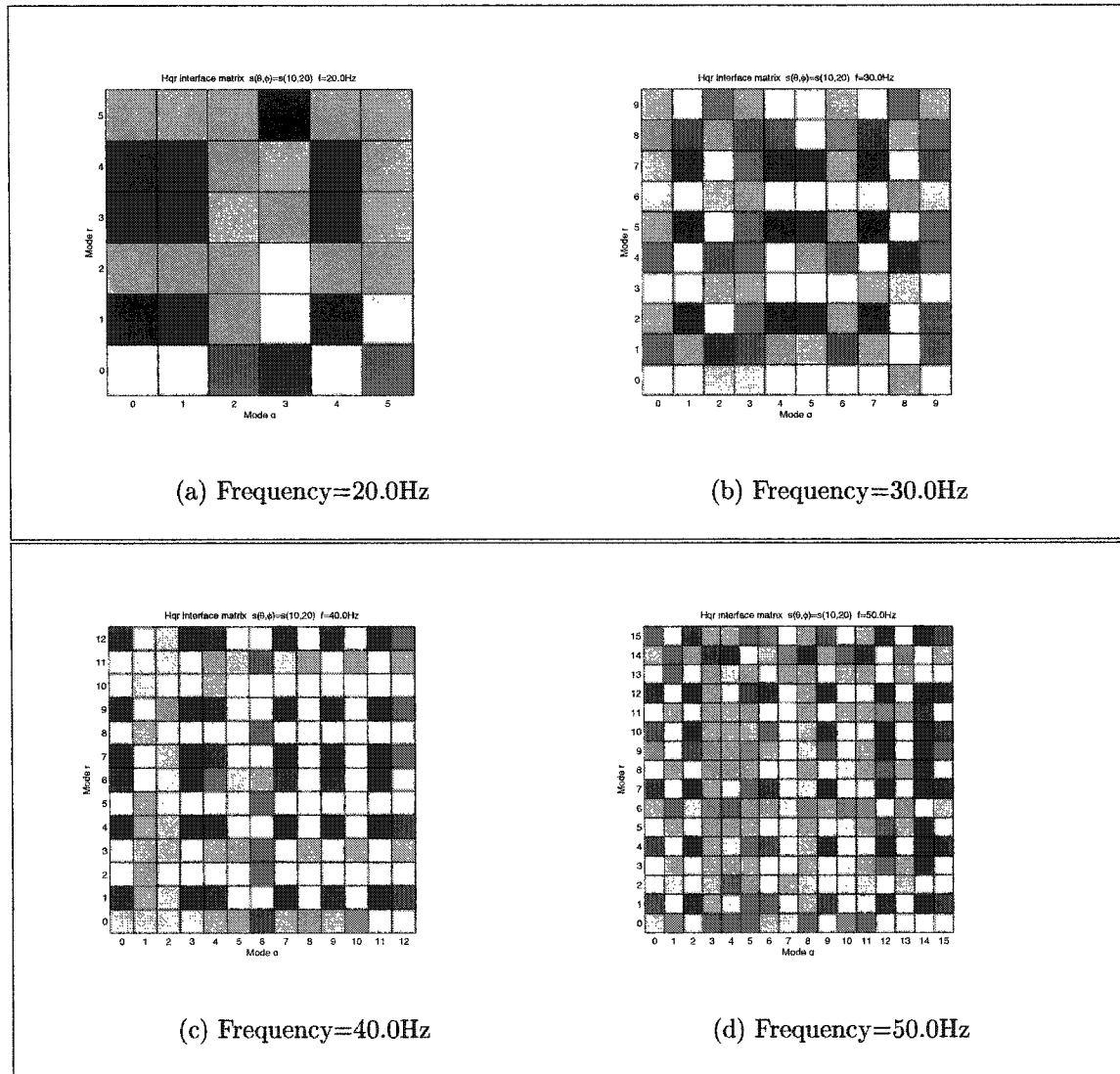


Figure 5.5: \mathbf{H}_{gr} stochastic interface terms for quasi-P-SV, quasi-SH, and P-SV-SH modes at 20.0Hz-50.0Hz. The tilting of the symmetry axis allows coherent quasi-SH modes to couple into scattered quasi-P-SV modes. The coherent quasi-SH modes experience the weakest scattering, similar to the VTI case where the SH coherent modes experience the weakest scattering.

H_{qr} Stochastic Volume Term Scattering Matrix for P-SV and SH modes

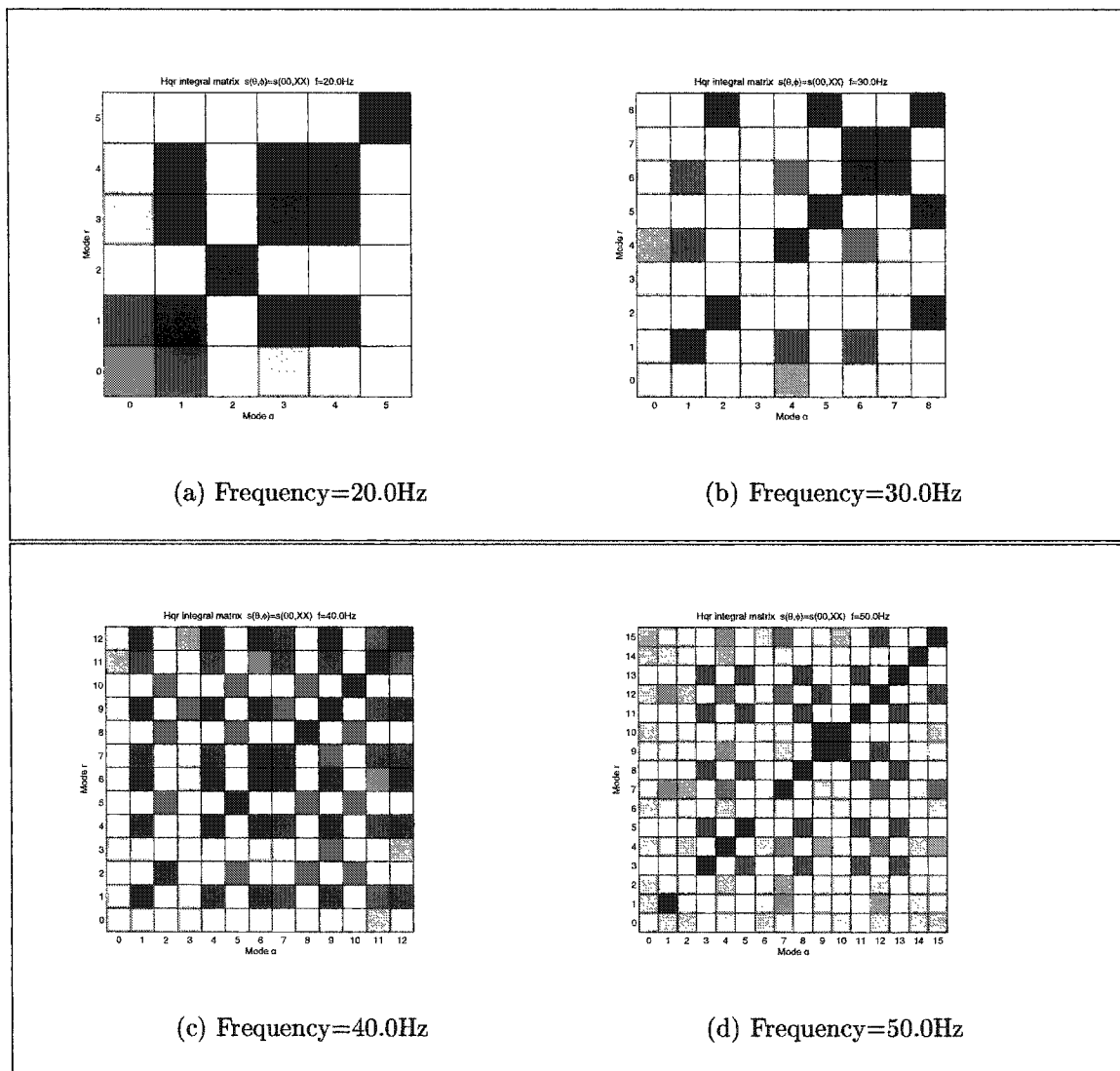


Figure 5.6: H_{qr} stochastic volume scattering coupling matrices for P-SV and SH modes at 20.0Hz-50.0Hz.

\mathbf{H}_{qr} Stochastic Interface Term Scattering Matrix for quasi-P-SV,
quasi-SH and P-SV-SH modes

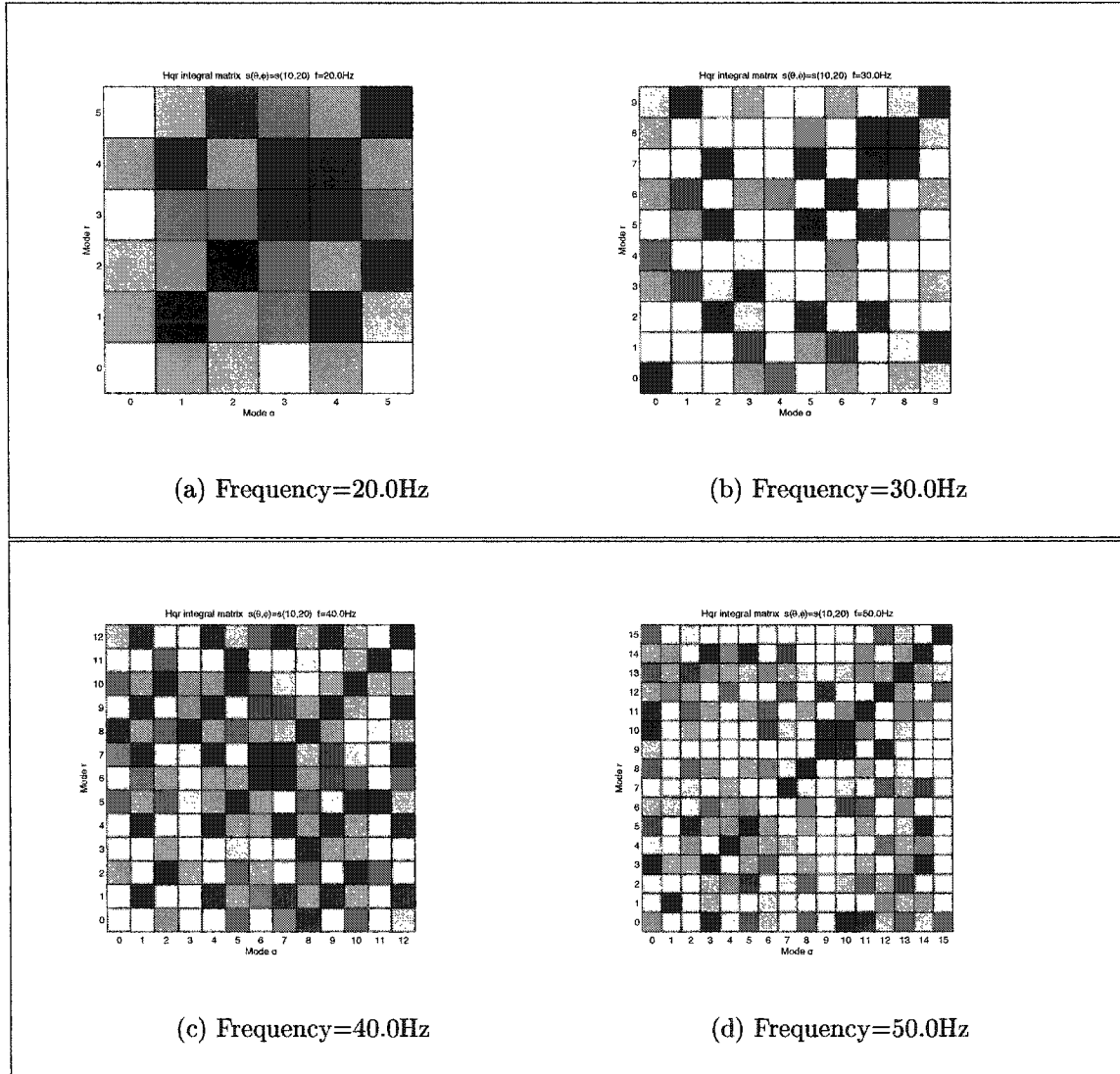


Figure 5.7: \mathbf{H}_{qr} stochastic volume scattering matrices for quasi-P-SV, quasi-SH, and P-SV-SH modes at 20.0Hz-50.0Hz. The coherent quasi-SH modes experience the weakest scattering, except when coherent quasi-SH modes \mathbf{u}_r coupling into their scattered mode counterpart \mathbf{u}_q where $q = r$. The strongest coupling occurs between coherent quasi-P-SV modes and scattered quasi-P-SV modes.

5.6 Chapter Summary

The inclusion of deterministic and stochastic scattering into the local coupled formalism provides an improvement in the forward problem of wave propagation in complex fluid-elastic media. The modal approach to wave propagation has the advantage of being formally exact, as well as giving physical insight into the physics of propagation. By utilizing perturbation theory to the coupled local mode formalism, a new scattering coupling matrix \mathbf{H}_{qr} is derived which describes how much energy of coherent mode \mathbf{u}_r is redistributed into scattered mode \mathbf{u}_q .

Lateral material heterogeneity and anisotropy allow for effective redistribution of energy. Energy can transfer between modes by deterministic variations and random, or stochastic variations. Perturbations in the elastic moduli and density contribute to elastic wave scattering, leading to apparent energy loss and complex waveforms or loss of signal coherence

The two key and distinguishing features of this research are the treatment of the bottom and subbottom as elastic solids, and the representation of the ocean acoustic signal as a superposition of modes. It is into this framework that the effects of rough surface scattering, anisotropy, and volume scattering are incorporated. Through theoretical and numerical work, the seismo-acoustic wave propagation is modeled in a realistic shallow water environment where anisotropy, gradients, discontinuities and random heterogeneities may occur.

Chapter 6

***T*-WAVE EXCITATION AND COUPLED LOCAL MODES**

Portions of this chapter have been previously published by Park *et. al.* (2001), in particular the introductory section of chapter 6, section 6.1 and parts of the chapter summary. A *T*-wave can be loosely defined as an almost horizontally propagating acoustic signal in which part or all of the propagation path is within the oceanic water column. *T*-waves are often the dominant signal in ocean acoustic records. These acoustic signals may be detected by hydrophones, or seismic stations along islands or coastlines. The coda are complex without any clear onset and the signal involves a significant amount of ringing. A *T*-wave may have a frequency range from 1Hz to 30Hz, where periods higher than 2 seconds are not observed. *T*-waves may be generated by earthquakes, underground or underwater explosions, submarine volcanism, or other marine and submarine sources. *T*-waves typically propagate at very low phase velocity, often exhibit generally weak dispersion, and correspond to sound waves trapped in the oceanic low velocity water layer, known as the SOFAR channel. At frequencies somewhat above the cut-off frequency for a given mode, the dispersion curves become asymptotically flat. This common characteristic of modal propagation accounts for the observed weak *T*-wave dispersion over quite a broad frequency range, since the *T*-wave itself comprises only a few low order modes. Since the attenuation of sea water is very low and the waveguide exhibits quasi-cylindrical spreading (Fox & Dziak, 1999), the energy can travel very long distances with low transmission loss. *T*-waves produced by even very small earthquakes (i.e. too small to be detected by land based seismic arrays) are detectable with ocean bottom hydrophones. *T*-waves are relevant to a broad range of geophysical studies as recently summarized by

Okal (2001). The detection of submarine volcanism, earthquake source tomography of abyssal plane events, relevance to tsunami generation, Comprehensive Test Ban Treaty verification and even thermal tomography of the oceans are mentioned.

T -waves have been observed for around 50 years, yet the mechanism for generating T -waves at the seafloor has not been thoroughly understood. Ray theory indicates that crustal seismic energy crossing the seafloor interface into the overlying water column experiences severe refraction toward vertical due to the large velocity contrasts between the water column and the seafloor bottom/subbottom. Several mechanisms have been proposed to explain how energy can propagate horizontally and become trapped in the oceanic sound channel: i) down-continental-slope conversion (Tolstoy and Ewing, 1950) and recently examined by Sperry et al. (1996), ii) Stoneley wave coupling (Biot, 1952), iii) sea-ice scattering (Keenan and Merriam, 1991), iv) seafloor-seasurface reflection scattering (Johnson *et. al.*, 1967), and v) seafloor roughness scattering (Fox *et. al.*, 1994). None of these mechanisms has yet been distinguished as the primary mode by which seismic energy becomes acoustic energy in the sound channel (Slack, *et. al.*, 1999).

That oceanic T -waves arise from the seismic waves scattered by a rough sea bottom was given support recently by de Groot-Hedlin and Orcutt (1999), who were able to reproduce realistic T -wave coda from several low-order acoustic modes excited by point sources distributed over the sea floor. Assuming the excitation to be proportional to the acoustic modal amplitude at the point where the exponential tail contacted the bottom, they synthesized T -wave signal envelopes, which showed good agreement with the measured envelopes. They suggest that the remaining discrepancies between the modeled and measured energy envelopes arise from coarse bathymetry, mode coupling and radiation pattern effects.

The excitation of such modes is addressed, where the most important feature of the modal representation is the mutual orthogonality of the modes, making it impossible to transfer energy from one mode to another if the earth were truly a layered semi-

infinite half-space or a radially symmetric sphere. The physical mechanism for T -wave generation requires something that breaks the strict modal orthogonality.

In this chapter, a coupled-mode based scattering theory (Park and Odom, 1999) and summarized in chapter 4 of this dissertation is applied to the excitation of the T -waves within the earthquake epicentral region. The modal scattering theory is a stochastic extension of Maupin's (1988) exact 2-D coupled mode theory, in which the medium is characterized by some deterministic range-dependent layered structure superposed with a random boundary fluctuation of strength ε . The actual wavenumber spectrum of the bathymetry is known to be a red power law (Fox and Hayes, 1985). However, this will have no significant effect on the main conclusions of this chapter. The modal scattering theory yields a stochastic correction d_q , which satisfies the evolution equation:

$$\frac{\partial d_q}{\partial x} = \sum_r B_{qr} d_r + \sum_r S_{qr} c_r, \quad (6.1)$$

where c_r and $d_{q,r}$ are the modal weighting coefficients of an incident wave and scattered waves, respectively and S_{qr} is the scattering matrix. Equation (6.1) is the same as equation (4.10) of chapter 4.

The coupling matrix B_{qr} accounts for energy redistribution among modes of the scattered waves due to a range-dependent reference structure, and the scattering matrix S_{qr} accounts for energy scattered from an incident wave interacting with the heterogeneous layer boundary.

Note that the matrix S_{qr} accounts for contributions from both random interface roughness and deterministic non-planar interfaces, i.e. sloping interfaces. Scattering from one mode to other modes will occur for: i) the case of plane layers with random boundary roughness, ii) the case of smooth, but non-planar layer boundaries, and iii) for the case of non-planar boundaries that are also rough. The contribution from non-planar boundaries is directly proportional to the boundary slope, which supports the

observation that T -wave excitation is more efficient for steeper slopes (e.g. Talandier and Okal, 1998).

6.1 Coupled-Mode Scattering Theory and T -wave excitation

The earth model for the excitation of T -waves consists of an overlying ocean, ocean bottom sediments, ocean crust and upper mantle.

The model (Figure 6.1a) corresponds to the ocean-earth structure in the epicentral region of a T -wave producing earthquake that occurred near the western tip of the Blanco Transform Fault Zone (TFZ) in the North Pacific (Lat 44.710, Lon -130.310, mb = 3.9, depth = 9 km). The ocean sound speed model comes from the Levitus ocean sound speed database (Levitus and Boyer, 1994) for the 2.25 km deep ocean, followed by a realistic ocean crustal model from 2.25 km - 4.3 km, and terminated by PREM below 4.3 km.

The 1st acoustic mode (the first three plots in Figure 6.1a decays exponentially in the water column and eventually becomes zero at depths well above that of even shallow earthquakes. Mode 1 is essentially zero at the ocean bottom for 5 Hz. This indicates that direct earthquake excitation of the lower order acoustic modes will be very weak at best. Explosions in the water column or marine volcanic eruptions, however, could possibly excite those lower order acoustic modes directly. The computations have been carried out for frequencies from 0.2 to 20 Hz, but the focus remains on 5 Hz because it is at the approximate center of the T -wave band.

Using the mode code DISPER80 (Saito, 1988), the initial wavefield excitation for the earthquake described above has been computed using the Oregon State University (OSU) moment tensor source solution. This yielded 185 seismo-acoustic modes at 5 Hz (Figure 6.2a), 75 at 2 Hz and 38 at 1 Hz.

The cut-off phase velocity has been set at 4.46 km/sec to exclude lower-mantle modes. However it should be mentioned that for deeper earthquakes, contributions

1st Acoustic Mode and Hybrid Crustal-Acoustic Mode

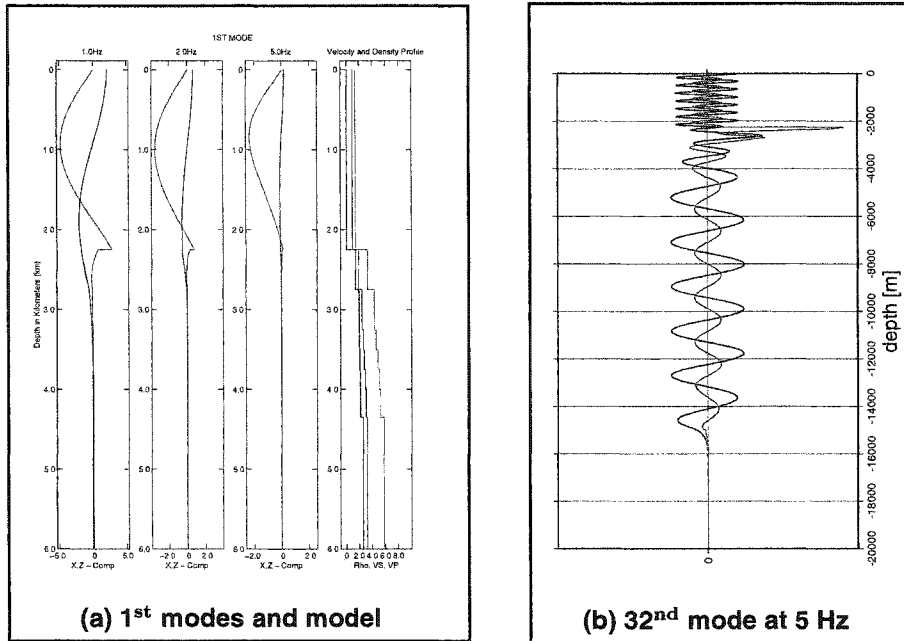


Figure 6.1: (a) The 1st acoustic mode at 1, 2 and 5 Hz and the velocity profile. Black and red lines in the mode function figures represent the vertical and horizontal components of the particle displacement, respectively. Blue, red and black lines in the profile represent the compressional wave speed, the shear wave speed and the density, respectively. The horizontal compression of the graphics suppresses sound speed detail in the water column. (b) Particle motion of the 32nd mode, an example of an ocean hybrid mode with characteristics of acoustic modes, ocean crustal modes and often strong interface waves.

from the continuum spectrum corresponding to steeper rays become increasingly important, and only the discrete spectrum is treated in this chapter. At 5 Hz, modes 0-19 are the fundamental Stoneley (mode 0) and the propagating acoustic modes. The 40th and higher modes are crustal and upper-mantle modes. Modes 20-39, hybrid modes with characteristics of acoustic modes, ocean crustal modes and interface waves, have

Initial Wave Excitation by Earthquakes: Source Depth

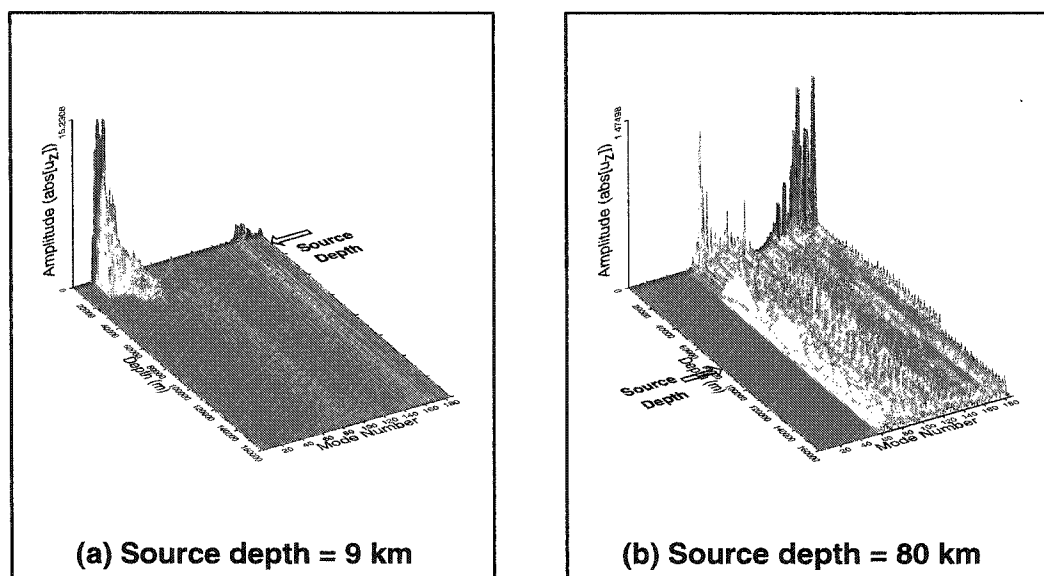


Figure 6.2: The initial seismo-acoustic wavefield at 5 Hz produced by a Blanco TFZ earthquake at two different source depth positions. (a) An initial excitation by a 9 km depth earthquake. Ocean hybrid modes, approximately 39 modes from mode 19 to mode 58, are strongly excited by the earthquake. Red and blue colors represent the vertical components of the particle displacement in the earth and the water column, respectively. (b) The initial excitation by a 80 km depth earthquake. A large number of crustal and upper mantle modes, starting with mode 60 are excited.

relatively large amplitudes in the ocean crust as well as significant water-borne components and often strong interface components at the water-bottom boundary. Figure 6.1b shows the particle displacement components of the 32nd mode at 5 Hz, a good example of the ocean hybrid modes with the characteristic large amplitude anti-node at the water-bottom boundary.

Approximately 39 modes from mode 19 to mode 58, mostly oceanic hybrid modes, are strongly excited by the earthquake. There is essentially no energy in the fundamental Stoneley or the propagating acoustic modes as they have vanishingly small amplitudes at a depth of 9 km (Figure 6.2a). The initial source excitation has also been computed using the same source solution, but for a source depth of 80 km (Figure 6.2b). The 80 km source depth is fairly extreme for T -wave producing earthquakes, because a source at that depth excites even higher order modes than the shallower source. The continuum spectrum (steeply arriving rays) will become more important. Mode numbers less than about 59 are not excited at all because the source is far below the exponential tail of those lower order modes, making direct T -wave excitation essentially impossible for such a deep earthquake. The modes have been truncated above their turning depths for plotting purposes only.

As a result of interactions with a sloping and/or rough sea bottom, energy is transferred from the higher order modes to the Stoneley fundamental and to the lower order acoustic modes that have some significant amplitude at the water-bottom interface. This is shown in Figures 6.3a (9 km depth), and 6.3b (80 km depth).

The absolute value of the z displacement component of the quantity may be plotted

$$\mathbf{u}_q = d_q \mathbf{u}_q^{(0)} = \left(\sum_r \mathbf{S}_{qr} c_r^{(0)} \right) \mathbf{u}_q^{(0)}, \quad (6.2)$$

where \mathbf{u}_q is the stress-displacement vector of the q^{th} scattered mode. This is just the spatially local excitation at one point, and in fact must be multiplied by the bottom slope or a random bathymetry function, and integrated over the bottom to compute the actual excitation. However, the actual T -wave excitation will be proportional to the quantity shown in Figure 6.3. The energy from the initial earthquake source has been down-scattered to lower order modes which cannot be excited directly by the earthquake. The Stoneley wave fundamental (mode 0) is excited because it has an anti-node near the water-bottom interface. However, the fundamental mode has been

**T-Wave Excitation by Seabottom-Scattering
(Without Fundamental Stoneley mode)**

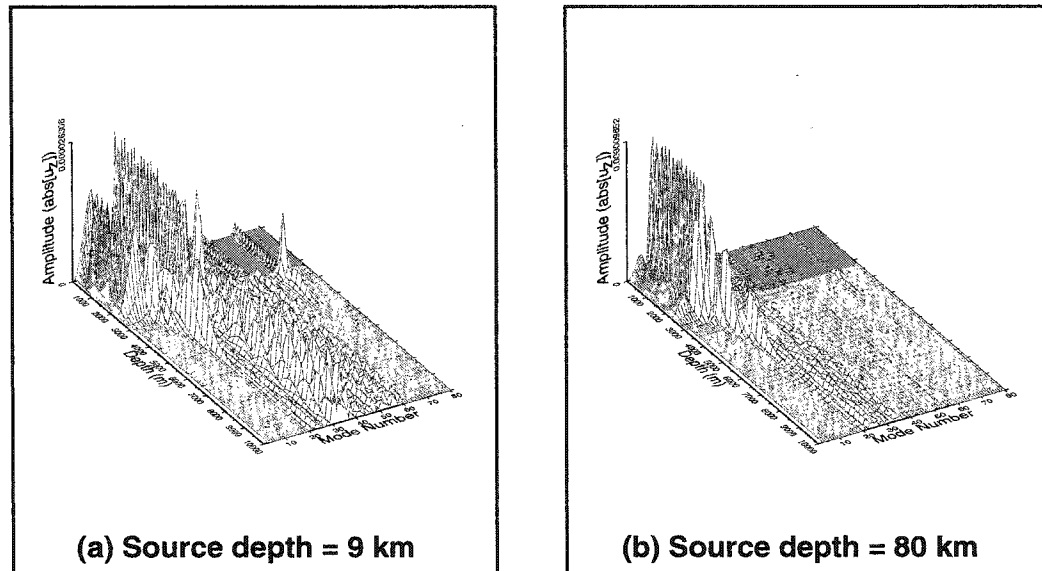


Figure 6.3: T -wave excitation by seabottom-scattering at 5 Hz. (a) The scattered wavefield from the 9 km deep source produced by lateral heterogeneities and fine-scale irregularities of bathymetry and upper ocean crust. Energy has been down-converted from the higher order modes by interaction with the heterogeneity. (b) Same as (a), but for an 80 km deep source.

removed from the plot to emphasize the excitation of the acoustic modes. Notice that even for the deeper 80 km earthquake, energy is being scattered into acoustic modes of order less than 10. Energy scattered into the Stoneley mode (mode 0), is available for re-scattering to other low order modes. Figure 6.3 represents a very significant result for the excitation of T -waves.

Figure 6.4 illustrates the effect of fault type on the initial source excitation at 9 km depth, showing the horizontal component of the particle displacement for a

normal fault (6.4a), from a Gorda Rise earthquake, and for a strike-slip fault (6.4b) from a Blanco TFZ earthquake. The source was normalized so that the strike-slip and normal fault sources have the same magnitude.

Initial Wave Excitation by Earthquakes: Fault types

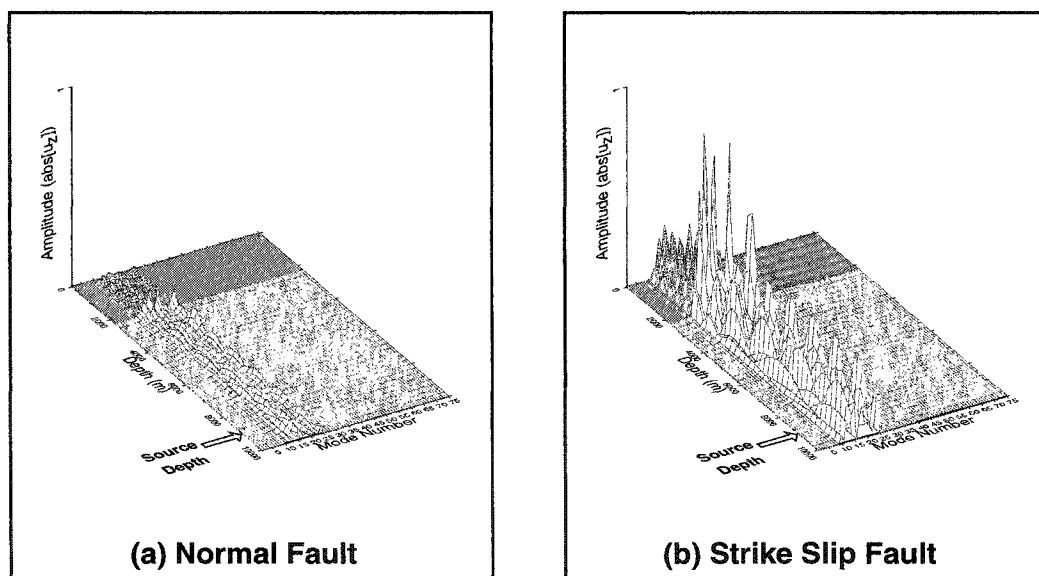


Figure 6.4: An initial seismo-acoustic wavefield at 5 Hz produced by a Blanco TFZ earthquake for two different fault types. (a) A normal fault earthquake. (b) A strike-slip fault earthquake. The results clearly indicate sensitivity to source type.

The normalized modal amplitudes for the strike-slip fault are much larger than for the normal fault. It is well known that Rayleigh wave excitation amplitude shows very strong dependence on source depth, frequency and source type (Aki & Richards, 1980, p.318), and the acoustic/ocean crustal modes are just generalized Rayleigh waves. Since the T -wave excitation is ultimately proportional to the initial source excitation,

this strong dependence on fault type should be reflected in the T -wave data, which indeed seems to be borne out by observation of 179 North Pacific earthquakes recorded on SOSUS arrays from 1992 to 1998 (R. Dziak, 2001).

6.2 Fault Type Events, Continuum Modes, and Sediment Cover Effects on T -wave Generation

The moment tensor source from the Blanco Transform Fault Zone (TFZ) earthquake event used in section 6.1 is rotated to represent specific fault type events. The three specific fault types used for comparison are a vertical normal fault, a 45° normal dip-slip fault, and a vertical strike-slip fault, as shown in Figure 6.5.

Seismic Fault Type Events

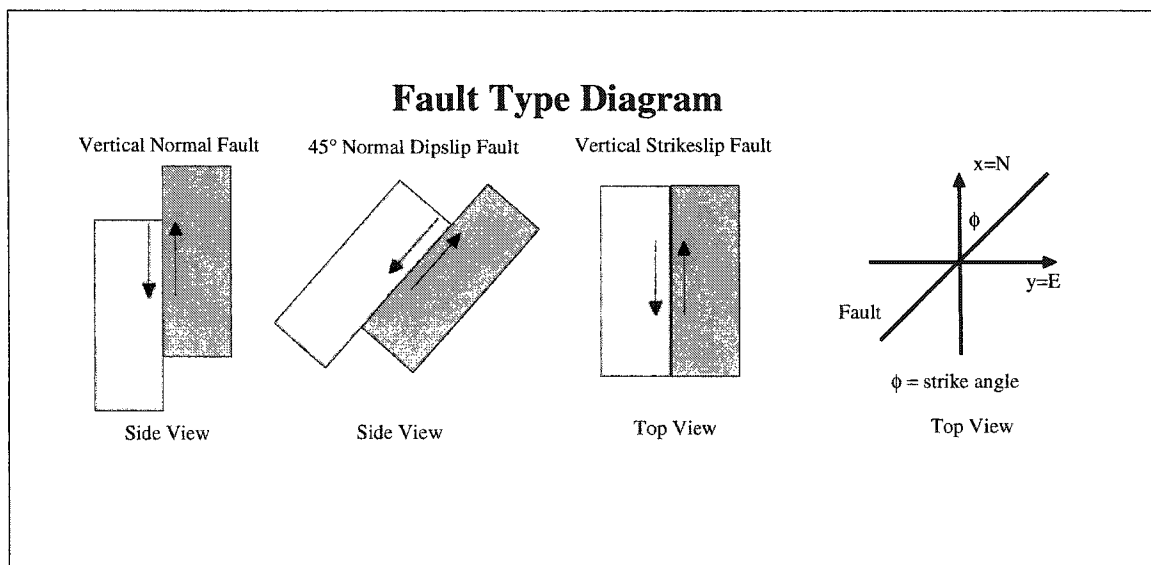


Figure 6.5: The three specific fault type events considered are a vertical normal fault, a 45° normal dip-slip fault, and a vertical strike-slip fault. A coordinate transformation rotates the TFZ earthquake event moment tensor source, allowing all three fault type events have the same moment magnitude.

The excitation of lower order acoustic modes from a seismic source has a strong de-

pendence on the strike angle (ϕ). The strike angle shown in Figure 6.5 is an azimuthal angle in the horizontal plane and measured clockwise from north (x-direction). Radiation pattern effects on T -wave generation from the three fault events in Figure 6.5 are considered. The excitation of the relative modal energy for the initial and scattered wavefields are a function of the strike angle. Figure 6.6 reveals the strong dependence on the strike angle.

Strike Angle Dependence

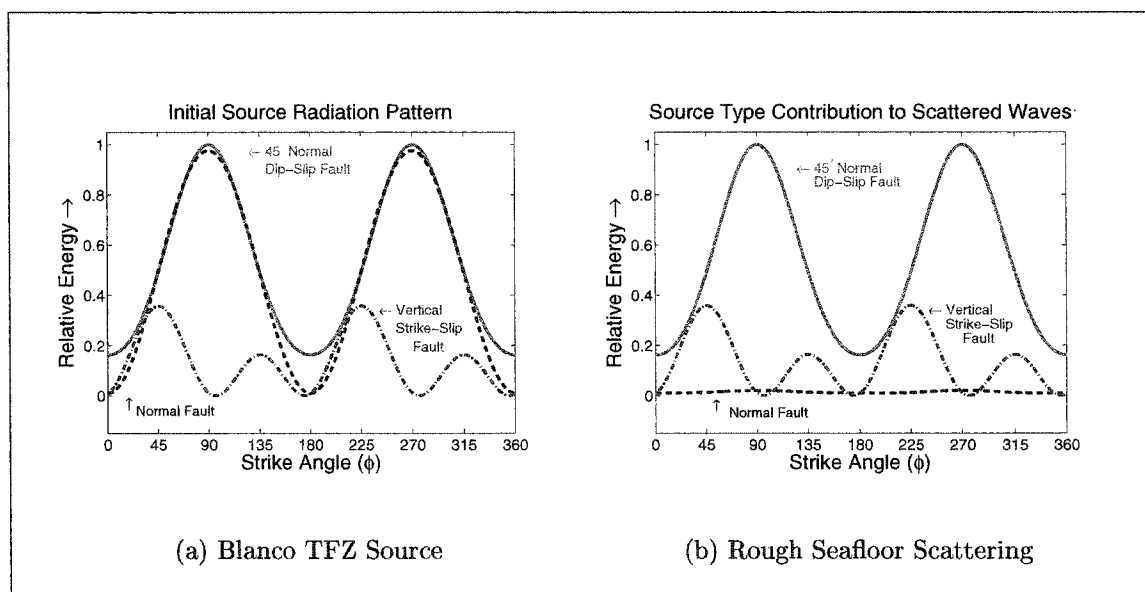


Figure 6.6: The figures show the energy sum for the excitation modes as a function of strike angle. The modal energy is for a 9km deep source. The black, blue and red lines represent normal, dip-slip, and strike-slip faults respectively. Fault type profoundly affects the degree of excitation of acoustic energy along the seafloor. Vertical normal faulting produces a much smaller scattered wavefield than other fault orientations.

The normal fault in Figure 6.6 excites a strong initial wavefield, but is inefficient at contributing to the lower modes of the scattered wavefield. Low order T -wave contributing modes are not directly excited by seismic sources, but are excited by scattering from heterogeneities at and near the seafloor boundary. It is therefore

likely that the normal fault excites modes with small displacement and tractions near and along the seabottom boundary. Large amplitude displacements and tractions in the x-direction are necessary to transmit energy into the horizontally propagating lower modes, since the scattered wavefield is dependent upon these x-direction eigenfunctions. Any mode without significant amplitudes along the seabottom boundary, will be less sensitive to scattering effects due to deterministic or stochastic heterogeneities along the seabottom. This appears to be the case for the normal fault type event. Both the strike-slip and normal dip-slip faults type events excite scattered modes with more significant displacements and tractions along the seafloor boundary. The stochastic scattering matrix \mathbf{S}_{qr} used in Figure 6.6(b) incorporates both a rough boundary terms and a sloping boundary of 5° . The sloping boundary and rough boundary effects can be considered separately since they contribute as separate terms to the modal scattering theory (see equations (4.13) and (4.14)).

Figure 6.7 shows the modal energy sums for both the rough interface terms and the deterministic bathymetry term for the first few acoustic scattered modes. The two terms are of similar magnitude and clearly of equivalent significance in the excitation of the scattered modes. The \mathbf{B}_{qr} terms can be interpreted as a downslope conversion mechanism, and the \mathbf{S}_{qr} terms can be interpreted as a rough boundary scattering mechanism for T -wave generation. It is likely that both term are responsible for transferring energy into the SOFAR channel. However, there may be regions where one mechanism may dominate over the other. For example, downslope conversion may dominate on continental margins and rough seafloor scattering may dominate in abyssal plain regions. The modal representation provides a convenient formalism in which to incorporate both effects into the scattered wavefield.

Note that from Figure 6.6(a) it is observed that the vertical normal, the 45° normal dip-slip, and vertical strike-slip faults contribute approximately the same amount of energy to the initial source wavefield when the strike angle is approximately 45° . Figure 6.8 shows the modes which contribute to the initial and scattered wavefields

Downslope Conversion and Scattering Comparison

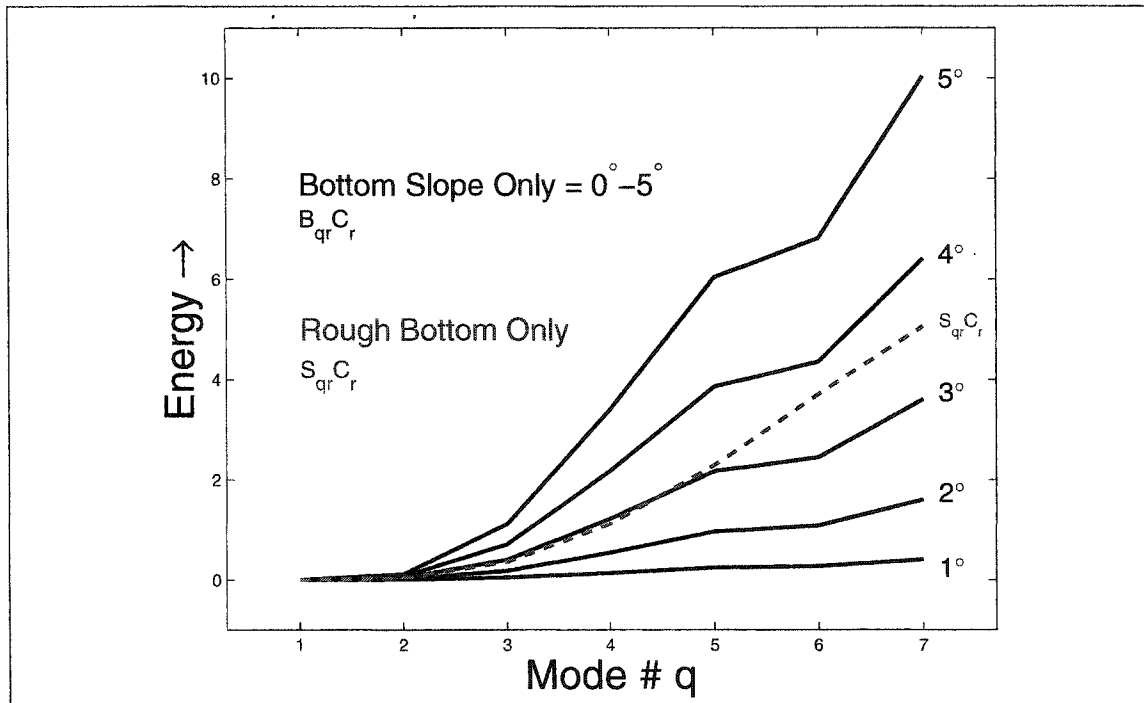


Figure 6.7: The effects of downslope conversion and scattering can be compared by considering the terms separately for the first few modes of the scattered wavefield. The black lines represent the energy of the first 7 acoustic modes for a sloping boundary, which have slopes varying from $1^\circ - 5^\circ$. The red line represents a rough planar boundary with no slope. The energy of the rough boundary scattered wavefield is comparable to that of the sloping boundaries. The modes are from the model in Figure 6.1 and calculated at a frequency of 5.0Hz

at the 45° strike angle ϕ . The normal fault type event has the largest initial wavefield, but the initial modes experience weak conversion to the low order scattered modes. The normal fault type event has the weakest scattered field of all three fault type events. The strike-slip fault type event has the smallest initial field, but the initial modes experience the strongest conversion to the low order scattered modes. The strike-slip event type is efficient at scattering energy into the SOFAR channel in the presence of any lateral heterogeneity. The dip-slip event type is more efficient than

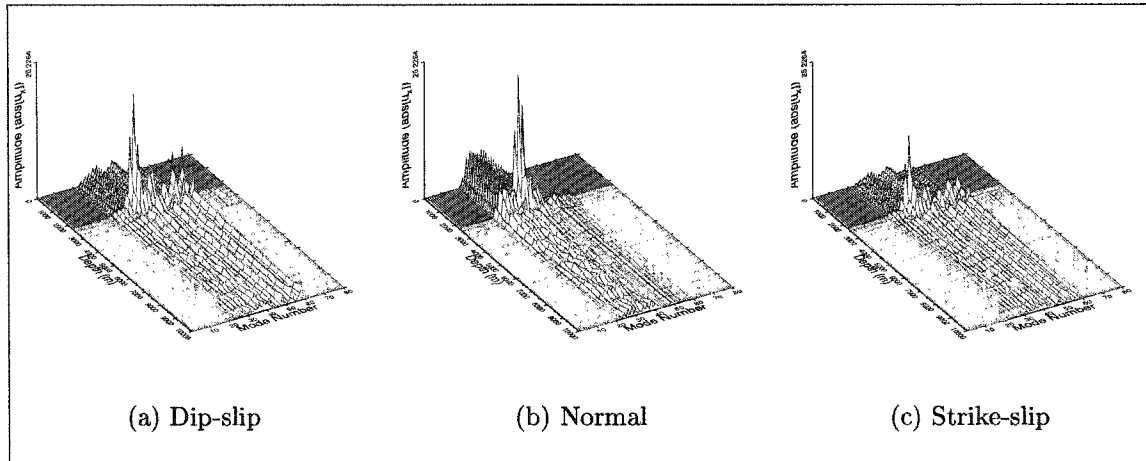
the normal fault type, but less efficient than the strike-slip fault type. This is a result that should be directly observable in T -wave data. The strike-slip source and the normal dip-slip source excite a similar set of seismic source modes. The normal fault source modes have noticeable different characteristics, with smaller values along the seafloor boundary. The normal fault source appears to excite a narrower band of modes than the other fault orientations. The energy available to the initial seismo-acoustic wavefield may be increased simply by rotating the moment tensor, where the excitation of any mode basis is sensitive to the fault type event.

At shallow source depths, the discrete modes contribute to the majority of the T -wave excitation. The continuum spectrum, however, becomes increasingly more important at greater source depths. The lower order modes may still contribute significantly to the T -wave generation for deep sources, but the continuum spectrum contribution cannot be neglected. Deep earthquake sources do not create a large initial seismo-acoustic wavefield, and the wavefield is more dependent upon the continuum spectrum (Figure 6.3). A locked mode approach is used to expand the discrete modes to include the continuum modes as source depth increases.

Figure 6.9 demonstrates the relationships between the modal wavefield as a function of mode number, phase velocity, and angle of incidence. For the 9km source a small number of the total number of modes are responsible for the majority of the wavefield. The wavefield for the 80km source clearly has not saturated yet, and is therefore more reliant upon the continuum spectrum. The wavefield is not entirely accounted for by employing the discrete modes only, since the discrete coupled local mode representation of the wavefield does not encompass all equivalent angles of incidence. The locked mode approach is not the most effective method of dealing with the continuum for large depths because of the large number of discrete modes involved.

Sediment on the seafloor enhances the efficiency of T -wave generation. Deep sediment cover over the seafloor appears to enhance the direct excitation of the initial

Initial Wave Excitation



Scattered Wave Excitation

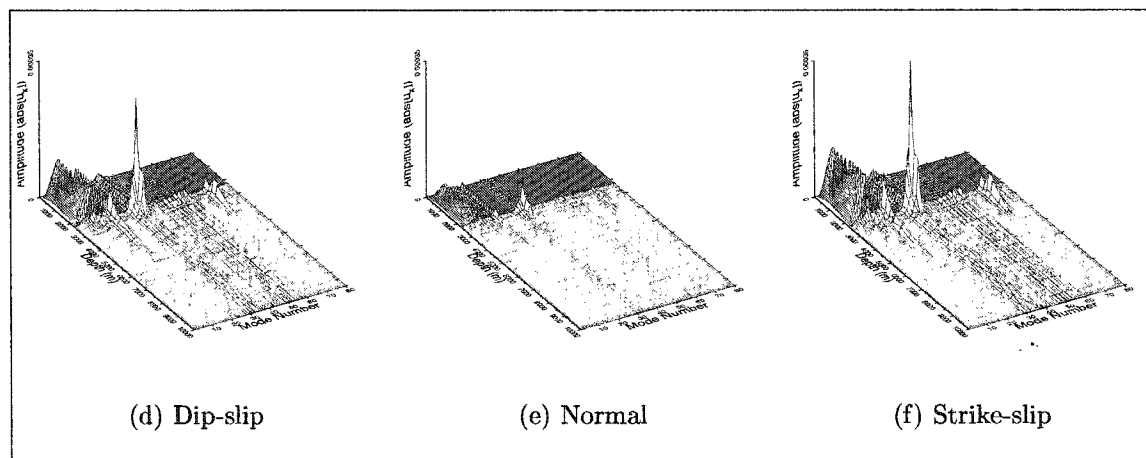


Figure 6.8: Figures (a), (b), and (c) show the initial x-displacement for dip-slip, normal, and strike-slip fault type events respectively. The amplitudes of the modes for each fault type correspond well with the energies of Figure 6.6 for a strike angle of 45° . Figures (d), (e), and (f) show the scattered z-displacements for dip-slip, normal, and strike-slip fault type events respectively. Note that the strike-slip event is the most efficient at scattering energy into the low order acoustic modes.

seismo-acoustic wavefield, as well as the resulting scattered wavefield. Figure 6.10 shows the initial and scattered wavefields for the non-sediment model used in section 6.1 and the sediment model. The sediment model is the same as the original model,

Continuum Modes

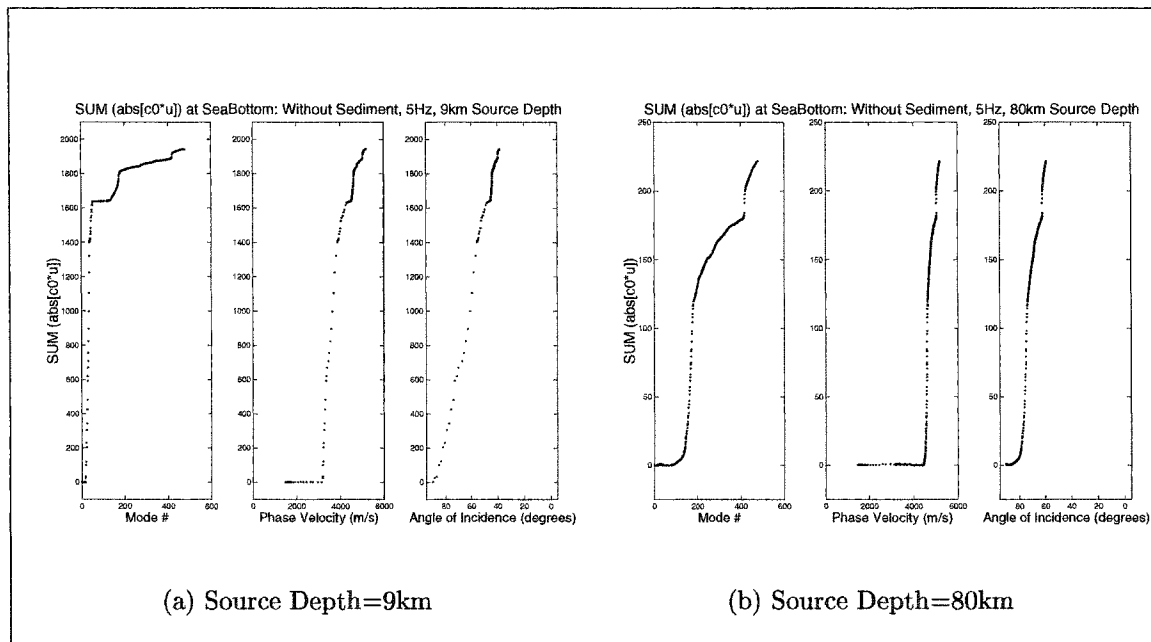
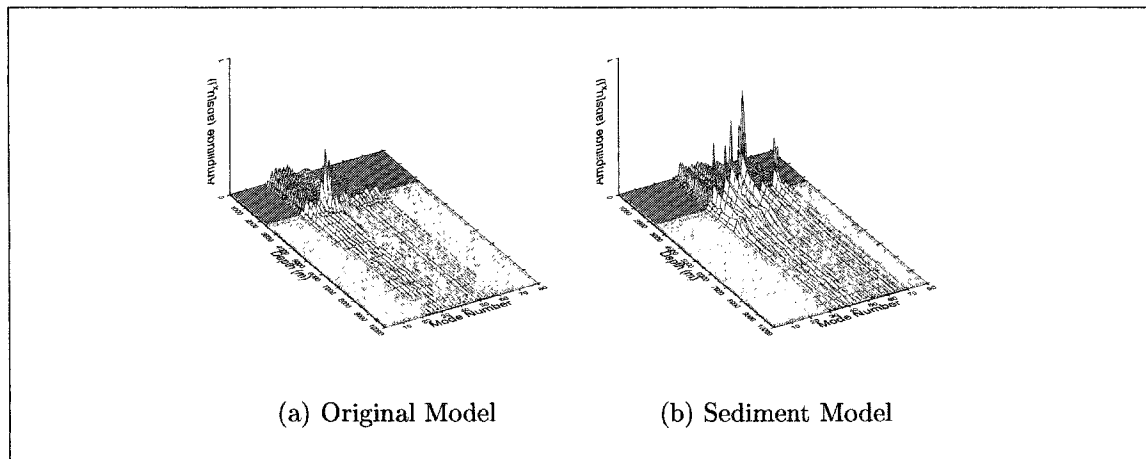


Figure 6.9: The relative energy contribution of the discrete modes are considered for a 9km source and 80km source in figures (a) and (b) respectively. A small number of low order modes contribute to the majority of the energy for the shallow 9km source. The energy sum for the 80km source does not level out, and the continuum modes are increasingly important as the source depth become greater. The initial wavefield was calculated using the original (non-rotated) Blanco TFZ earthquake event at a frequency of 50.0Hz.

with the addition of deep low shear speed sediment layers. The initial field from the original model indicates that the first 20 modes do not hold any significant amount of energy to contribute to T -wave signals. For the sediment model, the first 30 low order modes are not directly excited. However, the initial wavefield for the sediment model does have more energy which can cascade down to lower order modes through deterministic and stochastic scattering. The low speed sediment layers of the sediment model produce modes that have strong x -displacements along and near the seafloor boundary in the underlying sediments. The combination of low shear speed sediments

and lateral heterogeneity will increase the excitation of low order modes.

Initial Wave Excitation



Scattered Wave Excitation

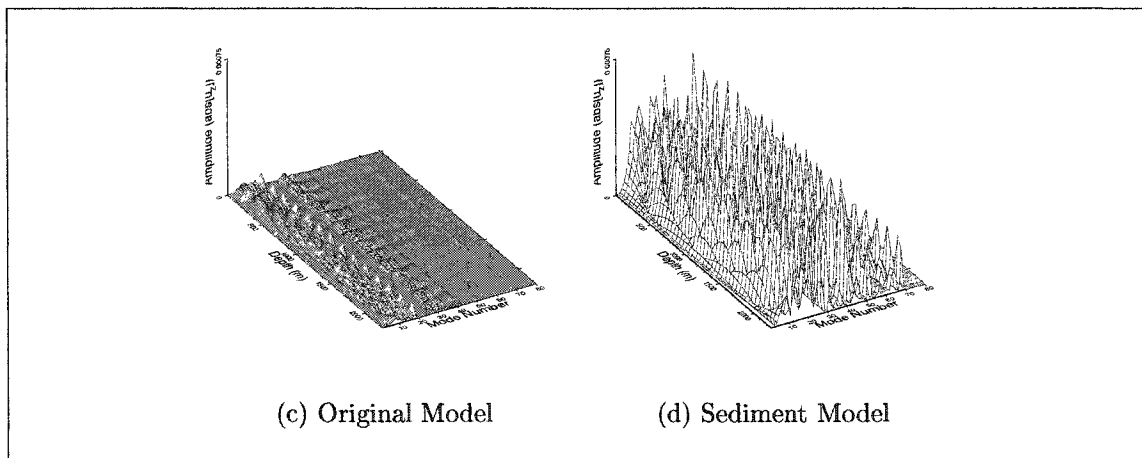
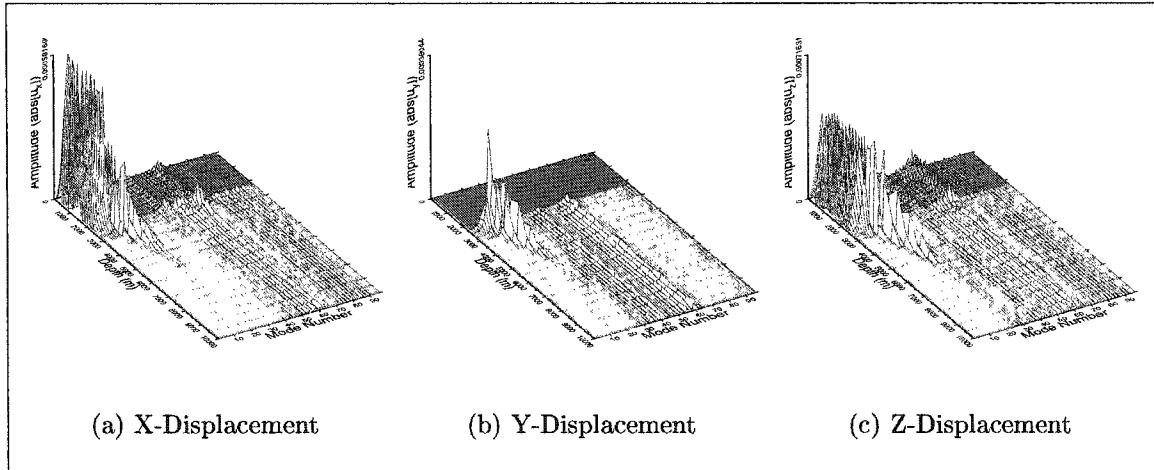


Figure 6.10: Figures (a) and (b) show the initial wavefield for the original Blanco TFZ earthquake event for a model without and with sediment cover respectively. Figures (c) and (d) show the scattered wavefield for the same models used in figures (a) and (b) respectively. The sediment cover enhances the scattering of modal energy into the low order acoustic modes, and will enhance T -wave excitation.

Figure 6.11 shows the scattered fields resulting from stochastic volume perturbations and stochastic interface roughness. Only the interface terms of \mathbf{H}_{qr} (which

come from integrating the volume integral by parts) are compared to \mathbf{S}_{qr} .

\mathbf{H}_{qr} Stochastic Interface Term Scattering Matrix



\mathbf{S}_{qr} Stochastic Interface Term Scattering Matrix

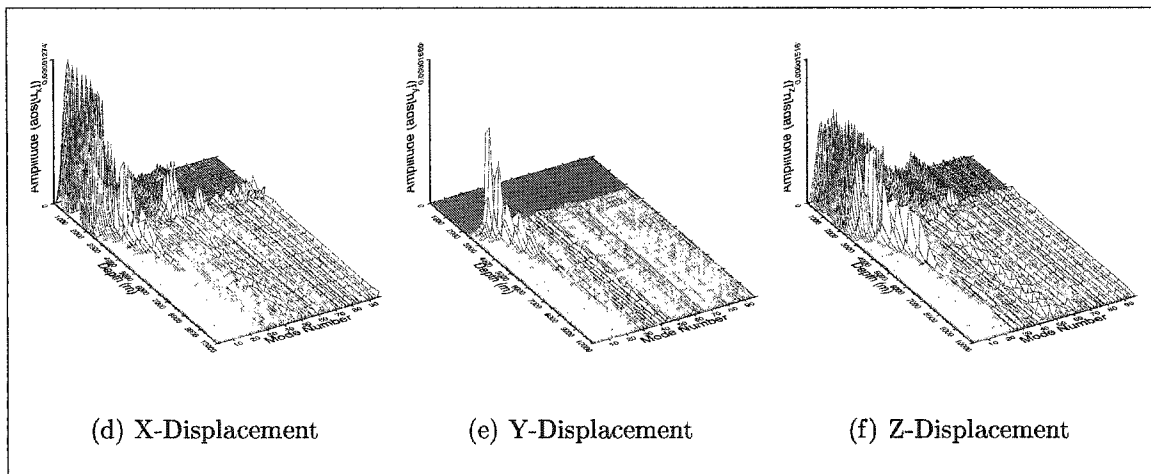


Figure 6.11: The \mathbf{H}_{qr} and \mathbf{S}_{qr} stochastic interface scattering matrices are compared for a tilted symmetry axis. A small amount of TI anisotropy was introduced into the first elastic layer of the velocity/density profile shown in Figure 6.1. Figures (a), (b), and (c) show the x, y, and z-displacement for the scattered field due to the \mathbf{H}_{qr} matrix respectively. Figures (d), (e), and (f) show the same for the \mathbf{S}_{qr} matrix. The results are very similar. Both random rough interface terms and stochastic volume perturbations can contribute to the excitation of T -waves.

The elastic treatment of the sediment and oceanic crust is crucial to obtaining T -wave excitation. The shear velocity in the model is responsible for the conversion of seismic energy into horizontally propagating acoustic energy. When shear motion is turned off for the model, by setting the shear velocity to zero, no energy is scattered into the low order acoustic modes. This makes the importance of shear motion to T -wave generation very clear.

6.3 Chapter Summary

A modal representation of the seismo-acoustic field provides a natural framework for modeling T -waves, and brings clarity to well known features of T -waves such as generally weak dispersion and the concentration of the energy near the SOFAR channel axis. The T -waves comprise just a few of the lowest order acoustic modes. Once one moves to frequencies just a short distance above the modal cut-off frequency, the dispersion curves for these low order acoustic modes are virtually flat. This means that even a broadband signal will be only very weakly dispersive. The concentration of energy near the SOFAR channel axis is obvious from Figure 6.1a. Higher order modes of course fill more of the channel, but the energy carried by the low order modes is still concentrated near the axis.

Because of mode orthogonality, T -waves would not exist if the earth was a laterally homogeneous plane-layered half-space or radially symmetric sphere. There is no way to directly excite low order propagating acoustic modes with a source placed well below the exponential tail, or ray equivalent turning point of the modes.

T -waves are excited by down-conversion modal scattering due to bathymetric irregularities and upper ocean crustal heterogeneities, with a large amplitude modal anti-node at the water-bottom boundary playing a significant role. Essentially any mechanism that breaks the strict mode orthogonality of the 1-D medium will scatter energy that can be interpreted as mode coupling. The modal scattering theory

(Park and Odom, 1999) explicitly includes the effects of random roughness as well as non-planar bathymetry. The presence of both features will increase the scattering, and therefore the strength of the T -wave. Steeply arriving rays corresponding to high order modes have very large horizontal phase velocities, from which energy can be relatively efficiently scattered into low order modes corresponding to nearly horizontally propagating rays. These low order modes propagate with the observed low group velocities and weak dispersion.

One benefit of the modal representation of an acoustic wavefield is that the low order modes are already propagating horizontally. Once energy has been transferred to the low order acoustic modes, it is able to propagate horizontally within the SOFAR channel. If any of the lower modes are excited, then the energy will be almost horizontally propagating by the nature of the modes. The modal basis allows the energy to be transferred from initial seismic source modes into the modes composing the T -wave. An advantage of being able to examine the physics of propagation on a mode by mode basis is that it be easily determined if the lower order modes, which compose the T -wave, are directly excited by a given source mechanism for a given model and source depth.

Fault type profoundly affects the degree of excitation of acoustic energy along the seafloor. Normal faulting events produces small scattered wavefields, producing smaller T -wave excitation than strike-slip and dip-slip faulting events. Since, effects of source characteristics appear to be reflected in the T -wave excitation, T -waves may be useful for source type discrimination. In addition, any low velocity sediment cover over the seafloor enhances the scattering of energy from higher order modes to the lower order T -wave carrying modes.

The coupled-mode representation of the wavefield does not encompass all equivalent angles of incidence. The continuum spectrum becomes a more significant portion of the T -wave signal as source depth increases. Only the discrete modes have been included, and deeper earthquakes require contributions from the continuum. While

a significant amount of energy is accounted for with shallow sources, the continuum spectrum becomes increasingly important at greater source depths.

The ability to model T -wave generation with the modal scattering theory is a direct result of including elastic properties into the bottom/subbottom structure to accurately model the excitation of the T -wave. The shear velocities and shear motion play an important role in T -wave generation. The modeling in this chapter has included the effects of scattering in the epicentral region only, neglecting cumulative propagation effects.

Chapter 7

SUMMARY AND CONCLUSIONS

Marine sediments, while being almost ubiquitously anisotropic and laterally heterogeneous, support shear motion, and therefore must be treated elastically. One method of treating the seafloor bottom and subbottom regions elastically is through a modal representation of the seismo-acoustic signal. The equation of motion can be expressed as a first order coupled equation that is directly dependent upon the elastic moduli. Therefore, the form of the elastic stiffness matrix, which describes any elastic anisotropy, will directly affect the formulation of the equation of motion, the characteristics of the modes, the frequency and angular dispersion curves, and the coupling of coherent and scattered modes in range-dependent media.

The Bond transformation is used to rotate the elastic stiffness matrix ${}^a C_{IJ}$ to an arbitrary orientation. Analytical forms of the rotated elastic stiffness matrix, and its sensitivity to angular rotations have been derived for TI elastic symmetry.

Whether the local modes propagate independently as P-SV and SH modes or coalesce into a set of quasi-P-SV, quasi-SH, and generalized P-SV-SH modes greatly affects the polarization of the propagating signal. An anisotropy medium may be ignored and treated as an equivalent isotropic medium when the elastic stiffness matrix is quasi-monoclinic or quasi-orthorhombic. These are instances where the P-SV and SH particle motions propagate independently. For more general quasi-triclinic forms of the elastic stiffness matrix (tilted TI medium), the modes are described as quasi-P-SV, quasi-SH, and generalized P-SV-SH modes with particle motions in all three Cartesian coordinate directions. The 3-D nature of the eigenfunctions cannot be approximated by an equivalent isotropic material, therefore a full anisotropic elastic

treatment of the problem is necessary. It is important to note that, the modal formalism does not require all of the modes to be individually identified as pure P-SV, pure SH, quasi P-SV, quasi SH or P-SV-SH. The only requirement is for all of the modes which contribute to the seismo-acoustics signal to be included into the modal superposition.

Seismo-acoustic signals can have a non-negligible portion of their energy in horizontally polarized shear motion, when they experience significant bottom interaction with elastic anisotropic marine sediments. Conversion of acoustic energy into horizontally polarized shear motion can be expected at fluid/solid boundaries, even in the absence of any range-dependence. SH plane wave motion experiences approximately 2-3 times more attenuation than P-SV plane wave motion, or even larger in low shear speed sediments. Therefore, horizontal shear motion can be an important loss mechanism for seismo-acoustic signals with significant seafloor interaction. The signal will experience more energy loss due to attenuation in an anisotropic environment than an equivalent signal propagating in an isotropic model or only within fluid layers. If anisotropy is present, but isotropy is assumed, then attenuation will be underestimated.

The combination of lateral heterogeneity and anisotropy can be effective at scattering a signal, and energy may become broadly redistributed among all of the propagating modes. The rotation of the symmetry axis away from vertical (e.g. non-horizontal bedding planes) will allow energy to be transferred between the modes, even if lateral variation is weak. The redistribution of energy can lead to the loss of signal coherence. With the introduction of even modest amounts of anisotropy, it becomes possible for higher order modes to directly transfer energy into lower order modes without cascading down through multiple nearest neighbor interactions. Acoustic energy can leave the water column through bottom interacting modes. The energy can then be attenuated by the low shear velocity sediments, and redistributed to other predominantly sediment modes. In addition, energy from other sources or

signals, such as noise, from the sediment and bottom layers can enter the water column through these bottom interacting modes.

For 2-D wave propagation in an isotropic medium, any heterogeneity will only promote scattering to modes of the same wavetype. With the introduction of anisotropy, heterogeneity may scatter energy into modes with displacements in all three coordinate directions. For a medium with a quasi-triclinic form of the elastic stiffness matrix all of the modes are excited regardless of source mode type, and all of the modes are involved in coupling. The inclusion of deterministic and stochastic scattering into the local coupled formalism provides an improvement in the forward problem of wave propagation in complex fluid-elastic media. By utilizing perturbation theory to the coupled local mode formalism, a new scattering coupling matrix \mathbf{H}_{qr} is derived which describes how much energy of coherent mode \mathbf{u}_r is redistributed into scattered mode \mathbf{u}_q . The coupling matrices \mathbf{B}_{qr} , \mathbf{S}_{qr} , and \mathbf{H}_{qr} indicate that the combination of tilted anisotropy and lateral heterogeneity is efficient at scattering the seismo-acoustic energy. Any lateral heterogeneity can cause the modes to couple, and the coupling tends to become stronger as the phase velocities associated with the local modes converge to similar values.

The solotone effects in both frequency and angular dispersion curves indicate the modes that are sensitive and insensitive to anisotropy. The frequency and angular dispersion curves give insight into the characteristics of specific modes. They indicate which modes are sensitive to anisotropy, and which modes remain invariant to the anisotropy and its symmetry axis orientation. A mode set divided into both sensitive and invariant modes may account for why anisotropy is often successfully introduced and modeled as a perturbation. Since not all of the modes are sensitive to the anisotropic layers, the impact of the anisotropy is limited by contribution of the sensitive modes, while the invariant modes still contribute an isotropic aspect to the seismo-acoustic signal.

A generalized set of P-SV-SH modes is required to correctly model seismo-acoustic

signals where tilted anisotropy is present. Since there no longer exists a clear distinction between pure P-SV and SH modes, all modes can carry energy for the seismo-acoustic signal. The implication is that all of the modes are intricately coupled for even weak anisotropy, and therefore more modes are available in anisotropic media for the redistribution of energy.

A modal representation of the seismo-acoustic field provides a natural framework for modeling T -waves excitation. An advantage of being able to examine the physics of propagation on a mode by mode basis is that it be easily determined if the lower order modes, which compose the T -wave, are directly excited by a given source mechanism for a given model and source depth. The T -waves comprise just a few of the lowest order acoustic modes.

Without lateral heterogeneity, there is no way to excite low order propagating acoustic modes with a source placed well below the exponential tail of the modes. T -waves are excited by modal scattering due to bathymetric irregularities and/or upper ocean crustal heterogeneities. The presence of both refraction from a sloping seafloor and seafloor scattering will increase the scattering, and therefore the strength of the T -wave. Once energy has been transferred to the low order acoustic modes, it is able to propagate horizontally within the SOFAR channel.

Fault type is strongly correlated with T -wave excitation efficiency and greatly affects the degree of excitation of acoustic energy along the seabottom. Normal faulting events cause smaller T -wave excitation than strike-slip and dip-slip faulting events. In addition, low velocity sediment cover enhances the scattering of energy from higher order modes to the lower order T -wave carrying modes.

The coupled-mode representation of the wavefield does not encompass all equivalent angles of incidence. Only the discrete modes have been included, and deeper earthquakes require contributions from the continuum. While a significant amount of energy is accounted for with shallow sources, the continuum spectrum becomes increasingly important at greater source depths.

The ability to model T -wave generation with the modal scattering theory is a direct result of including elastic properties into the bottom/subbottom structure to accurately model the excitation of the T -wave. The shear velocities and shear motion play an important role in T -wave generation. The modeling in this chapter has included the effects of scattering in the epicentral region only, neglecting cumulative propagation effects.

Future work may include the implementation of the Riccati equation solver to include propagation effects for the work presented in this dissertation. Attenuation and coupling to the continuum spectrum have not been included in this dissertation and could be pursued. The theory and numerical results of this dissertation have been restricted to the 2-D wave propagation problem. Further work could be done on extending the couple-mode formalism to the 3-D wave propagation problem. An inverse problem could be developed and applied to experimental data for a shallow water marine environment. The methods of coupled local modes could also be applied to other anisotropic and laterally heterogeneous regions. Appropriate geophysical applications would involve regions where the propagation of energy is confined to a waveguide. Sea ice and lake ice could be added to the shallow water waveguide. Surface waves and interface waves could be studied for crustal and crustal/mantle regions. Interface waves that travel along the crustal/mantle boundary or the core/mantle boundary could also be considered. These regions of the earth are known to have lateral heterogeneity and exhibit anisotropy.

GLOSSARY

$*$: Complex conjugate

$[quantity]_n$: Jump across the n^{th} interface discontinuity

\mathbf{A} : Differential operator from the first order form of the equation of motion

A, C, F, L, N : Five elastic moduli for VTI medium in Love notation

$\bar{A}, \bar{B}, \bar{C}, \bar{D}, \bar{E}$: Five elastic moduli for a VTI medium in Backus notation

\mathbf{B}_{qr} : coupling matrix

${}^a\mathbf{C} = {}^a C_{IJ}$: Elastic stiffness matrix in abbreviated subscript notation

C_{ijkl} : Fourth order elastic stiffness tensor

${}^w\mathbf{C}$: 9×9 matrix in Woodhouse notation

${}^w C_{ij}$: 3×3 submatrix in Woodhouse notation

c_r : Modal amplitude coefficient for coherent mode

\mathbf{D}_{qr} : Stochastic interface coupling matrix

d_r : Modal amplitude coefficient for interface scattered mode

\mathbf{E}_{qr} : Stochastic interface coupling matrix

$\mathbf{F} = F_i$: External force in first order form of the equation of motion

g_n : range-dependence of the elastic moduli for the n^{th} layer

\mathbf{H}_{qr} : Stochastic volume coupling matrix

h_n : range-dependence of the n^{th} interface boundary

HTI: TI medium with horizontal symmetry axis

k : Wavenumber

\mathbf{M}^y : Bond transform matrix for rotation about the y-axis.

\mathbf{M}^z : Bond transform matrix for rotation about the z-axis

Q_{ij} : 3X3 matrix of elastic moduli found in equation of motion

$\mathbf{R} = \mathbf{M}^y \mathbf{M}^z$: Bond transform matrix for tilted TI medium

\hat{s} : Infinite fold symmetry axis of a TI medium

\mathbf{S}_{qr} : Stochastic interface coupling matrix

s_r : Modal amplitude coefficient for volume scattered mode

\mathbf{t}_j : Traction vector

TTI: TI medium with tilted symmetry axis

\mathbf{u} : Displacement-stress vector

V : Velocity associated with elastic stiffness tensor element C_{ijkl}

VTI: TI medium with vertical symmetry axis.

- \mathbf{w} : Displacement vector
- X_{ij} : 3×3 matrix of elastic moduli defined in Appendix E
- Y_{ij} : 3×3 matrix of elastic moduli defined in Appendix E
- Z_{ij} : 3×3 matrix of elastic moduli defined in Appendix E
- α_H : Horizontal compressional velocity
- $\alpha_H, \beta_V, \phi, \xi, \eta$: Five elastic moduli for a VTI medium in Takeuchi and Saito notation
- α_V : Vertical compressional velocity
- β_H : Velocity of horizontally polarized shear wave
- β_V : Velocity of vertically polarized shear wave
- θ : Elevation angle
- ρ : Density
- φ : Azimuthal angle
- τ_{ij} : Stress tensor
- ω : Angular frequency

REFERENCES

- Alenitsyn, A., 1998. Double wave of Stoneley type on the interface of a stratified fluid layer and an elastic solid half-space, *J. Acoust. Soc. Am.*, **103**, 795-800.
- Aki, K. and Richards, P.G., 1980. *Quantitative Seismology, Vol. I*, W. H. Freeman and Company, New York, New York.
- Anderson, D.L., 1961. Elastic wave propagation in layered anisotropic media, *J. Geophys. Research*, **66**, 2953-2963.
- Auld, B.A., 1990. *Acoustic Fields and Waves in Solids*, Vol. I, 2nd ed., Krieger, Malabar, FL.
- Backus, G.E., 1962. Long-Wave Elastic Anisotropy Produced by Horizontal Layering *J. Geophys. Research*, **67**, 4427-4440.
- Backus, G.E., 1965. Possible Forms of Seismic Anisotropy of the Uppermost Mantle under Oceans *J. Geophys. Research*, **70**, 3429-3439.
- Beran, N., 1994. Scattering of flexural waves by random density fluctuations in a plate, *Waves in Random Media*, **4**, 221-232.
- Berge, P.A., Mallick, S., Fryer, G.J., Barstow, N., Carter, J.A., Sutton, G.H., and Ewing, J.I., 1991. In *situ* measurement of transverse isotropy in shallow-water marine sediments, *Geophys. J. Int.*, **104**, 241-254.
- Biot, M., 1952. The interaction of Rayleigh and Stoneley waves in the ocean bottom, *Bull. Seism. Soc. Am.*, **42**, 81-93.

- Budden, K.G., F.R.S and M. Eve, 1975. Degenerate modes in the Earth-ionosphere waveguide, *Proc. R. Soc. Lond. A.*, **342**, 175-190.
- Burridge, R. and Knopoff, L., 1964. Body-force equivalents for seismic dislocations, *Bull. Seism. Soc. Am.*, **54**, 1875-1888.
- Carlson, R.L., Schafternaar, C.H., and Moore, R.P., 1984. Causes of compression-al-wave anisotropy in carbonate-bearing, deep-sea sediments, *Geophysics.*, **49**, 525-532.
- Chen, X., 1993. A systematic and efficient method of computing normal modes for multilayered halfspace, *Geophys. J. Int.*, **115**, 391-409.
- Chiaruttini, C., Costa, G., and Panza, G.F., 1985. Wave propagation in multilayered media: the effect of waveguides in oceanic and continental Earth models, *J. Geophys.*, **58**, 189-196.
- Crampin, S., 1977. A review of the effects of anisotropic layering on the propagation of seismic waves, *Geophys. J. R. Astr. Soc.*, **45**, 9-27.
- Crampin, S., 1981. A review of wave motion in anisotropic and cracked elastic-media, *Wave Motion*, **3**, 343-391.
- Crampin, S., 1984. An introduction to wave propagation in anisotropic media, *Geophys. J. R. Astr. Soc.*, **760**, 17-28.
- Crampin, S., 1989. Suggestions for a consistent terminology for seismic anisotropy, *Geophys. Prospecting*, **37**, 753-777.
- Crampin, S., 1991. Effects of point singularities on shear-wave propagation in sedimentary basins, *Geophys. J. Int.*, **107**, 531-543.

- de Groot-Hedlin, C.D. and Orcutt, J.A., 1999. Synthesis of earthquake-generated *T*-waves, *Geophys. Res. Lett.* **26**, 1227-1230.
- Dziak, R.P., 2001. Empirical relationship of *T*-wave energy and fault parameters of northeast Pacific Ocean earthquakes, *Geophys. Res. Lett.*, **28**, 2537-2540.
- Ewing J., Carter J.A., Sutton G.H., and Barstow N., 1992. Shallow-water sediment properties derived from high-frequency shear and interface waves *J. Acoust. Soc. Am.*, **97**, 4739-4762.
- Fox, C.G. and Hayes, D.E., 1985. Quantitative methods for analyzing the roughness of the seafloor, *Rev. Geophys. Space Phys.*, **23**, 1-48.
- Fox, C.G., and Dziak, R.P., 1999. Internal deformation of the Gorda Plate observed by hydroacoustic monitoring, *J. Geophys. Research*, **104**, 17603-17616.
- Fox, C.G., Dziak, R.P., Matsumoto, H., and Schreiner, A.E., 1994. Potential for monitoring low-level seismicity on the Juan de Fuca Ridge using military hydrophone arrays, *Mar. Technol. Soc. J.*, **27**, 22-30.
- Friedman, S.P., and Jones, S.B., 2001. Measurement and approximate path analysis of the pore-scale-induced anisotropy factor of an unsaturated porous medium, *Water Resources Research*, **37**, 2929-2942.
- Hughes, S.J., Ellis, D.D., Chapman, D.M.F., and Staal, P.R., 1990. Low-frequency acoustic propagation loss in shallow water over hard-rock seabeds covered by a thin layer of elastic-solid sediment, *J. Acoust. Soc. Am.*, **88**, 283-297.
- Johnson, R.H., Norris, R.A., and Duennebieer, F.K., 1967. Abyssally generated *T* phases, *Hawaii Ins. Geophys. Rep. HIG-67-1*, 12 pp., Hawaii Institute of Geophysics, Honolulu, Hawaii.

- Keenan, R.E. and Merriam, L.R.L., 1991. Arctic abyssal *T*-phases: Coupling seismic energy to the ocean sound channel via under-ice scattering, *J. Acoust. Soc. Am.*, **89**, 1128-1133.
- Kennett, B.L.N. and Clarke, T.J., 1983. Seismic waves in a stratified half-space –IV: P-SV wave decoupling and surface wave dispersion, *Geophys. J. R. Astr. Soc.*, **72**, 633-645.
- Kennett, B.L.N., 1983. *Seismic wave propagation in stratified media*, Cambridge University Press, New York.
- Lapwood, E.R., 1975. The Effect of Discontinuities in Density and Rigidity on Torsional Eigenfrequencies of the Earth, *Geophys. J. R. Astr. Soc.*, **40**, 453-464.
- Levitus and Boyer, 1994. Levitus and Boyer, World Ocean Atlas 1994, *NOAA Atlas NESDIS 4*, Washington D.C.
- Love, A.E.H., 1944. *A Treatise on the Mathematical Theory of Elasticity*, Dover, New York, New York.
- Mallick, S. and Frazer, L.N., 1991. Reflection/transmission coefficients and azimuthal anisotropy in marine seismic studies, *Geophys. J. Int.*, **105**, 241-252.
- Martin, B.E., and Thomson, C.J., 1997. Modelling surface waves in anisotropic structures II: Examples, *Phys. Earth Planet. Inter.*, **103**, 253-297.
- Maupin, V., 1988. Surface waves across 2-D structures: a method based on coupled local modes, *Geophys. J.*, **93**, 173-185.
- Maupin, V., 1989. Surface waves in weakly anisotropic structures: on the use of ordinary or quasi-degenerate perturbation methods, *Geophys. J.*, **98**, 553-563.

- Maupin, V., 2001. A multiple-scattering scheme for modelling surface wave propagation in isotropic and anisotropic three-dimensional structures, *Geophys. J. Int.*, **146**, 332-348.
- Mochizuki, E., 1997. Nonuniqueness of Two-Dimensional Anisotropic Tomography, *Bull. Seism. Soc. Am.*, **87**, 261-264.
- Muyzert, E., and Snieder, R., 2000. An alternative parameterization for surface waves in a transverse isotropic medium, *Phys. Earth Planet. Inter.*, **118**, 125-133.
- Nye, J.F., 1957. *Physical Properties of Crystals*, Oxford University Press, London.
- Odom, R.I., 1986. A coupled-mode examination of irregular waveguides including the continuum spectrum, *Geophys. J. R. Astr. Soc.*, **86**, 425-454.
- Odom, R.I., Park, M., Mercer, J.A., Crosson, R.S. & Paik, P., 1996. Effects of transverse isotropy on modes and mode coupling in shallow water, *J. Acoust. Soc. Am.*, **100**, 2079-2092.
- Okal, E.A., 2001. *T*-phase Stations for the International Monitoring System of the Comprehensive Nuclear-Test Ban Treaty: A Global Perspective, *Seis. Res. Lett.*, **72**, 186-196.
- Okaya, D.A. and McEvelly, T.V., 2003. Elastic wave propagation in anisotropic crustal material possessing arbitrary internal tilt, *Geophys. J. Int.*, **153**, 344-358.
- Park, J., 1996. Surface waves in layered anisotropic structures, *Geophys. J. Int.*, **126**, 173-183.

- Park, M. and Odom, R.I., 1998. Effects of elastic heterogeneities and anisotropy on mode coupling and signals in shallow water, *J. Acoust. Soc. Am.*, **104**, 747-757.
- Park, M. and Odom, R.I., 1999. The effect of stochastic rough interfaces on coupled-mode elastic waves, *Geophys. J. Int.*, **136**, 123-143.
- Park, M., Odom, R.I., and Soukup, D., 2001. Modal scattering: a key to understanding oceanic *T*-waves, *Geophys. Res. Lett.*, **29**, 401-404.
- Park, M., 1997. Effects of anisotropy and lateral heterogeneities on elastic waves and mode coupling in shallow water, Ph.D. dissertation, University of Washington.
- Romanowicz, B. and Snieder, R., 1988. A new formalism for the effect of lateral heterogeneity on normal modes and surface waves - II. General anisotropic perturbation, *Geophys. J.*, **93**, 91-99.
- Saito, M., 1988. DISPER80: A Subroutine Package for the Calculation of Seismic Normal-Mode Solutions, in *SEISMOLOGICAL ALGORITHMS: Computational Methods and Computer Programs*, pp. 293-319, ed. Doornbos, D., Academic, San Diego, California.
- Schoenberg, M. and Costa, J., 1991. The insensitivity of reflected SH waves to anisotropy in an underlying layered medium, *Geophys. Prospecting*, **39**, 985-1003.
- Shearer, P.M. and Orcutt, J.A., 1986. Compressional and shear wave anisotropy in the oceanic lithosphere - the Ngendei seismic refraction experiment, *Geophys. J. R. Astr. Soc.*, **87**, 967-1003.
- Slack, P.D., Fox, C.G., and Dziak, R.P., 1999. *P* wave detection thresholds, *P_n* velocity estimates, and *T* wave location uncertainty from oceanic hydrophones, *J. Geophys. Research*, **104**, 13061-13072.

- Sperry, B., Goh, J.T., Baggeroer, A., and Schmidt, H., 1996. Possible mechanisms for *T*-phase generation, *J. Acoust. Soc. Am. (abstract)*, **100**, 2641.
- Stoll, R.D., Bryan G.M., and Bautista, E.O., 1994. Measuring lateral variability of sediment geoacoustic properties, *J. Acoust. Soc. Am.*, **96**, 427-438.
- Takeuchi, H. & Saito, M., 1972. Seismic surface waves, in *Seismology: Surface waves and earthquake oscillations* (methods in computational physics, Vol. 11), pp. 217-295, ed. Bolt, B.A., Academic Press, New York.
- Talandier, J. and Okal, E.A., 1998. On the mechanism of conversion of seismic waves to and from T waves in the vicinity of island shores, *Bull. Seism. Soc. Am.*, **86**, 1529-1544.
- Thomsen, L., 1986. Weak elastic anisotropy, *Geophysics.*, **51**, 1954-1966.
- Thomson, C.J., 1997. Modelling surface waves in anisotropic structures I: Theory, *Phys. Earth Planet. Inter.*, **103**, 195-203.
- Tolstoy, I. and Ewing, M., 1950. The *T* phase of shallow-focus earthquakes, *Bull. Seism. Soc. Am.*, **40**, 25-51.
- Tracey, B. and Schmidt, H., 1997. Seismo-Acoustic Field Statistics in Shallow Water, *IEEE J. Ocean. Eng.*, **22**, 317-331.
- Tromp, J., 1994. A coupled local-mode analysis of surface-wave propagation in a laterally heterogeneous waveguide, *Geophys. J. Int.*, **117**, 153-161.
- Wessel, P. and Smith, W. H. F., 1991. Free software helps map and display data, *EOS Trans. AGU*, **72**, 441

- Winterstein, D.F., 1990. Velocity anisotropy terminology for geophysicists, *Geophysics.*, **55**, 1070-1088.
- Woodhouse, J.H., 1974. Surface waves in a laterally varying layered structure, *Geophys. J. R. Astr. Soc.*, **37**, 461-490.
- Yin, J., and Cao, W., 2002. Effective macroscopic symmetries and material properties of multidomain $0.955\text{Pb}(\text{Zn}_{1/3}\text{Nb}_{2/3})\text{O}_3 - 0.045\text{PbTiO}_3$ single crystals, *J. Appl. Phys.*, **92**, 444-448.
- Zhu, J., and Dorman, J., 2000. Two-dimensional, three-component wave propagation in a transversely isotropic medium with arbitrary-orientation-finite-element modeling *Geophysics.*, **65**, 934-942.

Appendix A

VTI ANISOTROPY PARAMETERIZATION

The elements of the elastic stiffness tensor, C_{ijkl} , can be parameterized in a number of ways. Each parameterization results in the exact same elastic stiffness tensor. Love notation (1944), Backus notation (1965) and Takeuchi and Saito notation (1972) are each considered. The theory of Odom *et. al.* (1996) and Park *et. al.* (1998) use the Love parameterization where the five independent elastic constants for a VTI medium are expressed as the elastic moduli A, C, F, L, N . Both works relied on the DISPER80 code which uses Takeuchi and Saito notation (1972), where the five independent constants are expressed as velocities α_H and β_V along with ratios of the elastic moduli χ, ϕ, η . The ANIPROP code of Park (1996) uses the modified Backus notation (1965) where the five independent constants of a VTI medium are the elastic moduli $\bar{A}, \bar{B}, \bar{C}, \bar{D}, \bar{E}$. The relationships between the three parameterizations are contained in Tables A.1-A.3

Table A.1: Love Notation

Love Notation	Backus Notation	Takeuchi and Saito Notation	Isotropy
$A =$	$\bar{A} - \bar{B} + \bar{C}$	$\rho\alpha_H^2$	$\lambda + 2\mu$
$C =$	$\bar{A} + \bar{B} + \bar{C}$	$\rho\alpha_H^2\phi$	$\lambda + 2\mu$
$F =$	$\bar{A} - 3\bar{C} - 2(\bar{D} + \bar{E})$	$\rho\eta(\alpha_H^2 - 2\beta_V^2)$	λ
$L =$	$\bar{D} + \bar{E}$	$\rho\beta_V^2$	μ
$N =$	$\bar{D} - \bar{E}$	$\rho\beta_V^2\xi$	μ

Table A.1 shows A, C, F, L, N (Love, 1944) for a VTI medium described in terms of $\alpha_H, \beta_V, \phi, \xi, \eta$ (Takeuchi and Saito, 1972) and $\bar{A}, \bar{B}, \bar{C}, \bar{D}, \bar{E}$ (Backus, 1965). The interpretation of the elastic moduli is found in section 2.1 of the main text.

The anisotropy describe by Takeuchi and Saito (1972) is parameterized by a horizontal compressional velocity α_H , a vertical shear velocity β_V , a ratio of horizontal and vertical compressional velocities ϕ , a ratio of horizontal and vertical shear velocities ξ , and a third anisotropic ratio η . Table A.2 shows $\alpha_H, \beta_V, \phi, \xi, \eta$ described in terms of A, C, F, L, N , and $\bar{A}, \bar{B}, \bar{C}, \bar{D}, \bar{E}$. Note that the ratio ϕ is not to be confused with the azimuthal angle φ in the xy-plane describing the symmetry axis \hat{s} orientation.

Table A.2: Takeuchi and Saito Notation

Takeuchi and Saito Notation	Love Notation	Backus Notation	Isotropy
$\alpha_H =$	$\sqrt{\frac{A}{\rho}}$	$\sqrt{\frac{\bar{A} - \bar{B} + \bar{C}}{\rho}}$	$\sqrt{\frac{\lambda + 2\mu}{\rho}}$
$\beta_V =$	$\sqrt{\frac{L}{\rho}}$	$\sqrt{\frac{\bar{D} + \bar{E}}{\rho}}$	$\sqrt{\frac{\mu}{\rho}}$
$\xi =$	$\frac{N}{L}$	$\frac{\bar{D} - \bar{E}}{\bar{D} + \bar{E}}$	1
$\phi =$	$\frac{C}{A}$	$\frac{\bar{A} + \bar{B} + \bar{C}}{\bar{A} - \bar{B} + \bar{C}}$	1
$\eta =$	$\frac{F}{A - 2L}$	$\frac{\bar{A} - 3\bar{C} - 2(\bar{D} + \bar{E})}{\bar{A} - \bar{B} + \bar{C} - \bar{D} - \bar{E}}$	1

The previous works of Backus(1965), Crampin(1977), Shearer and Orcutt (1986) relate the five constants $\bar{A}, \bar{B}, \bar{C}, \bar{D}, \bar{E}$ to the individual elastic stiffness tensor elements for a HTI medium, with a symmetry axis in the x-direction . The values in

Table A.3: Backus Notation

Backus Notation	Love Notation	Takeuchi and Saito Notation	Isotropy
$\bar{A} =$	$\frac{3(A + C) + 2(F + 2L)}{8}$	$\frac{\alpha_H^2(3(1 + \phi) + 2\eta) + 2\beta_V^2(1 - \eta)}{8}$	$\lambda + 2\mu$
$\bar{B} =$	$\frac{4(C - A)}{2}$	$\frac{4\alpha_H^2(\phi - 1)}{8}$	0
$\bar{C} =$	$\frac{A + C - 2(F + 2L)}{8}$	$\frac{\alpha_H^2(1 + \phi - 2\eta) - 4\beta_V^2(1 - \eta)}{8}$	0
$\bar{D} =$	$\frac{L + N}{2}$	$\rho\beta_V^2 \left(\frac{1 + \xi}{2} \right)$	μ
$\bar{E} =$	$\frac{L - N}{2}$	$\rho\beta_V^2 \left(\frac{1 - \xi}{2} \right)$	0

Table A.3 are similar, except they describe the C_{ijkl} elastic stiffness tensor for a VTI medium. Table A.3 shows $\bar{A}, \bar{B}, \bar{C}, \bar{D}, \bar{E}$ for a VTI medium described in terms of A, C, F, L, N and $\alpha_H, \beta_V, \phi, \xi, \eta$.

Additional parameterizations of VTI media include the Thomsen parameterization (1986) and the alternate parameterization of Romanowicz and Snieder(1988) and Muzert and Snieder(2000).

Appendix B

ELASTIC STIFFNESS TENSOR AND MATRIX NOTATION

The fourth order elastic stiffness tensor C_{ijkl} has symmetries that allow the 21 independent elements to be expressed in more compact matrix notations. The elastic stiffness tensor obeys the following symmetry:

$$C_{ijkl} = C_{kilm} = C_{ikjl} = C_{ljik}.$$

which reduces the 81 components of C_{ijkl} to at most 21 independent components. The indices of the fourth order elastic stiffness tensor are $ijkl$ rather than the conventional $ijkl$ in order to facilitate the mapping between tensor notation and the matrix notation of Woodhouse (1974). Woodhouse's notation (1974) and abbreviated subscript notation (e.g. Auld, 1990) describe the exact same elastic parameters from the elastic stiffness tensor C_{ijkl} . However, the Woodhouse matrix and the abbreviated subscript matrix are not equivalent.

$$\begin{aligned} \mathbf{C} &= C_{ijkl} && \text{fourth order elastic stiffness tensor} \\ {}^a\mathbf{C} &= {}^aC_{IJ} && 6 \times 6 \text{ abbreviated subscript elastic stiffness matrix} \\ {}^w\mathbf{C} &= ({}^wC_{ij})_{kl} && 9 \times 9 \text{ Woodhouse elastic stiffness matrix} \\ {}^wC_{ij} &&& 3 \times 3 \text{ Woodhouse submatrix} \end{aligned}$$

Lower case suffixes such as $ijkl$ have values that range from $i, k, l, j = 1, 2, 3$. Upper case suffixes such as IJ have values that range from $I, J = 1, 2, 3, 4, 5, 6$. The individual elements of the elastic stiffness tensor can be put into a matrix format by using an abbreviated subscript notation, also known as Voigt notation (Nye, 1957) or matrix

Table B.1: Abbreviated Subscript Notation

ik or lj	I or J
11	1
22	2
33	3
23,32	4
13,31	5
12,21	6

notation. Table A.1 below describes how to transfer between traditional fourth order tensor notation and the abbreviated subscript notation for the individual elements of C_{ijkl} and C_{IJ} .

The four suffixes $ijkl$ are replaced with two suffixes IJ . Considering the Woodhouse elastic stiffness matrix first, which is composed of nine submatrices:

$${}^w\mathbf{C} = ({}^wC_{ij})_{kl} = \begin{bmatrix} ({}^wC_{11})_{kl} & ({}^wC_{12})_{kl} & ({}^wC_{13})_{kl} \\ ({}^wC_{21})_{kl} & ({}^wC_{22})_{kl} & ({}^wC_{23})_{kl} \\ ({}^wC_{31})_{kl} & ({}^wC_{32})_{kl} & ({}^wC_{33})_{kl} \end{bmatrix} \quad (\text{B.1})$$

The 9×9 Woodhouse matrix is a symmetric matrix, and there are only six unique submatrices, where:

$${}^wC_{ij} = {}^wC_{ij}^T = {}^wC_{ji} = {}^wC_{ji}^T \quad (\text{B.2})$$

The elements of the Woodhouse submatrices ${}^wC_{ij}$ expressed in traditional fourth order subscript notation, composing the 9×9 Woodhouse matrix:

$${}^w\mathbf{C} = \begin{bmatrix} C_{1111} & C_{1121} & C_{1131} & C_{1112} & C_{1122} & C_{1132} & C_{1113} & C_{1123} & C_{1133} \\ C_{1211} & C_{1221} & C_{1231} & C_{1212} & C_{1222} & C_{1232} & C_{1213} & C_{1223} & C_{1233} \\ C_{1311} & C_{1321} & C_{1331} & C_{1312} & C_{1322} & C_{1332} & C_{1313} & C_{1323} & C_{1333} \\ \hline C_{2111} & C_{2121} & C_{2131} & C_{2112} & C_{2122} & C_{2132} & C_{2113} & C_{2123} & C_{2133} \\ C_{2211} & C_{2221} & C_{2231} & C_{2212} & C_{2222} & C_{2232} & C_{2213} & C_{2223} & C_{2233} \\ C_{2311} & C_{2321} & C_{2331} & C_{2312} & C_{2322} & C_{2332} & C_{2313} & C_{2323} & C_{2333} \\ \hline C_{3111} & C_{3121} & C_{3131} & C_{3112} & C_{3122} & C_{3132} & C_{3113} & C_{3123} & C_{3133} \\ C_{3211} & C_{3221} & C_{3231} & C_{3212} & C_{3222} & C_{3232} & C_{3213} & C_{3223} & C_{3233} \\ C_{3311} & C_{3321} & C_{3331} & C_{3312} & C_{3322} & C_{3332} & C_{3313} & C_{3323} & C_{3333} \end{bmatrix} \quad (\text{B.3})$$

The elements of the Woodhouse submatrices as expressed in abbreviated subscript notation, composing the 9×9 Woodhouse matrix:

$${}^w\mathbf{C} = \begin{bmatrix} C_{11} & C_{16} & C_{15} & C_{16} & C_{12} & C_{14} & C_{15} & C_{14} & C_{13} \\ C_{61} & C_{66} & C_{65} & C_{66} & C_{62} & C_{64} & C_{65} & C_{64} & C_{63} \\ C_{51} & C_{56} & C_{55} & C_{56} & C_{52} & C_{54} & C_{55} & C_{54} & C_{53} \\ \hline C_{61} & C_{66} & C_{65} & C_{66} & C_{62} & C_{64} & C_{65} & C_{64} & C_{63} \\ C_{21} & C_{26} & C_{25} & C_{26} & C_{22} & C_{24} & C_{25} & C_{24} & C_{23} \\ C_{41} & C_{46} & C_{45} & C_{46} & C_{42} & C_{44} & C_{45} & C_{44} & C_{43} \\ \hline C_{51} & C_{56} & C_{55} & C_{56} & C_{52} & C_{54} & C_{55} & C_{54} & C_{53} \\ C_{41} & C_{46} & C_{45} & C_{46} & C_{42} & C_{44} & C_{45} & C_{44} & C_{43} \\ C_{31} & C_{36} & C_{35} & C_{36} & C_{32} & C_{34} & C_{35} & C_{34} & C_{33} \end{bmatrix} \quad (\text{B.4})$$

The above forms of the ${}^w\mathbf{C}$ are valid for any triclinic anisotropic medium with 21 independent constants, as well as for any medium with a higher degree of symmetry, such as TI. Substituting the Love notation (1944) elastic constants into the Woodhouse matrix for a TI elastically symmetric medium.

For $\hat{s}(\theta, \varphi) = \hat{s}(0^\circ, 0^\circ) = \hat{z}$

$${}^w\mathbf{C} = \begin{bmatrix} A & 0 & 0 & | & 0 & H & 0 & | & 0 & 0 & F \\ 0 & N & 0 & | & N & 0 & 0 & | & 0 & 0 & 0 \\ 0 & 0 & L & | & 0 & 0 & 0 & | & L & 0 & 0 \\ \hline 0 & N & 0 & | & N & 0 & 0 & | & 0 & 0 & 0 \\ H & 0 & 0 & | & 0 & A & 0 & | & 0 & 0 & F \\ 0 & 0 & 0 & | & 0 & 0 & L & | & 0 & L & 0 \\ \hline 0 & 0 & L & | & 0 & 0 & 0 & | & L & 0 & 0 \\ 0 & 0 & 0 & | & 0 & 0 & L & | & 0 & L & 0 \\ F & 0 & 0 & | & 0 & F & 0 & | & 0 & 0 & C \end{bmatrix} \quad (\text{B.5})$$

For $\hat{s}(\theta, \varphi) = \hat{s}(90^\circ, 0^\circ) = \hat{x}$

$${}^w\mathbf{C} = \begin{bmatrix} C & 0 & 0 & | & 0 & F & 0 & | & 0 & 0 & F \\ 0 & L & 0 & | & L & 0 & 0 & | & 0 & 0 & 0 \\ 0 & 0 & L & | & 0 & 0 & 0 & | & L & 0 & 0 \\ \hline 0 & L & 0 & | & L & 0 & 0 & | & 0 & 0 & 0 \\ F & 0 & 0 & | & 0 & A & 0 & | & 0 & 0 & H \\ 0 & 0 & 0 & | & 0 & 0 & N & | & 0 & N & 0 \\ \hline 0 & 0 & L & | & 0 & 0 & 0 & | & L & 0 & 0 \\ 0 & 0 & 0 & | & 0 & 0 & N & | & 0 & N & 0 \\ F & 0 & 0 & | & 0 & H & 0 & | & 0 & 0 & A \end{bmatrix} \quad (\text{B.6})$$

For $\hat{s}(\theta, \varphi) = \hat{s}(90^\circ, 90^\circ) = \hat{y}$

$${}^w\mathbf{C} = \begin{bmatrix} A & 0 & 0 & 0 & F & 0 & 0 & 0 & H \\ 0 & L & 0 & L & 0 & 0 & 0 & 0 & 0 \\ 0 & 0 & N & 0 & 0 & 0 & N & 0 & 0 \\ \hline 0 & L & 0 & L & 0 & 0 & 0 & 0 & 0 \\ F & 0 & 0 & 0 & C & 0 & 0 & 0 & F \\ 0 & 0 & 0 & 0 & 0 & L & 0 & L & 0 \\ \hline 0 & 0 & N & 0 & 0 & 0 & N & 0 & 0 \\ 0 & 0 & 0 & 0 & 0 & L & 0 & L & 0 \\ H & 0 & 0 & 0 & F & 0 & 0 & 0 & A \end{bmatrix} \quad (\text{B.7})$$

The 6×6 abbreviated subscript matrix is also a symmetric matrix, with the possibility of 21 unique and independent elements where:

$${}^aC_{IJ} = {}^aC_{IJ}^T = {}^aC_{JI} = {}^aC_{JI}^T. \quad (\text{B.8})$$

Any additional symmetry would reduce the number of independent elements. The elements of the abbreviated subscript elastic stiffness matrix expressed in traditional fourth order tensor notation for a general triclinic medium.

$${}^a\mathbf{C} = \begin{bmatrix} C_{1111} & C_{1122} & C_{1133} & C_{1123} & C_{1113} & C_{1112} \\ C_{2211} & C_{2222} & C_{2233} & C_{2223} & C_{2213} & C_{2212} \\ C_{3311} & C_{3322} & C_{3333} & C_{3323} & C_{3313} & C_{3312} \\ C_{2311} & C_{2322} & C_{2333} & C_{2323} & C_{2313} & C_{2312} \\ C_{1311} & C_{1322} & C_{1333} & C_{1323} & C_{1313} & C_{1312} \\ C_{1211} & C_{1222} & C_{1233} & C_{1223} & C_{1213} & C_{1212} \end{bmatrix} \quad (\text{B.9})$$

The abbreviated subscript elastic stiffness matrix with the elements expressed in

abbreviated subscript notation.

$${}^a\mathbf{C} = \begin{bmatrix} C_{11} & C_{12} & C_{13} & C_{14} & C_{15} & C_{16} \\ C_{21} & C_{22} & C_{23} & C_{24} & C_{25} & C_{26} \\ C_{31} & C_{32} & C_{33} & C_{34} & C_{35} & C_{36} \\ C_{41} & C_{42} & C_{43} & C_{44} & C_{45} & C_{46} \\ C_{51} & C_{52} & C_{53} & C_{54} & C_{55} & C_{56} \\ C_{61} & C_{62} & C_{63} & C_{64} & C_{65} & C_{66} \end{bmatrix} \quad (\text{B.10})$$

Consider a TI elastically symmetric medium as used in the main text of the paper.

The elastic moduli are expressed in Love notation (1944).

For $\hat{s}(\theta, \varphi) = \hat{s}(0^\circ, 0^\circ) = \hat{z}$

$${}^a\mathbf{C} = \begin{bmatrix} A & H & F & 0 & 0 & 0 \\ H & A & F & 0 & 0 & 0 \\ F & F & C & 0 & 0 & 0 \\ 0 & 0 & 0 & L & 0 & 0 \\ 0 & 0 & 0 & 0 & L & 0 \\ 0 & 0 & 0 & 0 & 0 & N \end{bmatrix} \quad \text{where } H = A - 2N \quad (\text{B.11})$$

For $\hat{s}(\theta, \varphi) = \hat{s}(90^\circ, 0^\circ) = \hat{x}$

$${}^a\mathbf{C} = \begin{bmatrix} C & F & F & 0 & 0 & 0 \\ F & A & H & 0 & 0 & 0 \\ F & H & A & 0 & 0 & 0 \\ 0 & 0 & 0 & N & 0 & 0 \\ 0 & 0 & 0 & 0 & L & 0 \\ 0 & 0 & 0 & 0 & 0 & L \end{bmatrix} \quad \text{where } H = A - 2N \quad (\text{B.12})$$

For $\hat{s}(\theta, \varphi) = \hat{s}(90^\circ, 90^\circ) = \hat{y}$

$${}^a\mathbf{C} = \begin{bmatrix} A & F & H & 0 & 0 & 0 \\ F & C & F & 0 & 0 & 0 \\ H & F & A & 0 & 0 & 0 \\ 0 & 0 & 0 & L & 0 & 0 \\ 0 & 0 & 0 & 0 & N & 0 \\ 0 & 0 & 0 & 0 & 0 & L \end{bmatrix} \quad \text{where } H = A - 2N \quad (\text{B.13})$$

The individual elements for a TI medium with an arbitrary symmetry axis $\hat{s}(\theta, \phi)$ can be determined by equation (2.11) from the main text. The elements of ${}^a\mathbf{C}$ will be linear combinations of the elastic moduli A, C, F, L, N .

Appendix C

BOND TRANSFORMATION OF TI SYMMETRIC STRUCTURES

Any arbitrary tilt of a TI symmetric medium can be obtained by rotating through the two angles θ and φ . The Bond transformation matrices described by Auld(1990) are found below.

$$\mathbf{M} = \begin{bmatrix} a_{xx}^2 & a_{xy}^2 & a_{xz}^2 & 2a_{xy}a_{xz} & 2a_{xz}a_{xx} & 2a_{xx}a_{xy} \\ a_{yx}^2 & a_{yy}^2 & a_{yz}^2 & 2a_{yy}a_{yz} & 2a_{yz}a_{yx} & 2a_{yx}a_{yy} \\ a_{zx}^2 & a_{zy}^2 & a_{zz}^2 & 2a_{zy}a_{zz} & 2a_{zz}a_{zx} & 2a_{zx}a_{zy} \\ a_{yz}a_{zx} & a_{yy}a_{zy} & a_{yz}a_{zz} & a_{yy}a_{zz} + a_{yz}a_{zy} & a_{yz}a_{zz} + a_{yz}a_{zx} & a_{yy}a_{zx} + a_{yx}a_{zy} \\ a_{zz}a_{xx} & a_{zy}a_{xy} & a_{zz}a_{xz} & a_{xy}a_{zz} + a_{xz}a_{zy} & a_{xz}a_{zx} + a_{xx}a_{zz} & a_{xx}a_{zy} + a_{xy}a_{zx} \\ a_{xx}a_{yx} & a_{xy}a_{yy} & a_{xz}a_{yz} & a_{xy}a_{yz} + a_{xz}a_{yy} & a_{xz}a_{yx} + a_{xx}a_{yz} & a_{xx}a_{yy} + a_{xy}a_{yz} \end{bmatrix} \quad (\text{C.1})$$

The Bond transformation matrix M is composed of the elements form the general transform matrix a .

$$\mathbf{a} = \begin{bmatrix} a_{xx} & a_{xy} & a_{xz} \\ a_{yx} & a_{yy} & a_{yz} \\ a_{zx} & a_{zy} & a_{zz} \end{bmatrix} \quad (\text{C.2})$$

The general transformation matrices for rotation about the y and z axes are a^y and a^z respectively.

$$\mathbf{a}^y = \begin{bmatrix} \cos \theta & 0 & -\sin \theta \\ 0 & 1 & 0 \\ \sin \theta & 0 & \cos \theta \end{bmatrix} \quad \mathbf{a}^z = \begin{bmatrix} \cos \varphi & \sin \varphi & 0 \\ -\sin \varphi & \cos \varphi & 0 \\ 0 & 0 & 1 \end{bmatrix} \quad (\text{C.3})$$

The corresponding Bond transformation matrices about the y and z axes are then M^y and M^z respectively.

$$M^y = \begin{bmatrix} \cos^2 \theta & 0 & \sin^2 \theta & 0 & -\sin 2\theta & 0 \\ 0 & 1 & 0 & 0 & 0 & 0 \\ \sin^2 \theta & 0 & \cos^2 \theta & 0 & \sin 2\theta & 0 \\ 0 & 0 & 0 & \cos \theta & 0 & \sin \theta \\ \frac{1}{2} \sin 2\theta & 0 & -\frac{1}{2} \sin 2\theta & 0 & \cos 2\theta & 0 \\ 0 & 0 & 0 & -\sin \theta & 0 & \cos \theta \end{bmatrix} \quad (C.4)$$

$$M^z = \begin{bmatrix} \cos^2 \varphi & \sin^2 \varphi & 0 & 0 & 0 & \sin 2\varphi \\ \sin^2 \varphi & \cos^2 \varphi & 0 & 0 & 0 & -\sin 2\varphi \\ 0 & 0 & 0 & 0 & 0 & 0 \\ 0 & 0 & 0 & \cos \varphi & -\sin \varphi & 0 \\ 0 & 0 & 0 & \sin \varphi & \cos \varphi & 0 \\ -\frac{1}{2} \sin 2\varphi & \frac{1}{2} \sin 2\varphi & 0 & 0 & 0 & \cos 2\varphi \end{bmatrix} \quad (C.5)$$

Applying the Bond transformation to the elastic stiffness matrix ${}^a\mathbf{C}$ to obtain a general rotation.

$${}^a\mathbf{C} = [\mathbf{R}] [{}^a\mathbf{C}''] [\mathbf{R}]^T \quad \text{where } \mathbf{R} = M^z M^y$$

The individual elements of the elastic-stiffness tensor for a TI elastically symmetric medium can be found by the following relation.

$$\begin{aligned} {}^a C_{IJ} &= A(R_{i1}R_{j1} + R_{i2}R_{j2}) + H(R_{i1}R_{j2} + R_{i2}R_{j1}) \\ &+ F(R_{i1}R_{j3} + R_{i2}R_{j3} + R_{i3}R_{j1} + R_{i3}R_{j2}) + CR_{i3}R_{j3} \\ &+ L(R_{i4}R_{j4} + R_{i5}R_{j5}) + NR_{i6}R_{j6} \end{aligned} \quad (C.6)$$

The \mathbf{R} transformation matrix for a general rotation of a VTI medium to any arbitrary

orientation is:

$$\mathbf{R} = \begin{bmatrix} \cos^2 \theta \cos^2 \varphi & \sin^2 \varphi & \sin^2 \theta \cos^2 \varphi \\ \cos^2 \theta \sin^2 \varphi & \cos^2 \varphi & \sin^2 \theta \sin^2 \varphi \\ \sin^2 \theta & 0 & \cos^2 \theta \\ -\frac{1}{2} \sin 2\theta \sin \varphi & 0 & \frac{1}{2} \sin 2\theta \sin \varphi \\ \frac{1}{2} \cos \theta \sin 2\varphi & 0 & -\frac{1}{2} \sin 2\theta \cos \varphi \\ -\frac{1}{2} \cos^2 \theta \sin 2\varphi & \frac{1}{2} \sin 2\varphi & -\frac{1}{2} \sin^2 \theta \sin 2\varphi \\ -\sin \theta \sin 2\varphi & -\sin 2\theta \cos^2 \varphi & \cos \theta \sin 2\varphi \\ \sin \theta \sin 2\varphi & -\sin 2\theta \sin^2 \varphi & -\cos \theta \sin 2\varphi \\ 0 & \sin 2\theta & 0 \\ \cos \theta \cos \varphi & -\cos 2\theta \sin \varphi & \sin \theta \cos \varphi \\ \cos \theta \sin \varphi & \cos 2\theta \cos \varphi & \sin \theta \sin \varphi \\ -\sin \theta \cos \varphi & \frac{1}{2} \sin 2\theta \sin 2\varphi & \cos \theta \cos 2\varphi \end{bmatrix} \quad (\text{C.7})$$

Once the rotated elastic moduli are determined for some symmetry axis $\hat{s}(\theta, \phi)$, they can be inserted into the elements of the differential operator A and the coupling matrix \mathbf{B}_{gr} . The elements of ${}^a C_{ij}$ need to be converted from abbreviated subscript notation into Woodhouse notation as done in Appendix A. It should be noted that the Bond Transformations that include rotations about both the y and z axes are best done numerically. Analytical results are not always insightful for most arbitrary symmetry axis orientations of $\hat{s}(\theta, \varphi)$.

The sensitivity of the elastic stiffness matrix to changes in θ and φ may also be considered.

$$\frac{\partial({}^a \mathbf{C})}{\partial \Delta} = \frac{\partial \mathbf{R}}{\partial \Delta} {}^a \mathbf{C} \mathbf{R}^T + \mathbf{R} {}^a \mathbf{C} \frac{\partial \mathbf{R}^T}{\partial \Delta} \quad \text{where } \mathbf{R} = \mathbf{M}^z \mathbf{M}^y \quad (\text{C.8})$$

The individual elements of the derivative of the elastic stiffness matrix with respect to the generic angle Δ is:

$$\frac{\partial({}^a C_{IJ})}{\partial \Delta} = A \left(\frac{\partial R_{i1}}{\partial \Delta} R_{j1} + R_{i1} \frac{\partial R_{j1}}{\partial \Delta} + \frac{\partial R_{i2}}{\partial \Delta} R_{j2} + R_{i2} \frac{\partial R_{j2}}{\partial \Delta} \right)$$

$$\begin{aligned}
& + H \left(\frac{\partial R_{i1}}{\partial \Delta} R_{j2} + R_{i1} \frac{\partial R_{j2}}{\partial \Delta} + \frac{\partial R_{i2}}{\partial \Delta} R_{j1} + R_{i2} \frac{\partial R_{j1}}{\partial \Delta} \right) \\
& + F \left(\frac{\partial R_{i1}}{\partial \Delta} R_{j3} + R_{i1} \frac{\partial R_{j3}}{\partial \Delta} + \frac{\partial R_{i2}}{\partial \Delta} R_{j3} + R_{i2} \frac{\partial R_{j3}}{\partial \Delta} \right. \\
& + \left. \frac{\partial R_{i3}}{\partial \Delta} R_{j1} + R_{i3} \frac{\partial R_{j1}}{\partial \Delta} + \frac{\partial R_{i3}}{\partial \Delta} R_{j2} + R_{i3} \frac{\partial R_{j2}}{\partial \Delta} \right) \\
& + C \left(\frac{\partial R_{i3}}{\partial \Delta} R_{j3} + R_{i3} \frac{\partial R_{j3}}{\partial \Delta} \right) \\
& + L \left(\frac{\partial R_{i4}}{\partial \Delta} R_{j4} + R_{i4} \frac{\partial R_{j4}}{\partial \Delta} + \frac{\partial R_{i5}}{\partial \Delta} R_{j5} \right) + R_{i5} \frac{\partial R_{j5}}{\partial \Delta} \\
& + N \left(\frac{\partial R_{i6}}{\partial \Delta} R_{j6} + R_{i6} \frac{\partial R_{j6}}{\partial \Delta} \right)
\end{aligned}$$

$$\frac{\partial \mathbf{R}}{\partial \theta} = \begin{bmatrix} -\sin 2\theta \cos^2 \varphi & 0 & \sin 2\theta \cos^2 \varphi \\ -\sin 2\theta \sin^2 \varphi & 0 & \sin 2\theta \sin^2 \varphi \\ \sin 2\theta & 0 & -\sin^2 \theta \\ \cos 2\theta \sin \varphi & 0 & \cos 2\theta \sin \varphi \\ -\frac{1}{2} \sin \theta \sin 2\varphi & 0 & -\cos 2\theta \cos \varphi \\ -\frac{1}{2} \sin 2\theta \sin 2\varphi & 0 & \frac{1}{2} \sin 2\theta \sin 2\varphi \end{bmatrix}$$

$$\begin{bmatrix} \cos \theta \sin 2\varphi & -2 \cos 2\theta \cos^2 \varphi & -\sin \theta \sin 2\varphi \\ \cos \theta \sin 2\varphi & -2 \cos 2\theta \sin^2 \varphi & \sin \theta \sin 2\varphi \\ 0 & 2 \cos 2\theta & 0 \\ -\sin \theta \cos \varphi & 2 \sin 2\theta \sin \varphi & \cos \theta \cos \varphi \\ -\sin \theta \sin \varphi & -2 \sin 2\theta \cos \varphi & \cos \theta \sin \varphi \\ -\cos \theta \cos \varphi & \cos 2\theta \sin 2\varphi & -\sin \theta \cos 2\varphi \end{bmatrix} \quad (\text{C.9})$$

$$\frac{\partial \mathbf{R}}{\partial \varphi} = \begin{bmatrix} -\cos^2 \theta \sin 2\varphi & \sin 2\varphi & -\sin^2 \theta \sin 2\varphi \\ \cos^2 \theta \sin 2\varphi & -\sin 2\varphi & \sin^2 \theta \sin 2\varphi \\ 0 & 0 & 0 \\ -\frac{1}{2} \sin 2\theta \cos \varphi & 0 & \frac{1}{2} \sin 2\theta \cos \varphi \\ \cos \theta \cos 2\varphi & 0 & \frac{1}{2} \sin 2\theta \sin \varphi \\ -\cos^2 \theta \cos 2\varphi & \cos 2\varphi & -\sin^2 \theta \cos 2\varphi \end{bmatrix}$$

$$\begin{bmatrix} -2 \sin \theta \cos 2\varphi & \sin 2\theta \sin 2\varphi & 2 \cos \theta \cos 2\varphi \\ 2 \sin \theta \cos 2\varphi & -\sin 2\theta \sin 2\varphi & -2 \cos \theta \cos 2\varphi \\ 0 & 0 & 0 \\ -\cos \theta \sin \varphi & -\cos 2\theta \cos \varphi & -\sin \theta \sin \varphi \\ \cos \theta \cos \varphi & -\cos 2\theta \sin \varphi & \sin \theta \cos \varphi \\ 2 \sin \theta \sin \varphi & \sin 2\theta \cos 2\varphi & -2 \cos \theta \sin 2\varphi \end{bmatrix}$$

(C.10)

Appendix D

SYMMETRY PLANES AND WAVE POLARIZATIONS

The polarization of the modes composing the seismo-acoustic wavefield depend on the propagation direction through the anisotropic medium. The polarization of any mode will change if the propagation direction changes or the elastic stiffness matrix is rotated. Pure P-SV and SH polarization directions exist in a TI elastically symmetric medium for specific propagation directions. The polarization of the modes is determined by the proximity of the propagation direction to the symmetry axis direction.

The form of the elastic stiffness matrix indicates the amount of symmetry and the location of symmetry planes for an anisotropic medium. These symmetry planes, help predict when transverse particle motion may propagate independently of the P-SV particle motion, or when quasi-SH particle motions propagates independently of quasi-P-SV particle motions.

Auld (1990) discusses pure plane-wave mode propagation directions in relation to symmetry planes and symmetry axes. The modes of a shallow water waveguide follow these same principles with a little modification. P, SV, and SH plane waves propagate independently for pure mode directions of propagation. For the modes of a shallow water wave guide, the P and SV particle motions are always coupled, but the SH particle motions may propagate independently for some geometries of the symmetry axis and propagation directions. If the SH motions coupled with either SV or P particle motions, then the modes will have polarizations in all three coordinate directions.

Whenever the propagation is within a symmetry plane, the single generalized

mode family splits into two independent mode families, and the SH modes will propagate independently of the P-SV modes. The propagation, in a sense will behave as quasi-isotropic. This is true regardless of whether the anisotropy is strong or weak. A VTI medium can be thought as a quasi-isotropic or quasi-orthorhombic medium. The wave propagation is similar to an isotropic medium, but the modes have slightly different shapes.

Consider rotating the elastic stiffness matrix, so that the symmetry axis \hat{s} first aligns with the three coordinate axes. When $\hat{s} = \hat{x}, \hat{y}$, or \hat{z} then the form of the elastic stiffness matrix remains in the *form* of a quasi-orthorhombic, with 12 non-zero matrix elements and the remainder having zero values:

$${}^a C_{IJ} = \begin{bmatrix} C_{11} & C_{12} & C_{13} & 0 & 0 & 0 \\ C_{21} & C_{22} & C_{23} & 0 & 0 & 0 \\ C_{31} & C_{32} & C_{33} & 0 & 0 & 0 \\ 0 & 0 & 0 & C_{44} & 0 & 0 \\ 0 & 0 & 0 & 0 & C_{55} & 0 \\ 0 & 0 & 0 & 0 & 0 & C_{66} \end{bmatrix} \quad \text{where } \hat{s} = \hat{x}, \hat{y}, \text{ or } \hat{z} \quad (\text{D.1})$$

For a VTI medium, all elements of the elastic stiffness matrix ${}^a C_{IJ}$ are unaltered by rotations about the z-axis.

An orthorhombic medium has the xy, xz, and yz-planes as symmetry planes, and the quasi-orthorhombic elastic stiffness matrix will have these symmetry planes as well. Applying symmetry principles for \hat{s} along any of the coordinate axes, the SH modes will propagate independently of the P-SV modes. The mode set is separated into two families of modes, the SH modes and the P-SV modes, when the \hat{s} is aligned with any of the three coordinate axes.

Now consider tilting the symmetry axis \hat{s} so that it remains in the xz-plane. The elastic stiffness matrix ${}^a C_{IJ}$ takes on the *form* of a monoclinic medium where the

single symmetry plane is orthogonal to the y-axis and parallel to the xz-plane.

$${}^a C_{IJ} = \begin{bmatrix} C_{11} & C_{12} & C_{13} & 0 & C_{15} & 0 \\ C_{21} & C_{22} & C_{23} & 0 & C_{25} & 0 \\ C_{31} & C_{32} & C_{33} & 0 & C_{35} & 0 \\ 0 & 0 & 0 & C_{44} & 0 & C_{46} \\ C_{51} & C_{52} & C_{53} & 0 & C_{55} & 0 \\ 0 & 0 & 0 & C_{64} & 0 & C_{66} \end{bmatrix} \quad \text{where } \hat{s}(\theta, \varphi) = \hat{s}(all, 0^\circ) \quad (D.2)$$

A monoclinic medium has a single plane of symmetry. Consider the form of the elastic stiffness matrix when the symmetry is parallel with the xz, yz, and xy-planes respectively. The tilted TI medium with the symmetry axis along one of the coordinate planes has the form of a monoclinic material, but with a higher degree of symmetry. A true monoclinic material has 13 independent parameters. The tilted TI medium only has five independent elastic moduli, even though the elastic stiffness matrix is populated the same as a monoclinic medium. The elastic stiffness tensor can be thought of exhibiting a quasi-monoclinic form, with higher symmetry due to a reduction in the number of independent elastic moduli.

For the symmetry axis in the xz-plane, the C_{22} element is insensitive to any variation in θ when $\varphi = 0^\circ$. This is of little consequence, since the C_{22} element is not included in the equation of motion for 2-D propagation along the x-direction. The horizontally polarized shear modes will propagate independently of the P-SV modes for all orientations of the symmetry axis that lie in the xz-plane. The modes are split into two families of propagating modes: P-SV modes with polarizations in the xz-plane and SH modes with polarizations in the transverse coordinate direction.

Now consider tilting the symmetry axis so that it remains in the yz-plane. The elastic stiffness matrix again takes on the *form* of a quasi-monoclinic medium where

the single symmetry plane is orthogonal to the x-axis and parallel to the yz-plane.

$${}^a C_{IJ} = \begin{bmatrix} C_{11} & C_{12} & C_{13} & C_{14} & 0 & 0 \\ C_{21} & C_{22} & C_{23} & C_{24} & 0 & 0 \\ C_{31} & C_{32} & C_{33} & C_{34} & 0 & 0 \\ C_{41} & C_{42} & C_{43} & C_{44} & 0 & 0 \\ 0 & 0 & 0 & 0 & C_{55} & C_{56} \\ 0 & 0 & 0 & 0 & C_{65} & C_{66} \end{bmatrix} \quad \text{where } \hat{s}(\theta, \varphi) = \hat{s}(all, 90^\circ) \quad (D.3)$$

The C_{11} element of the stiffness tensor is insensitive to any variations of θ when $\varphi = 90^\circ$.

The symmetry plane and symmetry axis principles indicate that no pure horizontally polarized modes should be expected when the elastic stiffness matrix is in this form, unless the symmetry axis \hat{s} is vertical or horizontal in the yz-plane. The principles indicate that the quasi-shear modes will have polarizations parallel to the symmetry axis, having both transverse and vertical components. The modes will likely consist of a single family of generalized P-SV-SH modes with polarizations in all three coordinate directions. The quasi-monoclinic elastic stiffness matrix has a higher degree of symmetry than a true monoclinic medium.

Next consider tilting the symmetry axis \hat{s} so that it remains in the xy-plane. The elastic stiffness matrix again takes on the *form* of a quasi-monoclinic medium with the single symmetry plane orthogonal to the z-axis and parallel to the xy-plane.

$${}^a C_{IJ} = \begin{bmatrix} C_{11} & C_{12} & C_{13} & 0 & 0 & C_{16} \\ C_{21} & C_{22} & C_{23} & 0 & 0 & C_{26} \\ C_{31} & C_{32} & C_{33} & 0 & 0 & C_{36} \\ 0 & 0 & 0 & C_{44} & C_{45} & 0 \\ 0 & 0 & 0 & C_{54} & C_{55} & 0 \\ C_{61} & C_{62} & C_{63} & 0 & 0 & C_{66} \end{bmatrix} \quad \text{where } \hat{s}(\theta, \varphi) = \hat{s}(90^\circ, all) \quad (D.4)$$

The C_{33} element of the elastic stiffness matrix is insensitive to any variations of φ for $\theta = 90^\circ$.

Now consider tilting the symmetry axis to a general orientation that excludes the coordinate axes directions and the xy , xz , and yz coordinate planes. The general *form* of the rotated ${}^a C_{IJ}$ elastic stiffness matrix is quasi-triclinic in nature with a higher degree of symmetry than a true triclinic elastic stiffness matrix. Similar to the monoclinic comparison, a true triclinic material has 21 independent elastic moduli. The rotated elastic stiffness matrix in equation (D.5) still only has 5 independent elastic moduli. Each element remains a linear combination of the five elastic moduli. So the rotated elastic stiffness matrix can be thought of being quasi-triclinic, with a higher degree of symmetry due to the reduction in the number of independent elastic moduli.

$${}^a C_{IJ} = \begin{bmatrix} C_{11} & C_{12} & C_{13} & C_{14} & C_{15} & C_{16} \\ C_{21} & C_{22} & C_{23} & C_{24} & C_{25} & C_{26} \\ C_{31} & C_{32} & C_{33} & C_{34} & C_{35} & C_{36} \\ C_{41} & C_{42} & C_{43} & C_{44} & C_{45} & C_{46} \\ C_{51} & C_{52} & C_{53} & C_{54} & C_{55} & C_{56} \\ C_{61} & C_{62} & C_{63} & C_{64} & C_{65} & C_{66} \end{bmatrix} \quad \text{where } \hat{s}(\theta, \varphi) \quad (\text{D.5})$$

Except when the symmetry axis \hat{s} is aligned with the x -axis or y -axis, the mode set consists of quasi-P-SV, quasi-SH, or generalized P-SV-SH modes.

The *form* of the elastic stiffness tensor may change as a TI medium rotates from a general orientation to more specific orientations. The elastic stiffness tensor of a TTI medium would be described as quasi-triclinic, the elastic stiffness tensor for a symmetry axis within any of the coordinate planes would be described as quasi-monoclinic, and the elastic stiffness tensor when the symmetry axis is aligned with any of the three coordinate axes would be quasi-orthorhombic.

Figure D.1 shows the *form* the elastic stiffness matrix takes for orientations of the symmetry axis $\hat{s}(\theta, \varphi)$ in the first quadrant. The vertical axis is the angle φ in 10° increments and the horizontal axis is the angle θ in 10° increments. Each matrix

represents the form of the elastic stiffness matrix ${}^a\mathbf{C}_{IJ}$ for a specific symmetry axis \hat{s} orientation. The first row shows the form of ${}^a\mathbf{C}_{IJ}$ for $\varphi = 0^\circ$ and $\theta = 0^\circ - 90^\circ$. This represents the symmetry axis within the sagittal plane and the elastic stiffness matrix has the *form* of a quasi-monoclinic medium. The first column shows the elastic stiffness matrix for $\hat{s} = \hat{z}$, with the form of a quasi-orthorhombic medium or VTI. The corner matrices of Figure D.1 in the tenth column also have the quasi-orthorhombic form and correspond to HTI media with the symmetry axis \hat{s} aligned parallel to the \hat{x} and \hat{y} axes. The tenth column shows the form of ${}^a\mathbf{C}_{IJ}$ for $\theta = 90^\circ$ and $\varphi = 0^\circ - 90^\circ$. This represents the symmetry axis within the xy-plane and the matrices have the form of a quasi-monoclinic medium. This also is a HTI medium where $\hat{s}(\theta, \varphi) = \cos \varphi \hat{x} + \sin \varphi \hat{y}$. The tenth row shows the form of the elastic stiffness matrices for $\phi = 90^\circ$ and $\varphi = 0^\circ - 90^\circ$. The matrices for \hat{s} in the yz-plane also have a quasi-monoclinic form. All other orientations of the symmetry axis for ${}^a\mathbf{C}_{IJ}$ produce the form of a quasi-triclinic medium. Okaya and McEvelly (2003) noticed similar results for rotations of hexagonal symmetry about the x, y, and z axes, and mentioned the appearance of monoclinic symmetry for rotations about the y-axis. Shoenberge and Costa (1991) also state that hexagonal anisotropy behaves as monoclinic when the symmetry axis is within the sagittal plane.

Yin and Cao (2002) report similar findings where a rhombohedral crystal symmetry can take the form of orthorhombic, monoclinic, and triclinic configurations. The difference between a true elastic stiffness matrix configuration and a quasi elastic stiffness configuration is in the number of independent moduli. The true elastic stiffness matrix configuration has a higher number of independent elastic moduli than the quasi elastic stiffness matrix of the same name. There are 21, 13, and 9 independent elastic moduli for the triclinic, monoclinic, and orthorhombic symmetric mediums respectively. For a rotated TI medium, the quasi-triclinic, quasi-monoclinic, and quasi-orthorhombic forms of the elastic stiffness matrix will only have 5 independent parameters.

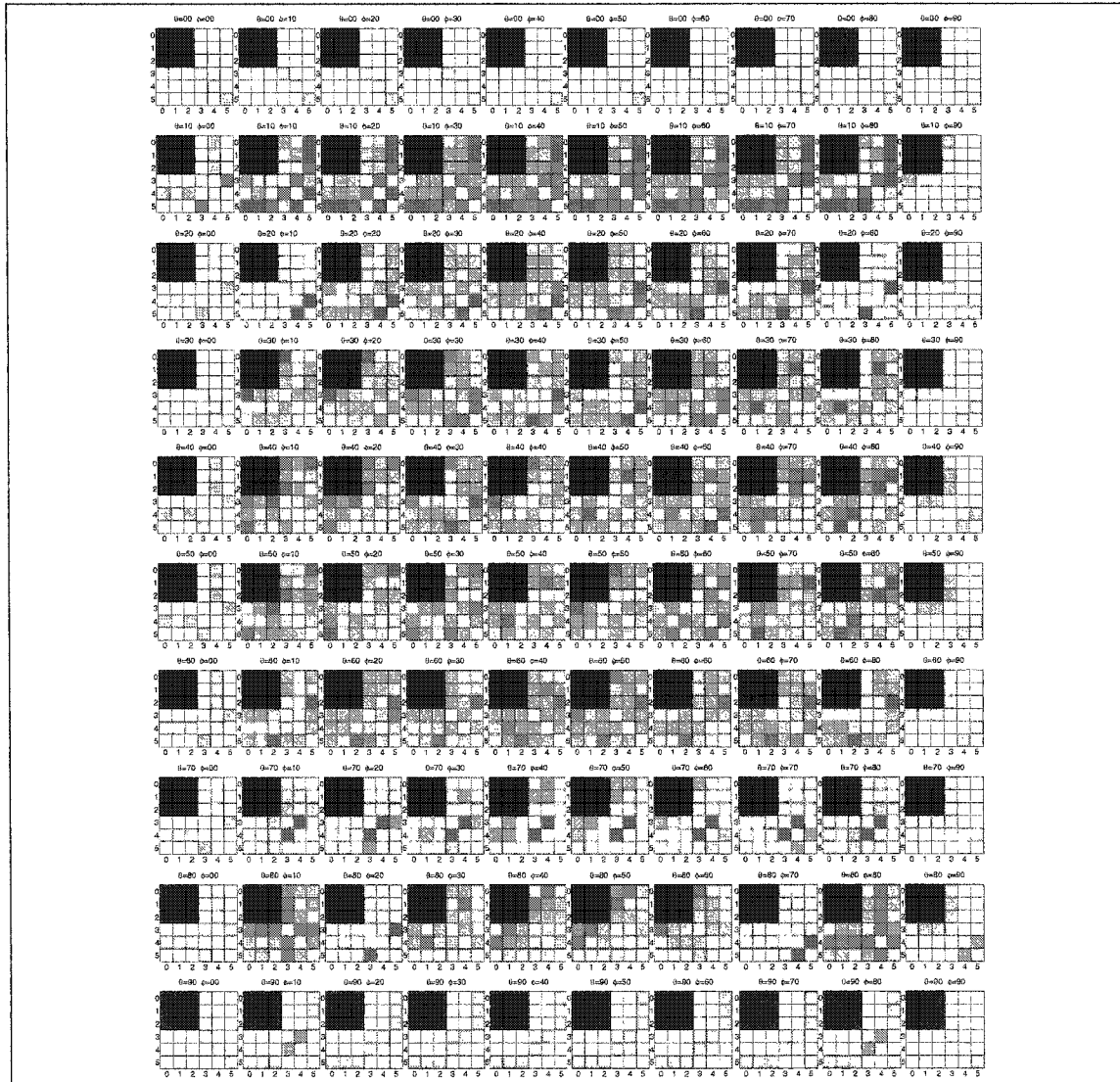
Bond Transformation of ${}^a C_{IJ}$ Matrix

Figure D.1: Each 6×6 matrix in the figure represents the elastic stiffness matrix ${}^a C_{IJ}$ for specific orientations of the symmetry axis \hat{s} , and indicates how ${}^a C_{IJ}$ is populated as \hat{s} is rotated. Each matrix in a horizontal row represents a 10° increment in φ for a fixed value of θ . Likewise, each matrix in a vertical column represents a 10° increment of θ for a fixed value of φ . The first row represents rotations about the y -axis, the last row represents rotations about the x -axis, and the last column represents rotations about the z -axis when \hat{s} is within the xy -plane. All of the matrices on the outside edges of the figure represent the elastic stiffness matrix being rotated about a coordinate axis and have a quasi-monoclinic form.

Appendix E

EQUATIONS OF MOTION AND FIRST ORDER EQUATIONS

Consider the equations of motion for elastic waves in anisotropic structures as described equation (3) of Maupin (1988).

$$-\rho\omega^2\mathbf{w} = \frac{\partial\mathbf{t}_1}{\partial x} + \frac{\partial\mathbf{t}_2}{\partial y} + \frac{\partial\mathbf{t}_3}{\partial z} + \mathbf{F}$$

$$\mathbf{t}_i = {}^w C_{ij} \frac{\partial\mathbf{w}}{\partial x_j} \quad (\text{E.1})$$

The characteristic equation can be expanded out for each individual traction vector.

$$\mathbf{t}_1 = {}^w C_{11} \frac{\partial\mathbf{w}}{\partial x} + {}^w C_{12} \frac{\partial\mathbf{w}}{\partial y} + {}^w C_{13} \frac{\partial\mathbf{w}}{\partial z} \quad (\text{E.2})$$

$$\mathbf{t}_2 = {}^w C_{21} \frac{\partial\mathbf{w}}{\partial x} + {}^w C_{22} \frac{\partial\mathbf{w}}{\partial y} + {}^w C_{23} \frac{\partial\mathbf{w}}{\partial z} \quad (\text{E.3})$$

$$\mathbf{t}_3 = {}^w C_{31} \frac{\partial\mathbf{w}}{\partial x} + {}^w C_{32} \frac{\partial\mathbf{w}}{\partial y} + {}^w C_{33} \frac{\partial\mathbf{w}}{\partial z} \quad (\text{E.4})$$

Now consider the the derivative with respect to x of \mathbf{w} and \mathbf{t}_1 . The derivatives are chosen to be expressed only in terms of material properties and the vectors \mathbf{w} and \mathbf{t}_1 :

$$\frac{\partial\mathbf{w}}{\partial x} = {}^w C_{11}^{-1} \mathbf{t}_1 - {}^w C_{11}^{-1} {}^w C_{12} \frac{\partial\mathbf{w}}{\partial y} + {}^w C_{11}^{-1} {}^w C_{13} \frac{\partial\mathbf{w}}{\partial z} \quad (\text{E.5})$$

$$\begin{aligned} \frac{\partial\mathbf{t}_1}{\partial x} = & -\rho\omega^2\mathbf{w} - \frac{\partial}{\partial y} \left(X_{22} \frac{\partial\mathbf{w}}{\partial y} \right) - \frac{\partial}{\partial y} \left(X_{23} \frac{\partial\mathbf{w}}{\partial z} \right) - \frac{\partial}{\partial y} \left({}^w C_{21} {}^w C_{11}^{-1} \mathbf{t}_1 \right) \\ & - \frac{\partial}{\partial z} \left(X_{32} \frac{\partial\mathbf{w}}{\partial y} \right) - \frac{\partial}{\partial z} \left(X_{33} \frac{\partial\mathbf{w}}{\partial z} \right) - \frac{\partial}{\partial z} \left({}^w C_{31} {}^w C_{11}^{-1} \mathbf{t}_1 \right) - \mathbf{F} \end{aligned} \quad (\text{E.6})$$

where the ${}^w X_{ij}$ matrix is defined as:

$${}^w X_{ij} = {}^w C_{ij} - ({}^w C_{i1})({}^w C_{11}^{-1})({}^w C_{1j}) \quad (\text{E.7})$$

Note that the ${}^w X_{ij}$ matrix is the same as Maupin's (1988) ${}^w Q_{ij}$ matrix.

Now consider \mathbf{w} and \mathbf{t}_2 and their derivative with respect to y . The derivatives are chosen to be expressed only in terms of material properties and the vectors \mathbf{w} and \mathbf{t}_2 :

$$\frac{\partial \mathbf{w}}{\partial y} = {}^w C_{22}^{-1} \mathbf{t}_2 - {}^w C_{22}^{-1} {}^w C_{21} \frac{\partial \mathbf{w}}{\partial x} + {}^w C_{22}^{-1} {}^w C_{23} \frac{\partial \mathbf{w}}{\partial z} \quad (\text{E.8})$$

$$\begin{aligned} \frac{\partial \mathbf{t}_2}{\partial y} = & -\rho\omega^2 \mathbf{w} - \frac{\partial}{\partial x} \left(Y_{11} \frac{\partial \mathbf{w}}{\partial x} \right) - \frac{\partial}{\partial x} \left(Y_{13} \frac{\partial \mathbf{w}}{\partial z} \right) - \frac{\partial}{\partial x} \left({}^w C_{12} {}^w C_{22}^{-1} \mathbf{t}_2 \right) \\ & - \frac{\partial}{\partial z} \left(Y_{31} \frac{\partial \mathbf{w}}{\partial x} \right) - \frac{\partial}{\partial z} \left(Y_{33} \frac{\partial \mathbf{w}}{\partial z} \right) - \frac{\partial}{\partial z} \left({}^w C_{32} {}^w C_{22}^{-1} \mathbf{t}_1 \right) - \mathbf{F} \end{aligned} \quad (\text{E.9})$$

where the ${}^w Y_{ij}$ matrix is defined as:

$${}^w Y_{ij} = {}^w C_{ij} - ({}^w C_{i2}) ({}^w C_{22}^{-1}) ({}^w C_{2j}) \quad (\text{E.10})$$

Similarly the derivatives of \mathbf{w} and \mathbf{t}_2 with respect to z may be considered. The derivatives are chosen to be expressed only in terms of material properties and the vectors \mathbf{w} and \mathbf{t}_3 :

$$\frac{\partial \mathbf{w}}{\partial z} = {}^w C_{33}^{-1} \mathbf{t}_3 - {}^w C_{33}^{-1} {}^w C_{31} \frac{\partial \mathbf{w}}{\partial x} + {}^w C_{33}^{-1} {}^w C_{32} \frac{\partial \mathbf{w}}{\partial y} \quad (\text{E.11})$$

$$\begin{aligned} \frac{\partial \mathbf{t}_3}{\partial z} = & -\rho\omega^2 \mathbf{w} - \frac{\partial}{\partial x} \left(Z_{11} \frac{\partial \mathbf{w}}{\partial x} \right) - \frac{\partial}{\partial x} \left(Z_{12} \frac{\partial \mathbf{w}}{\partial y} \right) - \frac{\partial}{\partial x} \left({}^w C_{13} {}^w C_{33}^{-1} \mathbf{t}_3 \right) \\ & - \frac{\partial}{\partial y} \left(Z_{21} \frac{\partial \mathbf{w}}{\partial x} \right) - \frac{\partial}{\partial y} \left(Z_{22} \frac{\partial \mathbf{w}}{\partial y} \right) - \frac{\partial}{\partial y} \left({}^w C_{23} {}^w C_{33}^{-1} \mathbf{t}_3 \right) - \mathbf{F} \end{aligned} \quad (\text{E.12})$$

where the ${}^w Z_{ij}$ matrix is defined as:

$${}^w Z_{ij} = {}^w C_{ij} - ({}^w C_{i3}) ({}^w C_{33}^{-1}) ({}^w C_{3j}) \quad (\text{E.13})$$

These three sets of equations can be reformulated into a single set of generalized equations of motion.

$$\begin{aligned} \frac{\partial \mathbf{w}}{\partial x_m} = & {}^w C_{mm}^{-1} \mathbf{t}_m - {}^w C_{mm}^{-1} {}^w C_{mi} \frac{\partial \mathbf{w}}{\partial x_i} + {}^w C_{mm}^{-1} {}^w C_{mj} \frac{\partial \mathbf{w}}{\partial x_j} \\ \frac{\partial \mathbf{t}_m}{\partial x_m} = & -\rho\omega^2 \mathbf{w} - \frac{\partial}{\partial x_i} \left(({}^w C_{ii} - {}^w C_{im} {}^w C_{mm}^{-1} {}^w C_{mi}) \frac{\partial \mathbf{w}}{\partial x_i} \right) \end{aligned} \quad (\text{E.14})$$

$$\begin{aligned}
& -\frac{\partial}{\partial x_i} \left(({}^w C_{ij} - {}^w C_{im} {}^w C_{mm}^{-1} {}^w C_{mj}) \frac{\partial \mathbf{w}}{\partial x_j} \right) \\
& -\frac{\partial}{\partial x_i} ({}^w C_{im} {}^w C_{mm}^{-1} \mathbf{t}_m) \\
& -\frac{\partial}{\partial x_j} \left(({}^w C_{ji} - {}^w C_{jm} {}^w C_{mm}^{-1} {}^w C_{mi}) \frac{\partial \mathbf{w}}{\partial x_i} \right) \\
& -\frac{\partial}{\partial x_j} \left(({}^w C_{jj} - {}^w C_{jm} {}^w C_{mm}^{-1} {}^w C_{mj}) \frac{\partial \mathbf{w}}{\partial x_j} \right) \\
& -\frac{\partial}{\partial x_j} ({}^w C_{jm} {}^w C_{mm}^{-1} \mathbf{t}_m) - \mathbf{F}
\end{aligned} \tag{E.15}$$

where $i, j, m = 1, 2, 3$, $i \neq m$, $j \neq m$, $i \neq j$, and $x_{i,j} = x, y, z$ and

An eigenvalue problem may be formulated from the generalized equations of motion, which results in a generalized first order coupled equation.

$$\frac{\partial \mathbf{u}^m}{\partial x_m} = \mathbf{A}^m \mathbf{u}^m - \mathbf{F} \quad \text{where } \mathbf{u}^m = (\mathbf{w}, \mathbf{t}_m)^T \tag{E.16}$$

$$\mathbf{A} = \begin{pmatrix} A_{11}^m & A_{12}^m \\ A_{21}^m & A_{22}^m \end{pmatrix} \tag{E.17}$$

For a solid triclinic anisotropic medium, the sub-operators for the generalized first order coupled equation are:

$$\begin{aligned}
A_{11}^m &= \left(-({}^w C_{mm}^{-1}) ({}^w C_{ii}) \frac{\partial}{\partial x_i} + ({}^w C_{mm}^{-1}) ({}^w C_{jj}) \frac{\partial}{\partial x_j} \right), \\
A_{12}^m &= ({}^w C_{mm}^{-1}), \\
A_{21}^m &= \left(-\rho \omega^2 \mathbf{w} - \frac{\partial}{\partial x_i} \left(({}^w C_{ii} - {}^w C_{im} {}^w C_{mm}^{-1} {}^w C_{mi}) \frac{\partial}{\partial x_i} \right) \right. \\
&\quad - \frac{\partial}{\partial x_i} \left(({}^w C_{ij} - {}^w C_{im} {}^w C_{mm}^{-1} {}^w C_{mj}) \frac{\partial}{\partial x_j} \right) - \frac{\partial}{\partial x_i} \\
&\quad - \frac{\partial}{\partial x_j} \left(({}^w C_{ji} - {}^w C_{jm} {}^w C_{mm}^{-1} {}^w C_{mi}) \frac{\partial}{\partial x_i} \right) \\
&\quad \left. - \frac{\partial}{\partial x_j} \left(({}^w C_{jj} - {}^w C_{jm} {}^w C_{mm}^{-1} {}^w C_{mj}) \frac{\partial}{\partial x_j} \right) - \frac{\partial}{\partial x_j} \right), \\
A_{22}^m &= \left(-\frac{\partial}{\partial x_i} ({}^w C_{im}) ({}^w C_{mm}^{-1}) - \frac{\partial}{\partial x_j} ({}^w C_{jm}) ({}^w C_{mm}^{-1}) \right),
\end{aligned} \tag{E.18}$$

Appendix F

DIFFERENTIAL OPERATOR A

The differential operator \mathbf{A} from the equation of motion (3.4) in the main text and in equation (F.1) below is described in greater detail.

$$\frac{\partial \mathbf{u}}{\partial x} = \mathbf{A} \mathbf{u} - \mathbf{F} \quad (\text{F.1})$$

where \mathbf{u} is the stress-displacement vector, \mathbf{A} is a differential operator which contains the combinations of the elastic stress matrix ${}^w C_{ij}$ and its derivatives, and \mathbf{F} is an external force.

The operator lacks any horizontal derivatives and the only derivatives are vertical derivatives of the elastic moduli, horizontal slowness, and eigenfunctions. For a fluid medium or a solid anisotropic structure, the differential operator \mathbf{A} may be expressed in terms of sub-operators:

$$\mathbf{A} = \begin{pmatrix} A^{11} & A^{12} \\ A^{21} & A^{22} \end{pmatrix} \quad (\text{F.2})$$

For a solid triclinic anisotropic medium, the sub-operators are:

$$\begin{aligned} A^{11} &= \left(-({}^w C_{11}^{-1})({}^w C_{13}) \frac{\partial}{\partial z} + ({}^w C_{11}^{-1})({}^w C_{12}) ip \right) \\ A^{12} &= ({}^w C_{11}^{-1}) \\ A^{21} &= \left(-\rho \omega^2 - \frac{\partial}{\partial z} ({}^w Q_{33} \frac{\partial}{\partial z}) + ip {}^w Q_{23} \frac{\partial}{\partial z} + \frac{\partial}{\partial z} ({}^w Q_{32} ip) + p^2 ({}^w Q_{22}) \right) \\ A^{22} &= \left(-\frac{\partial}{\partial z} ({}^w C_{31}) ({}^w C_{11}^{-1}) + ip ({}^w C_{21}) ({}^w C_{11}^{-1}) \right) \end{aligned} \quad (\text{F.3})$$

where the ${}^w Q_{ij}$ matrix is defined as:

$${}^w Q_{ij} = {}^w C_{ij} - ({}^w C_{i1}) ({}^w C_{11}^{-1}) ({}^w C_{1j}) \quad (\text{F.4})$$

This general form is valid for any triclinic anisotropic structure. The differential operator \mathbf{A} for a TI elastically symmetric medium can be obtained by substituting the elastic stiffness submatrices from Appendix A into equations (F.3),(F.3),F.3), and (F.3). The differential operator \mathbf{A} is then expressed analytically for the case when the symmetry axis \hat{s} is aligned with the Cartesian coordinate axes.

For $\hat{s}(\theta, \varphi) = \hat{s}(0^\circ, 0^\circ) = \hat{z}$:

$$\begin{aligned}
 A^{11} &= \begin{pmatrix} 0 & ik_y \frac{A-2N}{A} & -\frac{F}{A} \frac{\partial}{\partial z} \\ ik_y & 0 & 0 \\ -\frac{\partial}{\partial z} & 0 & 0 \end{pmatrix} \\
 A^{12} &= \begin{pmatrix} \frac{1}{A} & 0 & 0 \\ 0 & \frac{1}{N} & 0 \\ 0 & 0 & \frac{1}{L} \end{pmatrix} \\
 A^{21} &= \begin{pmatrix} -\rho\omega^2 & 0 & 0 \\ 0 & -\rho\omega^2 - \frac{\partial}{\partial z} \left(L \frac{\partial}{\partial z} \right) + k_y^2 \left(\frac{4N(N-A)}{A} \right) & ik_y \frac{2NF}{A} \frac{\partial}{\partial z} + \frac{\partial}{\partial z} (ik_y L) \\ 0 & ik_y L \frac{\partial}{\partial z} + \frac{\partial}{\partial z} \left(ik_y \frac{2NF}{A} \right) & -\rho\omega^2 - \frac{\partial}{\partial z} \left(\frac{AC-F^2}{A} \frac{\partial}{\partial z} \right) + k_y^2 L \end{pmatrix} \\
 A^{22} &= \begin{pmatrix} 0 & ik_y & -\frac{\partial}{\partial z} \\ ik_y \frac{A-2N}{A} & 0 & 0 \\ -\frac{\partial}{\partial z} \frac{F}{A} & 0 & 0 \end{pmatrix} \tag{F.5}
 \end{aligned}$$

Note that equations F.5-F.5 corrects equations (3.11)-(3.14) from Minkyu Park's dissertation (1997)

For $\hat{s}(\theta, \varphi) = \hat{s}(90^\circ, 0^\circ) = \hat{x}$:

$$\begin{aligned}
 A^{11} &= \begin{pmatrix} 0 & ik_y \frac{F}{C} & -\frac{F}{C} \frac{\partial}{\partial z} \\ ik_y & 0 & 0 \\ -\frac{\partial}{\partial z} & 0 & 0 \end{pmatrix} \\
 A^{12} &= \begin{pmatrix} \frac{1}{C} & 0 & 0 \\ 0 & \frac{1}{L} & 0 \\ 0 & 0 & \frac{1}{L} \end{pmatrix}
 \end{aligned}$$

$$\begin{aligned}
A^{21} &= \begin{pmatrix} -\rho\omega^2 & 0 & 0 \\ 0 & -\rho\omega^2 - \frac{\partial}{\partial z} \left(N \frac{\partial}{\partial z} \right) + k_y^2 \left(\frac{AC-F^2}{C} \right) & ik_y \left(\frac{AC-2CN-F^2}{C} \right) \frac{\partial}{\partial z} + \frac{\partial}{\partial z} (ik_y N) \\ 0 & ik_y N \frac{\partial}{\partial z} + \frac{\partial}{\partial z} \left(ik_y \frac{AC-2CN-F^2}{C} \right) & -\rho\omega^2 - \frac{\partial}{\partial z} \left(\frac{AC-F^2}{C} \frac{\partial}{\partial z} \right) + k_y^2 N \end{pmatrix} \\
A^{22} &= \begin{pmatrix} 0 & ik_y & -\frac{\partial}{\partial z} \\ ik_y \frac{F}{C} & 0 & 0 \\ -\frac{\partial}{\partial z} \frac{F}{C} & 0 & 0 \end{pmatrix} \tag{F.6}
\end{aligned}$$

For $\hat{s}(\theta, \varphi) = \hat{s}(90^\circ, 90^\circ) = \hat{y}$:

$$\begin{aligned}
A^{11} &= \begin{pmatrix} 0 & ik_y \frac{F}{A} & -\frac{A-2N}{A} \frac{\partial}{\partial z} \\ ik_y & 0 & 0 \\ -\frac{\partial}{\partial z} & 0 & 0 \end{pmatrix} \\
A^{12} &= \begin{pmatrix} \frac{1}{A} & 0 & 0 \\ 0 & \frac{1}{L} & 0 \\ 0 & 0 & \frac{1}{N} \end{pmatrix} \\
A^{21} &= \begin{pmatrix} -\rho\omega^2 & 0 & 0 \\ 0 & -\rho\omega^2 - \frac{\partial}{\partial z} \left(L \frac{\partial}{\partial z} \right) + k_y^2 \left(\frac{AC-F^2}{A} \right) & ik_y \left(\frac{2NF}{A} \right) \frac{\partial}{\partial z} + \frac{\partial}{\partial z} (ik_y L) \\ 0 & ik_y L \frac{\partial}{\partial z} + \frac{\partial}{\partial z} \left(ik_y \frac{2NF}{A} \right) & -\rho\omega^2 - \frac{\partial}{\partial z} \left(\frac{4N(N-A)}{A} \frac{\partial}{\partial z} \right) + k_y^2 L \end{pmatrix} \\
A^{22} &= \begin{pmatrix} 0 & ik_y & -\frac{\partial}{\partial z} \\ ik_y \frac{F}{A} & 0 & 0 \\ -\frac{\partial}{\partial z} \frac{A-2N}{A} & 0 & 0 \end{pmatrix} \tag{F.7}
\end{aligned}$$

Additional symmetry, where the TI elastic symmetry reduces to isotropic symmetry may be considered. When $A = C$, $L = N$, $H = F$, and $F = A - 2L$, then all planes within medium are symmetry planes, and therefore all directions are equivalent:

$$A^{11} = \begin{pmatrix} 0 & ik_y \frac{F}{A} & -\frac{F}{A} \frac{\partial}{\partial z} \\ ik_y & 0 & 0 \\ -\frac{\partial}{\partial z} & 0 & 0 \end{pmatrix}$$

$$\begin{aligned}
A^{12} &= \begin{pmatrix} \frac{1}{A} & 0 & 0 \\ 0 & \frac{1}{L} & 0 \\ 0 & 0 & \frac{1}{L} \end{pmatrix} \\
A^{21} &= \begin{pmatrix} -\rho\omega^2 & 0 & 0 \\ 0 & -\rho\omega^2 - \frac{\partial}{\partial z} \left(L \frac{\partial}{\partial z} \right) + k_y^2 \left(\frac{A^2 - F^2}{A} \right) & ik_y \left(\frac{AF - F^2}{A} \right) \frac{\partial}{\partial z} + \frac{\partial}{\partial z} (ik_y L) \\ 0 & ik_y L \frac{\partial}{\partial z} + \frac{\partial}{\partial z} \left(ik_y \left(\frac{AF - F^2}{A} \right) \right) & -\rho\omega^2 - \frac{\partial}{\partial z} \left(\frac{F^2 - A^2}{A} \frac{\partial}{\partial z} \right) + k_y^2 L \end{pmatrix} \\
A^{22} &= \begin{pmatrix} 0 & ik_y & -\frac{\partial}{\partial z} \\ ik_y \frac{F}{A} & 0 & 0 \\ -\frac{\partial}{\partial z} \frac{F}{A} & 0 & 0 \end{pmatrix} \tag{F.8}
\end{aligned}$$

where $A = \lambda + 2\mu$, $L = \mu$, and $F = \lambda$.

This is the same result as reported by Park and Odom (1998) and Maupin (1988).

Consider the case where $\mu = 0$ and the isotropic medium becomes an isotropic fluid.

As stated by Maupin (1988), the ${}^w C_{11}$ matrix becomes singular for a fluid layer. A simple solution is to define the ${}^w C_{11}$ matrix and its inverse ${}^w C_{11}^{-1}$ within a fluid as Kennett (1983) does in his monograph:

$$({}^w C_{11})_{fluid} = \begin{pmatrix} A & 0 & 0 \\ 0 & 0 & 0 \\ 0 & 0 & 0 \end{pmatrix} \quad ({}^w C_{11}^{-1})_{fluid} = \begin{pmatrix} \frac{1}{A} & 0 & 0 \\ 0 & 0 & 0 \\ 0 & 0 & 0 \end{pmatrix} \tag{F.9}$$

Therefore, a form of the differential operator and equation of motion for any fluid layers may be formulated.

$$\begin{aligned}
A^{11} &= \begin{pmatrix} 0 & ik_y & -\frac{\partial}{\partial z} \\ ik_y & 0 & 0 \\ -\frac{\partial}{\partial z} & 0 & 0 \end{pmatrix} \\
A^{12} &= \begin{pmatrix} \frac{1}{A} & 0 & 0 \\ 0 & 0 & 0 \\ 0 & 0 & 0 \end{pmatrix}
\end{aligned}$$

$$\begin{aligned}
A^{21} &= \begin{pmatrix} -\rho\omega^2 & 0 & 0 \\ 0 & -\rho\omega^2 & 0 \\ 0 & 0 & -\rho\omega^2 \end{pmatrix} \\
A^{22} &= \begin{pmatrix} 0 & ik_y & -\frac{\partial}{\partial z} \\ ik_y & 0 & 0 \\ -\frac{\partial}{\partial z} & 0 & 0 \end{pmatrix}
\end{aligned} \tag{F.10}$$

After some algebra, the system of equations can be reduced to a two component displacement-stress vector form.

$$\mathbf{A}_{fluid} = \begin{pmatrix} 0 & -\frac{ik_y^2}{\rho\omega^2} + \frac{\partial}{\partial z} \frac{1}{\rho\omega^2} \frac{\partial}{\partial z} + \frac{1}{A} \\ -\rho\omega^2 & 0 \end{pmatrix} \tag{F.11}$$

where \mathbf{u} , w_2 , w_3 , and t are defined as:

$$\mathbf{u} = (w_1, t)^T \tag{F.12}$$

$$w_2 = \frac{ik_y}{\rho\omega^2} t \tag{F.13}$$

$$w_3 = -\frac{1}{\rho\omega^2} \frac{\partial t}{\partial z} \tag{F.14}$$

$$t = t_{ii} \tag{F.15}$$

This is Maupin's (1988) result for a fluid layer. The fluid/solid coupling terms used in the main text are the same as those reported in Maupin (1988). Tromp (1994) also has described fluid/solid coupling terms using a slightly different modal notation.

Appendix G

**DETERMINISTIC AND STOCHASTIC COUPLING
MATRICES**

The \mathbf{B}_{qr} coupling matrix as described by Maupin (1988) and the main text is defined as:

$$\mathbf{B}_{qr} = \left(- \left\langle \mathbf{u}^q, \frac{\partial \mathbf{u}^r}{\partial x} \right\rangle + i \sum_n \dot{h}_n \mathbf{w}^{q*} [\mathbf{t}^r]_n \right) \exp \left(i \int_0^x (k^q - k^r) d\xi \right) \quad (\text{G.1})$$

where the Hermitian scalar product is defined as

$$\langle \mathbf{u}^q, \mathbf{u}^r \rangle = i \int_0^\infty (\mathbf{w}^q \mathbf{t}^r - \mathbf{t}^q \mathbf{w}^r) dz \quad (\text{G.2})$$

The traction \mathbf{t} may be discontinuous across the interfaces, resulting in the evaluation of an improper integral. This leads to interface summation terms that include jumps across the boundary discontinuities. The coupling matrix for an unperturbed, deterministic structure has the expanded form:

$$\begin{aligned} \mathbf{B}_{qr} = & \frac{1}{k^q - k^r} \left(\int_0^{h_f(x)} \left(w_1^{q*} \dot{\rho} \omega^2 w_1^r + \mathbf{t}^{q*} \left(\frac{1}{\lambda} - \frac{p^2}{\rho \omega^2} \right) \mathbf{t}^r - \frac{\partial \mathbf{t}^{q*}}{\partial z} \frac{i}{\rho \omega^2} \frac{\partial \mathbf{t}^r}{\partial z} \right) dz \right. \\ & + \int_{h_f(x)}^\infty \left(\mathbf{w}^{q*} \dot{\rho} \omega^2 \mathbf{w}^r - \frac{\partial \mathbf{w}^{q*}}{\partial z} Q_{33} \frac{\partial \mathbf{w}^r}{\partial z} - \mathbf{w}^{q*} ip Q_{23} \frac{\partial \mathbf{w}^r}{\partial z} + \frac{\partial \mathbf{w}^{q*}}{\partial z} Q_{32} ip \mathbf{w}^r \right. \\ & - \mathbf{w}^{q*} Q_{22} \mathbf{w}^r p^2 - \frac{\partial \mathbf{w}^{q*}}{\partial z} (C_{31} C_{11}^{-1}) \mathbf{t}^r - \mathbf{w}^{q*} ip (C_{21} C_{11}^{-1}) \mathbf{t}^r - \mathbf{t}^{q*} (C_{11}^{-1} C_{13}) \frac{\partial \mathbf{w}^r}{\partial z} \\ & \left. \left. + \mathbf{t}^{q*} (C_{11}^{-1} C_{12}) ip \mathbf{w}^r + \mathbf{t}^{q*} C_{11}^{-1} \mathbf{t}^r \right) dz \right. \\ & + \sum_n \dot{h}_n \left[- \mathbf{w}^{q*} \rho \omega^2 \mathbf{w}^r - \frac{\partial \mathbf{w}^{q*}}{\partial z} Q_{33} \frac{\partial \mathbf{w}^r}{\partial z} + \mathbf{w}^{q*} Q_{22} \mathbf{w}^r p^2 - \frac{\partial \mathbf{w}^{q*}}{\partial z} (C_{31} C_{11}^{-1}) \mathbf{t}^r \right. \\ & \left. - \mathbf{t}^{q*} (C_{11}^{-1} C_{13}) \frac{\partial \mathbf{w}^r}{\partial z} + \mathbf{t}^{q*} C_{11}^{-1} \mathbf{t}^r \right]_n \end{aligned}$$

$$\begin{aligned}
& - \dot{h} \left(-\frac{\partial t_{33}^{q*}}{\partial z} \frac{1}{\rho\omega^2} \frac{\partial t_{33}^r}{\partial z} - t_{33}^{q*} \left(\frac{1}{\lambda} - \frac{p^2}{\rho\omega^2} \right) t_{33}^r + w_1^{q*} \rho\omega^2 w_1^r \right) \Big|_{h_f(x)^-} \\
& - i\dot{h} \left((k^q - k^r)(w_1^{q*} t_{33}^r + t_{33}^{q*} w_1^r) \right) \Big|_{h_f(x)^+} \exp \left(i \int_0^x (k^q - k^r) d\xi \right) \quad (G.3)
\end{aligned}$$

When the horizontal derivatives of the elastic moduli are zero, the volume terms of the coupling matrix \mathbf{B}_{qr} become zero, and only the interface terms of the \mathbf{B}_{qr} matrix remain. All fluid-fluid interface terms have been neglected and their contribution to the coupling terms is assumed negligible. Therefore, in the absence of material property variations, the coupling matrix reduces to:

$$\begin{aligned}
\mathbf{B}_{qr} &= \frac{1}{k^q - k^r} \left(\sum_n \dot{h}_n \left[-\mathbf{w}^{q*} \rho\omega^2 \mathbf{w}^r - \frac{\partial \mathbf{w}^{q*}}{\partial z} Q_{33} \frac{\partial \mathbf{w}^r}{\partial z} + \mathbf{w}^{q*} Q_{22} \mathbf{w}^r p^2 \right. \right. \\
&\quad \left. \left. - \frac{\partial \mathbf{w}^{q*}}{\partial z} (C_{31} C_{11}^{-1}) \mathbf{t}^r - \mathbf{t}^{q*} (C_{11}^{-1} C_{13}) \frac{\partial \mathbf{w}^r}{\partial z} + \mathbf{t}^{q*} C_{11}^{-1} \mathbf{t}^r \right]_n \right) \\
&- \dot{h} \left(-\frac{\partial t_{33}^{q*}}{\partial z} \frac{1}{\rho\omega^2} \frac{\partial t_{33}^r}{\partial z} - t_{33}^{q*} \left(\frac{1}{\lambda} - \frac{p^2}{\rho\omega^2} \right) t_{33}^r + w_1^{q*} \rho\omega^2 w_1^r \right) \Big|_{h_f(x)^-} \\
&- i\dot{h} \left((k^q - k^r)(w_1^{q*} t_{33}^r + t_{33}^{q*} w_1^r) \right) \Big|_{h_f(x)^+} \exp \left(i \int_0^x (k^q - k^r) d\xi \right) \quad (G.4)
\end{aligned}$$

This is the \mathbf{B}_{qr} deterministic interface term coupling matrix.

When the horizontal derivatives of the interface boundaries are zero, the interface terms of the coupling matrix \mathbf{B}_{qr} become zero, and only the volume terms of the \mathbf{B}_{qr} matrix remain. All fluid-fluid volume terms have been neglected and their contribution to the coupling terms is assumed negligible. Therefore, in the absence of geometrical boundary variations, the coupling matrix reduces to:

$$\begin{aligned}
\mathbf{B}_{qr} &= \frac{1}{k^q - k^r} \left(\int_{h(x)}^\infty \left(\mathbf{w}^{q*} \rho\omega^2 \mathbf{w}^r - \frac{\partial \mathbf{w}^{q*}}{\partial z} Q_{33} \frac{\partial \mathbf{w}^r}{\partial z} - \mathbf{w}^{q*} ip Q_{23} \frac{\partial \mathbf{w}^r}{\partial z} \right. \right. \\
&\quad + \frac{\partial \mathbf{w}^{q*}}{\partial z} Q_{32} ip \mathbf{w}^r - \mathbf{w}^{q*} Q_{22} \mathbf{w}^r p^2 - \frac{\partial \mathbf{w}^{q*}}{\partial z} (C_{31} C_{11}^{-1}) \mathbf{t}^r - \mathbf{w}^{q*} ip (C_{21} C_{11}^{-1}) \mathbf{t}^r \\
&\quad \left. \left. - \mathbf{t}^{q*} (C_{11}^{-1} C_{13}) \frac{\partial \mathbf{w}^r}{\partial z} + \mathbf{t}^{q*} (C_{11}^{-1} C_{12}) ip \mathbf{w}^r + \mathbf{t}^{q*} C_{11}^{-1} \mathbf{t}^r \right) dz \right) \quad (G.5)
\end{aligned}$$

This is the \mathbf{B}_{qr} deterministic volume term coupling matrix.

The scattered coupling matrix \mathbf{H}_{qr} is defined similarly to the \mathbf{B}_{qr} matrix:

$$\mathbf{H}_{qr} = (\langle \mathbf{u}^q, A_1 \mathbf{u}^r \rangle) \exp \left(i \int_0^x k^r(\xi) d\xi \right) \quad (\text{G.6})$$

The terms of the scattering coupling matrix contain the stochastic function $\gamma(x, z)$:

$$\begin{aligned} \mathbf{H}_{qr} = & i \left(\int_{h_f(x)}^{\infty} \left(-\mathbf{w}^{q*} \gamma(x, z) \rho' \omega^2 \mathbf{w}^r + \frac{\partial \mathbf{w}^{q*}}{\partial z} \gamma(x, z) Q'_{33} \frac{\partial \mathbf{w}^r}{\partial z} \right. \right. \\ & + \mathbf{w}^{q*} i p \gamma(x, z) Q'_{23} \frac{\partial \mathbf{w}^r}{\partial z} - \frac{\partial \mathbf{w}^{q*}}{\partial z} \gamma(x, z) Q'_{32} i p \mathbf{w}^r + \mathbf{w}^{q*} \gamma(x, z) Q'_{22} \mathbf{w}^r p^2 \\ & + \frac{\partial \mathbf{w}^{q*}}{\partial z} \gamma(x, z) (C_{31} C_{11}^{-1})' \mathbf{t}^r + \mathbf{w}^{q*} i p \gamma(x, z) (C_{21} C_{11}^{-1})' \mathbf{t}^r \\ & + \mathbf{t}^{q*} \gamma(x, z) (C_{11}^{-1} C_{13})' \frac{\partial \mathbf{w}^r}{\partial z} + \mathbf{t}^{q*} \gamma(x, z) (C_{11}^{-1} C_{12})' i p \mathbf{w}^r \\ & \left. \left. - \mathbf{t}^{q*} \gamma(x, z) C_{11}^{-1} \mathbf{t}^r \right) dz + i \sum_n \left[\mathbf{w}^{q*} \gamma(x, z) \left(Q'_{33} \frac{\partial \mathbf{w}^r}{\partial z} - Q'_{32} i p \mathbf{w}^r \right. \right. \right. \\ & \left. \left. \left. + (C_{31} C_{11}^{-1})' \mathbf{t}^r \right) \right] \right) \exp \left(i \int_0^x (k^q - k^r) d\xi \right) \quad (\text{G.7}) \end{aligned}$$

The volume scattering matrix \mathbf{H}_{qr} contains both volume terms and interface terms. The interface terms arise out of evaluating the volume integral and integrating by parts.

VITA

Darin J. Soukup earned a Bachelor of Science degree in Physics from California Polytechnic State University, San Luis Obispo, CA in 1996. He earned a Doctor of Philosophy in Geophysics from the University of Washington in 2004.

Orcutt, J., C. de Groot-Hedlin, W. Hodgkiss, W. Kupwerman, W. Munk, F. Vernon, P. Worcester, E. Bernard, R. Dziak, C. Fox, C.S. Chiu, C. Collins, J. Mercer, R. Odom, M. Park, D. Soukup, R. Spindel, 2000. Long-term Observations in Acoustics - the Ocean Acoustic Observatory Federation, *Oceanography*, Vol. **13**, 57-63.

Park, M., R.I. Odom, and D. Soukup, 2001. Modal scattering: a key to understanding oceanic *T*-waves, *Geophys. Res. Lett.*, Vol. **28**, 3401-3404.

Hoffman, K.A. and D.J. Soukup, 1996. Evidence for episodes of predictable field behavior during the Matuyama-Brunhes reversal from Tahitian lavas, (Abstract), *EOS Trans. AGU*, Vol. **77**, Fall Meet. Suppl., F171.

Soukup, D.J., R.I. Odom, J. Park, 1997. Mode Coupling in Laterally Heterogeneous Layered Anisotropic Media, (Abstract), *EOS Transactions*, Vol. **78**, F424.

Soukup, D.J., R.I. Odom, J. Park, 1998. Mode Coupling of quasi-Love and quasi-Rayleigh Waves in Laterally Heterogeneous Media, (Abstract), *EOS Trans. AGU*, Vol. **79**, Fall Meet. Suppl., F625.

Soukup, D.J., R.I. Odom, and J. Park, 1999. Coupling to SH as a Loss Mechanism in Shallow Water Acoustic Propagation, (Abstract), *J. Acoust. Soc. Am.*, Vol.

105, 1362.

Soukup, D.J., R.I. Odom, and J. Park, 1999. A Mode Coupling Mechanism for Scattering Quasi-Love and Quasi-Rayleigh Waves in Heterogeneous Anisotropic Media, (Abstract), *Seis. Res. Lett.*, Vol. **70**, 258.

Soukup, D.J. and R.I. Odom , 1999. Local Coupled Mode Approach to Volume Scattering in Anisotropic Laterally Heterogeneous Media, (Abstract), *EOS Trans. AGU*, Vol. **80**, Fall Meet. Suppl., F917.

Park, M., D.J. Soukup, and R.I. Odom, 2000. Effects of Fault Orientation and Seabottom Roughness on *T*-phase Excitation, (Abstract), *EOS Trans. AGU*, Vol. **81**, F844.

Park, M., D.J. Soukup, and R.I. Odom, 2000. Modal Conversion by Rough Surface Scattering: The Key to the *T*-phase, (Abstract), *J. Acoust. Soc. Am.*, Vol. **108**, Pt. 2, 2486.

Soukup, D.J. and R.I. Odom , 2000. Volume Scattering in Anisotropic Laterally Heterogeneous Media - Modeling Wave Propagation with Local Coupled Modes, (Abstract), *EOS Trans. AGU*, Vol. **81**, F916.

Soukup, D.J. and R.I. Odom , 2001. Continuum Spectrum and Radiation Pattern Contributions to *T*-wave excitation, *EOS Trans. AGU*, Vol. **92**, Fall Meeting Suppl., (Abstract), Vol. S21A-0556, F832.

Odom, R.I. and D.J. Soukup , 2002. *T*-wave sources, slopes, rough bottoms and continuum, (Abstract), *J. Acoust. Soc. Am.*, Vol. **111**, Pt. 2, 2387.

Soukup, D.J. and R.I. Odom , 2003. Local coupled modes and volume scattering in heterogeneous anisotropic shallow water environments, (Abstract), *J. Acoust.*

Soc. Am., Vol. **113**, Pt. 2, 2334.

Odom, R.I., and D.J. Soukup , 2004. Modal scattering and *T*-waves: Sediment amplification and source effects, (Abstract), *J. Acoust. Soc. Am.*, Vol. **115**, Pt. 2, 2445.